Department of Mechanical Engineering

Large-Eddy Simulations of Flow and Heat Transfer for Jet Impingement on Static and Vibrating Surfaces

Thangam Natarajan

This thesis is presented for the Degree of
Doctor of Philosophy
of
Curtin University

March 2017

Declaration

To the best of my knowledge and belief this thesis contains no material previously published by any other person except where due acknowledgement has been made.
This thesis contains no material which has been accepted for the award of any other degree or diploma in any university.

Signature: .....

Date: 17 - 03 - 2017

Acknowledgements

I am indebted to Prof. Tony Lucey, Dr Ramesh Narayanaswamy, Dr James Jewkes (now at Coventry) and Dr Yongmann Chung (Warwick) for giving me this opportunity in the first place and allowing me to learn from your collective knowledge and experience over the last four years. Dr James has always been a great source of inspiration and support who always confided in me and never stopped encouraging. Prof. Tony's patience, knowledge of Fluid Mechanics and advice on research, in general, was inspiring. Dr Ramesh has been a great source of support and his nature of always willing to help has made this PhD experience all the more cherishable. Special thanks to Dr Yongmann for hosting me at the University of Warwick and for all his patience, and his insights on CFD and turbulence research was a treat.

I am thankful to the members of the FDRG group at Curtin for all the wonderful discussions on all aspects of fluid dynamics. I especially thank Dr Abishek Sridhar for all the insightful discussions and support which have been immensely helpful. I also thank Dr Kristoffer Mckee for providing me with an opportunity to teach and was a remarkable experience working with him. I am grateful to Dr Andrew King for helping me with various issues with fluid dynamics and OpenFOAM. I wish to thank the administrative team Ms Sucy Leong, Ms Sharon Quek, Ms YingHong Lin, Ms Margaret Brown and Mr Frankie Sia for always being friendly, ready to help and being on top of their roles all the time. You made my life much easier.

Thanks to Vishal Chaugule and all the others on "Team Curtin" for their constant support and random outings making my stay more memorable. I am also thankful to Mr Sathish for his constant support and continued guidance. Chandru anna and Neela for always being there. Santhosh, Bala, Aparna, Ravi, Yadi, Mire & Isa who have never failed to poke fun at me. I also thank my in-laws Mr & Mrs Subramaniam for their kind support. Finally, words aren't enough to thank my family. I am so grateful to my wife Divya for bearing with me. Whether be it the long hours at work or me being a stressed PhD student, she has always been understanding and

been a great source of strength and comfort. My mother who sacrificed her life and dreams so that I could fulfil mine. My father whom I dearly miss and hope is watching from above - I dedicate this thesis to you.

Abstract

Jet impingement on a surface is a canonical flow field that has been exploited for its efficient heat and mass transfer across a range of applications despite its simple geometric construction. This research was motivated by the applications where the jet impinges on a dynamic target surface as opposed to a static surface. The present work serves to understand the flow dynamics and thermal characteristics of a turbulent impinging air jet under highly dynamic flow and geometric conditions.

This study attempts to address two problems: Firstly, the development of a computational framework that is capable of using Large-eddy simulations (LES) to simulate turbulent flow and heat transfer under jet impingement on static and dynamic target surfaces, and secondly, the simulation of jet impingement on a dynamic, heated target surface and the variations in the parameter space. The approach involved assembling the framework through validation of sub-systems; in particular, the method for generating the turbulent jet inflow, the spatially developing free jet, and the baseline circular jet impingement configuration on a static impingement surface. The recycled boundary condition was successfully applied to a smooth pipe flow at $Re_D = 24{,}600$ to generate a fully-developed turbulent inflow. This technique was deemed suitable and was adapted to turbulent inflow for simulations needing such inlet conditions (such as nozzle inlet for impinging jet simulations) without having to run redundant pipe flow simulations externally. A spatially developing free jet was simulated, and the spatial accuracy requirements and the need to capture the instabilities addressed. A quality index or 'resolvedness' was used to measure the quality of the LES and showed that the shear layer in a jet is the most mesh-intensive region and requires a greater resolution to capture precisely its dynamics characteristics. The near-wall anisotropy was studied for both the round and planar jet impingement configurations through invariant maps. The model developed in this study is capable of predicting the nature of near-wall turbulence accurately. Significant differences in the near-wall statistics of a two-dimensional planar jet and a three-dimensional round jet impingement configuration are shown.

With the combination of all these fully-evaluated methods, the framework was applied to a turbulent jet impingement configuration with a static impingement surface supplied with a uniform heat flux; first simulated using Reynolds Averaged Navier-Stokes (RANS) method and then using LES. The RANS results showed that the mean flow statistics were reproduced with reasonable accuracy whereas the lack of instantaneous data and the poor predictions of surface heat transfer required a highly resolved LES to capture the flow and heat transfer precisely. Both the first order and second order turbulence statistics were reproduced with great accuracy when compared with published experimental studies. It was also shown that the azimuthal resolution was far more important compared to the radial resolution to reproduce the secondary Nusselt number peak.

High-resolution simulations (LES) were then performed for an incompressible turbulent circular jet impinging upon a vibrating heated wall supplied with a uniform heat flux. The baseline circular vibrating-wall jet impingement configuration undergoes a forced vibration in the wall-normal direction at the frequency, $f = 100$ Hz. The jet Reynolds number based on the nozzle diameter D, the bulk velocity V_b and kinematic viscosity ν is $Re = DV_b/\nu =$ 23,000 and the nozzle-exit is located at $y/D = 2$, where the wall vibrates between 0 and $0.5D$ with amplitude of vibration, $A = 0.25D$. The mean radial velocity increases upon positive displacement of the wall and decreases upon negative displacement but this correlation changes with increased radial distance from the stagnation point. Vortical structures are shown to play a major role in convective heat transfer under both static and vibrating conditions of the impingement wall. Periodic shifts in the secondary Nusselt number peak are observed that depend upon the travelling eddy location and strength of large-eddy structures. Enhancement in heat transfer is seen in the stagnation region, but the beneficial effect of vibration on heat transfer is confined to the impingement region, $r/D < 1.5$, for the cases investigated.

The effect of forcing parameters was explored in the parameter space for a jet impingement configuration at Re of 10,000 with a mean nozzle-to-wall distance of $2.0D$. Four configurations were chosen with a diverse set of forcing parameters based on the natural frequency of the jet impinging on a static wall. Based on this information, two amplitudes, $0.125D$, $0.25D$ and two frequencies, 60 Hz and 120 Hz were used for the investigations. The instantaneous, phase-averaged and time-averaged quantities showed that the impingement surface vibration affects the large-scale structures in the fluid domain. Reverse flows and low-velocity pockets are seen to increase with the increase in the magnitude of forcing parameters creating a weak stagnation plane in the axial jet. In addition, the fluid leaving through the top boundary of the domain substantially increased. The large-scale structures were excited irrespective of the Reynolds number and resonated at the applied impingement wall frequency. However, with

the increase in the magnitude of the forcing parameters, the flow field was found to become increasingly unsteady, making it harder to visualise large-scale primary and secondary structures in the domain. The counter-rotating secondary vortical structures were not detected in the extreme forcing case. These structures were found to be depend strongly on the amplitude of vibration rather than the frequency of wall vibration. The heat transfer was also seen to be affected by the impingement surface vibration; however, the effect diminishes beyond a radial distance of $r/D = 1.5$ across all the configurations investigated.

Publications arising from this work

Peer reviewed journal publications

T. Natarajan, J.W. Jewkes, A.D. Lucey, R. Narayanaswamy and Y.M. Chung. "Large-eddy simulations of a turbulent round jet impinging on a vibrating wall", *International Journal of Heat and Fluid Flow*, **65:** 277–298, 2017.(doi = "https://doi.org/10.1016/j.ijheatfluidflow.2016.11.006")

T. Natarajan, J.W. Jewkes, A.D. Lucey, R. Narayanaswamy and Y.M. Chung. "Large-eddy simulations of a turbulent jet impinging on a vibrating wall and the effect of forcing parameters on flow and thermal fields", *International Journal of Heat and Fluid Flow*, (to be submitted), 2017.

Peer reviewed conference proceedings

T. Natarajan, J.W. Jewkes, A.D. Lucey, R. Narayanaswamy and Y.M. Chung. "Flow and heat-transfer under circular jet-impingement on a sub-harmonically excited impingement wall", *Proceedings of the 20th Australasian Fluid Mechanics Conference, Perth, 2016 Published by the Australasian Fluid Mechanics Society.*

T. Natarajan, J.W. Jewkes, R. Narayanaswamy, A.J. King, Y.M. Chung, and A.D. Lucey. "Analysis of Turbulence Statistics and Thermofluidic Characteristics under Circular Jet Impingement", *Proceedings of the 19th Australasian Fluid Mechanics Conference, Melbourne, 2014 Published by the Australasian Fluid Mechanics Society.*

T. Natarajan, J.W. Jewkes, R. Narayanaswamy, Y.M Chung, and A.D Lucey. "Large Eddy Simulations of Flow Field and Heat Transfer Under Partially Confined Slot Jet Impingement on a Vibrating Constant Heat Flux Surface", *Proceedings of the 19th Australasian Fluid Mechanics Conference, Melbourne, 2014 Published by the Australasian Fluid Mechanics Society.*

T. Natarajan, J.W. Jewkes, R. Narayanaswamy Y.M. Chung and A.D. Lucey. Reynolds Averaged and Large Eddy Computations of Flow and Heat Transfer Under Round Jet Impingement, *Proceedings of the ASME 2014 - 4th Joint US-European Fluids Engineering Division Summer Meeting and 11th International Conference on Nanochannels, Microchannels, and Minichannels, Paper No. FEDSM2014-21435, FEDSM2014, August 3-7, 2014, Chicago, Illinois, USA.*

Abstract only conference

T. Natarajan, J.W. Jewkes, A.D. Lucey, R. Narayanaswamy and Y.M. Chung. "Numerical simulations of flow and heat-transfer under a turbulent jet impinging on a vibrating wall". *Proceedings of the 11th European Fluid Mechanics Conference, Seville, Spain, 2016.*

Book Chapter

T. Natarajan, J.W. Jewkes, R. Narayanaswamy, Y.M. Chung, and A.D. Lucey, "Near-Wall Anisotropy under Round and Planar Jet Impingement", *Fluid-Structure-Sound-Interactions and Control, Zhou Y., Lucey A., Liu Y., Huang L. (Eds.), Springer Berlin Heidelberg (pp. 253-257), 2016.*

Contents

List of Figures

List of Symbols

Roman Symbols

A	amplitude of wall vibration	m
B	potential core	dimensionless
c_p	specific heat capacity	$J/kg\ K$
C_{ij}	Cross terms in subgrid scale modelling	N/m^2
C_{vel}	convection velocity	m/s
d	displacement or cell center vector	m
E	energy	m^2/s
F	face flux	m^3/s
g	acceleration due to gravity = 9.81	m/s^2
g_b	fixed gradient	dimensionless
L_{ij}	Leonard stress terms	N/m^2
P	cell centroid position	m
r, R	radius or radial coordinate	m
R^+	Karman number	dimensionless
R_{ij}	Reynolds stress terms	N/m^2
S_ϕ	Source term	dimensionless
S_{ij}	Strain rate tensor	$1/s$
St	Strouhal number	dimensionless

T	temperature	K
t	time	s
U	mean velocity	m/s
V	volume	m^3
y	distance along y-coordinate	m
q''	heat flux	W/m^2
$\mathcal{P}_k$	turbulence kinetic energy production	m^2/s^3
C_s	Smagorinsky coefficient	dimensionless
D	pipe diameter or diameter of jet nozzle	m
f	frequency	Hz
h	heat transfer coefficient	$W/m^2\ K$
k	thermal conductivity of air	$W/m\ K$
L	characteristic length	m
Nu	Nusselt number	dimensionless
p	pressure	N/m^2
Pr	Prandtl number	dimensionless
Pr_t	turbulent Prandtl number	dimensionless
r, θ, z	Cylindrical–polar coordinates	m
U_b	bulk velocity of the flow	m/s
u_τ	friction velocity of the flow	m/s
x, y, z	length along Cartesian coordinates	m
y^+	wall distance	dimensionless

Greek Symbols

Ω	vorticity	$1/s$

ω	specific dissipation rate	$1/s$
Ω_{ij}	Strain rate of rotation tensor	$1/s$
ρ	density	kg/m^3
α	thermal diffusivity	m^2/s
β	thermal expansion coefficient	$1/K$
Δ	filter width	m
δ	distance from the wall to the grid cell centre	
δ_ν	viscous length scale	m
δ_{ij}	Kronecker delta	dimensionless
ϵ	dissipation of turbulent kinetic energy	m^2/s^3
η_k	Kolmogorov length scale	m
Γ_ϕ	diffusivity coefficient	dimensionless
μ	dynamic viscosity	$kg/m\ s$
ν	kinematic viscosity	m^2/s
ν_t	turbulent eddy viscosity	m^2/s
ϕ	transported quantity or phase of wall vibration	dimensionless
τ	stress magnitude and tensor	N/m^2

Subscripts

$(\cdot)_w$	wall or impingement surface values
$(\cdot)_\tau$	frictional quantity
$(\cdot)_b$	bulk
$(\cdot)_m$	maximum
$(\cdot)_n$	normal component
$(\cdot)_{ref}$	reference values

$(\cdot)_{rms}$	root mean square
$(\cdot)_{SGS}$	subgrid scale
$(\cdot)_t$	tangential component
$< \cdot >$	ensemble averaged quantity

Superscripts

$(\cdot)^+$	wall units
$(\cdot)'$	fluctuating quantities
$(\cdot)^c$	cell centre based quantity
$(\cdot)^f$	face based quantity

Acronyms

AIM	Anisotropy Invariant Map
CFD	Computational Fluid Dynamics
CFL	Courant-Friedrich-Lewis number
DDM	Domain Decomposition Method
DNS	Direct Numerical Simulation
ERCOFTAC	European Research Community on Flow, Turbulence, and Combustion
LES	Large Eddy Simulation
LHS	Left Hand Side
MOL	Method of Lines
MPI	Message Passing Interface
PISO	Pressure-Implicit Method for Splitting of Operators
RANS	Reynolds Averaged Navier-Stokes
RHS	Right Hand Side

RNG	Renormalization Group Theory
SEM	Scanning Electron Microscopy
SGS	Subgrid Scale Model
SIMPLE	Semi-Implicit Method for Pressure-Linked Equations
SST	Shear Stress Transport
STOVL	Short take-off or Vertical Landing
SWJ	Static-wall Circular Jet-impingement
TKE	Turbulence Kinetic Energy
VWJ	Vibrating-wall Circular Jet-impingement

Part I

Background
&
Problem Definition

Chapter 1

Introduction

1.1 The Impinging Jet

Impinging jets have played a pivotal role in applications that require efficient heat- and mass-transfer. The canonical jet-impingement problem presents a deceptively simple configuration that produces a complex array of flow features. The analysis of impinging jets has grown in sophistication with improvements in experimental measurement techniques as well as numerical methods that enable powerful and accurate simulations by harnessing the rapid growth of affordable computing power.

Impinging jets are the most conventionally used methods for efficient heat transfer due to their simple configuration. For example, they have found an increasing application in cooling high-powered electronics, drying applications in textile industries and other process industries. Although impinging jets are simplistic in their geometric construction, their flow behaviour is extremely complex, and has posed a challenge for researchers both experimentally and numerically.

The normally impinging jet from a circular nozzle is a part of the classic database collection for standard test cases maintained by the European Research Community on Flow, Turbulence, and Combustion (ERCOFTAC[1]) which emphasises the importance of the research in the field of impinging jets. Numerically, the problem poses a significant challenge due to the complex

[1]ERCOFTAC *ERCOFTAC test cases* http://cfd.mace.manchester.ac.uk/ercoftac/ Accessed Dec 17, 2016

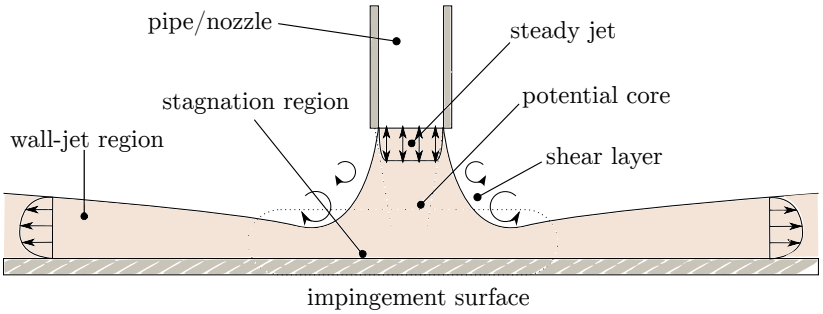

Figure 1.1: Schematic of a simple jet impingement configuration.

and varied flow physics produced by the jet.

A normal jet impinging on a flat impingement surface is shown in figure 1.1. The jet issues from the nozzle, producing a free-jet region, a stagnation region, and a wall jet region. The free-jet region comprises a potential core and a shear layer. The potential core is a region of flow at the centre of the jet, unaffected by the surrounding fluid. The shear layer is a growing region of significant entrainment at the edge of the jet, characterised by Kelvin-Helmholtz instabilities. The potential core is gradually eroded by the shear-layer until it disappears completely, and in configurations with a large nozzle to impingement surface spacing, the core is replaced by a fully developed region, which becomes self-similar. Self-similarity is characterized by linear growth of the layer, and turbulent statistics that become independent of the downstream distance when normalized by appropriate length and velocity scales[2].

The stagnation region is caused by the wall, forcing the jet to lose its centreline velocity, and deflect in a transverse direction, and is characterised by a rapid increase in static pressure and high normal and shear stresses. Turbulent kinetic energy (TKE) dissipation prevails in this region and has always been problematic from a turbulence modelling perspective. Finally, the jet forms a wall-jet boundary layer, which becomes self-similar at large radial distances from the stagnation region. Wall-jet boundary layers are similar in many ways to conventional turbulent flat plate boundary layers, with high levels of mixing occurring in the near-wall region; however, there is an additional region of entrainment at the top of the boundary layer, with the surrounding fluid.

Figure 1.2 shows the broad classification of the impinging jets using appropriate schematics. They are conventionally classified based on the construction of nozzles (rectangular or round, single or array) and the domain bounding the nozzle. In a free surface jet, the impinging fluid

[2]Elias Balaras et al. *J. Fluid Mech.*, **446**: 1–24, 2001.

exits from the nozzle onto a different (usually immiscible) fluid. When both the fluids have the same transport properties, they are termed submerged jets. When the fluid from the nozzle exit issues on to a pool of a fluid with different properties, the jet is termed a plunging jet. All of these configurations can be confined to a wall near the nozzle exit to bound the domain and represent the category of a confined jet impingement configuration. The wall-jets are similar to free surface jets except that they are wall-bounded and are not axisymmetric.

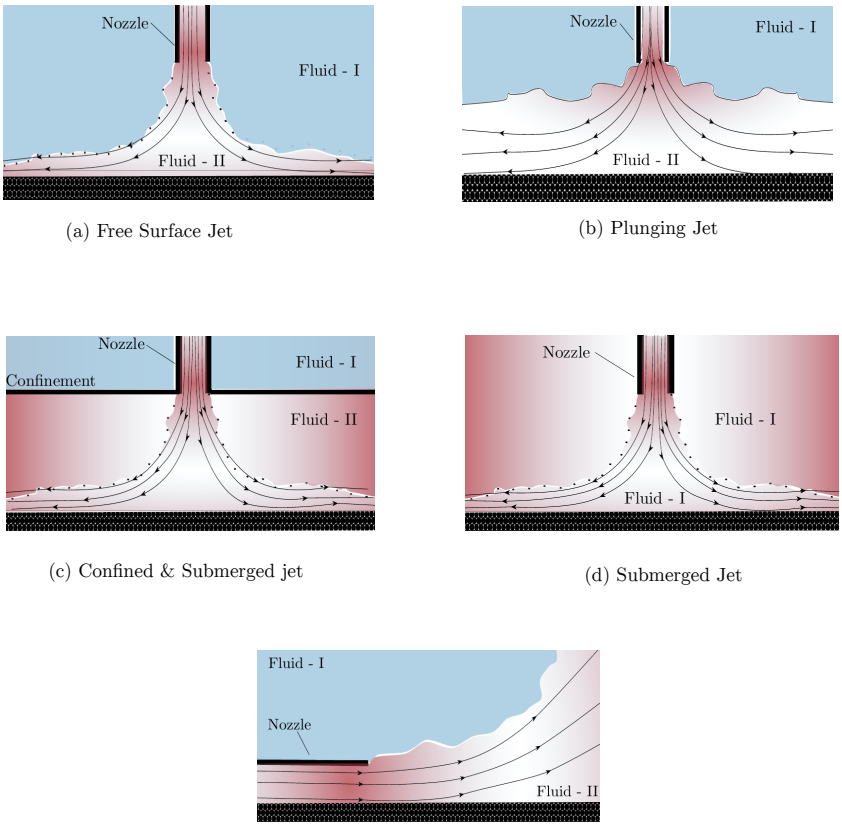

(a) Free Surface Jet

(b) Plunging Jet

(c) Confined & Submerged jet

(d) Submerged Jet

(e) Wall Jet (Free Surface)

Figure 1.2: Schematic of jet impingement configurations.

1.1.1 Jet Impingement Applications

The advantages of impinging jets are employed in some of the most common industrial settings where efficient heat and mass transfer is required. In process industries, they are used to cool, heat and dry sheets of materials ranging from textiles and paper to printed circuit boards. They find applications in almost all metal cutting and annealing industries including the glass

manufacturing sector where cold jets are used to temper the glass.

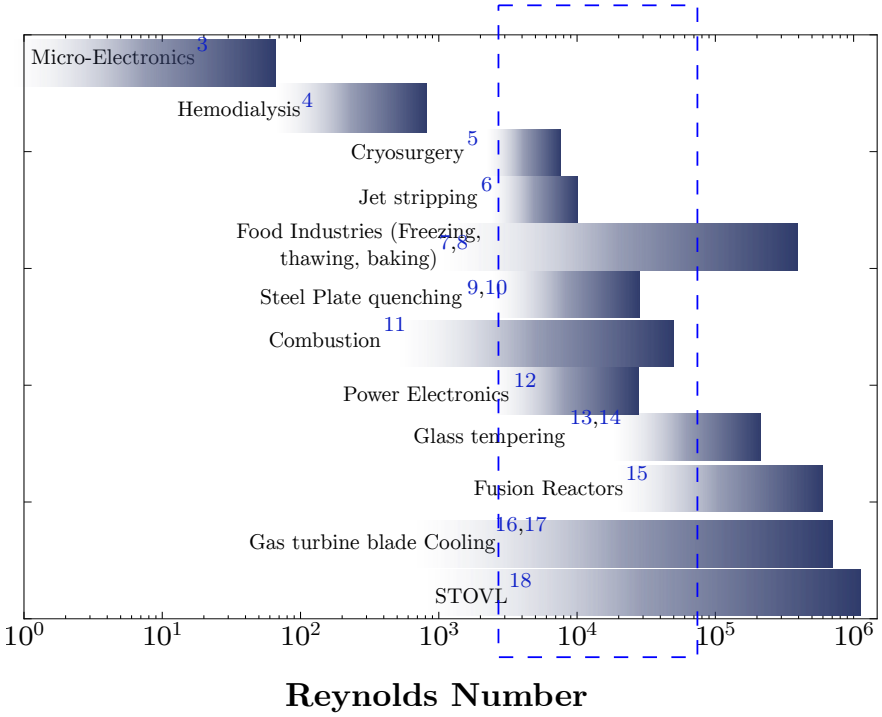

Figure 1.3: Typical range of Reynolds numbers in different applications involving impinging jets.

Figure 1.3 illustrates the typical ranges of Reynolds numbers obtained for various impingement cooling/drying techniques. It is interesting to note that most of the applications fall within the operating range between 5,000 to 30,000. Applications in micro-chip cooling and hemodialysis are on the lower end of the Reynolds number range whereas short take-off or vertical landing (STOVL) aircraft and turbine blade cooling technologies operate in the higher range of Reynolds numbers.

In the context of electronics cooling, the coolant (issuing from a nozzle - as a jet) is in direct contact with the electronic component which enables the chip or processor to be cooled to the desired operating temperature. Efficient heat removal dictates both the life of the component and the performance of the processor. IBM employs a miniaturised submerged jet impingement cold plate with a nozzle array for cooling the processors[3]. Figure 1.4(a) shows the schematic of the setup and figure 1.4(b) shows the Scanning Electron Microscopy (SEM) image of the configuration, where blue lines indicate the water flow. This system employs a multi-level jet impingement technique to cool the processor chip. The jet impingement technique is now widely explored in data-center cooling (of large supercomputer clusters) to increase the efficiency of the

[3]T. Brunschwiler et al. *ITHERM'06*, 196–203, 2006.

heat removal.

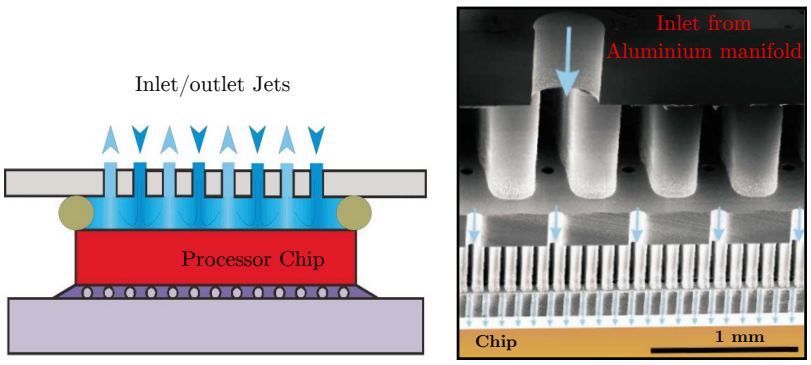

(a) Schematic (b) SEM image

Figure 1.4: Schematic of the chip cooling arrangement and the corresponding SEM image of jet-impingement[3].

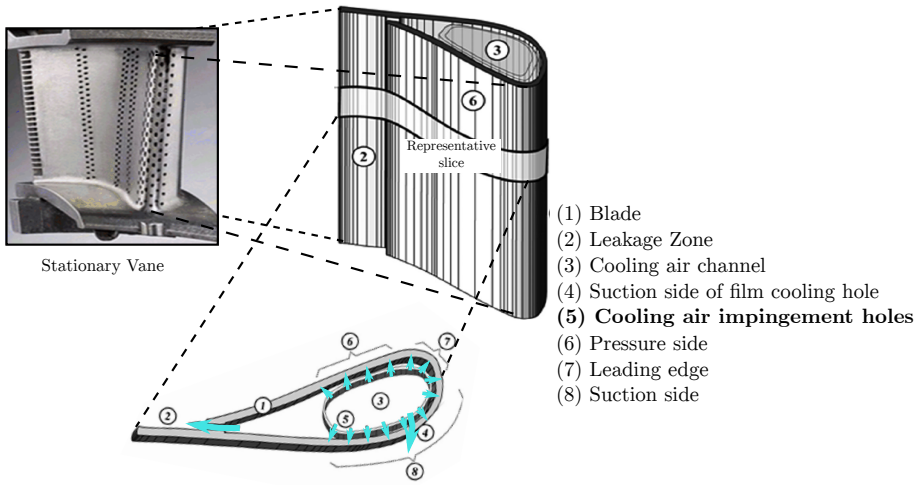

Figure 1.5: Turbine blade and representative slice (Images reproduced from Girardeau et al.[16] and Han[17]).

From an aeronautical engineering perspective, cooling the high-pressure vanes and their temperature control has a direct effect on the operation of the turbine and the lifetime of the blades. A typical turbine blade and its representative slice is shown in figure 1.5 where the cold jets (region (5)) from the inner side of the blade impinge on the surface to remove the heat experienced by the blade, due to hot combustion gases.

At ground level, the icing on the aircraft's wing and fuselage is a potential hazard and poses a significant threat during the plane's flight. De-icing is carried out by impinging a hot fluid (usually ethylene glycol) on the target surface to assist in the removal of ice. Figure 1.6 shows a

Figure 1.6: Impingement spray techniques for ground level de-icing (Images from http://substance-en.etsmtl.ca accessed Jan'17).

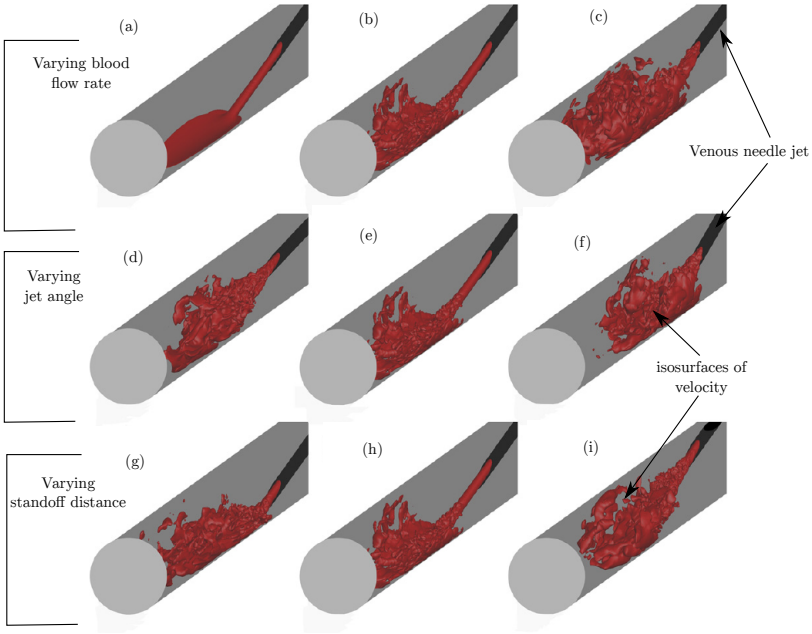

Figure 1.7: Venous needle jet impingment application in hemodialysis (adapted from Fulker et al.[4])

typical de-icing procedure carried out on an aircraft on the ground where a spray of liquid jet used for the removal of ice.

Impinging jets find applications not just at the macroscopic scale but also at a microscopic level when arterial needles and venous needles are used to inject fluids. Figure 1.7 shows the application of a jet impinging onto the endothelium (tissue that lines the interior of the blood vessels) at different configurations. It is important to study the features of the jet in such contexts because minor changes to the wall shear stress can vary the extent of damage done to the endothelium[4].

In summary, impinging jets find an array of applications ranging from electronics cooling at micro-level to de-icing a high speed aircraft. The following section describes the impinging jet setup in more detail along with the various terminologies involved with impinging jet configurations.

1.1.2 Flow Physics and Heat Transfer

A detailed description of the construction, flow and heat transfer characteristics of a canonical jet impingement configuration is now presented. Figure 1.8 shows the various parameters that will serve as 'basis functions' that are discussed at length in the present work. A.J. Reynolds[19] attempted to characterise the flow in impinging jets based on instabilities along the jet and the characteristic flow rate. With this preliminary work as the basis, McNaughton & Sinclair[20] conducted further experiments on submerged jets and eventually classified the impinging jet flow into four main regimes based on the jet Reynolds number, Re_D defined as,

$$Re_D = \frac{\rho D U_m}{\mu} \tag{1.1}$$

where ρ is the density of the fluid, D the characteristic length, U_m, the characteristic velocity, and μ, the dynamic viscosity of the fluid. The four main flow regimes that could exist in an impinging jet according to McNaughton & Sinclair[20] are as follows:

1. Dissipated-laminar jet ($Re_D < 300$)
2. Fully laminar jet ($300 < Re_D <$ 1,000)
3. Semi-turbulent jet ($1000 < Re_D <$ 3,000)

[4]D. Fulker et al. *J. Biomech. Eng.*, **139**: 011005, 2017.
[19]A.J. Reynolds. *J. Fluid Mech.*, **14**: 552–556, 1962.
[20]K.J. McNaughton and C.G. Sinclair. *J. Fluid Mech.*, **25**: 367–375, 1966.

4. Fully turbulent jet ($Re_D > 3{,}000$)

Across all the regimes (barring the dissipated-laminar jet), the impinging jet is bound to have four distinct regions with varying flow features.

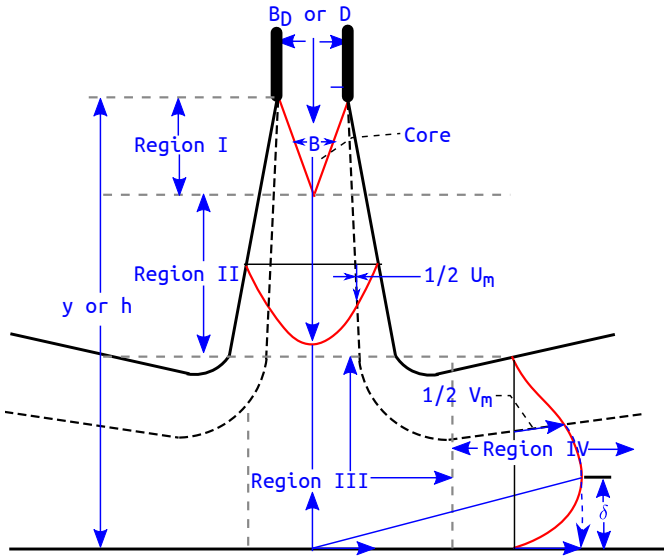

Figure 1.8: Schematic of flow domains in an impinging jet (reproduced from Gauntner et al.[21]).

Gauntner et al.[21] describe these four regions in an impinging jet domain as follows:

1. **Region - I (Flow establishment):** The fluid is issued through a circular nozzle with a diameter D and is allowed to exit the nozzle. Upon exit, the jet interacts with the quiescent fluid, impinges on the target surface and spreads radially. Region-I in figure 1.8 shows the bounds of this region extending from the nozzle exit to the edge of the potential core B. In this zone, the velocity remains constant, almost equal to the velocity of the jet at nozzle exit, and is not affected by the growth or spread of the annular shear layer.

2. **Region - II (Free jet):** The region from where the potential core 'B' ends and the axial velocity begins to decelerate due to the spatial expansion of the jet is termed the free jet region. As the fluid discharges into the still or quiescent fluid, it undergoes a shear instability (Kelvin-Helmholtz type) and rapidly grows to become unstable, and the result is a series of ring vortices or primary vortices with a low-pressure core region (see figure 1.9 adapted from Reynolds et al.[22]). The instability to perturbations (natural

[21] J.W. Gauntner et al. *NASA Technical Report*, 19, 1970.
[22] W.C. Reynolds et al. *Annu. Rev. Fluid Mech.*, **35**: 295–315, 2003.

and forced) can occur over a wide range of perturbation frequencies, and the most amplified frequency appears at the end of the potential core[23]. This most amplified frequency is termed the *'jet preferred'* or *'column mode'* and equal to a Strouhal number, $St = fD/U = 0.3$ according to Crow & Champagne[23]. These axisymmetric primary vortices travel downstream, coalesce, pair with similar structures and eventually break down with large nozzle-to-wall spacing or upon impact onto the impingement surface. Existing literature commonly refers to these vortices as *'coherent'* or *'large-scale structures'*. Upon impingement, these primary structures result in the formation of the secondary vortices and convect radially downward.

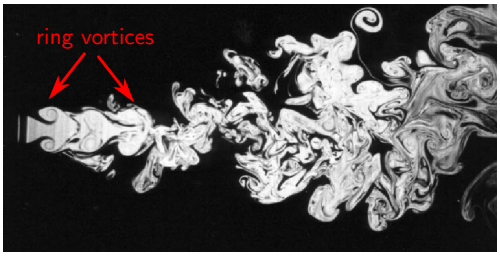

Figure 1.9: Bisecting plane on a water jet at Re = 4,300 from Reynolds et al.[22]

3. **Region - III (Stagnation Region):** As the jet impinges on the target surface that is perpendicular to the nozzle exit, the flow is brought to a halt momentarily resulting in the formation of the stagnation region. The stagnation point is the location in the zone where the velocity is zero, accompanied by a maximum static pressure. This high-pressure region is of a hemispherical dome shape with its radius extending to approximately one diameter with its centre at the stagnation point. When this pressure gradient (relative to atmospheric) reduces, the radial flow begins.

4. **Region - IV (Wall-jet region):** The wall-jet region develops subsequent to the stagnation region and accelerates radially to attain a local maximum (V_m) and eventually decelerate on moving away from the stagnation region. The wall-jet typically begins with the laminar boundary layer region followed by the viscous similarity region where the viscous effect extends to the thickness of the fluid and eventually transitions to fully turbulent. Along the wall-normal direction, there exist two regions; an inner layer (in which the log-law applies) and outer layer characterised based on the effect of the wall. The viscous effects are dominant in the inner layer whereas inviscid effects dominate the outer layer.

[23]S.C. Crow and F.H. Champagne. *J. Fluid Mech.*, **48**: 547–591, 1971.

As stated earlier, impinging jets are used when efficient heat or mass transfer from/to a target surface is required. The amount of heat removed from a target impingement surface is characterised by the thermal profiles on the impingement surface. The Fourier law for conduction heat transfer gives the heat flux, q'' or the amount of energy that flows through a unit area per unit time through the thin fluid layer at the target surface. The law states that the local heat flux is equal to the product of the thermal conductivity of the fluid under consideration, k and the negative of the local temperature gradient normal to the impingement surface and is given as,

$$q'' = -k \left(\frac{\partial T}{\partial y} \right)_{y=0} \tag{1.2}$$

The heat transfer from the impingement surface is predominantly through convection. The local heat transfer coefficient, h is correlated to the conductive heat flux as,

$$q'' = h(T_w - T_\infty) \tag{1.3}$$

where T_w is the local wall temperature, and T_∞ is the reference temperature or bulk temperature (normally the inlet jet temperature). Rearranging equations 1.2 and 1.3, a non-dimensional term to quantify the heat transfer on the impingement surface is obtained and is given by the Nusselt number, Nu written as,

$$Nu = \frac{hL}{k} \tag{1.4}$$

with L being the characteristic length. The Nusselt number is essentially the ratio of the convective heat transfer to the conductive heat transfer. Figure 1.10 illustrates a typical radial distribution of time-averaged Nusselt number (reproduced from the experiments of Baughn & Shimizu[24]) obtained for circular-jet impingement with air as the working fluid at Re_D = 23,750 for nozzle-to-wall spacing, y/D = 2.0 - 14.0.

All the curves exhibit a common feature whereby they all attain a maximum at the stagnation point and monotonously decrease with increase in the radial distance. This maximum achieved by the curves are dubbed as primary or inner Nusselt number peaks. The inner peak appears in the stagnation region ($r/D < 0.5$) due to the high level of turbulent kinetic energy contained in the axial jet. It is also evident that this inner peak does not correlate directly with the nozzle-to-wall spacing (y/D). As the distance y/D increases, there is initially an increase in the Nusselt number and a maximum in the stagnation region for y/D = 6.0. Further increase in the spacing shows a decrease in the value of the inner Nusselt peak.

[24] J.W. Baughn and S. Shimizu. *J. Heat Transfer*, **111**: 1096–1098, 1989.

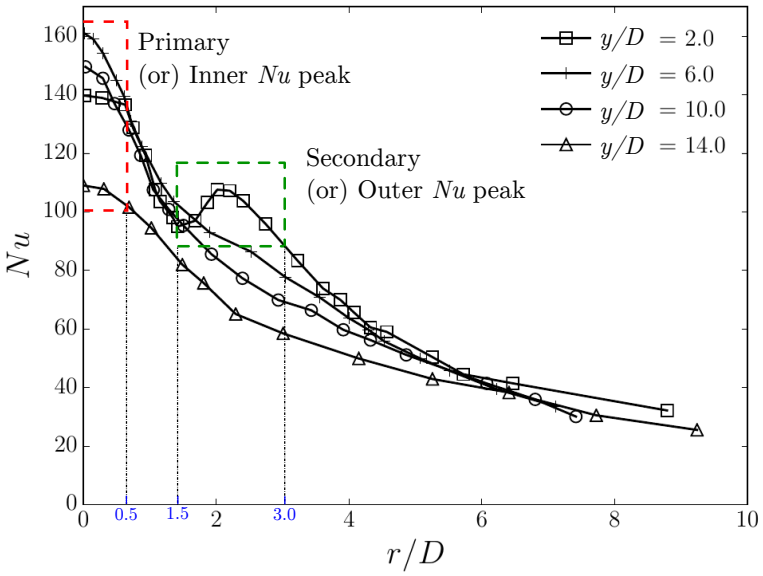

Figure 1.10: Nusselt number distribution along the impingement surface (reproduced from the experiments of Baughn & Shimizu[24]) for nozzle-to-wall spacing, y/D = 2.0 - 14.0.

With reduced nozzle-to-wall spacing (y/D = 2.0), there appears another region of increased heat transfer visualised as the secondary Nusselt number peak or the outer peak. The outer peak is observed for $y/D < 4.0$ across both laminar and turbulent jet impingement. This particular feature of the impinging jet has been the focus of several studies since merely adjusting the spacing between the nozzle exit and the target surface can result in a net increase in heat transfer. Therefore, the appearance of both the inner and outer peaks warrant a detailed investigation and forms an integral part of the current research.

The resulting heat transfer on the impingement surface is a function of several parameters of the domain, and can be sensitive to various aspects of the flow. The following section briefly introduces these parameters that are known to affect the flow and heat transfer in a jet impingement configuration.

1. **Inflow:** The inflow conditions regulate the flow either through changes in the geometry of the nozzle or forcing the fluid through an external mechanism to achieve the desired level perturbations, turbulence intensities and velocity profiles at the nozzle exit. The level of perturbations determines the stability of the free jet. Therefore the formation of the vortex rings is modified, which eventually impinge, and in turn, affect the flow and thermal characteristics near/on the target surface. The turbulence intensity is argued to be the reason for the formation of the outer Nusselt number peak; the nozzle shape can also influence the level of turbulence intensity. Techniques such as nozzle-inlet chamfering,

use of sharp-edged orifices and nozzles with different aspect ratios are known to affect the thermal characteristics positively (see Lee & Lee[25], Brignoni & Garimella[26]). Dairay et al.[27] observed huge differences in stagnation heat transfer where a convergent nozzle profile gave a decreased inner peak but enhanced the outer peak when compared to a long tube profile. The diameter of the nozzle dictates the length scale of the largest eddy structure that can be formed (see Violato et al.[28]). Lee et al.[29] state that increasing the nozzle diameter increased the stagnation region heat transfer at a given nozzle-to-wall spacing and Reynolds number, attributing this effect to momentum and turbulence intensity levels. For the velocity profiles at the nozzle exit, fully developed flows are often preferred as an experimental standard in order to have a clearly defined inflow. Several other profiles such as flat, sinuous, rectangular and triangular are known to affect the impingement heat transfer (see Middleberg & Herwig[30]) and both enhancement and depreciation of heat transfer were observed.

2. **Nozzle-to-wall spacing (y/D):** The distance between nozzle exit and the target impingement surface controls the spatial development of the jet in both axial and radial directions. The establishment of the flow is based on this distance. As seen earlier, the secondary Nusselt peak appears when the impingement surface is at a smaller nozzle-to-wall spacing (i.e., $y/D < 4$). As y/D increases, the Nusselt number changes:there is initially an increase and a maximum for $y/D = 6.0$. Increasing the nozzle-to-wall spacing beyond 6.0 diameters results in the decrease in the value of the inner Nusselt peak. Shifts in the location of the primary Nusselt peak were also observed as the spacing between the nozzle, and the impingement surface was increased. Decreasing the nozzle-to-wall spacing below 2.0, Cornaro et al.[31] noted that the coherent structures were more closely spaced and shedding of vortices occurred in the wall jet. Goldstein et al.[32] observed that the recovery factor on the impingement surface and the net effectiveness of heat transfer were found to be strongly dependent on the spacing from the jet exit to the impingement plate, but did not depend on jet Reynolds number.

[25] J. Lee and S-J. Lee. *Int. J. Heat Mass Transfer*, **43**: 3497–3509, 2000.
[26] L.A. Brignoni and S.V. Garimella. *Int. J. Heat Mass Transfer*, **43**: 1133–1139, 2000.
[27] T. Dairay et al. *J. Fluid Mech.*, **764**: 362–394, 2015.
[28] D. Violato et al. *Int. J. Heat Fluid Flow*, **37**: 22–36, 2012.
[29] D.H. Lee et al. *J. Heat Transfer*, **126**: 554–557, 2004.
[30] G. Middelberg and H. Herwig. *Heat Mass Transfer*, **45**: 1519–1532, 2009.
[31] C. Cornaro et al. *Exp. Therm. Fluid Sci.*, **20**: 66–78, 1999.
[32] R.J. Goldstein et al. *J. Heat Transfer*, **112**: , 1990.

3. **Bounding domains:** The bounding sides of the impingement configuration essentially control the entrainment and outflow conditions of the jet impingement configuration. Hollworth & Gero[33] first studied the effect of entrainment from the quiescent fluid and reported that temperature mismatch between the issuing fluid and the quiescent fluid had a significant effect on the impingement heat transfer rates for an unconfined jet impingement configuration. However, Behnia et al.[34] state that there was no significant effect of the confinement; both the confined and unconfined jet impingement configurations did not show any considerable changes in the resulting heat transfer.

4. **Impingement surface:** Jet impingement on flat surfaces are the most prevalent in literature and have been extensively studied by using both experimental and numerical techniques. Small structural modifications to the impingement surfaces such as dimples, roughness, protrusions, cavities, convex and concave shapes have been investigated and compared with smooth flat surfaces. Ekkad & Kontrovitz[35] reported a reduction in heat transfer coefficients when jets impinged on dimpled surfaces and linked the reduction to the perturbations experienced by the large scale structures. Surface roughness disrupts the boundary layer and promotes turbulence to enhance the impingement heat transfer positively (see Beitelmal et al.[36], Zhou et al.[37]). Often surfaces with curved or convex protrusions have been reported (see Lee et al.[38]) to enhance the heat transfer on the surface, however, when the effective area considerations compared with flat surfaces are included, the difference in augmentation of heat transfer is minimal.

In summary, this section has introduced the concept of jet impingement, the flow features that arise upon impingement and the possible jet impingement configurations. The introduction was followed by a short section noting the breadth of applications the simple configuration can possess from the microscopic level such as intra-venal hemodynamics to the largest flying machines in air transport. Different components and their role in a jet impingement framework along with their capacity to affect both flow and heat transfer were presented.

[33]B.R. Hollwoth and L.R. Gero. *J. Heat Transfer*, **107**: 910–915, 1985.
[34]M. Behnia et al. *Int. J. Heat Fluid Flow*, **20**: 1–9, 1999.
[35]S.V. Ekkad and D. Kontrovitz. *Int. J. Heat Fluid Flow*, **23**: 22–28, 2002.
[36]A.H. Beitelmal et al. *Int. Commun. Heat Mass Transfer*, **27**: 1–12, 2000.
[37]J.W. Zhou et al. *Int. Commun. Heat Mass Transfer*, **36**: 103–110, 2009.
[38]D.H. Lee et al. *Int. J. Heat Fluid Flow*, **18**: 160–169, 1997.

1.2 Motivation and Research Objectives

Here we describe the motivation for the current research and specific objectives that were met during the research. We begin with a description of the need for a highly resolved numerical technique such as LES in simulating turbulent impinging jets followed by objectives that were formulated to achieve the overall research goals.

1.2.1 Motivation

Jets provide a canonical fluid flow field, with a range of flow characteristics despite their simple geometric construction. In particular, jets are convective flows with a predisposition toward instability, which renders them well suited to the mixing and transport of fluids and have played a pivotal role in applications that require efficient heat- and mass-transfer.

Understanding the intrinsic flow features through experimental methods can be costly and time-consuming; thus, interest has grown in the numerical modelling of flow fields. However, the numerical modelling of impinging jets presents the predicament of computational expense since highly-resolved models of such complex flow fields are computationally expensive. The analysis of impinging jets has grown in sophistication with improvements in experimental measurement techniques as well as numerical methods that enable powerful and accurate simulations by harnessing the rapid growth of affordable computing power. Predicting accurate flow features of a jet impinging upon a stationary wall is in itself demanding considering the complex flow physics it presents. These include Kelvin-Helmholtz type shear layer development in the free-jet, a high static pressure region generated upon impingement, change in flow streamline curvature into the wall-jet region, development of a boundary layer along the wall and entrainment along the exit boundaries of the domain.

Computational Fluid Dynamics (CFD) has become a fundamental tool in aiding the understanding of complex turbulent flows. Although experiments can provide accurate measurements of the flow in question, it is certainly not possible to provide measurements with a complete data set at every point in the three-dimensional domain. However, when dealing with complex turbulent flows, to visualise and understand the nature and the physics of the flow, single point measurements are often insufficient. Thus, CFD has gained popularity in both academia and industrial sectors in assessing turbulent flows.

Within the domain of CFD, several numerical techniques exist which have been retrofitted

based on the nature of the flow and computational intensity. The main numerical techniques that have dominated the CFD domain are Direct Numerical Simulations (DNS), Large-Eddy Simulations (LES) and Reynolds Averaged Navier-Stokes (RANS) simulations. DNS among other numerical techniques provide the most robust and accurate solutions to fluid flow problems. However, their major drawback is huge computational expenses. Thus, DNS has predominantly been used for low Reynolds number flows and fundamental studies within academia. Conversely, RANS handles extremely high Reynolds numbers providing statistically steady state solutions with reasonable accuracy. Thus RANS has been the industrial standard since most of the 'real-world' flows are of high Reynolds number, and inherently turbulent. A suitable intermediate between these extremes is the Large-Eddy Simulation. LES provides both instantaneous and time averaged data over the domain with accuracy greater than RANS, at a remarkably reduced computational cost compared to DNS and thus making it a preferred choice for both academic research and industrial applications.

Large-eddy simulations serve the purpose of providing a holistic picture of the flow characteristics, but present a set of modelling requirements. With requirements for a high-resolution mesh, near-wall grid refinements, severe constraints on time-stepping, suitable sub-grid scale modelling and heat transfer implementations along with the turbulent inflow make the use of LES more challenging when generating a highly resolved reference quality data set of any complex fluid flow. With the need to understand the complexity of the impinging jet aided by a highly resolved data set stems the first objective of this thesis which focuses on the comprehensive studies of a turbulent round jet impinging on a static hot surface supplied with a known heat flux. In addition to this canonical impinging jet configuration, other turbulent flows such as those through pipes and a spatially developing jet are also considered to validate the numerical methodology adopted herein. Along with the LES, the RANS modelling methodology is also studied and briefly discussed to address the shortcomings present thereof.

Conventionally, jet-impingement studies have either been performed with jets discharging cold fluid on a heated wall or conversely impingement of a hot fluid on a cold wall. Several studies have been carried out on this basic configuration with changes to the geometry besides the fluid parameters. There have been few studies with impingement-wall vibrations (see Ichimiya & Yoshida[39], Wen[40]), that focus predominantly on the heat transfer characteristics with inadequate or only qualitative data on the flow physics that cause heat-transfer variations on the impingement wall. Both augmentation and reduction in heat-transfer have been observed. Noticeably absent is information on the flow dynamics either at the near-wall region or elsewhere

[39]K. Ichimiya and Y. Yoshida. *J. Heat Transfer*, **131**: 11701, 2009.
[40]M-Y. Wen. *Int. J. Heat Mass Transfer*, **48**: 545–560, 2005.

in the domain that is directly responsible for the resulting thermal signatures on the impingement wall in the context of forced convection. This has been overlooked by previous studies creating a gap in the understanding of the cause of the changes observed on the impingement wall. The flow physics generated by a turbulent circular jet impinging upon a vibrating wall remains largely unknown. The present work attempts to close this gap by establishing the relationship between the flow features and the resulting heat transfer on the impingement wall.

The boundary layer originates from the stagnation region and grows gradually, moving away from the stagnation region into the wall jet region. The wall-jet profile formation occurs as a result of the simultaneous growth of wall boundary layer and the free-jet boundary. Since the boundary layer has a shearing influence upon the wall, increasing the shear on a stationary wall may be favourable in terms of increasing heat and mass transfer. This can be achieved by setting the impingement wall in a periodic oscillatory motion perpendicular to the nozzle-exit, to modify the boundary layer formation and the corresponding events within it. A clear relationship between the vortical structures and their influence on the heated wall can be established since the vortical structures will oscillate (vertically) due to the wall motion.

Further motivation for the present study was to understand the changes to these flow characteristics under dynamic conditions such as an induced impingement surface vibration. Forcing the impingement surface was an attempt to study the flow and thermal boundary layer and the associated turbulent structures associated with it and their behaviour under 'real-world' dynamic conditions where innate surface vibrations exist. The periodic forcing adds another dimension to the complexity of this canonical jet impingement configuration wherein a fundamental understanding of the coupling of fluid dynamics and heat transfer behaviour arising from inherent and induced boundary-layer unsteadiness in jet-impingement would be assessed. The subtask also was to develop a coupled numerical model that performs all the required tasks in hand which can be summarised as solving the turbulent fluid flow, heat transfer combined with automatic mesh motion simultaneously using LES.

1.2.2 Research Objectives

With the outlined motivation in the previous section, the following objectives are formulated:

1. Develop a modelling framework that uses Large-eddy simulation to predict the flow and heat transfer of a turbulent round jet impinging on a static hot surface supplied with a uniform heat flux.

2. Develop a modelling framework to perform LES of a turbulent round jet impinging on a vibrating hot surface supplied with a uniform heat flux.

3. Perform LES with the developed model to create a data set similar to that of the static wall case with comprehensive turbulent statistics and heat transfer.

4. Investigate and explain the flow and thermal characteristics and the changes observed between the two sets of configurations both qualitatively and quantitatively.

5. Perform a parametric variation in the impinging jet case with a vibrating surface to understand the role of amplitude, frequency, and jet Reynolds number and suggest optimum parameters to control the flow and thermal characteristics of such configurations.

6. Conclude on the findings of the research and propose future developments.

1.3 Thesis Outline

This thesis consists of seven chapters and is constructed in the following manner.

Chapter 2 provides a summary of relevant background relating to the underlying physics behind impinging jets, their corresponding flow structures, and heat transfer signatures. The chapter covers an extensive survey of literature in both experimental and numerical fronts, identifying the gap in knowledge and the need to address them.

In Chapter 3 an outline of the numerical methods used in the present research is presented with a brief introduction to turbulence modelling. The existing modelling techniques are discussed in §3.2 that then presents the discretization practice in OpenFOAM in §3.2.1. The boundary conditions used in the research are discussed in §3.2.2 and §3.2 concludes with the discussion on heat transfer treatment in §3.2.3.

The model validations are presented in Chapter 4. Three cases are discussed with §4.1 on the pipe flow at $Re_D = 24{,}600$, with anisotropy studies in §4.2, and §4.3 presenting the spatially developing axisymmetric round jet. All the cases are examined and tested for the different boundary conditions that will be used in simulations discussed in Chapters 5 and 6.

Chapters 5 presents the results of the turbulent round jet impingement with a static impingement surface starting with the RANS simulations in §5.1 followed by the LES results in §5.2. The first order instantaneous and mean flow turbulent statistics are discussed in §5.2.1 followed by the second order statistics in §5.2.1. The findings in these sections are supported by

the analysis of the turbulent kinetic energy budgets in §5.2.1. The effects on the impingement surface are discussed in §5.2.1 in the form of instantaneous and time-averaged Nusselt number distributions.

The LES results of the jet impingement on a vibrating surface are presented in Chapter 6. Both fluid flow and heat transfer characteristics are discussed in detail for a baseline case. The remainder of the chapter is dedicated to the investigation in the parameter space with two different vibration amplitudes and frequencies of the target surface.

Chapter 7 contains general conclusions from the research presented in this thesis.

Chapter 2

Literature Review

This chapter focusses on the present state of knowledge available on heat and fluid flow data of impinging jets from both experimental and numerical investigations. The chapter begins with the brief discussion on single-phase jet impingement studies on stationary surfaces followed by a critical analysis of the secondary Nusselt peak before describing the available literature on jets impinging on dynamic or moving target surfaces.

2.1 Jet Impingement on Stationary Surfaces

The Nusselt number (Nu) is broadly used as an indicator of the heat-transfer rate on the impingement wall. Analytical solutions to predict the impingement surface heat transfer were prominent among other investigations reported in the 1930's to 1950's where the stagnation Nusselt number was correlated to the jet Reynolds number and Prandtl number using dimensional homogeneity. According to Gauntner et al.[21] the average Nusselt number was of the general form,

$$\overline{Nu} = C\ Pr^m\ Re^n \tag{2.1}$$

where the constant $m = 1/3$, $n = 1/2$ and the constant C varied from 0.88 to 1.09. The experimental work of Perry[41] reported a jet of hot gas impinging on a plane surface at various angles and proposed different values for the constant C for various impingement angles. Gardon

[21] J.W. Gauntner et al. *NASA Technical Report*, 19, 1970.

[41] K.P. Perry. *Proc. Inst. Mech. Eng.*,, **168**: 775–784, 1954.

& Cobonpue[42] focussed exclusively on the dependence of Nusselt number with a change in the nozzle-to-wall spacing of the jet. It was in this study that Gardon & Cobonpue[42] observed two distinct peaks in the radial Nusselt number profiles as the nozzle-to-wall spacing was reduced to below three nozzle diameters. At small nozzle-to-wall distances, a secondary Nu number peak is observed in the radial distribution of the mean Nusselt number in addition to the primary Nu number peak within the stagnation region. Further analysis by Gardon & Akfirat[43] on the formation of a secondary Nu peak for various Reynolds numbers reported that a local thinning of the boundary layer was the cause of the secondary Nu peak. The reported secondary Nusselt peak by Gardon has driven extensive research on the reasons for the formation of this secondary peak even until this decade.

A substantial amount of work has been carried out since then to analyse impinging jet configurations, in which the nozzle-to-wall distance (y/D), the jet Reynolds number (Re), inflow conditions of the jet, types of nozzles and jet combinations (single vs. multiple jets) over an extensive range of parametric combinations, with both experimental and numerical techniques. Review articles often serve to summarize a significant volume of relavant literature on the matter of interest. These review articles reported their perspective on the subject area and served give an update on current trends at the time of their writing. The earliest consolidated review by Gauntner et al.[21] reported heat transfer from a jet impinging on flat surfaces. The paper focussed on the analytical correlations for heat transfer under single and an array of round and slot jets. Conclusions were drawn citing the need for the study of turbulence characteristics and simultaneous heat transfer measurements. Martin,[44] in his review article, reported the key aspects of several investigations on both round and slot jets along with various empirical correlations necessary for the prediction of both heat and mass transfer.

Polat et al.[45] produced the first review of numerical techniques that were employed in the prediction of jet impingement heat transfer. Polat et al.[45] identified the gaps in predicting heat and fluid flow accurately for turbulent jet impingement and the need for developing highly accurate near-wall models. Jambunathan et al.[46] specifically collected data on jet impingement studies with heat transfer measurements for Reynolds numbers in the range of 5,000 to 124,000. In his review of the existing literature, a new correlation was proposed wherein the nozzle-to-wall spacing, and the radial displacement from the stagnation point were taken into account in

[42]R. Gardon and J. Cobonpue. *Int. Dev. Heat Transfer (ASME)*, 454–460, 1962.
[43]R. Gardon and J.C. Akfirat. *Int. J. Heat Mass Transfer*, **8**: 1261–1272, 1965.
[44]H. Martin. *Adv. Heat Transfer*, **13**: 1–60, 1977.
[45]S. Polat et al. *Annu. Rev. Heat Transfer*, **2**: 157–197, 1989.
[46]K. Jambunathan et al. *Int. J. Heat Fluid Flow*, **13**: 106–115, 1992.

the prediction of the Nusselt number. Viskanta[11] reviewed air and flame jets for both single and multiple isothermal jet impingement systems that focussed on the industrial (specifically materials processing and drying) applications of these configurations. Reviews in the past decade by Zuckerman & Lior[47,48] have become more exhaustive due to the amount of work done in the field of jet impingement heat transfer. They systematically addressed the trends on experiments, correlations as well as computational investigations for both single and multiple jet impingement configurations. Few other reviews targeted specific industrial applications such as the review by Han & Goldstein[49] that focussed on the gas turbine applications, while the assessment of impinging jet applications in food processing was presented by Sarkar et al.[8] Recently Carlomagno & Laniro[50] presented a survey of submerged jets with small nozzle-to-wall spacing alone and identified the need for understanding the dynamics. After Polat et al.[45] and Zuckerman & Lior,[47,48] a more recent review of the computational trends was presented by Dewan et al.[51] The review article focussed on the three most important numerical techniques (RANS, LES and DNS) that are used for prediction of jet impingement heat transfer.

Cooper et al.[52] were the first to present an in-depth experimental analysis of impinging jets with varying nozzle-to-wall spacings. Their experiments reported turbulent flow field statistics for varying nozzle-to-wall distances and Reynolds numbers. A companion paper to this work by Craft et al.[53] examined the development of eddy-viscosity models to model turbulence. Although the models initially demonstrated poor agreement in the stagnation region, improvements have been made to the turbulent viscosity parameters, yielding better agreement with experimental data[54]. Baughn & Shimizu[24] presented experimental results for a simple impinging jet flow, featuring an impingement wall that produced uniform heat flux. This work has proven valuable as a benchmark for numerical work since uniform heat flux boundary conditions are straightforward to model. These results were later investigated numerically by several researchers including Yan

[11] R. Viskanta. *Exp. Therm. Fluid Sci.*, **6**: 111–134, 1993.
[47] N. Zuckerman and N. Lior. *J. Heat Transfer*, **127**: 544–552, 2005.
[48] N. Zuckerman and N. Lior. *Adv. Heat Transfer*, **39**: 565–631, 2006.
[49] B. Han and R.J. Goldstein. *Ann. N. Y. Acad. Sci.*, **934**: 147–161, 2001.
[8] A. Sarkar et al. *J. Food Sci.*, **69**: 113–122, 2004.
[50] G.M. Carlomagno and A. Ianiro. *Exp. Therm. Fluid Sci.*, **58**: 15–35, 2014.
[51] A. Dewan et al. *Heat Transfer Eng.*, **33**: 447–460, 2012.
[52] D. Cooper et al. *Int. J. Heat Mass Transfer*, **36**: 2675–2684, 1993.
[53] T.J. Craft et al. *Int. J. Heat Mass Transfer*, **36**: 2685–2697, 1993.
[54] T.J. Craft et al. *Flow, Turbul. Combust.*, **63**: 59–80, 2000.
[24] J.W. Baughn and S. Shimizu. *J. Heat Transfer*, **111**: 1096–1098, 1989.

& Saniei[55], Katti & Prabhu[56], Bovo & Davidson[57] for Re = 23,750.

The experimental and numerical works that have reported the appearance of the secondary Nusselt peak at low nozzle-to-wall spacings are listed in Tables 2.1 and 2.2 respectively. The tables show that the secondary Nu number peak was found in all the regimes of the flow since it was observed for a jet Reynolds as low as 300 (Chung & Luo[58]) and to an extremely high Reynolds number of 173,000 (Meola et al.[59]). The possible reasons for the formation of the secondary peak are also indicated in the table, and it is evident that there is no consensus on the explanation of the physics behind the secondary Nu peak. It is also interesting to note that while several experimental data-sets exist, the amount of numerical data, in particular with LES is relatively less for the outer peak related computations.

Another important aspect of the secondary peak is its location along the radial profile of Nusselt number at which it appears. Several correlations have been proposed taking into account the jet Reynolds number and nozzle-to-wall spacing. Lytle & Webb correlated the Reynolds number and the nozzle-to-wall spacing to the location of the outer Nusselt peak. The correlation is given as,

$$(r/D)_{sec\_Nu} = 0.188 Re^{0.241} (y/D)^{0.224} \tag{2.2}$$

This correlation was based on the data for ranges from 11,000 $< Re <$ 27,600 and $0.1 < y/D < 1.0$ with maximum errors of 2.4% and 8.6%. Lee & Lee[63], however, proposed a modification to this correlation and suggested that the location of the secondary Nusselt peak was better predicted with the following correlation for a nozzle-to-wall spacing of two diameters given as,

$$(r/D)_{sec\_Nu} = 0.137 Re^{0.265} \tag{2.3}$$

Lee & Lee considered the investigation range of Reynolds numbers of 5,000 to 30,000. To obtain better clarity, the experimental and numerical data from Tables 2.1 and 2.2 is used to verify the correlation proposed by Lytle & Webb with a wider range of data set.

Figure 2.1 shows the plot with the location of the secondary Nusselt number peak as a function of Reynolds number and nozzle-to-wall spacings. The figure shows extensive data for a range of Reynolds number from 5,000 to 50,000 and y/D of 0.1 to 4.0. The first observation from

[55]X. Yan and N. Saniei. *Proc. Int. Heat Transfer Conf.*, **5**: 497–502, 1998.
[56]V. Katti and S.V. Prabhu. *Int. J. Heat Mass Transfer*, **51**: 4480–4495, 2008.
[57]M. Bovo and L. Davidson. *Numer. Heat Transfer, Part A*, **64**: 290–316, 2013.
[58]Y.M. Chung and K.H. Luo. *J. Heat Transfer*, **124**: 1039, 2002.
[59]C. Meola et al. *Exp. Therm. Fluid Sci.*, **13**: 29–37, 1996.
[63]J. Lee and S-J. Lee. *Exp. Heat Transfer*, **12**: 137–156, 1999.

Previous studies	Re_D	y/D	Comment on Secondary Nu peak
	Experimental studies		
Gardon & Akfirat [43]	450-28,000	2.0	LBLT
Popiel et al. [60]	1,050-1,860	2.0-10.0	LBLT
Ashforth-Frost et al. [61]	20,000	1.0–8.0	LBLT
Lee et al. [62]	4,000-14,400	2.0–10.0	LBLT
Lee & Lee [63]	5,000-30,000	2.0–10.0	LBLT
Hwang et al. [64]	34,000	2.0–16.0	LBLT
Hwang & Cho [65]	34,000	2.0–16.0	LBLT
Colucci & Viskanta [66]	10,000-50,000	0.25–6.0	LBLT
Katti & Prabhu [56]	12,000-28,000	0.5–8.0	LBLT
Hoogendoorn [67]	66,000	2.0 & 10.0	TL
Lytle & Webb [68]	3,600-27,600	0.1–6.0	TL
ODonovan & Murray [69]	10,000-30,000	0.5–8.0	TL
ODonovan & Murray [70]	10,000-30,000	0.5–8.0	TL
Roux et al. [71]	28,000	3.0 & 5.0	TL
Meola et al. [59]	10,000-173,000	2.0–100.0	SVS
Fénot et al. [72]	23,000	2.0 & 5.0	SVS†
Goldstein et al. [73]	61,000-124,000	2.0-12.0	VR
Baughn & Shimizu [24]	23,750	2.0-14.0	–
Baughn et al. [74]	23,000 & 55,000	2.0,6.0 & 10.0	–
Yan & Saniei [55]	23,750	2.0–9.0	–
Guerra et al. [75]	35,000	2.0	–
Hofmann et al. [76]	14,000-78,000	2.0–8.5	–
Sagot et al. [77]	23,000	2.0–6.0	–

Table 2.1: Overview of previous experimental studies that demonstrate the secondary Nusselt peak with small nozzle-to-wall spacing. Re_D was calculated from $Re_D = U_m D/\nu$.(See end of Table 2.2 for key to abbreviations)

Previous studies	Re_D	y/D	Comment on Secondary Nu peak
	DNS studies		
Chung & Luo [58]	300-1,000	4.0–10.0	SVS
Dairay et al. [27]	10,000	2.0	SVS‡
Wilke & Sisterhenn [78]	3,300	5.0	SVS
	LES studies		
Hällqvist [79]	20,000	2.0	SVS
Hadžiabdić & Hanjalić [80]	20,000	2.0	SVS
Jefferson-Loveday & Tucker [81]	23,000	2.0 & 6.0	SVS
Kubacki & Dick [82]	5,000-70,000	2.0, 6.0 & 13.5	NWS
Uddin et al. [83]	13,000 & 23,000	2.0	FA
Dairay et al. [84]	10,000	2.0	–

Table 2.2: Overview of previous numerical studies that demonstrate the secondary Nusselt peak with small nozzle-to-wall spacing. Re_D was calculated from $Re_D = U_m D/\nu$.

LBLT – Transition of the laminar boundary layer to fully developed turbulent and increased turbulence levels in wall jet

TL – Turbulence level in the boundary layer

VR – From entrainment caused by vortex rings in shear layer

SVS† – Disappearance of secondary vortex structures

SVS – Flow reattachment, Unsteady separation of secondary vortex structures

SVS‡ – Azimuthal distortion of Secondary vortex structures

NWS – Breakup of near-wall structures into fine scale turbulence

FA – Flow acceleration in the developing boundary layer

– No Comment

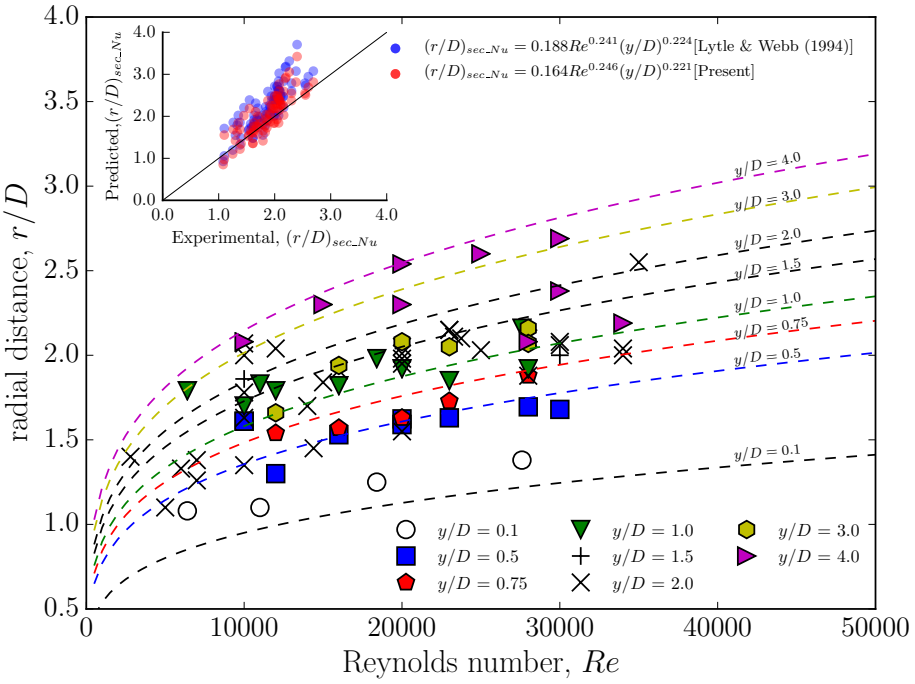

Figure 2.1: Location of secondary Nu peak as a function of Reynolds number, Re, and nozzle-to-wall spacing y/D.

the scatter is the extent of the radial location at which the secondary Nusselt peak is formed and is predominantly in the radial range of $1.0 < r/D < 2.5$. It is also apparent that for a given nozzle-to-wall spacing, the radial location of the secondary Nusselt peak moves radially outward or increases with the increase in jet Reynolds number. Similarly, for a given Reynolds number, the increase in the nozzle-to-wall spacing also shifts the location of the secondary Nusselt peak radially outward. Based on this data, a modification to the correlation of Lytle & Webb was formulated and is given as,

$$(r/D)_{sec\_Nu} = 0.164Re^{0.246}(y/D)^{0.221} \tag{2.4}$$

The correlation is plotted as dashed lines in the plot for varying nozzle-to-wall spacings. A small modification to the correlation of Lytle & Webb correlates well for the entire range of data surveyed. To substantiate the difference between the two correlations, a parity plot is used. The parity plot on the inset shows the predicted secondary peak location with both the correlations. It can be seen that this modified correlation predicts the location of the secondary Nusselt peak with greater accuracy.

It is also interesting to note a striking difference in the explanations provided for the appearance of the secondary peak at a defined radial location between the experimental and

numerical investigations. The majority of the experimental investigations have resorted to transition of the laminar boundary layer to a fully developed turbulent wall jet as the prime factor though few studies report the role of secondary vortex structures and the turbulence levels in the boundary layer. Alternatively, the numerical investigations, in general, agree that the role of secondary vortical structures plays a dominant role in the formation of the outer peak. It can be argued that numerical investigations can provide a fully three-dimensional dataset that could offer greater insights into the flow, and experimental measurement technologies can often be a limiting factor when there is a pressing need for capturing the near-wall physics.

The observation that local thinning of the boundary layer was the cause of the secondary Nu peak was reported in the work of Gardon & Akfirat[43] and later by Chung & Luo[58] for laminar flow. They attributed the reduction in thermal boundary layer thickness to the large-scale interaction between the jet vortices and the impinging wall that resulted in the secondary Nu peak. Direct numerical simulations (DNS) of a laminar flow jet-impingement by Chung et al.[85] showed that heat transfer at the impingement wall is very unsteady, and caused by the primary vortices emanating from the jet nozzle that interacts with the wall shear layer. It was shown that the vortex location has a much stronger effect on Nu than the vortex strength. Although a correlation between the Nu and the flow field was seen, a breakdown in the Reynolds analogy was seen at downstream radial distances. Recent DNS performed by Dairay et al.[27] for a turbulent jet with $Re = 10{,}000$ showed that the primary and secondary vortices are responsible for the increased heat transfer since they constantly renew the wall with cold fluid due to their inherent induced velocity. The DNS of Rohlfs et al.[86] for laminar flow, reported similar observations.

In the recent experimental work of Tummers at al.[87], the turbulent characteristics of an impinging jet (Reynolds number comparable to Baughn & Shimizu[24]) were studied, and near-wall measurements revealed that flow reversals were related to the formation of secondary vortices. Uddin et al.[83] later conducted LES of these experiments. They used digital filtering of random data to generate the inflow velocity fluctuations. Hadžiabdić & Hanjalić[80] used inflow conditions from a pipe flow. However, only a quarter of the full three-dimensional domain was used in their LES study. They showed that the vortex roll-up phenomenon along the impingement wall is the main event governing the flow. The connections between the convection of the primary vortices, the formation of the counter-rotating secondary vortices and the unsteady separation phenomena

[85] Y.M. Chung et al. *Int. J. Heat Fluid Flow*, **23**: 592–600, 2002.
[27] T. Dairay et al. *J. Fluid Mech.*, **764**: 362–394, 2015.
[86] W. Rohlfs et al. *Int. J. Heat Mass Transfer*, **55**: 7728–7736, 2012.
[87] M.J. Tummers et al. *Int. J. Heat Mass Transfer*, **54**: 4939–4948, 2011.
[83] N. Uddin et al. *Int. J. Heat Mass Transfer*, **57**: 356–368, 2013.
[80] M. Hadžiabdić and K. Hanjalić. *J. Fluid Mech.*, **596**: 221–260, 2008.

were elucidated. Also, a recent DNS study by Dairay et al.[27] states that the secondary Nusselt number peak becomes less pronounced when a long tube (fully developed) profile is used for the inflow. A similar observation has been made in the experimental work of Roux et al.[71] indicating a requirement for further investigation of this effect.

Tsubokura et al.[88] presented the development or transition of both plane and circular jets and identified the large-scale structures based on the Laplacian of pressure. They found that the eddy structures differed for the plane and circular jet configurations, and no organised structures were seen at the stagnation zone of the circular jet. Özdemir & Whitelaw[89] visualised these coherent structures in a jet impinging at an angle and concluded that they were crucial to the large-scale convective transport especially for scalar quantities such as temperature. A similar effect was observed by Fox et al.[90] where the wall temperature was modified due to the presence of the primary and secondary vortical structures. Popiel & Trass[91] stated that the development of these large-scale vortex structures considerably enhanced the entrainment rate and mixing processes. An interaction of the well-ordered toroidal vortex structures convected downstream from a transient circular shear layer of a natural free-jet with the normally impinged flat wall was shown. It was inferred that these near-wall eddies are responsible for the additional enhancement of local momentum, and heat or mass transfer. The wall eddies are rolled up on the wall between the large-scale toroidal vortices, which diverge in the radial direction.

2.2 Jet Impingement on Dynamic Surfaces

Surface vibrations are often encountered in practical applications of the impinging jet. The surface oscillations are more prominent in cases such as engine piston cooling or engine surface cooling where the surface to be cooled vibrates due to the thermodynamic and hydrodynamic states of the engine power cycle. One of the earliest heat transfer measurements that were carried out on dynamic or oscillating surfaces was for a circular cylinder by Davidson[92]. The vibrating cylinder placed normal to an air stream was assessed at both uniform and non-uniform surface temperatures. Experimental work on vibrating impingement walls was first carried out

[71] S. Roux et al. *Int. J. Heat Mass Transfer*, **54**: 3277–3290, 2011.
[88] M. Tsubokura et al. *Int. J. Heat Fluid Flow*, **24**: 500–511, 2003.
[89] I. B. Özdemir and J.H. Whitelaw. *J. Fluid Mech.*, **240**: 503–532, 1992.
[90] M.D. Fox et al. *J. Fluid Mech.*, **255**: 447–472, 1993.
[91] C.O. Popiel and O. Trass. *Exp. Therm. Fluid Sci.*, **4**: 253–264, 1991.
[92] B.J. Davidson. *Int. J. Heat Mass Transfer*, **16**: 1703–1727, 1973.

by Ichimiya & Yoshida[39], for plane impinging jets. They considered the range of Reynolds numbers 1,000 $< Re <$ 10,000 and concluded that both enhancement and reduction of heat transfer could occur as a result of vibration. Numerically, Ichimiya & Watanabe[93] examined moderate Reynolds numbers of 200 and 500 and observed improved heat-transfer in the wall jet region. Since the investigations were carried out for such low Reynolds numbers, the effect of turbulence, (which is a key contributor to heat transfer improvement) is neglected.

Jet impingement on reciprocating discs were numerically investigated by Agarwal et al.[94] to understand the thermal dynamics on the underside of the piston. They showed that the relative velocity of the impingement fluid had significant impact on the resulting heat transfer coefficient. It was also noted that at high amplitudes and frequency, resulting in added momentum to the impinging fluid, the fluid film did not extend smoothly at the disk-fluid interface. Nasif et al.[95,96] performed numerical simulations for a similar configuration and the spreading of the fluid at the disk-fluid interface was smoother with a larger nozzle compared to a smaller one. Investigations by Hetsroni & Klein[97] used vibrations generated by a piezoelectric actuator for a micro liquid jet. An increase in heat transfer was observed for micro-amplitudes. Wen[40] conducted experimental studies on impingement wall undergoing forced vibrations. The focus was on tubes with swirling stripes and micro vibrations. The study concluded that the Nu was strongly dependent upon the wall vibration frequency, f, wall vibration amplitude, A, and the jet Reynolds number. However, a substantial dependence on the Nusselt number upon the nozzle-to-wall distance was not observed. Since smoke visualisations were used, the flow was analysed qualitatively.

2.3 Summary

A brief review of existing literature reveals the events within the hydrodynamic boundary layer that are largely accountable for the variations in the thermal characteristics of the impingement wall. This section was followed by a detailed discussion on the origin of the secondary Nu number peak and related correlations. It illustrates that there is no consensus in the literature

[39]K. Ichimiya and Y. Yoshida. *J. Heat Transfer*, **131**: 11701, 2009.
[93]K. Ichimiya and S. Watanabe. *J. Heat Transfer*, **131**: 094505, 2009.
[94]A.K. Agarwal et al. *Int. Commun. Heat Mass Transfer*, **38**: 1080–1085, 2011.
[95]G. Nasif et al. *J. Heat Transfer*, **138**: 122201, 2016.
[96]G. Nasif et al. *Heat Transfer Eng.*, **37**: 1507–1520, 2016.
[97]D. Klein and G. Hetsroni. *Int. J. Heat Mass Transfer*, **55**: 4183–4194, 2012.
[40]M-Y. Wen. *Int. J. Heat Mass Transfer*, **48**: 545–560, 2005.

as to the origin of the secondary Nu number peak from both experimental and numerical data. However, numerical investigations offer better insights compared to experiments. The literature shows that no concrete knowledge of the flow dynamics leading to changes in the Nu profiles has been established so far to the knowledge of the author. This gap is even more pronounced when the configurations are dynamic where the impingement surface is in motion and thus becomes the main focus of the present study.

Part II

Methodology

Chapter 3

Methodology

We begin with an introduction to a generic jet impingement modelling framework and the modelling assumptions leading to the governing equations in modelling turbulence. This section is followed by a discussion of the numerical methods, boundary conditions and the parallelization strategies used to discretize the computational domain on high-performance computers.

Figure 3.1 shows a schematic of the three-level approach to achieve the desired objective of developing a framework to study single-phase jet impingement heat transfer with and without impingement surface vibrations. To develop a methodology for such configurations, the task is broken down at the first level to a static impingement surface setup and a vibrating impingement surface configuration. The requirements of the code that needs to be met for both these configurations are identified at the second level. At the third level, proper validations and verifications are done for each criterion identified at level 2. Once the code performs satisfactorily for all the individual cases as well as with the combination of one or more of the listed criterion, these elements are integrated into a single piece of code capable of efficiently predicting turbulent jet impingement heat transfer for both static and dynamic target surface configurations.

The schematic provides a broad context of the overall approach used in the current research to produce highly resolved simulations of jets impinging on static and vibrating heated surfaces. The computational methodology, generic computational template, mathematical formulations of the governing equations are discussed in the section below.

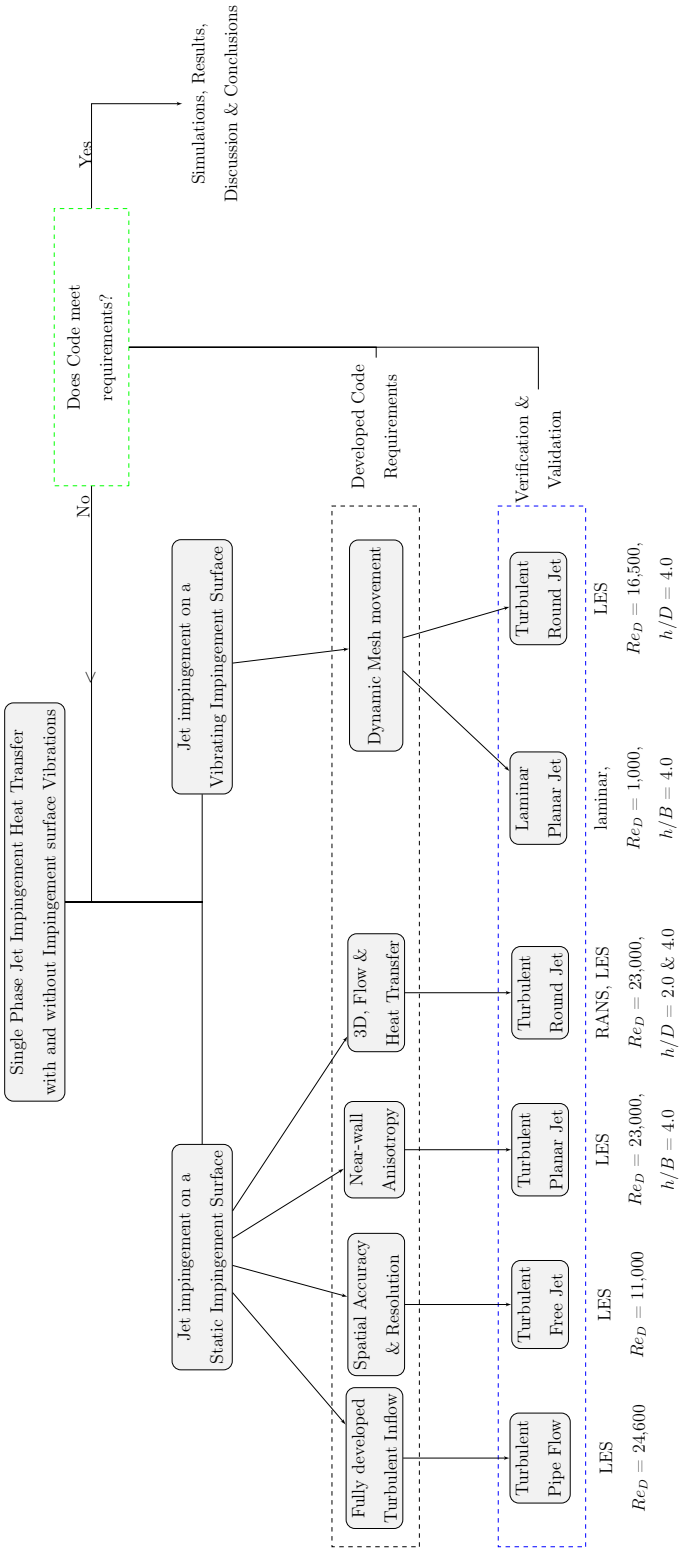

Figure 3.1: Schematic of the methodology employed in the current research

3.1 Configuration, Computational Domain, and Model Assumptions

The current research uses different configurations of impinging jets to verify and validate the developed code and are presented in detail during the relevant discussions. Though it is not possible to define a single universal configuration in terms of the computational domain used in the research, it is necessary to introduce a generic framework or a template. The minor deviations from this stencil will be addressed nevertheless when a new configuration is introduced. Therefore, the objective here is to provide an overview of the salient features of the configuration to follow the model assumptions, mathematical formulations, numerics and boundary conditions that are to be discussed in detail in the latter sections.

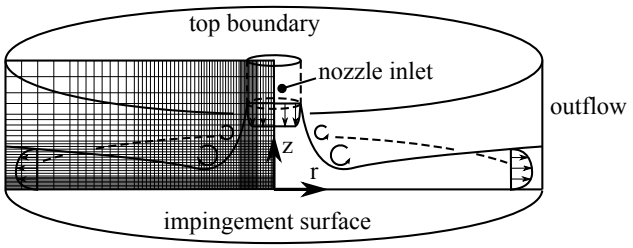

Figure 3.2: General configuration of the domain.

Figure 3.2 shows a schematic for the jet impingement computational domain used. The framework consists of a round pipe with a diameter, D that serves as an inlet nozzle that allows the fluid (air) to be transported and issued onto a target impingement surface that is located at a specified distance from the nozzle exit. The nozzle inlet is supplied with a boundary condition that generates fully-developed turbulent inflow to mimic the experimental work that uses long tubes. The domain dimensions are represented as a function of this nozzle diameter, D. The top boundary is treated as open to the atmosphere where both entrainment and outflow of the fluid is possible. The incoming fluid and the quiescent fluid have the same properties and therefore represent an unconfined, submerged jet impingement. The boundaries on the skirting sides of the domain are similar to the top boundary representing ambient conditions where both inflow and outflow of the fluid occurs. The impingement surface is a smooth horizontal surface, supplied with a uniform heat flux and can be static or oscillating perpendicular to the issuing jet based on the predefined choice of forcing parameters. The radial extent of this impingement surface or the *'heater'* is no less than $10D$ from the centerline of the jet. A typical computational mesh is shown in a plane of the domain. A multi-grading algorithm is used to

control the refinements of the spatially non-uniform mesh. For the framework as mentioned above, a mathematical model is developed to meet the set objectives described earlier. The general assumptions of the mathematical model developed are as follows:

(i) The fluid is considered as a single continuum phase that is continuously and indefinitely divisible. Therefore all macroscopic quantities such as momentum, energy, density, and temperature are finite and are uniformly assigned as a point value over any infinitesimal small size of the discretized control volume.

(ii) The characteristic macroscopic flow scales are much larger compared to the molecular length scale characterising the structure of the fluid.

(iii) The flow is considered inherently 'unsteady' and 'stationarity' is only assumed for time-averaged values of flow parameters.

(iv) The fluid is considered 'incompressible' as the density of the flowing fluid is essentially constant and the maximum Mach number encountered is 0.04. Therefore, the compressibility effects are neglected in the flow.

(v) The fluid is considered viscous, and the corresponding viscous effects or the transport effects such as diffusion and convection of heat and mass transfer are taken into account.

(vi) The macroscopic system is assumed to operate at $293.15K$ (20°C). The corresponding fluid properties of air at $293.15K$ are as follows:

- Density, ρ - 1.2047 (kg/m^3)
- Dynamic Viscosity, μ - 1.8205 $\times$ 10^{-5} (kg/m^3)
- Kinematic Viscosity, ν - 1.5111 $\times$ 10^{-5} (m^2/s)
- Specific Heat, c_p - 1.0061 $\times$ 10^3 (J/kgK)
- Conductivity, k - 0.02559 (W/mK)
- Thermal Diffusivity, α - 2.1117 $\times$ 10^{-5} (m^2/s)
- Thermal Expansion Coefficient, β - 3.4112 $\times$ 10^{-3} $(1/K)$

(vii) The fluid properties are assumed to be invariant with temperature and the Boussinesq approximation is valid.

(viii) The Prandtl number (Pr) is assumed to be a constant $(Pr = 0.71)$ which is valid for the current operating temperatures.

(ix) As the fluid is considered viscous, we assume the *'no-slip condition'* on the target impingement surface.

(x) The acceleration due to gravity, g (9.81 m/s^2) acts against the normal of the target impingement surface.

3.2 Modelling Turbulence

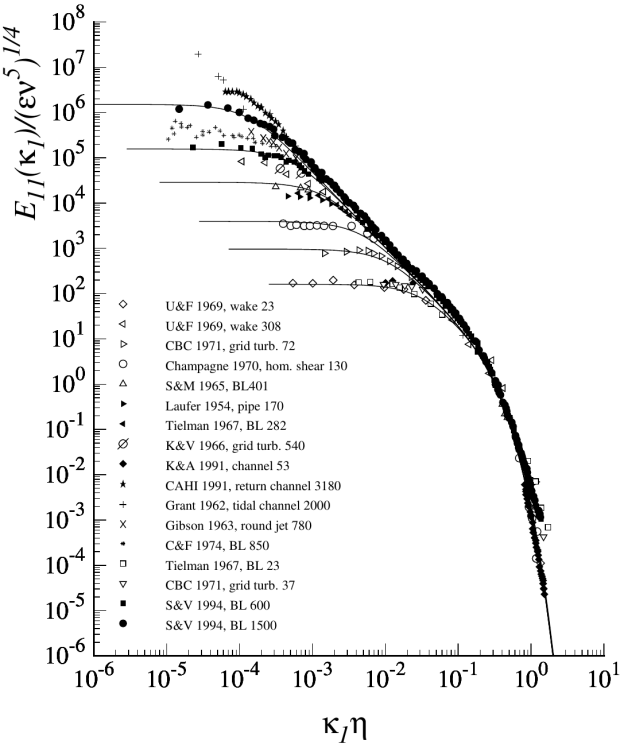

Figure 3.3: Turbulent kinetic energy spectra reproduced from Pope[98]

Kolmogorov[99] proposed a universal hypothesis that energy is transferred from the large-scale eddies to the small-scale eddies, and is in turn successively transferred to the smaller eddies where viscous effects become significant. Thus, the energy density in the sub-inertial range is proportional to the wavenumber as given by Kolmogorov[99] is,

$$E(k) = \mathcal{C}\epsilon^{2/3}k^{-5/3} \tag{3.1}$$

where $\mathcal{C}$ is a universal constant (approximately 1.5). The turbulent kinetic energy in the wave number space visualised through spectral analysis (see figure 3.3) for various flows proves the

[99] A.N. Kolmogorov. *Dokl. Akad. Nauk SSSR*, **30**: 301–305, 1941.

validity of the Kolmogorov hypothesis. Broadly, this energy spectrum can be classified into three turbulent length scales namely, the energy containing scales or the large scales, the sub-inertial scales and finally the dissipation scales.

The turbulence length scales in the domain under investigation can be modelled through various numerical techniques. Each technique offers its advantages and disadvantages, and it is at the discretion of the user to adopt the right technique depending on several factors such as computational expense, flow/length scales that need to be resolved, steady or transitional flow field data requirement and accuracy levels. Some of the state-of-the-art numerical techniques that are in use include Direct Numerical Simulation (DNS), Large-eddy Simulation (LES), Reynolds-Averaged-Navier-Stokes Simulations (RANS) and techniques such as Detached-eddy simulation (DES) and Unsteady-Reynolds-Averaged-Navier-Stokes (URANS) are popular industry choices. Direct Numerical Simulation provides an accurate description of all the eddies whereas the RANS provides the statistical description of the eddies through an averaged flow field and the LES is intermediate between DNS and RANS providing a partial description of the eddies.

The simulations in this study were performed using LES with the code Open Field Operation and Manipulation (OpenFOAM) to solve the incompressible Navier–Stokes equations. The code is an object-oriented numerical simulation toolkit for continuum mechanics coded in the C++ language[100]. The code is capable of implementing an operator-based implicit and explicit second and fourth-order finite volume discretization in three-dimensional space. The object-oriented techniques support datatypes similar to those of continuum mechanics thus allowing mathematical modelling through operator overloading. OpenFOAM also supports handling of every mesh of arbitrary polyhedral bounded by arbitrary polygons with runtime modifications to the configuration set-up and automatic mesh motion methodologies.

3.2.1 Large Eddy Simulation (LES)

Large eddy simulations are a compromise between the DNS and RANS methods of solving the governing equations of the fluid flow. LES is based on the Kolmogorov's hypothesis that the large eddies are responsible for the energy and momentum transfer, and hence need to be resolved and the smaller scales that are dependent on the large scales can be modelled. The separation between the large scales and the small scales is done through a filtering operation where the filter width determines the size of these scales. These filtered small scales are then modelled using a sub-grid scale model to bring closure to the system of equations.

[100]H.G. Weller et al. *Comput. Phys.*, **12**: 620–631, 1998.

A flow variable ϕ having both the large and small scales can be written as,

$$\phi = \overline{\phi} + \phi' \tag{3.2}$$

where the over-bar denotes the large scales and the prime denotes the small scales. A filtering operation to separate the large scales from the small scales can be applied such as,

$$\overline{\phi}(x) = \oint G(x, x'; \Delta)\phi(x')dx' \tag{3.3}$$

where $G(x, x'; \Delta)$ is the filter kernel with Δ being the filter width. Some of the filters that have been applied to classical LES include the Gaussian filter, the top-hat filter or the Box filter and the sharp Fourier cutoff filter. These filters are shown in figure 3.4. Lesser known filters include the Cauchy and the Pao filters. It is seen in figure 3.4 that the Gaussian filter is smooth in both the cases and is given in the wave space as,

$$G(x) = \sqrt{\frac{6}{\pi\bar{\Delta}^2} exp\left(-\frac{6x^2}{\bar{\Delta}^2}\right)}, \tag{3.4}$$

The top-hat filter is essentially an average over a rectangular region and in real space is given as,

$$G(x) = \begin{cases} 1/\bar{\Delta} & \text{if } |x| \leq \bar{\Delta}/2, \\ 0 & \text{otherwise,} \end{cases} \tag{3.5}$$

The top-hat filter is employed in the current research work as it averages over the grid volume of the mesh whereby the grid spacing becomes the filter width Δ. The sharp Fourier cutoff filter is defined in the Fourier space as,

$$\hat{G}(x) = \int_D G(x')e^{-ikx'}dx' = \begin{cases} 1 & \text{if } k \leq \pi/\bar{\Delta} \\ 0 & \text{otherwise.} \end{cases} \tag{3.6}$$

and is known to affect the scales below the cutoff wave number hence used with spectral methods.

After a typical filtering operation, the governing equations for the LES are the filtered continuity and incompressible Navier-Stokes equations given as,

$$\frac{\partial u_i}{\partial x_i} = 0, \tag{3.7}$$

$$\frac{\partial \overline{u}_i}{\partial t} + \frac{\partial(\overline{u}_i\overline{u}_j)}{\partial x_j} = -\frac{1}{\rho}\frac{\partial \overline{p}}{\partial x_i} + \nu\frac{\partial}{\partial x_j}\left(\frac{\partial \overline{u}_i}{\partial x_j} + \frac{\partial \overline{u}_j}{\partial x_j}\right) - \frac{\partial \tau_{ij}}{\partial x_j} \tag{3.8}$$

for which the closure is provided with a suitable sub-grid scale (SGS) model. The SGS stress, τ_{ij}, is modelled since the resolved and unresolved scales interact through the SGS stress τ_{ij}. The sub-grid stress τ_{ij} is generally decomposed as,

$$\tau_{ij} = \overline{u_i u_j} - \overline{u}_i\overline{u}_j = L_{ij} + C_{ij} + R_{ij}, \tag{3.9}$$

where $L_{ij} = \overline{\overline{u}_i\overline{u}_j} - \overline{u}_i\overline{u}_j$ are the Leonard stresses, $C_{ij} = \overline{\overline{u}_i u'_j} + \overline{u'_j\overline{u}_i}$ are the cross terms, and $R_{ij} = \overline{u'_i u'_j}$ are the SGS Reynolds stresses.

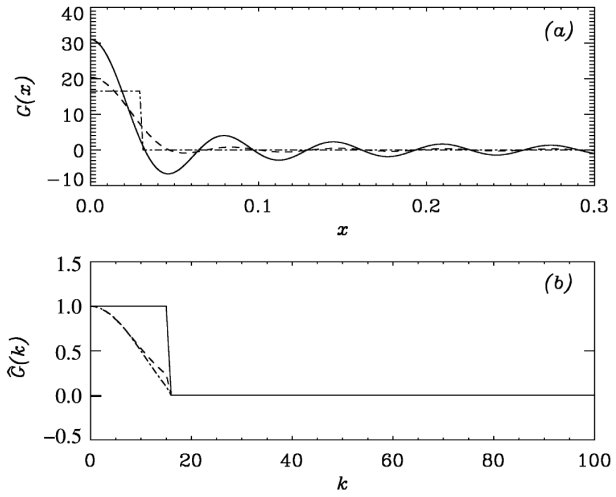

Figure 3.4: Typical filter functions reproduced from Piomelli[101] – – –– sharp Fourier cutoff; – – – truncated Gaussian; – · – · – top hat. (a) real space (b) Fourier space

Sub-grid scale modelling

The main function of the sub-grid scale model is to extract the energy from the resolved large eddies to resemble the dissipation of energy cascade. Several forms of these sub-grid scale models exist. However, a large majority of them are based on the RANS counterparts which rely on the eddy viscosity hypothesis. Smagorinsky[102] derived the *'Smagorinsky model'* based on the assumption that the small scales receiving the energy from the large scales dissipate the energy instantaneously. The Smagorinsky model approximates the SGS stress as,

$$\tau_{ij} - \frac{1}{3}\delta_{ij}\tau_{kk} = 2C_s\Delta^2|\overline{S}|\overline{S}_{ij} \tag{3.10}$$

where δ_{ij} is the Kronecker delta function. The sub-grid scale eddy-viscosity is given as $\nu_t = (C_s\Delta)^2|\overline{S}|$ where C_s is the Smagorinsky constant that ranges between 0.18 and 0.23; Δ, the filter width governed by the mesh size ($\Delta = (\Delta V)^{\frac{1}{3}}$) and the magnitude of the strain rate tensor, $|\overline{S}| = (2(\overline{S_{ij}}\ \overline{S_{ij}}))^{1/2}$, $\overline{S_{ij}}$ is the rate of strain tensor of the resolved velocity field where $\overline{S}_{ij} = (\partial u_i/\partial x_j + \partial u_j/\partial x_i)/2$.

Although this model has been successfully used, a particular drawback is the constant value for C_s. In certain flow conditions where high shear occurs, the value of C_s must be decreased and needs to be countered using a damping function. Although this is beneficial, the value of the constant must be dependent on the local flow properties hence dynamically computed rather

[102] J. Smagorinsky. *Mon. Weather Rev.*, **91**: 99–164, 1963.

than restricting it to one value. Germano et al.[103] proposed these changes for the dynamic computation of the Smagorinsky constant C_s which was later remedied by the error minimization using the least-squares method by Lilly[104]. This modified version of the dynamic Smagorinsky model is employed in the current research.

Discretisation

The general transport equation for the scalar quantity ϕ inside a domain can be written as,

$$\underbrace{\frac{d}{dt}\int_V \phi dV}_{\text{Temporal derivative}} + \underbrace{\int_V \nabla\cdot(\bar{u}\phi)dV}_{\text{Convection term}} - \underbrace{\int_V \nabla\cdot(\Gamma_\phi \nabla\phi)dV}_{\text{Diffusion term}} = \underbrace{\int_V S_\phi(\phi)dV}_{\text{Source term}} \tag{3.11}$$

The transport equation is of second-order (diffusion term) therefore, the order of discretisation must be of second order or higher hence all the dependent variables are assumed to vary linearly around the point P.

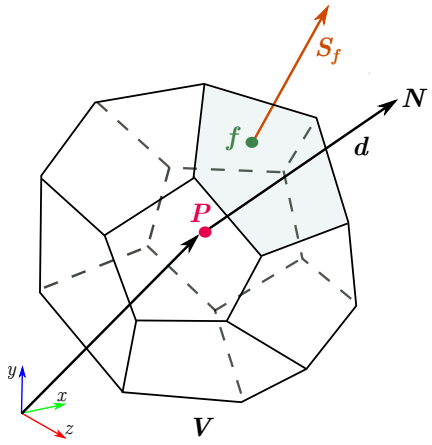

Figure 3.5: Control volume for a finite volume discretisation.

For a control volume V as shown in figure 3.5 which has a centroid P, face f and face area vector $\boldsymbol{S_f}$ located at the face centroid, the variation of ϕ and X is represented by a piecewise constant profile,

$$\phi_P = \bar{\phi} = \frac{1}{V}\int_V \phi(X)dV \tag{3.12}$$

where V is the cell volume and the centroid is given as,

$$\int_V (X - X_P)dV = 0 \tag{3.13}$$

[103]M. Germano et al. *Phys. Fluids*, **3**: 1760–1765, 1991.
[104]D.K. Lilly. *Phys. Fluids*, **4**: 633–635, 1992.

Using Gauss's theorem, the volume integrals are converted into surface integrals yielding discrete equations for each term in the transport equation. Therefore, equation 3.11 appears as,

$$\frac{d}{dt}\int_V \phi dV + \underbrace{\oint_{\partial V} d\boldsymbol{S}\cdot(\bar{u}\phi)}_{\text{Convective flux}} - \underbrace{\oint_{\partial V} d\boldsymbol{S}\cdot(\Gamma_\phi \nabla\phi)}_{\text{Diffusive flux}} = \int_V \boldsymbol{S_\phi}(\phi)dV \tag{3.14}$$

Convective term

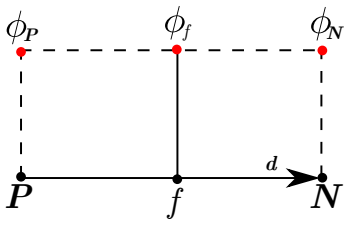

Figure 3.6: Stencil showing face interpolation between two adjacent cells.

The convective terms can be obtained from equation 3.14 as,

$$\underbrace{\int_V \nabla\cdot(\bar{u}\phi)dV}_{\text{Convection term}} = \underbrace{\oint_{\partial V} d\boldsymbol{S}\cdot(\bar{u}\phi)}_{\text{Convective flux}} = \sum_f \int_f d\boldsymbol{S}\cdot(\bar{u}\phi)_f \approx \sum_f \boldsymbol{S_f}\cdot(\overline{u\phi})_f = \sum_f \boldsymbol{S_f}\cdot(u\phi)_f \tag{3.15}$$

The face centered values are determined from the interpolation of the cell values at the centroid P and the neighbouring cell N (see figure 3.6) using a central differencing method. The interface value ϕ_f can be determined by,

$$\phi_f = \lambda\phi_P + (1-\lambda)\phi_N, \tag{3.16}$$

where the interpolation factor, $\lambda = fN/PN$. This second order accurate central differencing scheme is used throughout the current research.

Diffusion term

The diffusion terms can be obtained from equation 3.14 as,

$$\begin{aligned}\underbrace{\int_V \nabla\cdot(\Gamma_\phi\nabla\phi)dV}_{\text{Diffusion term}} = \underbrace{\oint_{\partial V} d\boldsymbol{S}\cdot(\Gamma_\phi\nabla\phi)}_{\text{Diffusive flux}} = \sum_f \int_f d\boldsymbol{S}\cdot(\Gamma_\phi\nabla\phi)_f \approx \sum_f \boldsymbol{S_f}\cdot(\overline{\Gamma_\phi\nabla\phi})_f \\ = \sum_f \boldsymbol{S_f}\cdot(\Gamma_\phi\nabla\phi)_f\end{aligned} \tag{3.17}$$

The diffusion terms are again discretised similar to the convective terms and for an orthogonal mesh (e.g. in figure 3.5, vectors $\boldsymbol{d}$ and $\boldsymbol{S_f}$ are parallel), the gradient term can be represented as,

$$\boldsymbol{S} \cdot (\nabla\phi)_f = |\boldsymbol{S}| \frac{(\phi_N - \phi_P)}{|\boldsymbol{d}|}. \tag{3.18}$$

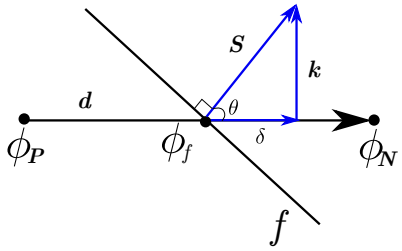

Figure 3.7: Representation of grid non-orthogonality.

In cases where the mesh is non-orthogonal (see figure 3.7), the gradient term is split into an orthogonal part and a non-orthogonal part as follows,

$$\boldsymbol{S} \cdot (\nabla\phi)_f = \underbrace{\boldsymbol{\delta} \cdot (\nabla\phi)_f}_{\text{orthogonal}} + \underbrace{\boldsymbol{k} \cdot (\nabla\phi)_f}_{\text{non-orthogonal}} \tag{3.19}$$

Here $\boldsymbol{\delta}$ represents the vector component parallel to $\boldsymbol{d}$ and $\boldsymbol{k}$ must satisfy $\boldsymbol{S} = \boldsymbol{k} + \boldsymbol{\delta}$. The value of the correction $\boldsymbol{\delta}$ has to be as small as possible after the decomposition of $\boldsymbol{S}$ and the non-orthogonal component $\boldsymbol{k}$. An *'over-relaxed'* approach was found by Jasak[105] to be more robust compared several other configurations in calculating the orthogonal component such as,

$$\boldsymbol{\delta} = \frac{\boldsymbol{d}}{\boldsymbol{d} \cdot \boldsymbol{S}} |\boldsymbol{S}|^2 \tag{3.20}$$

Moreover, when θ increases, $\boldsymbol{d} \cdot \boldsymbol{S}$ decreases through the dot product identity. Hence it is necessary to keep the mesh-orthogonality under reasonable limits such that the diffusion term remains bounded and the solution is stable.

Source term

The source terms obtained from equation 3.11 can be discretised to fit into a matrix such that it has a constant term and a linear term as,

$$\int_V S_\phi(\phi) dV = \underbrace{S_c V}_{\text{constant term}} + \underbrace{S_p V \phi}_{\text{linear term}} \tag{3.21}$$

[105] H. Jasak. *Error analysis and estimation for finite volume method with applications to fluid flow.* PhD thesis, 1996.

Time Integration

The temporal discretisation is carried out after the spatial discretization using the Method of Lines (MOL). This technique enables the user to have different accuracy levels for the spatial and temporal terms. The semi-discrete form of the transport equation can be written as,

$$\int_t^{t+\Delta t} \left[\left(\frac{\partial \phi}{\partial t} \right)_P V + \sum_f \boldsymbol{S_f} \cdot (\bar{u}\phi)_f - \sum_f \boldsymbol{S_f} \cdot (\Gamma_\phi \nabla_\phi)_f \right] dt = \int_t^{t+\Delta t} (S_c V + S_p V \phi_P) dt \quad (3.22)$$

A suitable discretization scheme can be used for the above equation such as a Crank-Nicholson scheme, forward Euler or backwards differencing to obtain the system of linear algebraic equations for the transported quantity ϕ.

Second Order Backward Differencing

The temporal derivative from equation 3.22 can be calculated as,

$$\left(\frac{\partial \phi}{\partial t} \right)_P = \frac{\phi_P^n - \phi_P^{n-1}}{\Delta t}, \quad (3.23)$$

$$\int_t^{t+\Delta t} \phi(t) dt = \frac{1}{2}(\phi^{n-1} + \phi^n)\Delta t \quad (3.24)$$

where $\phi^n = \phi(t + \Delta t)$ and $\phi^{n-1} = \phi(t)$ represent the value of the dependent variable at the new and previous times respectively. Equation 3.23 provides a second order accurate representation at $t + \frac{1}{2}\Delta t$ only. If the same value is assumed for the derivative at time t, the overall accuracy of the transport equation reduces to first order. The Backward Differencing scheme overcomes this drawback by using three levels of time to calculate the temporal derivative by,

$$\phi^{n-2} = \phi^{t-\Delta t} \quad (3.25)$$

$$\phi^{n-1} = \phi^t \quad (3.26)$$

$$\phi^n = \phi^{t+\Delta t} \quad (3.27)$$

Equation 3.25 on Taylor expansion around n is written as,

$$\phi^{n-2} = \phi^n - 2\left(\frac{\partial \phi}{\partial t} \right)^n \Delta t + 2\left(\frac{\partial^2 \phi}{\partial t^2} \right)^n \Delta t^2 + \mathcal{O}(\Delta t^3) \quad (3.28)$$

Similary for equation 3.26 the expansion is given by,

$$\phi^{n-1} = \phi^n - 2\left(\frac{\partial \phi}{\partial t} \right)^n \Delta t + \frac{1}{2}\left(\frac{\partial^2 \phi}{\partial t^2} \right)^n \Delta t^2 + \mathcal{O}(\Delta t^3) \quad (3.29)$$

Combining equations 3.29 and 3.28 we get,

$$\left(\frac{\partial \phi}{\partial t}\right)^n = \frac{\frac{3}{2}\phi^n - 2\phi^{n-1} + \frac{1}{2}\phi^{n-2}}{\Delta t} \tag{3.30}$$

By neglecting the temporal variation in the face fluxes and derivatives equation 3.30 produces a fully implicit second order accurate discretisation of the general transport equation,

$$\frac{\frac{3}{2}\phi^n - 2\phi^{n-1} + \frac{1}{2}\phi^{n-2}}{\Delta t} V_P + \sum_f F\phi_f^n - \sum_f (\Gamma_\phi)_f \boldsymbol{S} \cdot (\nabla\phi)_f^n = S_c V_P + S_p V_P \phi_P^n \tag{3.31}$$

This backward differencing scheme creates an added diffusion due to the lack of temporal variation in face fluxes and derivatives. In order to stabilise the solution, the Courant-Friedrich-Lewy[106] (CFL) number defined with reference to figure 3.5 as,

$$CFL = \frac{\bar{u}_f \; n}{|d|} \tag{3.32}$$

has to be less than 1, creating a much smaller time-step therefore reducing the size of the temporal diffusion. This second-order backward differencing scheme is used in the current research. The temporal resolution is dynamically adjusted through a variable time-stepping technique such that the CFL number was less than or equal to 0.6 at all times.

Pressure-Velocity Coupling

Two types of pressure-velocity coupling procedure are employed. For the RANS cases, the Semi-Implicit Method for Pressure-Linked Equations (SIMPLE) algorithm proposed by Patankar & Spalding[107] is used. For the LES cases, as they are inherently unsteady, the Pressure Implicit with Splitting of Operators algorithm (PISO developed by Issa[108,109]) merged with the SIMPLE algorithm resulting in a PISO-SIMPLE or PIMPLE algorithm is used.

The pressure equation can be written from equation 3.22 as,

$$a_P \bar{u}_P = \boldsymbol{H} - \nabla \bar{p} \tag{3.33}$$

where a_P is the sum of the coefficients of $\bar{u_P}$ through convection, diffusion and temporal discretisation as,

$$a_P = a_{cP} + a_{dP} + a_{tp} \tag{3.34}$$

[106] R. Courant et al. *IBM J.*, **11**: 215–234, 1967.
[107] S.V. Patankar and D.B. Spalding. *Int. J. Heat Mass Transfer*, **15**: 1787–1806, 1972.
[108] R.I. Issa. *J. Comput. Phys.*, **62**: 40–65, 1986.
[109] R.I. Issa et al. *J. Comput. Phys.*, **93**: 388–410, 1991.

and the vector $\boldsymbol{H}$ is the volumetric vector field calculated from the latest values. Dividing equation 3.33 by a_P,

$$\bar{u}_P = \frac{\boldsymbol{H}}{a_P} - \frac{\nabla \bar{p}}{a_P} \tag{3.35}$$

and the corresponding interpolation on a face can be written as,

$$\bar{u}_f = \left(\frac{\boldsymbol{H}}{a_P}\right)_f - \left(\frac{\nabla \bar{p}}{a_P}\right)_f \tag{3.36}$$

The discretised form of the continuity equation can now be written as:

$$\nabla \cdot \bar{u} = \sum_f A \cdot \bar{u}_f = 0 \tag{3.37}$$

and using u_f from 3.36, the above equation becomes,

$$\nabla \cdot \left(\frac{1}{a_P} \nabla \bar{p}\right) = \nabla \cdot \left(\frac{\boldsymbol{H}}{a_P}\right) = \sum_f A \cdot \left(\frac{\boldsymbol{H}}{a_P}\right)_f \tag{3.38}$$

The Laplacian on the LHS of equation 3.38 and the pressure gradient on the RHS of equation 3.33 can be discretised to get the final form of the Navier-Stokes system:

$$a_P \bar{u}_P = \boldsymbol{H} - \sum_f A \cdot \bar{p}_f \tag{3.39}$$

$$\sum_f A \cdot \left(\frac{1}{a_P}\right) (\nabla \bar{p})_f = \sum_f A \cdot \left(\frac{\boldsymbol{H}}{a_P}\right)_f \tag{3.40}$$

Figure 3.8, 3.9 and 3.10 show the sequence of operations that are carried out in a in SIMPLE, PISO and PIMPLE algorithms for an incompressible fluid.

For the current research, the PIMPLE algorithm is used, and the procedure of the solution steps to solve the unknown variables $\bar{p}$ and $\bar{u}$ are as follows:

- The procedure starts with the initial conditions for the unknown variables ($\bar{u}, \bar{p}$) and face flux ϕ_f. The initial values of the LES fields are derived from RANS simulations (see Chapter 4 for more on RANS simulations).
- The previous or initial time step values are used to update the properties of the unknown variables ($\bar{u}, \bar{p}$ and ϕ_f)
- **Momentum predictor:** The momentum equation is solved where the pressure field from the previous time-step is used at this "momentum predictor" stage. The solution of the matrix is achieved by using an iterative Conjugate Gradient method resulting in an approximate velocity field.

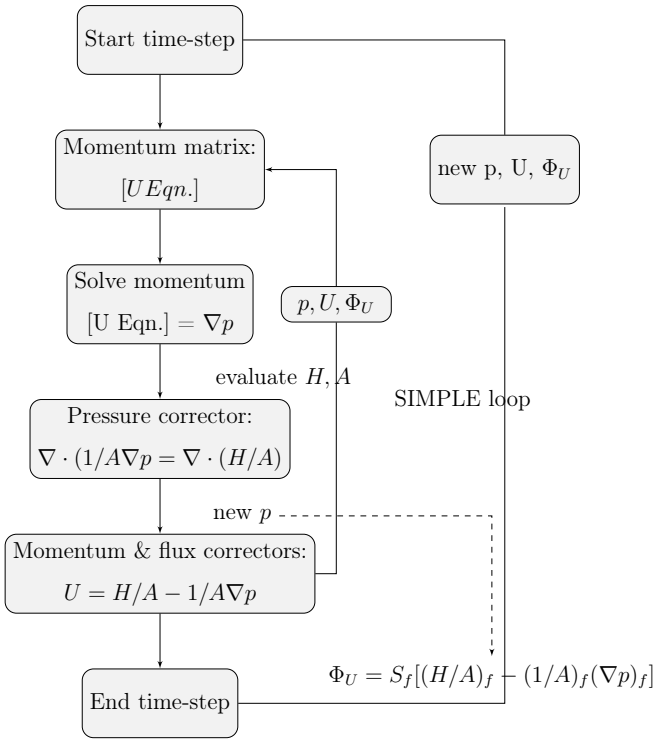

Figure 3.8: Schematic of the SIMPLE algorithm

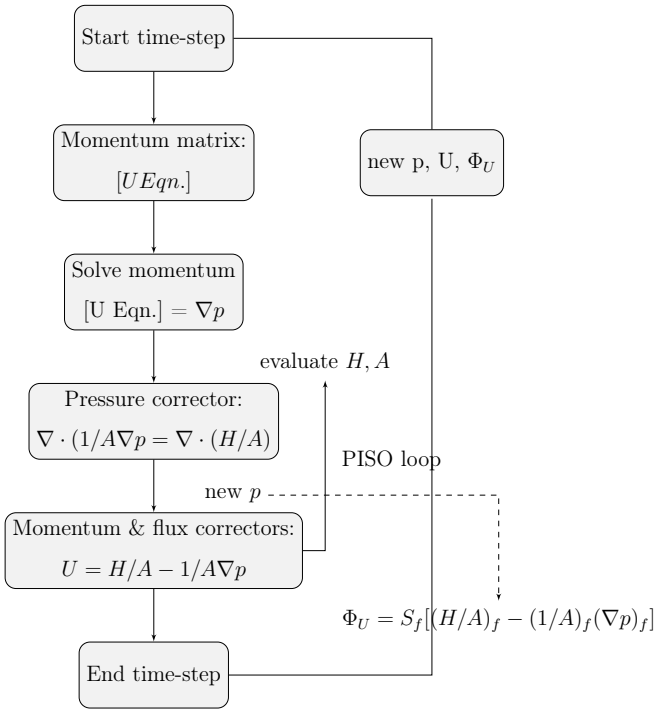

Figure 3.9: Schematic of the PISO algorithm

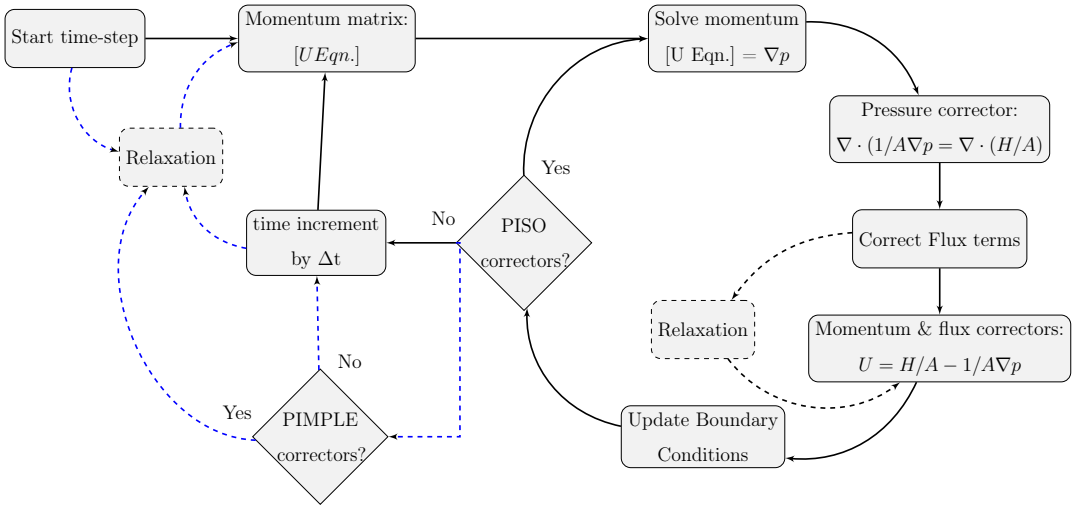

Figure 3.10: Schematic of the PIMPLE algorithm; dotted blue lines indicate the PIMPLE steps and solid black lines indicate PISO steps.

- **Pressure solution:** The updated velocity field is used in the solution of the pressure equation with an Incomplete Cholesky preconditioned Conjugate Gradient method.

- **Explicit velocity correction:** The solution of the pressure is followed by updating the velocity field into a divergence-free form and are repeated until the variables tend to become constant. The velocity and pressure are corrected in loops to ensure that the continuity equation is satisfied. This method also ensures an oscillation-free velocity field with an implicit treatment in line with the Rhie–Chow correction[110].

- The current values are then used as an initial guess for the next cycle of the solution process.

The above procedure is more generalised, and the difference between the SIMPLE, PISO and PIMPLE algorithms exist in how they loop over the equations. The PIMPLE enables the looping over the entire system of equations within one time-step representing the total number of times the system of equations is solved. When the number of loops is set to 1, the PIMPLE algorithm in principle behaves like a PISO algorithm, and when the number of these outer correcting loops are ≥ 2, the conventional PISO algorithm is forced to loop converting it to a PIMPLE algorithm.

[110]C.M. Rhie and W.L. Chow. *AIAA J.*, **21**: 1525–1532, 1983.

3.2.2 Boundary Conditions

The following presents a brief description of the basic boundary conditions used in the current research. The Dirichlet (fixed value), Neumann (fixed gradient) and mixed boundary conditions are the basic types used in the simulations.

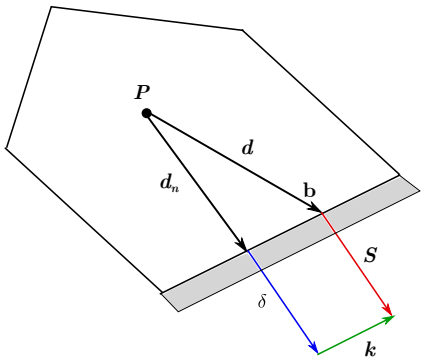

Figure 3.11: Control volume with a boundary face.

Consider the control volume as shown in figure 3.11 with a boundary face b where the vector $\boldsymbol{k}$ is parallel to the face and the orthogonal part $\delta = \boldsymbol{S}$. The vector $\boldsymbol{d_n}$ can then be given as,

$$\boldsymbol{d_n} = \frac{\boldsymbol{S}}{|\boldsymbol{S}|}\frac{\boldsymbol{d}\cdot\boldsymbol{S}}{|\boldsymbol{S}|} \tag{3.41}$$

The Dirichlet or fixed-value boundary condition prescribes the value of the transport quantity ϕ at the face b given as ϕ_b. Correspondingly, during discretisation, the convection and the diffusion terms are updated with the term ϕ_b on the boundary face such that the convection term becomes,

$$\int_V \nabla\cdot(\bar{u}\phi)dV = \sum_f F\phi_f \tag{3.42}$$

and on the boundary face, $\phi = \phi_b$ and $F = F_b$ where F_b is the flux through the face.

Similarly, the diffusion term is written as,

$$\int_V \nabla\cdot(\Gamma_\phi\nabla_\phi)dV = \sum_f (\Gamma_\phi)_f\boldsymbol{S}\cdot(\nabla\phi)_f \tag{3.43}$$

and the face gradient at b is calculated from the known face value and the cell centre value as,

$$\boldsymbol{S}\cdot(\nabla\phi)_b = |\boldsymbol{S}|\frac{\phi_b - \phi_P}{|\boldsymbol{d_n}|} \tag{3.44}$$

The Neumann or the fixed gradient boundary condition prescribes the dot product of the gradient and the outward pointing normal on the boundary such as,

$$\left(\frac{\boldsymbol{S}}{|\boldsymbol{S}|}\cdot\nabla\phi\right)_b = g_b \tag{3.45}$$

and the face value of the transported quantity ϕ for the convection term is calculated from the cell center and the prescribed gradient as,

$$\begin{aligned} \phi_b &= \phi_P + \boldsymbol{d_n} \cdot (\nabla\phi)_b \\ &= \phi_P + |\boldsymbol{d_n}| g_b \end{aligned} \tag{3.46}$$

and the diffusion term is the dot product between the face area vector and $(\nabla\phi)_b$ is,

$$|\boldsymbol{S}| g_b \tag{3.47}$$

and the resulting term is:

$$(\Gamma_\phi)_b |\boldsymbol{S}| g_b \tag{3.48}$$

In summary, the mathematical formulation underlying the discretization of the complex governing equations and the solution procedures were explicitly described. The physical description of the boundary conditions relevant to the current research is presented in the section that follows.

Turbulent inflow generation

During the simulation of unsteady flows and especially impinging jets, the boundary condition at the inlet is often less obvious when it comes to accurately representing experimental conditions. Experiments have often resorted to using fully developed inflows by using sufficiently long pipe lengths (on the order of $75D$ to $100D$) with flow straighteners to have fully developed flow. However, numerically, this is not possible due to the computational expenses involved. Thus it is imperative to produce or mimic the turbulent inflow as close as possible to the experimental conditions with minimal computational expense.

The turbulent inlet is bound to contain a random unsteady velocity field which is divergence free and also visually representative of a turbulent flow field. A variety of techniques exist, and have been employed to produce turbulent inflow resulting in different degrees of success. Some of the methods are discussed briefly below.

Random perturbations: This method imposes random perturbations on a mean velocity field such that these perturbations get amplified over the downstream flow. A typical inlet velocity profile from this technique can be represented as

$$u(r,t) = U(r) + 0.5A(rand(r,t) - 0.5) \tag{3.49}$$

where U is the mean velocity, A the amplitude of the perturbations and a function *'rand'* that generates a random number between the specified intervals. This method is known to damp out the fluctuations rapidly due to the lack of turbulent structures in the flow.

Synthetic turbulence: This method uses artificial turbulent structures to create the velocity distribution with the scales in the order of the mesh size and the integral length scale. These methods are often based on digital filtering of random data. Klein et al.[111] proposed this approach and was applied by Uddin et al.[83] for an LES of a turbulent impinging jet. The Synthetic perturbations of the form,

$$u' = f(r) \sum_{m=1}^{N} A_m(t) \cos(m\theta + \phi_m(t)) \tag{3.50}$$

were used for a DNS of an impinging jet by Dairay et al.[27] where for every velocity component, the number of excited azimuthal modes *(N)* were generated randomly up to a given cutoff frequency with amplitude A_m and phase ϕ_m.

Precursor simulations: The technique is straightforward as it uses a precursor simulation to generate the turbulent data. The data is generated for a sufficiently long time interval and then stored in a database to be used at the inlet for the main simulation. This technique produces accurate inflow, however, at the cost of increased computational time and storage. This also poses rigid usage constraints when minor changes to the flow field are necessary. Hällqvist[79] and Hadžiabdić & Hanjalić[80] have used this method to generate inflow data from the precursor pipe flow simulation and used it at the inlet plane of an impinging jet at $Re_D = 20{,}000$.

Recycling (Inlet Mapping): The inflow conditions are generated by a similar method as the precursor simulation technique except that it is performed simultaneously in a single simulation. Figure 3.12 shows the schematic of this mapping technique. Calculations are performed at a recycle plane downstream of the pipe flow inlet, and transient data from this sample plane is fed back to the inlet at every time-step (see Tabor & Baba-Ahmadi[112]). This method creates a fully developed turbulent velocity profile at the outflow of the pipe due to the flow loop, resembling an infinitely long pipe. However, this technique can be open to

[111] M. Klein et al. *J. Comput. Phys.*, **186**: 652–665, 2003.
[83] N. Uddin et al. *Int. J. Heat Mass Transfer*, **57**: 356–368, 2013.
[27] T. Dairay et al. *J. Fluid Mech.*, **764**: 362–394, 2015.
[79] T. Hällqvist. *Large eddy simulation of impinging jets with heat transfer*. PhD thesis, 2006.
[80] M. Hadžiabdić and K. Hanjalić. *J. Fluid Mech.*, **596**: 221–260, 2008.
[112] G.R. Tabor and M.H. Baba-Ahmadi. *Comput. Fluids*, **39**: 553–567, 2010.

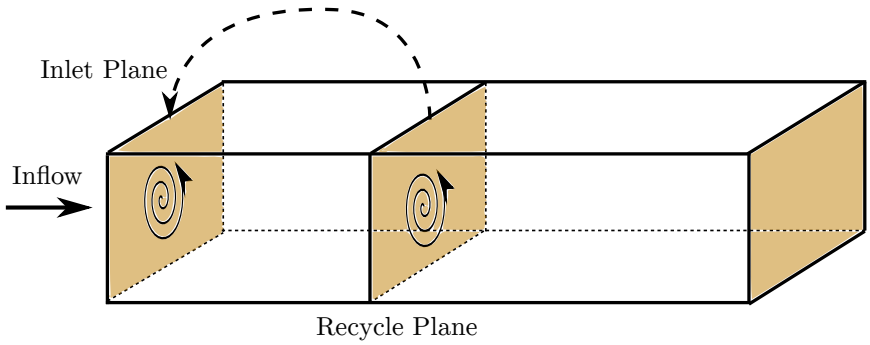

Figure 3.12: Representation of Recycled boundary condition.

non-physical interactions between the recycle plane and the inlet, and may introduce periodicity and streamwise repetition of flow features (Jewkes et al.[113]). This technique is employed in the current research after validation with published experimental and DNS data.

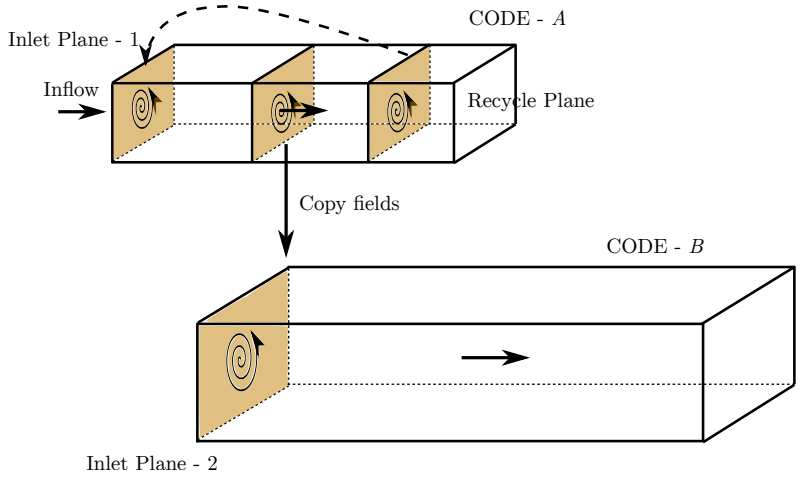

Figure 3.13: Representation of Lund et al.[114] recycled boundary condition.

Other methods: Lund et al.[114] proposed an approach using a rescaling method to generate the inflow velocity. With this method, a code-A generates a turbulent field by mapping velocity field at a downstream distance, and then code-B utilises a plane from simulation with code-A as an inlet to code-B. The figure 3.13 shows the schematic of the method. This technique is widely used in spatially developing boundary layer flows. A modification to this technique was proposed by Jewkes et al.[113] (see figure 3.14). In this method, an 'inflow mirroring' technique was proposed which involved recycling a downstream plane, rescaling and then mirroring the

[113]J.W. Jewkes et al. *AIAA J.*, **49**: 247–250, 2011.
[114]T.S. Lund et al. *J. Comput. Phys.*, **140**: 233–258, 1998.

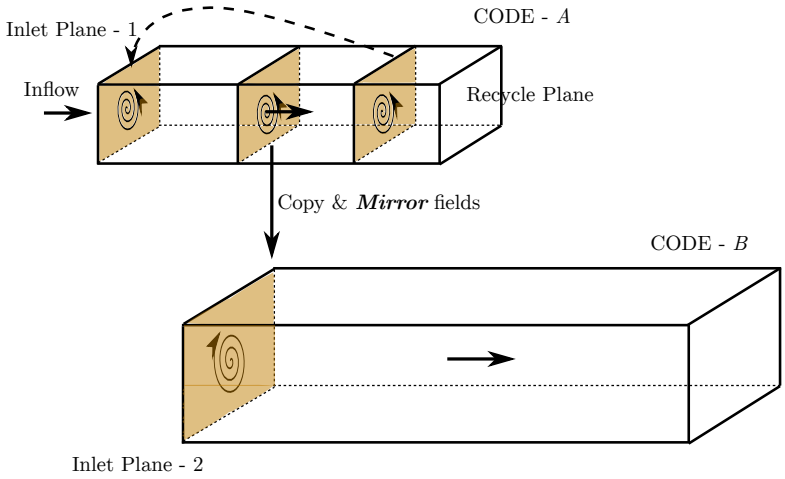

Figure 3.14: Representation of Jewkes et al.[113] mirrored boundary condition.

velocity fields spanwise and introducing again at the inlet.

Outflow conditions

The choice of outflow boundary conditions on the bounding sides of the domain plays a significant role even more so when the nozzle-to-wall spacing is small, and the impingement surface is non-stationary. The boundary condition should be accurate enough to account for the outflow as well as predict the inflow without resulting in any spurious or numerical oscillations. Conventional boundary conditions at the boundaries where both outflow and backflow are expected are as follows:

Convective boundaries: The convective boundaries are usually defined by a hyperbolic convection equation and is given as,

$$\frac{\partial U}{\partial t} + C_{vel}\frac{\partial U}{\partial r} = 0, \tag{3.51}$$

where C_{vel} is the constant convection velocity of the large-scale structures and U is the radial component of the velocity vector field. The convective boundary conditions were used by Hadžiabdić & Hanjalić[80] and Uddin et al.[83] among others for LES of impinging jets, and have obtained reasonable agreement with the experimental measurements.

Pressure boundaries: The pressure boundaries allow for both the influx and outflux of the fluid from the domain based on the local pressure values. Figure 3.15 shows the schematic

of such a boundary condition used in the current research.

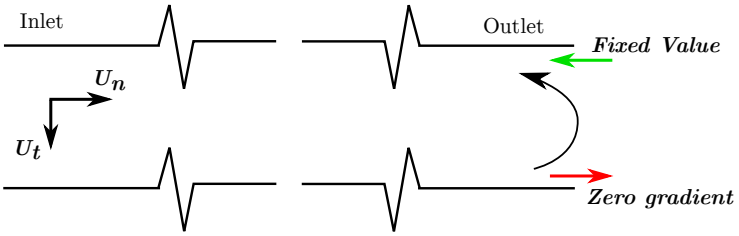

Figure 3.15: Representation of mixed boundary condition.

With this boundary condition, for an inbound flow, the velocity is obtained using the flux from the first adjacent cell of the boundary and for outward flow, a zero-gradient is applied. A Dirichlet boundary condition is applied for pressure at the outlets, using the reference pressure of the flow field, $p_0 = p + 0.5|U|^2$, where p_0 is the stagnation pressure, and p is the static pressure at the boundary and is dependent upon **U**.

Fringe Method: The fringe method was proposed by Nordström et al.[115] This technique essentially adds a volume force $\mathcal{F}$ to the Navier-Stokes equation as,

$$\mathcal{F} = \lambda(r)(\tilde{u} - u) \tag{3.52}$$

where $\tilde{u}$ is a target velocity field and $\lambda(r)$ is a modulation function given by,

$$\lambda(r) = \frac{1}{2}(1 + \tanh(\beta(r - r_m) - 4D)) \tag{3.53}$$

and a purely radial flow is assumed as the target velocity field. Dairay et al.[27,84] have used these boundaries for both LES and DNS of turbulent impinging jets.

Wall and Near-Wall treatment

The choice of near-wall treatment is often difficult when the geometries are complex, and the Reynolds number high. Several wall models exist such as the universal profile or Spalding's law[116] which assume a velocity profile from the wall to the first grid point in the wall-normal direction based on the equation,

$$y^+ = u^+ + \frac{1}{E}\left[e^{\kappa u^+} - 1 - \kappa u^+ - \frac{1}{2}(\kappa u^+)^2 - \frac{1}{6}(\kappa u^+)^3\right] \tag{3.54}$$

[115] J. Nordström et al. *SIAM J. Sci. Comput.*, **20**: 1365–1393, 1999.
[84] T. Dairay et al. *Int. J. Heat Fluid Flow*, **50**: 177–187, 2014.
[116] D.B. Spalding. *J. Appl. Mech.*, **28**: 455–458, 1961.

where the constants κ and E are 0.42 and 9.1 respectively. On the contrary, to resolve the near-wall by increasing the resolution not just in the wall-normal direction but also in the radial and azimuthal direction is the solution when the Reynolds number is moderate, and the geometry is simple in construction.

As no-slip boundaries are implemented on the impingement surfaces, the velocity is zero at the wall, and no wall functions are used in the current research. The resolution is based on the y^+ estimate given as

$$y^+ = \frac{yu_\tau}{\nu} \tag{3.55}$$

where the friction velocity u_τ is given by $\sqrt{\frac{\tau}{\rho}}$ with τ being the wall shear stress.

3.2.3 Treatment of Heat Transfer

The convective heat transfer from the impingement wall is a function of the convective heat transfer coefficient h. As mentioned previously, the Nusselt number based on the heat transfer coefficient h and the diameter of the nozzle D is defined as

$$Nu = \frac{hD}{k} \tag{3.56}$$

where h is given as,

$$h = \frac{-k\partial T/\partial n}{T_{wall} - T_f} \tag{3.57}$$

where $\partial T/\partial n$ is the temperature gradient normal to the impingement wall, T_{wall} is the measured local wall temperature, T_f is the inlet temperature of the fluid and k is its corresponding thermal conductivity. The flow field is assumed to be unaffected by the temperature variations on the impingement wall and is advected by the fluid momentum along with molecular diffusion. Hence, the scalar transport equation for heat transfer can be solved with temperature as a passive scalar is given by,

$$\frac{\partial T}{\partial t} + u_j \frac{\partial T}{\partial x_j} = \alpha \frac{\partial^2 T}{\partial {x_j}^2} \tag{3.58}$$

where α represents the thermal diffusivity and is given as $(\nu/Pr + \nu_t/Pr_t)$. Pr and Pr_t are the laminar and turbulent Prandtl numbers, and ν and ν_t are their corresponding viscosities. The transport equation is coupled with the Navier-Stokes equations through the velocity field. The boundary condition for temperature on the wall is a uniform heat flux along with the no-slip boundary condition for velocity.

3.2.4 Reynolds Averaged Navier-Stokes Simulations (RANS)

Direct numerical simulations are the most accurate method of resolving all the scales of motion. The simulation methodology provides a full description of the eddies up to the Kolmogorov's length scale given by,

$$\eta_k = \left(\frac{\nu^3}{\epsilon}\right)^{1/4} \tag{3.59}$$

where ν is the kinematic viscosity and ϵ, is the dissipation rate. There is no modelling involved since all the length scales are resolved. However, the resolution requirement $N_x \times N_y \times N_z$ is equal to Re^3 where $N_{x,y,z}$ represents the number of grid points required in the three-dimensional grid space. Hence, DNS tends to be computationally expensive for higher Reynolds numbers. Although DNS offers complete data sets with accuracies on par with experiments, there are other challenges in solving the governing equations of fluid flow through a DNS which include an exact specification of the initial and boundary conditions. The other extreme in solving the governing equations are by using the RANS approach where the solution is obtained as mean or averaged quantities ignoring the fluctuating components of the flow. All the length scales involved are modelled using turbulence closures for the Reynolds stress tensor. The grid resolution requirements are not as rigorous as a DNS and therefore provides useful insights where the Reynolds numbers are extremely high (e.g., external aerodynamics).

The RANS models are primarily categorised into three main types namely Linear, Nonlinear eddy viscosity models and Reynolds stress model. The linear eddy viscosity models are by far the most widely used RANS-based turbulence models compared to their non-linear counterparts. The theory behind the turbulence models that have been used in the current research is briefly presented in the following section.

Standard k-ϵ model: The standard k-ϵ model was formulated by Launder & Spalding[117] essentially solves two transport equations each for the turbulent kinetic energy, k and the dissipation rate of turbulent kinetic energy, ϵ. The turbulent viscosity ν_T is calculated as,

$$\nu_T = C_\mu \frac{k^2}{\epsilon} \tag{3.60}$$

where C_μ is a constant. The exact equation for the turbulent kinetic energy k is given by,

$$\frac{\bar{D}k}{\bar{D}t} = -\nabla \cdot \phi' + \mathcal{P} - \epsilon \tag{3.61}$$

[117] B.E. Launder and D.B. Spalding. *Lectures in mathematical models of turbulence.* 1972.

where ϕ' is the flux of the Reynolds stress and $\mathcal{P}$ is the rate of turbulent kinetic energy production given by,

$$\mathcal{P} = -\langle u_i u_j \rangle \frac{\partial \langle U_i \rangle}{\partial x_j} \tag{3.62}$$

Here ϕ' needs a closure based on the gradient-diffusion hypothesis resulting in the model transport equation as,

$$\frac{\bar{D}k}{\bar{D}t} = \nabla \cdot \left(\frac{\nu_T}{\sigma_k} \nabla k \right) + \mathcal{P} - \epsilon \tag{3.63}$$

where σ_k is a model constant. The dissipation rate ϵ is given by,

$$\epsilon = \nu \left\langle \frac{\partial u_i}{\partial x_j} \frac{\partial u_i}{\partial x_j} \right\rangle \tag{3.64}$$

and the corresponding model transport equation for the dissipation rate ϵ is given by,

$$\frac{\bar{D}\epsilon}{\bar{D}t} = \nabla \cdot \left(\frac{\nu_T}{\sigma_k} \nabla \epsilon \right) + C_{\epsilon 1} \frac{\mathcal{P}\epsilon}{k} - C_{\epsilon 2} \frac{\epsilon^2}{k} \tag{3.65}$$

the model constants are $C_\mu = 0.09$, $C_{\epsilon 1} = 1.44$, $C_{\epsilon 2} = 1.92$, $\sigma_k = 1.0$ and $\sigma_\epsilon = 1.3$. The standard k-ϵ model is known for poorly predicting the heat transfer in the stagnation region when applied to jet impingement problems (see Seyedein et al.[118]).

RNG k-ϵ model: The RNG k-ϵ model was derived by Yakhot & Orszag[119] based on the renormalization group theory (RNG). The model is very similar to the standard k-ϵ model except that additional terms related to mean strain are considered. Here the flux of Reynolds stress, ϕ' needs a closure based on the gradient-diffusion hypothesis resulting in the model transport equation as,

$$\frac{\bar{D}k}{\bar{D}t} = \nabla \cdot \left(\frac{\nu_T}{\sigma_k} \nabla k \right) + \mathcal{P} - \epsilon \tag{3.66}$$

where σ_k is a model constant and the corresponding model transport equation for the dissipation rate ϵ is given by,

$$\frac{\bar{D}\epsilon}{\bar{D}t} = \nabla \cdot \left(\frac{\nu_T}{\sigma_k} \nabla \epsilon \right) + C_{1\epsilon 1} \frac{\mathcal{P}\epsilon}{k} - C^*_{\epsilon 2} \frac{\epsilon^2}{k} \tag{3.67}$$

where

$$C^*_{\epsilon 2} = C_{\epsilon 2} + \frac{C_\mu \eta^3 (1 - \eta/\eta_0)}{1 + \beta \eta^3} \tag{3.68}$$

and $\eta = Sk/\epsilon$ and $S = (2S_{ij}S_{ij})^{1/2}$. The model constants are $C_\mu = 0.09$, $C_{\epsilon 1} = 1.42$, $C_{\epsilon 2} = 1.68$, $\sigma_k = 0.7194$, $\sigma_\epsilon = 0.7194$, $\eta_0 = 4.38$ and $\beta = 0.012$. The model has been reported for improving the predictions for low Reynolds number flows and wall heat and mass transfer; however, it still fails to predict the spreading rate of a round jet.

[118] S.H. Seyedein et al. *Appl. Math. Modell.*, **18**: 526–537, 1994.

[119] V. Yakhot and S.A. Orszag. *J. Sci. Comput.*, **1**: 3–51, 1986.

Realizable k-ϵ model: This model was developed by Shih et al.[120] essentially based on the transport equations of the standard k-ϵ model with an improvement to the calculation of ϵ and an alternative formulation for computing the turbulent viscosity, ν_T. The turbulent viscosity is represented as,

$$\nu_T = C_\mu \frac{k^2}{\epsilon} \tag{3.69}$$

where C_μ is given by,

$$C_\mu = \frac{1}{A_0 + A_S \frac{k u^*}{\epsilon}} \tag{3.70}$$

Here, $A_0 = 4.04, A_S = \sqrt{6}\cos\phi$, $u^* \equiv \sqrt{S_{ij}S_{ij} + \bar{\Omega}_{ij}\bar{\Omega}_{ij}}$ and $\bar{\Omega}_{ij}$ is the mean rate of rotation tensor. The model transport equation for the turbulent kinetic energy, k is given as,

$$\frac{\bar{D}k}{\bar{D}t} = \nabla \cdot \left(\frac{\nu_T}{\sigma_k} \nabla k \right) + \mathcal{P}_k + \mathcal{P}_b - \epsilon - Y_M + S_k \tag{3.71}$$

where $\mathcal{P}_k$ and $\mathcal{P}_b$ represent the turbulent kinetic production based on the mean velocity gradients and buoyancy forces respectively. The model transport equation for the turbulent kinetic energy dissipation, ϵ is given as,

$$\frac{\bar{D}\epsilon}{\bar{D}t} = \nabla \cdot \left(\frac{\nu_T}{\sigma_\epsilon} \nabla \epsilon \right) + C_1 S\epsilon - C_2 \frac{\epsilon^2}{k + \sqrt{\nu\epsilon}} + C_{1\epsilon} \frac{\epsilon}{k} C_{3\epsilon} \mathcal{P}_b + S_\epsilon \tag{3.72}$$

where

$$C_1 = max\left[0.43, \frac{\eta}{\eta + 5}\right], \quad \eta = S\frac{k}{\epsilon} \quad \& \quad S = \sqrt{2S_{ij}S_{ij}} \tag{3.73}$$

The model constants are $C_{\epsilon 1} = 1.44$, $C_{\epsilon 2} = 1.92$, $\sigma_k = 1.0$ and $\sigma_\epsilon = 1.2$. This model is known to predict the jet spreading angles however showed large inconsistencies in predicting velocity gradients in axisymmetric flows.

Standard k-ω model: The standard k-ω model (or Wilcox k-ω model) was developed by Wilcox[121] based on solving two additional transport equations for a modified turbulent kinetic energy and specific dissipation rate ω. The specific dissipation rate ω is computed as,

$$\omega = \frac{\epsilon}{k} \tag{3.74}$$

The model transport equation based on the turbulent kinetic energy, k, is given as,

$$\frac{\bar{D}k}{\bar{D}t} = \nabla \cdot [(\nu + \sigma\nu_T)\nabla k] + \mathcal{P} - \epsilon \tag{3.75}$$

[120] T-H. Shih et al. *Comput. Fluids*, **24**: 227–238, 1995.

[121] D.C. Wilcox. *Turbulence modeling for CFD.* vol. 2 1998.

and the corresponding model transport equation for the specific dissipation rate ω is,

$$\frac{\bar{D}\omega}{\bar{D}t} = \nabla \cdot [(\nu + \sigma\nu_T)\nabla\omega] + \alpha\frac{\mathcal{P}}{k} - \beta\omega^2 \tag{3.76}$$

The model constants are $\sigma = 0.5$, $\alpha = 0.52$ and $\beta = 0.072$. The numerical behaviour is similar to that of k-ϵ models.

SST k-ω model: Menter[122] proposed the shear stress transport (SST) k-ω model which is a combination of both the k-ω and the k-ϵ models and well suited for wall-bounded flows. Essentially the model behaves as a k-ω model in the near-wall region and switches to a k-ϵ formulation in the far field.

The definition of ω in terms of k and ϵ can be written as,

$$\omega = \frac{\epsilon}{\beta^* k} \tag{3.77}$$

where $\beta^* = C_\mu$. The model transport equation for turbulent kinetic energy k is given as,

$$\frac{\bar{D}k}{\bar{D}t} = \nabla \cdot \left(\frac{\nu_T}{\sigma_k}\nabla k\right) + \mathcal{P}_k - \beta^* k\omega \tag{3.78}$$

and the corresponding model equation for the specific dissipation rate ω is given as,

$$\frac{\bar{D}\omega}{\bar{D}t} = \nabla \cdot \left(\frac{\nu_T}{\sigma_\omega}\nabla\omega\right) + \mathcal{P}_\omega - \beta\omega^2 + 2(1 - F_1)\sigma_{\omega 2}\frac{1}{\omega}\nabla k\nabla\omega \tag{3.79}$$

where the blending function F_1 is evaluated as,

$$F_1 = \tanh(\zeta^4), \zeta = min\left[max\left(\frac{\sqrt{k}}{\beta^*\omega y}, \frac{500\nu}{y^2\omega}\right), \frac{4\sigma_{\omega 2}k}{CD_\omega y^2}\right] \tag{3.80}$$

The blending functions serves to switch between the k-ω and k-ϵ models based on the value it takes between 0 and 1. For the value 0, it behaves as a k-ϵ model. The corresponding model constants are also modified which is done based on the function ϕ as,

$$\phi = F_1\phi_1 + (1 - F_1)\phi_2 \tag{3.81}$$

where ϕ_i denotes either α_i or β_i, or according to,

$$\frac{1}{\psi} = F_1\frac{1}{\psi_1} + (1 - F_1)\frac{1}{\psi_2}, \tag{3.82}$$

where ψ_j denotes either σ_{kj} or $\sigma_{\omega j}$. The cross diffusion term CD_ω is given by,

$$CD_\omega = max\left(2\sigma_{\omega 2}\frac{1}{\omega}\frac{\partial k}{\partial x_i}\frac{\partial \omega}{\partial x_i}, 10^{-10}\right) \tag{3.83}$$

[122]F.R. Menter. *AIAA J.*, **32**: 1598–1605, 1994.

The values of the model constants are $\alpha_1 = 5/9$; $\alpha_2 = 0.44$; $\beta_1 = 3/40$; $\beta_2 = 0.0828$; $\frac{1}{\sigma_{k1}} = 0.85$; $\frac{1}{\sigma_{k2}} = 1$; $\frac{1}{\sigma_{\omega_1}} = 0.5$; $\frac{1}{\sigma_{\omega_2}} = 0.856$.

Though several other RANS formulations exist, for the sake of brevity and the scope of the current research, they are not discussed in great detail. The work of Hofmann et al.[123] (among many others) provides a comprehensive analysis of the most widely used RANS turbulence models specifically applied to impinging jets. The RANS models described above have been used for impinging jet simulations and the results are discussed in greater detail in Chapter 4.

3.3 Parallelization Strategy

The parallelization strategy used for the simulations is briefly discussed here. The parallelization of a computational domain is essentially splitting or decomposing the entire domain into smaller sized fragments (using a graph-partitioning) and each of those little fragments being assigned to an individual processor in a high-performance computer. Therefore, multiple processors are allocated to the same domain, but each processor works on different fragments or sections of the domain while simultaneously interacting with each other to provide the solution. This is possible in OpenFOAM through the Domain Decomposition Method (DDM) since the code enables process-level parallelism where a halo-layer approach is used to treat the processor boundaries as internal edges with boundary conditions[100].

Several methods of domain decomposition are available and are discussed briefly below:

Simple: The 'simple' method of decomposition divides the computational domain into sub-domains based on the direction (x, y & z) alone. This approach allows the user to specify the sub-domains in each coordinate in space. For example, a pipe flow would have more sub-domains in the axial flow direction.

Hierarchical: The 'hierarchical' method of decomposition is similar to the 'Simple' decomposition except that the hierarchy in which the decomposition is performed can be controlled with this method. For example, order *'yzx'* will start distribution of cells in y, and end in the x coordinate.

[123] H.M. Hofmann et al. *Numer. Heat Transfer, Part B*, **51**: 565–583, 2007.

Manual: The 'manual' method as the name implies, allows the user to manually specify each location in the sub-domain to a particular processor. This approach can be particularly useful when the domain has to be split into sub-domains at an exact location or when a small portion of the domain (in micro-fluidic applications) has to be preserved into a single sub-domain.

METIS: The METIS decomposition method requires no geometric input from the user and attempts to minimise the number of processor boundaries based on a weighting factor specified by the user. Reduction in processor boundaries minimises the communication volume between processors, and hence the overall computing time which can be useful on hardware configurations that have performance varying between processors.

SCOTCH: SCOTCH[124] uses a similar technique as 'METIS' but with a more flexible open-source license and applies graph theory, with a multi-branched recursion approach for partitioning and ordering graph and mesh and attempts to minimise the number of internal boundaries. The domain decomposition can be modelled as graph partitioning problems on the adjacency graph of matrices. The main purpose is to separate the edges in a way to cause minimal communication between internal boundaries. This library implements the multilevel FM-like algorithms, k-way graph partitioning, and recursive bi-partitioning. The user can specify the strategy and the weights of the subdomains.

Figure 3.16 shows the result of decomposing a cubical domain among 8 processors with the above mentioned decomposition methods. Several other user decomposition methods such as 'structured' and 'multilevel' exist. However, they are mostly based on the concepts of the methods described above. The code developed in the present study is parallelized using the Message Passing Interface (MPI) protocol and the graph partitioning algorithm SCOTCH[124] was used to decompose the solution domain into the required number of sub-domains for parallel computing. The algorithm has been widely tested and accounts for the differing performances among processors. Since this algorithm reduces the number of processor boundaries, thus reducing the interconnect message passing, it results in higher performance. SCOTCH is used as the decomposition method for the current research work.

The performance of the code, especially the influence of the boundary conditions, cost of communication was evaluated on a high-performance computer. A strong scaling was performed

[124]F Pellegrini and J Roman. "Scotch: A software package for static mapping by dual recursive bipartitioning of process and architecture graphs" in: *High-Performance Computing and Networking*. vol. 1067 Springer Berlin Heidelberg, 1996. 493–498

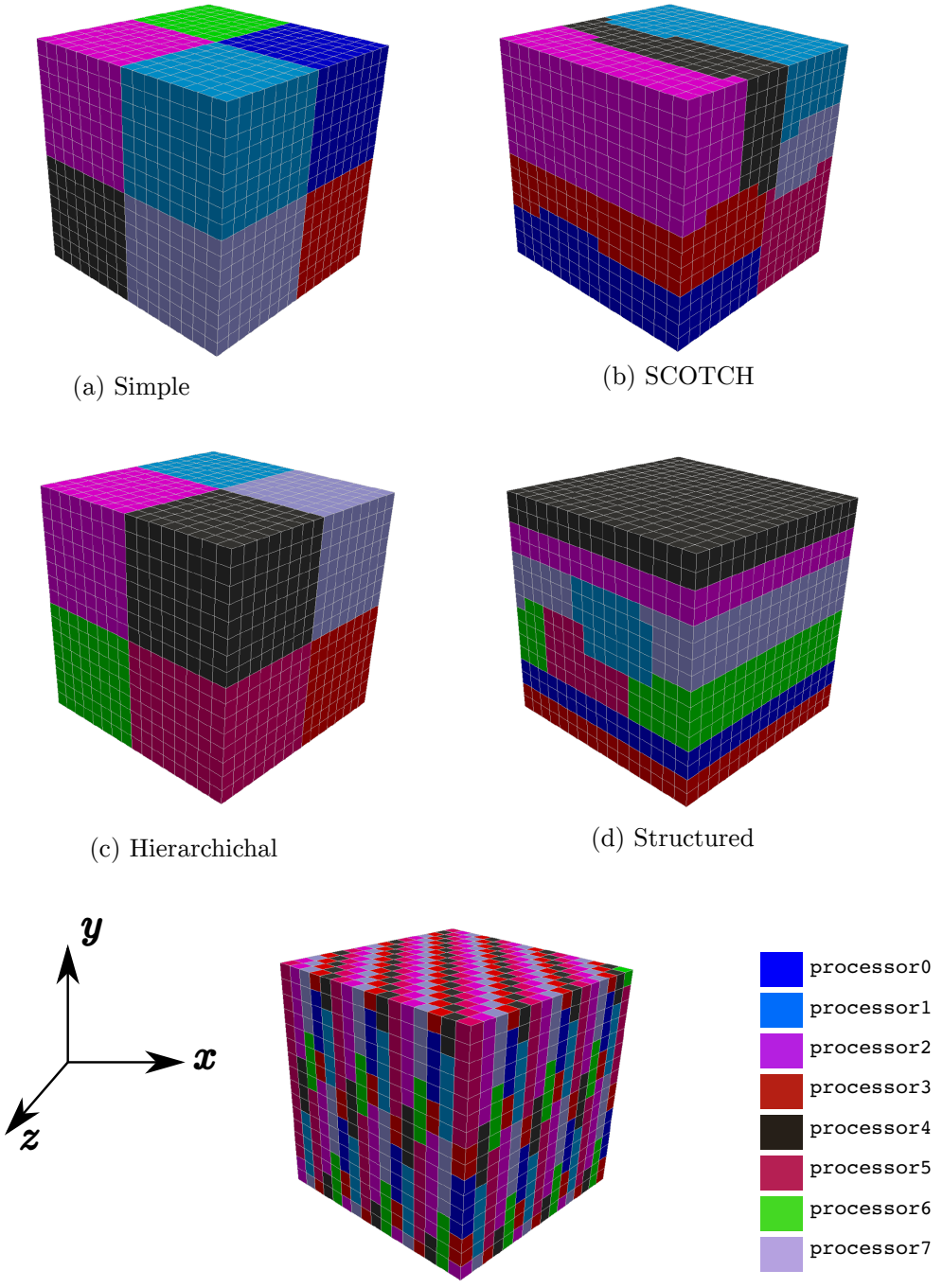

(a) Simple

(b) SCOTCH

(c) Hierarchichal

(d) Structured

(e) Manual

Figure 3.16: Domain decomposition of a simple cube with different decomposition methods.

where the number of processors is increased for the same domain size with decreasing cells per processor. At 288 processors, the code scales well with about nearly 90% of the time spent doing computation, and almost all of it is in the preconditioned conjugate gradient step and matrix multiplication. Only 8% of the time was spent on MPI calls.

All the calculations in the present research were performed on the 'Magnus', a Cray XC40 supercomputer with a massively parallel architecture of 1488 nodes located at the Pawsey supercomputing centre, Western Australia. With 24 cores per node, the machine has a total of 35,712 cores delivering a peak performance of 1.097 PetaFlops. The interconnect is based on a hierarchical organisation allowing efficient Message Passing (see Pawsey[125]).

3.4 Summary

This chapter has detailed the computational strategies employed that will be used as a basis for the results presented in the following chapters. The need for turbulent inflow generation techniques, the numerical discretization of the code, and the mathematical formulation of the boundary conditions in the code were discussed in detail.

[125]Pawsey *Magnus Technical Specifications* https://www.pawsey.org.au/our-systems/magnus-technical-specifications/ Accessed July 7, 2016

Part III

Results & Discussion

Chapter 4

Model Validation

This chapter describes the verification and validation of the code applied to three separate sub-systems. We begin by first validating the method of generating fully-developed turbulent inflow by modelling a turbulent pipe flow. This is followed by the near-wall anisotropy analysis of round and planar jets. The chapter concludes with a brief discussion on modelling a spatially developing axisymmetric free jet and the necessary boundary conditions with comments on the spatial accuracy and mesh resolution requirements.

4.1 Turbulent Pipe Flow

In experiments, fully developed flows are commonly generated by having sufficiently long pipe lengths. To replicate this physical phenomenon in a computational model, it is customary to use data from the exit plane of a pipe flow simulation or a precomputed library technique to account for the velocity scales at the nozzle exit at each time-step. It is necessary that the flow is invariant in the flow direction. However, this method requires two separate simulations and a re-run of any precursor pipe flow simulations for small changes when varying the inlet parameters of the jet-impingement simulation.

In the present modelling, the inflow conditions are generated by a similar method except that it is performed simultaneously in a single simulation. Precursor calculations are performed at a recycle plane downstream of the pipe flow inlet, and transient data from this sample plane

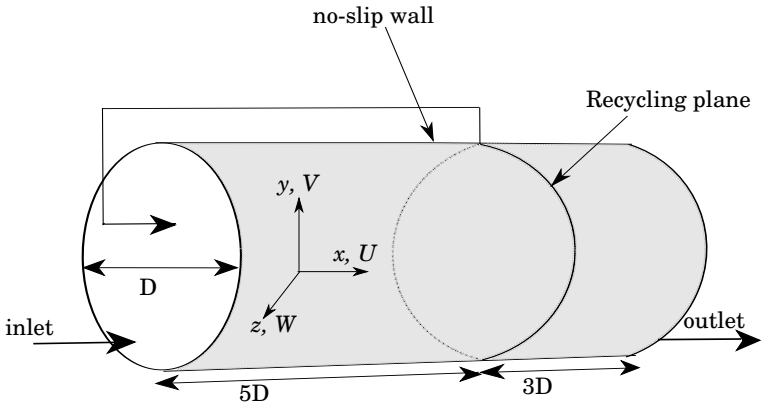

Figure 4.1: Schematic representation of the turbulent pipe flow geometry and the coordinate system used for the simulations

is fed back to the inlet at every time-step[112]. This method creates a fully developed turbulent velocity profile at the outflow of the pipe due to the flow loop, resembling an infinitely long pipe. However, this technique can be open to non-physical interactions between the recycle plane and the inlet, and may introduce periodicity and streamwise repetition of flow features[113]. To evaluate this technique, LES of an incompressible fully developed turbulent pipe flow was carried out comparable to the experiments of Toonder & Nieuwstadt[126]. The Reynolds number based on the pipe diameter defined as $Re_D = U_b D/\nu$ was set to 24,600 and the corresponding Kármán number based on friction velocity is defined as $R^+ = u_\tau R/\nu$ is 690, where $u_\tau = (\tau_w/\rho)^{1/2}$, R is the pipe radius, τ_w is the wall shear stress and ρ the fluid density.

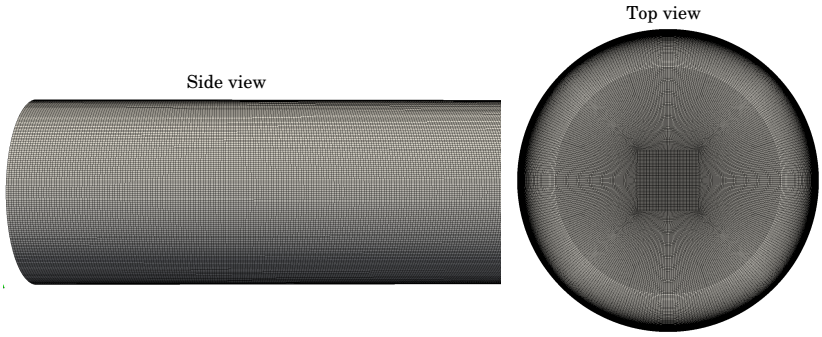

Figure 4.2: Hexahedral mesh used for the pipe flow simulations.

A schematic representation of the pipe flow geometry and the coordinate system used is shown

[112]G.R. Tabor and M.H. Baba-Ahmadi. *Comput. Fluids*, **39**: 553–567, 2010.
[113]J.W. Jewkes et al. *AIAA J.*, **49**: 247–250, 2011.
[126]J.M.J. den Toonder and F.T.M Nieuwstadt. *Phys. Fluids*, **9**: 3398–3409, 1997.

in figure 4.1. The computation was performed on a finite volume mesh of 600 × 240 × 240 grid points along the x, y and z directions respectively. In the (x, y)-plane, the radial direction $r = \sqrt{(y^2 + z^2)}$ is given by y (at azimuthal direction, $z = 0$) and the azimuthal angle $\theta = \arctan(y/z)$. The pure hexahedral mesh (shown in figure 4.2) was generated with the native OpenFOAM utility *'blockMesh'*. The mean velocity components (U, V, W) and the fluctuating components (u, v, w) are solved using second-order accurate schemes. The superscript + represents quantities scaled by friction velocity u_τ for velocity components and the viscous length scale $\delta_{nu} = \nu/u_\tau$ for the distance. A second-order accurate backward implicit scheme for time discretization is used. The convection terms are discretised by a second-order accurate central differencing scheme. The pressure-velocity coupling is solved with PISO–SIMPLE (PIMPLE), an algorithm that merges Pressure Implicit with Splitting of Operator algorithm (PISO) and a Semi-Implicit Method for Pressure-Linked Equations (SIMPLE) algorithm that allows the calculation of pressure on a mesh from velocity components by coupling the Navier–Stokes equations through iterations. The temporal resolution is dynamically adjusted through a variable time-stepping technique so that the CFL number was less than or equal to 0.5 at all times. The code is parallelized using the MPI protocol, and the graph partitioning algorithm SCOTCH was used to decompose the solution domain into the required number of sub-domains for parallel computing.

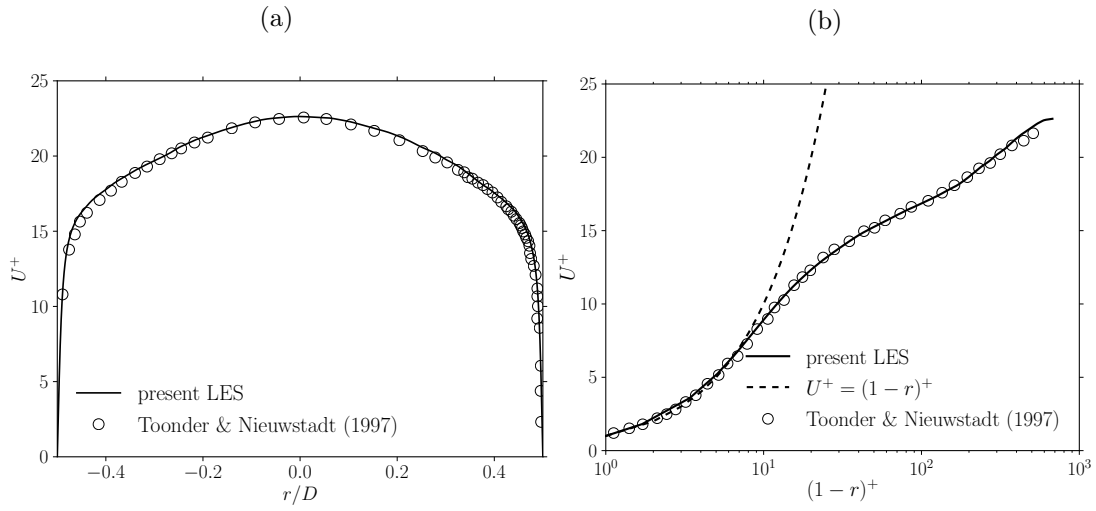

Figure 4.3: (a) Mean velocity U^+ as a function of r/D for a turbulent pipe flow, and (b) mean velocity U^+ as a function of $(1 - r)^+$. ——: present LES at Re_D = 24,600; ○: Toonder & Nieuwstadt[126] at Re_D = 24,600.

Previous experiments have reported the maximum wavelength of large-scale motions ranging

from $4D$ to $8D$ (see Guala et al.[127], Morrison et al.[128]) and several DNS studies utilized this range of domain length for their simulations (see Wu & Moin[129], Eggels et al.[130]). Accordingly, the domain length, L, of the pipe is $8D$, and the recycle plane was located at $5D$ from the inlet. The mesh was refined close to the walls so that the non-dimensional wall distance, $(1-r)^+ < 1$. No-slip boundary conditions were used on the walls, and a pressure boundary was prescribed at the outlet. The results are time-averaged along the entire length of the domain and converted to a $2D$ plane by an azimuthal average.

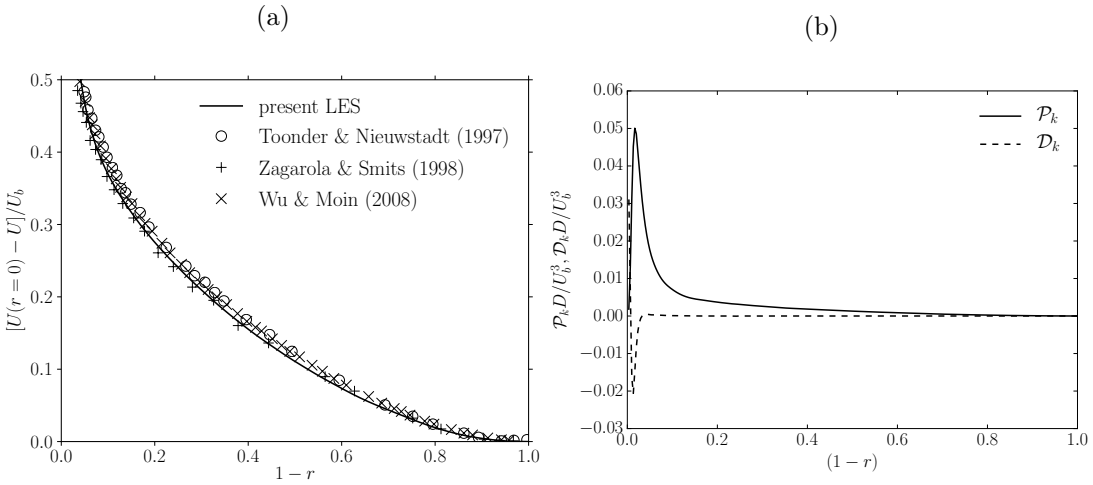

Figure 4.4: (a) Mean velocity defect, $[U(r=0)-U]/U_b$ as a function of $(1-r)$. ——: present LES at Re_D = 24,600; ○: Toonder & Nieuwstadt[126] at Re_D = 24,600; +: Zagarola & Smits[131] at Re_D = 31,000; ×: Wu & Moin[129] at Re_D = 44,000; (b) budgets of turbulent kinetic energy as a function of $(1-r)$ of present LES at Re_D = 24,600

Figure 4.3(a) shows the mean axial velocity profile over the cross section of the pipe compared against the experiments of Toonder & Nieuwstadt[126]. A fully developed symmetric mean flow velocity profile is achieved and is in good agreement with the experimental data. Mean velocity statistics at the near-wall region as a function of wall units $(1-r)^+$ is shown in figure 4.3(b). The resolution chosen for the simulation proves to be adequate as seen in the log-law profile for the mean axial velocity. The profile follows the law of the wall and accurately predicts the velocity within the viscous sub-layer ($(1-r)^+ < 5$). Further, into the buffer layer and the outer layer, excellent agreement is observed with the experimental data. To enable comparison across a range of Re_D and partially due to the invalidity of the universal velocity defect law, Wu & Moin[129]

[127]M. Guala et al. *J. Fluid Mech.*, **554**: 521–542, 2006.
[128]J.F. Morrison et al. *J. Fluid Mech.*, **508**: 99–131, 2004.
[129]X. Wu and P. Moin. *J. Fluid Mech.*, **608**: 81–112, 2008.
[130]J.G.M. Eggels et al. *J. Fluid Mech.*, **268**: 175–210, 1994.

used the mean velocity defect, $[U(r=0)-U]/U_b$, normalised by the bulk velocity, U_b. The trend of the mean velocity defect for the outer layer is shown in figure 4.4(a). The velocity defect is high closer to the wall and gradually vanishes on moving towards the pipe axis. The results show excellent agreement with the experimental data of Toonder & Nieuwstadt[126](Re_D = 24,600), Zagarola & Smits[131](Re_D = 31,000), and the DNS of Wu & Moin[129](Re_D = 44,000). The turbulent kinetic energy production and the viscous dissipation term are shown in figure 4.4(b). The trends are reproduced accurately for both the terms.

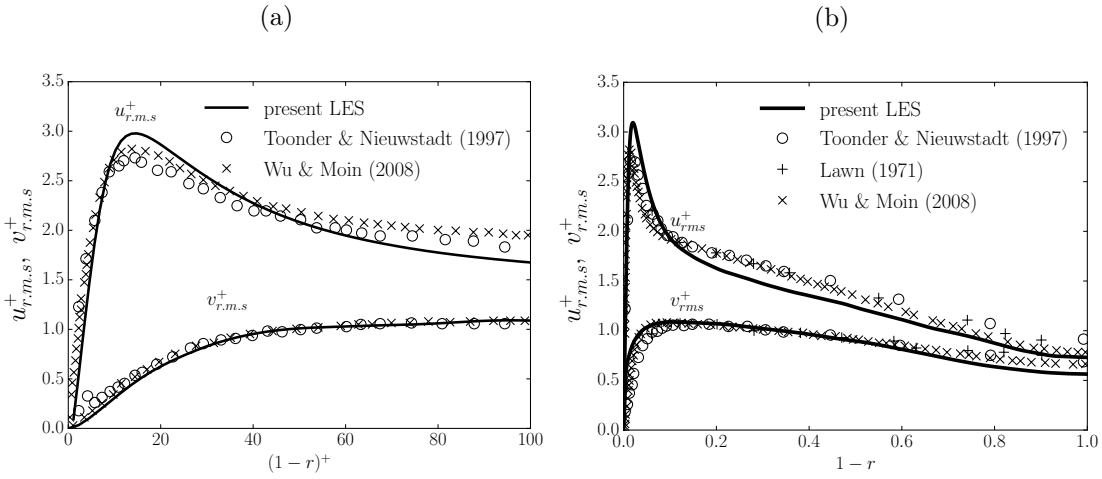

Figure 4.5: (a) Axial and radial r.m.s velocity profiles as a function of $(1-r)^+$ in the near-wall region.——: present LES at Re_D = 24,600; ○: Toonder & Nieuwstadt[126] at Re_D = 24,600; ×: Wu & Moin[129] at Re_D = 44,000, and (b) axial and radial r.m.s velocity profiles as a function of radial coordinate $(1-r)$. ——: present LES at Re_D = 24,600; ○: Toonder & Nieuwstadt[126] at Re_D = 24,600; +: Lawn[132] at Re_D = 38,000; ×: Wu & Moin[129] at Re_D = 44,000.

The root-mean-square (r.m.s) values of the fluctuating components of velocity normalized by u_τ, as a function of inner wall units $(1-r)^+$ are shown in figure 4.5(a). Good agreement is observed between the experimental data of Toonder & Nieuwstadt[126](Re_D = 24,600), the DNS of Wu & Moin[129](Re_D = 44,000) and the current LES. The computed values of the axial and radial fluctuations are predicted accurately using the present numerical framework. The peak values and the location of the fluctuations agree well with the previously mentioned studies (see Wu & Moin[129], Eggels et al.[130]). In figure 4.5(b), the turbulence intensities are shown across the outer unit $(1-r)$, and compared with the experimental data sets of Nieuwstadt[126](Re_D = 24,600) and Lawn[132](Re_D = 38,000) along with the DNS of Wu & Moin[129](Re_D = 44,000)

[131]M.V. Zagarola and A.J. Smits. *J. Fluid Mech.*, **373**: 33–79, 1998.
[132]C.J. Lawn. *J. Fluid Mech.*, **48**: 477–505, 1971.

for completeness. The axial fluctuation is marginally under-predicted in the radial range of 0.2 $< (1 - r) <$ 0.4 however, the radial fluctuation has very good agreement with the representative data across the entire range.

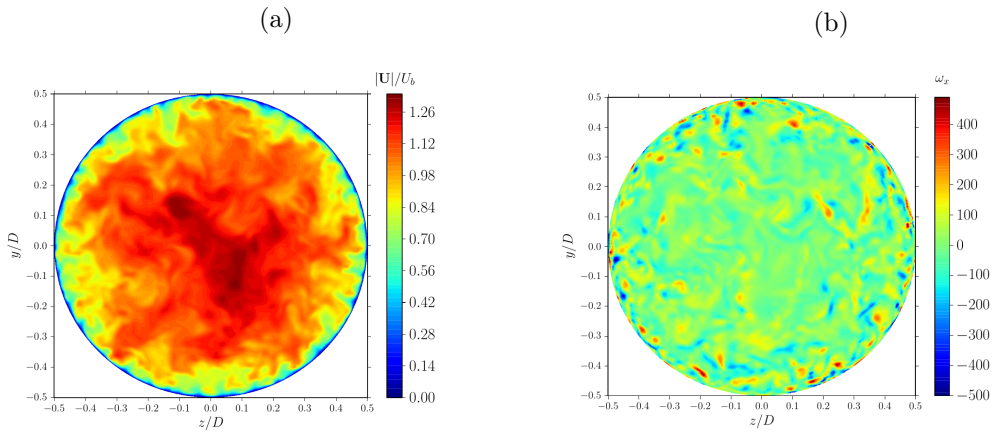

Figure 4.6: Visualization of the turbulent pipe flow at Re_D = 24,600 over a constant x plane with contours of (a) instantaneous velocity magnitude, $|\mathbf{U}|$ normalized by bulk velocity, U_b, and (b) instantaneous streamwise vorticity (ω_x).

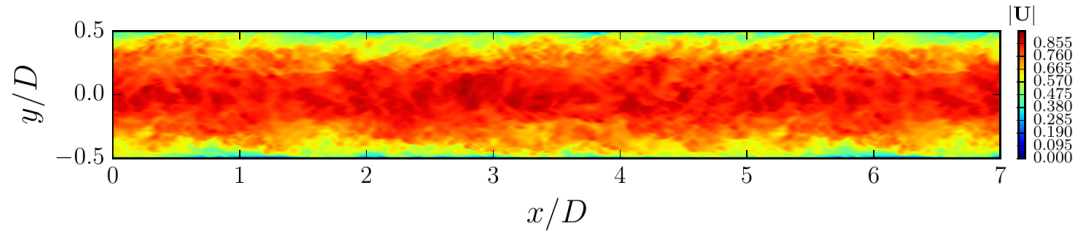

Figure 4.7: Visualization of the turbulent pipe flow, instantaneous velocity magnitude over a constant θ plane.

To demonstrate that the flow structures are preserved, the instantaneous velocity and vorticity profiles in a cross-sectional plane of the pipe are visualized in figures 4.6(a) and (b) in which the contours of instantaneous velocity magnitude, $|\mathbf{U}|$ normalized by the bulk velocity, U_b along with the vorticity in the streamwise direction (ω_x) are presented for the same location of the plane at the same instant in time. The characteristic mushroom-shaped bulges with lower fluid velocity appear closer to the wall, and on moving closer to the pipe core, the structures of the fluid are more disordered and exhibit high momentum as expected. The vorticity profile shows more counter-rotating vortices closer to the pipe wall than at the pipe core as expected.

Figure 4.7 shows the contours of the instantaneous velocity magnitude over a constant θ plane at Re_D = 24,600. The characteristic features are seen along the plane, and the flow is

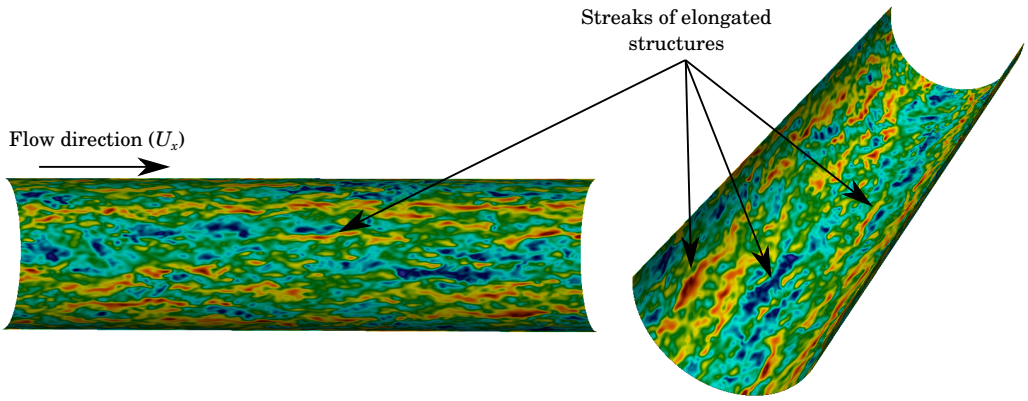

Figure 4.8: Flow structures in the near-wall region.

seen to be highly turbulent and unsteady. The turbulent structures are preserved with evident random motion. To view these turbulent structures much closer to the wall, figure 4.8 shows a cut section of the cylindrical plane at $(1 - r) = 0.1$ where the footprints of the long elongated structures are seen.

Overall, the mean and instantaneous turbulent characteristics are in good agreement with the experimental data, and the flow structures are well preserved. These results indicate that the computed LES of an incompressible turbulent flow in a smooth pipe at $Re_D = 24{,}600$ with a recycled inflow boundary condition can be adapted to generate a fully developed turbulent inflow for simulations needing such inlet conditions without having to run redundant pipe flow simulations externally.

4.2 Near-Wall Anisotropy

While having investigated the fully-developed turbulent inflow generation method through a pipe flow and the corresponding mesh requirements, the near-wall behaviour of a wall-bounded flow is now examined. Anisotropic Invariant Mapping (AIM) is used to explain the nature of turbulence in the near-wall region of impinging jets. AIM is plotted to gain an understanding of the turbulent stress tensor under round and planar jet impingement and also to demonstrate the capability of the current Large-eddy simulations to capture the near-wall behaviour accurately.

Upon impingement, a jet results in various flow fields within the domain, and it is important that the employed numerical modelling captures all aspects of the flow field for a complete

understanding. Tracking the expected anisotropy in the resulting flow field presents valuable information about the nature of the turbulence within the flow and its deviation from isotropy. The Reynolds stress anisotropy tensor is used to characterise the flow anisotropy. Anisotropy Invariant Mapping (AIM) proposed by Lumley & Newman[133] is used to represent the degree of anisotropy in the turbulent flow as these maps present a domain within which all realisable turbulence must lie. In the present work, AIM is used to represent the near-wall flow anisotropy under round and planar jet impingement. The jet Reynolds number in both the cases is 23,000 based on the jet diameter and nozzle width, and a non-dimensional stand-off distance between the nozzle exit and the impingement surface is kept at 4. Thus, the scope of this section is not to compare the two different configurations, but to understand the nature of turbulence under the two most widely used jet impingement configurations independently for a better understanding of anisotropy in their respective flow fields and simultaneously serve as an endorsement to pursue the current methods of simulating large-eddies.

The anisotropy tensor b_{ij} is given as,

$$b_{ij} = \frac{\overline{u_i' u_j'}}{2k} - \frac{\delta_{ij}}{3} \tag{4.1}$$

where u_i', u_j' are instantaneous velocity fluctuations in directions i & j, while k, is the turbulent kinetic energy and δ_{ij}, the Kronecker delta. The invariants are expressed as,

$$II = I_2 = -\left(\frac{1}{2}\right) b_{ij} b_{ji} \tag{4.2}$$

and,

$$III = I_3 = \left(\frac{1}{3}\right) b_{ij} b_{jk} b_{ki} \tag{4.3}$$

Since the flow is incompressible and by the definition of b_{ij}, the first Invariant $I = b_{ii} = 0$.

Figure 4.9 shows an AIM which is a plot of $-II$ versus III along with the definitive bounds within which all realisable turbulence of the flow exists. Lumley & Newman[133] have shown that the cross plots of the invariants II and III for axisymmetric turbulence and two-component turbulence define the AIM that bounds all physically realisable turbulence. In this AIM, the turbulence must exist within these three bounding lines. The boundaries are,

- **The right bounding line:** The right bounding line ($III = 2(-II/3)^{3/2}$) represents axisymmetric expansion where the turbulence is of rod-like or prolate shaped.
- **The left bounding line:** The left bounding line ($III = 2(-II/3)^{3/2}$) represents axisymmetric contraction where the turbulence is of disc-like or oblate in nature.

[133] J.L. Lumley and G.R. Newman. *J. Fluid Mech.*, **82**: 161, 1977.

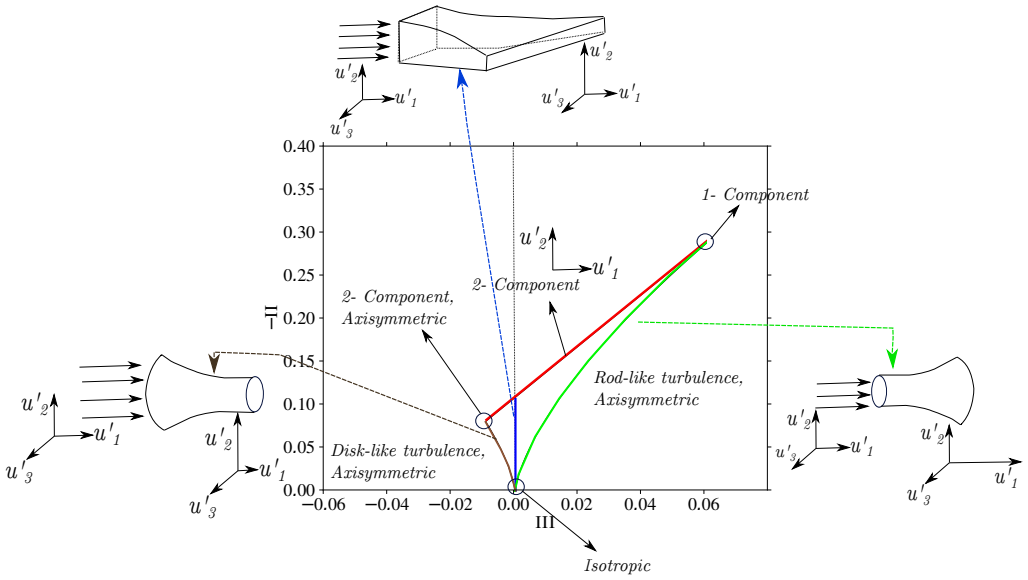

Figure 4.9: Anisotropy invariant map and the possible states of turbulence in invariant coordinates $-II$ *vs.* III reproduced based on Lumley & Newman[133]

- **The upper straight line:** This line $\frac{1}{9} + 3III + II = 0$ represents a 2-component state of anisotropic turbulence
- **The bottom cusp:** The bottom cusp at $(III, -II) = (0, 0)$ represents the 3-component isotropic turbulence state where $\bar{u^2} = \bar{v^2} = \bar{w^2} = \frac{2}{3}k$ where (u, v, w) are the fluctuating components of velocity and k the turbulent kinetic energy.
- **The left vertex:** The left vertex at $(III, -II) = (-\frac{1}{108}, \frac{1}{12})$ represents the 2-component isotropic turbulence where $\bar{u^2} = \bar{w^2} = k; \bar{v^2} = 0$.
- **The right vertex:** The right most vertex at $(III, -II) = (\frac{2}{27}, \frac{1}{3})$ represents the 1-component isotropic turbulence where $\bar{u^2} = 2k; \bar{v^2} = \bar{w^2} = 0$.

AIM was applied to impinging jets by Nishino et al.[134] and Uddin et al.[83]. Nishino et al.[134] showed that the turbulence was close to an axisymmetric state in the stagnation region. Uddin et al.[83] used AIM to analyse the turbulence fluctuations and made similar observations to those of Nishino et al.[83] The shape of the stress tensor and other terminologies about AIM plotting theory, are presented in greater details in the work of Simonsen[135] and Lumley[133].

[134]K. Nishino et al. *Int. J. Heat Fluid Flow*, **17**: 193–201, 1996.
[83]N. Uddin et al. *Int. J. Heat Mass Transfer*, **57**: 356–368, 2013.
[135]A.J. Simonsen and P. Krogstad. *Phys. Fluids*, **17**: 088103, 2005.

4.2.1 Computational Set-up

Round jet impingement The solution domain is a collocated grid system with Cartesian coordinates, $\mathbf{X} = (x, y, z)$; with 0 as the origin at the center of the domain Ω, where $\Omega = [0, r] \times [0, L_y]$ with $L_y = 9D$ and radius, $r = 10D$. The instantaneous velocity components are denoted $\mathbf{u} = (u, v, w)$ and the mean velocity components are denoted by $\mathbf{U} = (U, V, W)$. In the (x, y)-plane, the radial direction $r = \sqrt{x^2 + z^2}$ is given by x (at azimuthal direction, $z = 0$) and the azimuthal angle $\theta = \arctan(x/z)$. The Reynolds number based on the jet-nozzle diameter D, bulk velocity V_b, and the kinematic viscosity ν is given as $Re = V_b\ D/\nu = 23{,}000$.

At the inlet, fully-developed turbulent flow is generated by the recycle plane at an upstream distance of $1D$ from the nozzle exit. At the impingement wall, $y = 0$, a Dirichlet (no-slip) boundary condition is applied hence $\mathbf{U}(x, y = 0, z, t) = 0$. For pressure, a Neumann boundary condition is used which implies $\partial p/\partial y = (x, y = 0, z) = 0$ and a uniform heat flux boundary condition is applied at the wall for temperature. On the bounding sides of the domain (i.e., $r/D = \pm 10$, and $y/D = L_y/3$), a mixed boundary condition is applied for velocity where $\mathbf{U}$ is evaluated from the flux when the pressure is known. With this boundary condition, for an inbound flow, the velocity is obtained using the flux from the first adjacent cell of the boundary, and for outward flow, a zero-gradient is applied. A Dirichlet boundary condition is applied for pressure at the outlets, using the reference pressure of the flow field, $p_0 = p + 0.5|U|^2$, where p_0 is the stagnation pressure, and p is the static pressure at the boundary and is dependent upon $\mathbf{U}$. Turbulence statistics are averaged in space and time after ten flow cycles where one flow cycle means that a fluid particle has travelled through the axial and radial dimensions i.e. $9D + 10D$ at the bulk velocity, V_b. The statistical averaging continues for 30 flow cycles. The entire domain was initialized with a converged Reynolds-averaged Navier–Stokes (RANS) simulation.

Planar jet impingement The solution domain for the planar jet impingement case is a collocated grid system with Cartesian coordinates, $\mathbf{X} = (x, y, z)$; with 0 as the origin at the center of the domain Ω, where $\Omega = [0, x] \times [0, L_y]$ with $L_y = 8B$ and width, $x = 15B$. The instantaneous velocity components are denoted $\mathbf{u} = (u, v, w)$ and the mean velocity components are denoted by $\mathbf{U} = (U, V, W)$. The Reynolds number based on the jet-nozzle width B, bulk velocity V_b, and the kinematic viscosity ν is given as $Re = V_b\ 2B/\nu = 23{,}000$. The boundary conditions were kept similar to the round jet case as detailed in the section above.

4.2.2 Results

Large-eddy simulations were performed for both these cases, and the near-wall anisotropy was examined at similar locations for both the jet-impingement configurations. As a check, the near-wall anisotropy from the nozzle flow of the round jet is compared to previous experiments and DNS data. Figure 4.10 shows the comparison of near-wall anisotropy between the results of pipe flow experiments by Krogstad & Torbergsen[136] and results obtained at the nozzle exit of the present work. This is carried out as a preliminary validation of the technique used to plot AIM. Good agreement is observed with the experimental data. The near-wall anisotropy at the nozzle exit follows similar turbulent characteristics to that of a pipe flow for the same Reynolds number and also substantiates the inlet boundary condition used to generate fully-developed flow at the nozzle exit.

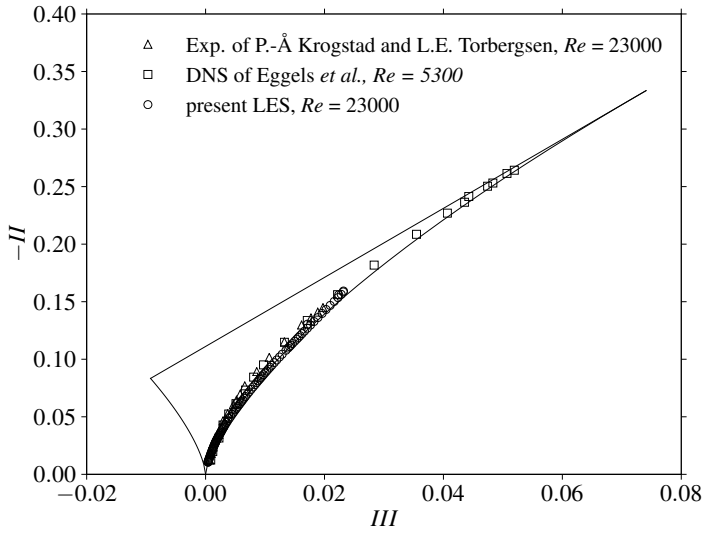

Figure 4.10: Anisotropy invariant map of Reynolds stress near pipe wall compared to turbulence at round jet nozzle exit of the present work

AIMs at four different locations on the impingement surface, starting from stagnation zone and extending radially outwards into the wall-jet are examined for the round jet impingement configuration. Figure 4.11(a) shows the AIM plot of invariants at the stagnation zone of the flow domain. The nature of turbulence is partly axisymmetric contraction and a three-component isotropic state. This is due to turbulent fluctuations being similar in magnitude, resulting in similar magnitude of anisotropy tensors ($b_{11} = b_{22} = b_{33}$). This result is in good agreement with the experimental findings by Nishino et al.[134] and the numerical work by Uddin et al.[83].

[136]P. Krogstad and L.E. Torbergsen. *Flow, Turbul. Combust.*, **64**: 161–181, 2000.

At $r/D = 1$ (figure 4.11(b)), there is considerable deviation from isotropy. At this point, the near-wall eddies undergo an axisymmetric contraction and after $y/D = 0.9$, they undergo axisymmetric expansion due to the change in flow direction. At $r/D = 2$ (figure 4.11c), the near-wall turbulence follows a two-component anisotropic state and also the flow is in an axisymmetric expansion state up to about $y/D = 0.35$.

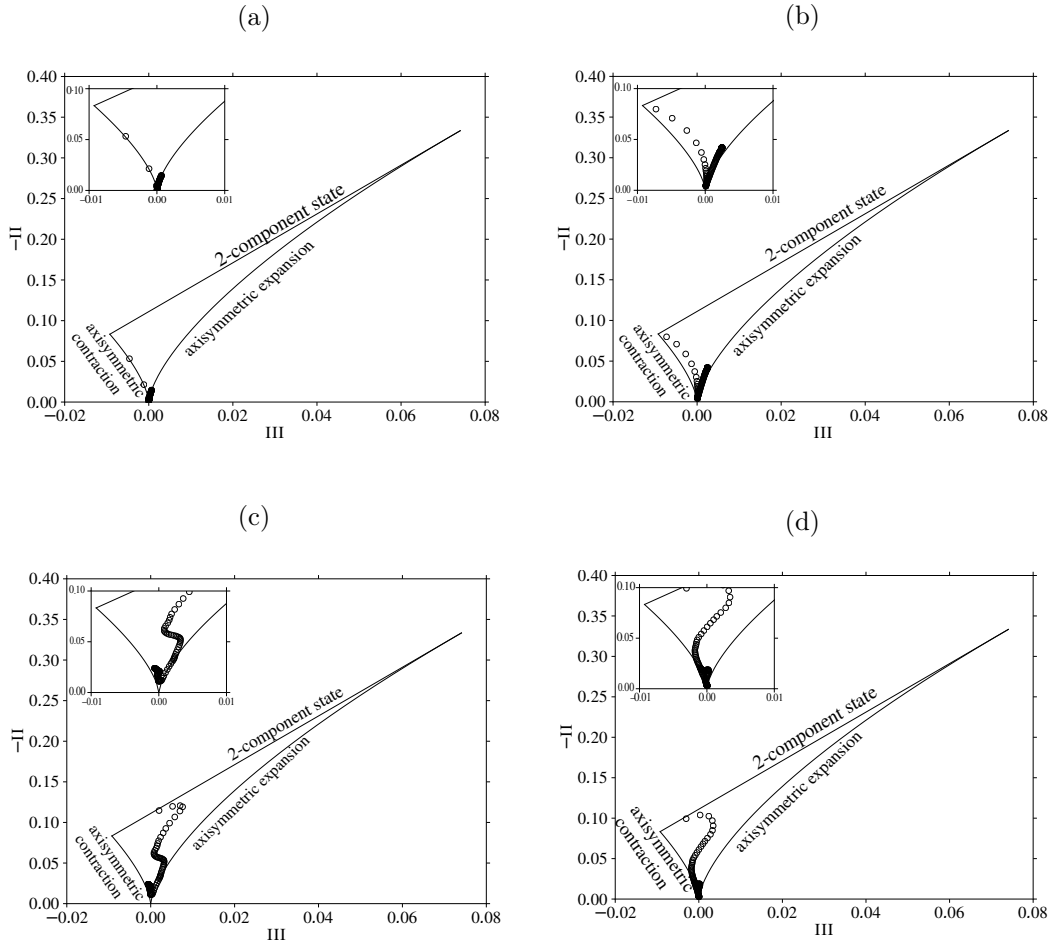

Figure 4.11: Anisotropic invariant maps for round jet impingement configuration at (a) $r/D = 0$; (b) $r/D = 1$; (c) $r/D = 2$; (d) $r/D = 3$.

However, at about $y/D \simeq 0.5$, the anisotropy shows axisymmetric contraction. This contraction could be due to the possible formation of secondary vortices causing flow structures to contract and stretch resulting in a mixed state of anisotropy. After $r/D = 3$ (figure 4.11(d)), when the flow has developed into the wall-jet region, and further, the nature of turbulence straddles an axisymmetric expansion state and a two-component state. This occurrence is expected as the flow moves radially outward losing its momentum and kinetic energy; there is no further formation of vortices and turbulent structures, and the flow is essentially dominated

by two components alone. The anisotropy remains the same until the flow completely exits the computational domain.

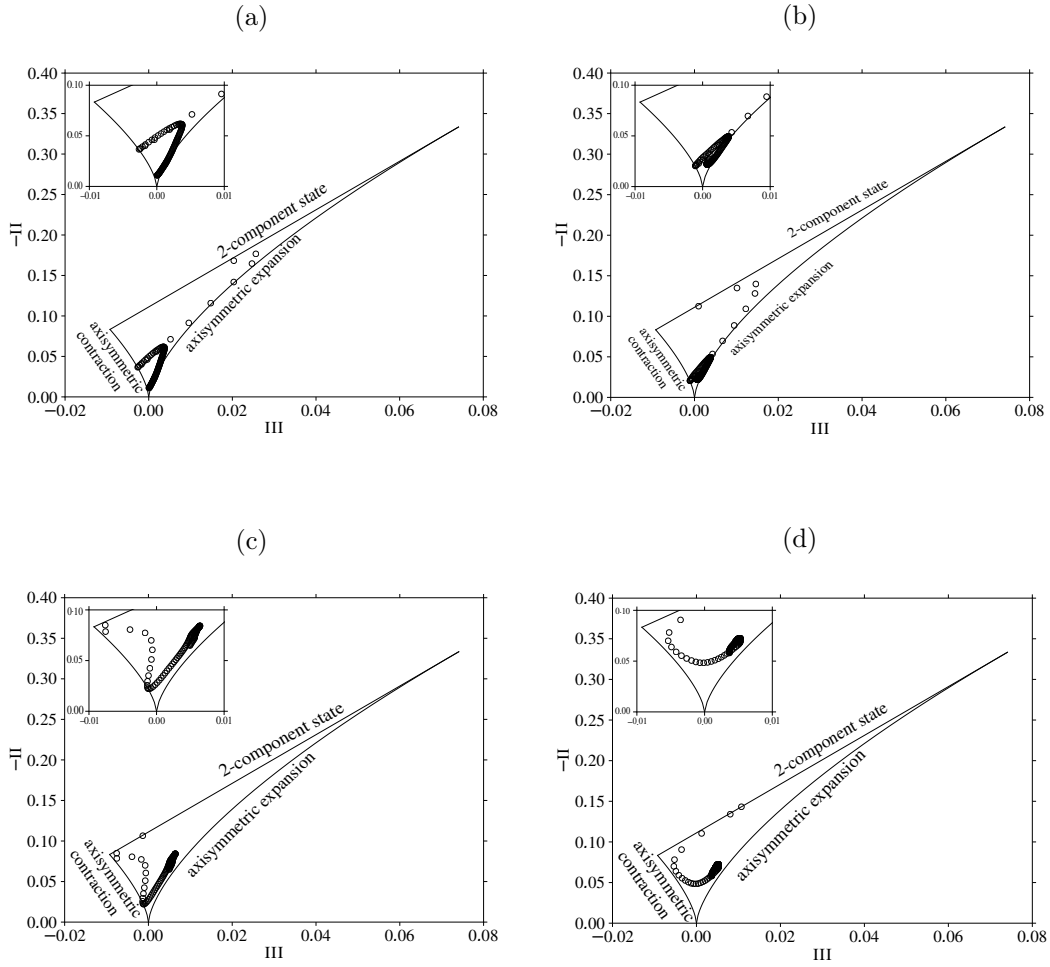

Figure 4.12: Anisotropic invariant maps for planar jet configuration at (a) $x/B = 0$; (b) $x/B = 1$; (c) $x/B = 2$; (d) $x/B = 3$.

The AIMs for the planar jet configuration are presented in figure 4.12. Figure 4.12(a) shows the AIM at the stagnation zone of the jet where the near-wall anisotropy is largely between a two-component state and axisymmetric expansion. The flow is not isotropic as in the case of a round jet impingement. The contribution from the third component of the flow is negligible even in the stagnation region of the flow. At $x/B = 1$ (figure 4.12(b)), it largely remains as a two-component dominated flow and far from three-component isotropic turbulence. At $x/B = 2$ (figure 4.12(c)), the nature of turbulence undergoes both axisymmetric expansion and contraction due to changes in flow direction and formation of secondary vortices. After $x/B = 3$ (figure 4.12(d)), the nature of the flow essentially remains the same and largely is a

two-component state. The contribution from the third component of the anisotropic tensor is negligible compared to the other tensors.

In summary, turbulence and near-wall anisotropy have been studied using AIM for round and planar impinging jets. In round jets, near-wall anisotropy exhibits contraction and isotropy at the stagnation zone, and on moving away, the flow undergoes axisymmetric expansion and contraction. In planar jets, the flow does not exhibit any isotropy and remains largely dominated by two-component turbulence. However, similar expansion and contraction of eddies are observed at regions where flow reversal and secondary vortex formation occurs. Thus, it is clear that the current computational model predicts the nature of turbulence accurately through anisotropic invariant mapping and shows the significant differences between a two-dimensional planar jet and a three-dimensional round jet impingement configurations.

4.3 Axisymmetric Turbulent Free Jet

With the method of generating fully developed inlet turbulence being satisfactorily validated with a pipe flow, and careful analysis of the near-wall anisotropy, the next phase is to validate the boundary conditions for an impinging jet with static and vibrating heated impingement surfaces. However, an intermediate simulation was performed to simulate the free jet before moving into the fluid flow and heat transfer simulations of an impinging jet. The purpose is to validate the boundary conditions for a freely expanding free jet into a quiescent fluid, estimate the mesh requirements, and eventually perform an assessment on the quality of the results. The underlying motive here is to gain an understanding of the shear instabilities of a jet issuing into a quiescent fluid, the grid resolution requirements to resolve them and the necessary boundary conditions to have an accurate representation of the physical flow. The impinging jet heat transfer is a strong function of the vortical structures, and it is essential that they are reproduced accurately. Once the configuration is satisfactorily reproduced, similar boundary conditions can be adopted by essentially adding a wall with a uniform heat flux to the configuration.

Fiedler[137] describes three regions within the axisymmetric round jet. The near-field, the intermediate-field and the far-field. The near-field region ($0 \leq x/D \leq 6$) is usually the region in which the potential core is present. Following this region, ($6 \leq x/D \leq 30$) is the intermediate-field where the fluid develops axially and radially due to the instabilities and eventually reaches

[137]H.E. Fiedler. "Control of free turbulent shear flows" in: *Flow Control*. Springer, 1998. 335–429

the self-similar region or the fully-developed region described as the far-field ($x/D \geq 30$). It is essential that the current mesh and computational methodology precisely capture these regions. An axisymmetric submerged jet at a Reynolds number, $Re_j = 1.1 \times 10^4$ is simulated using Large-eddy simulation. The jet Reynolds number, $Re_j = u_j D/\nu$, where u_j is the jet nozzle exit velocity, $D = 2r_0$, the diameter of the nozzle and ν the kinematic viscosity of the fluid.

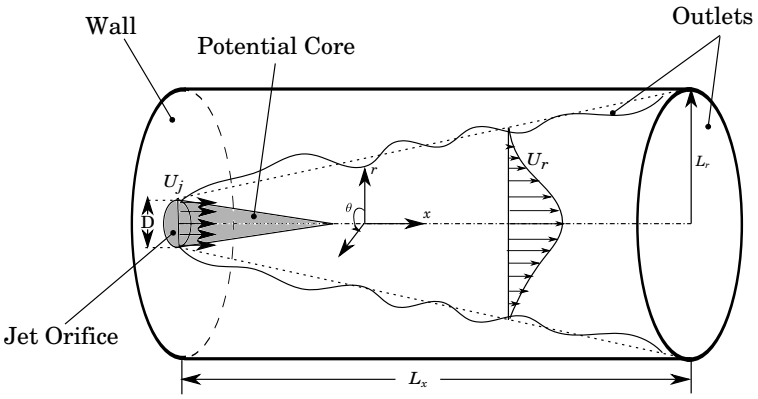

Figure 4.13: Schematic of the computational domain

A schematic of the computational domain is shown in figure 4.13. The computational domain follows the experimental setup of Panchapakesan & Lumley[138]. The self-similarity region was reached at $50D$ downstream from the inlet for their experiments. Bogey & Bailly[139] have used a grid extending up to $75D$ in the axial direction to reproduce the experiments of Panchapakesan & Lumley[138] using LES. The present computation uses the same extent in the axial direction and $30D$ in the radial direction. The axial, radial and azimuthal directions are denoted by x, r and θ respectively. The wall confining the nozzle is treated with a no-slip and a zero-entrainment again similar to a sudden entry as carried out in the experiments.

Figure 4.14 shows the grid used in the study (resolution reduced to $1/7^{th}$ of the full $3D$ mesh used for simulations for the sake of clarity). The pure hexahedral mesh was generated with the native OpenFOAM utility *'blockMesh'*. This utility uses a separate dictionary to divide the domain into one or more hexahedral *'blocks'* and the vertices and edges can be modified based on the requirement. The circular shape of the domain was based on such *'blocks'* that were created with a square outline and edges gradually curved into a circular shape to arrive at the *'butterfly'* mesh topology. Multi-grading functionality was used to generate spatially varying resolutions such that the near-field and the intermediate-field are clustered with layers of cells more than the far-field region of the jet e.g. at least 10 grid points are located inside

[138]N.R. Panchapakesan and J.L. Lumley. *J. Fluid Mech.*, **246**: 197–223, 1993.
[139]C. Bogey and C. Bailly. *J. Fluid Mech.*, **627**: 129–160, 2009.

the initial shear layer at the jet exit. The mesh contains $n_x \times n_y \times n_z = 1000 \times 220 \times 220$ hexahedral control volumes and the mesh was arrayed with uniform cells along the trajectory of the developing jet. The cells were graded along the radial direction with a uniform grading ratio. A geometric expansion ratio of the mesh was maintained below 1.2 for the mesh to expand smoothly in the radial direction in the critical areas of interest.

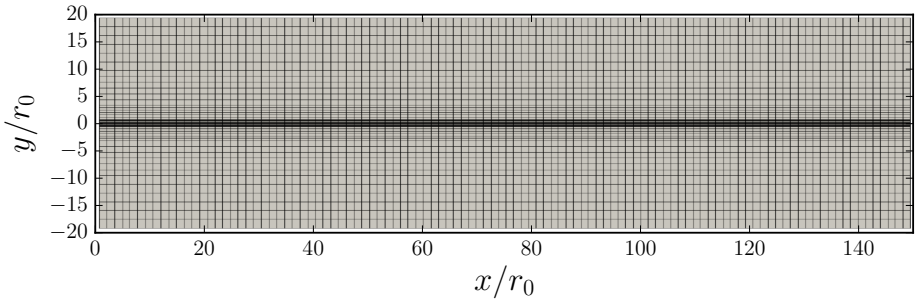

Figure 4.14: Centre slice of the computational domain ($1/7^{th}$ of the full $3D$ resolution)

The jet inlet was prescribed with a top-hat velocity profile to mimic the experimental set up of Panchapakesan & Lumley[138]. The fluid develops in the lateral zone due to entrainment and expands on moving downstream. The lateral boundaries are provided with a mixed boundary condition. At the outflow, a Dirichlet boundary condition is applied for pressure. A second-order accurate backward implicit scheme for time discretization is used. The convection terms are discretised by a second-order accurate central differencing scheme. The pressure-velocity coupling is solved with PISO–SIMPLE (PIMPLE) algorithm. The modified version of the dynamic Smagorinsky model was used as the model the subgrid scales. The temporal resolution is dynamically adjusted through a variable time-stepping technique such that the CFL number was less than or equal to 0.6 at all times. The code is parallelized using the MPI protocol, and the graph partitioning algorithm SCOTCH was used to decompose the solution domain into the required number of sub-domains for parallel computing.

4.3.1 Flow Dynamics

Mean statistics

The mean flow statistics are discussed briefly in this section. The results are compared to the experimental work of Panchapakesan & Lumley[138] and the LES results of Bogey & Bailly[139]. Figure 4.15 shows the mean axial velocity, $[u]$ and the inverse of mean axial velocity $[u_j]$,

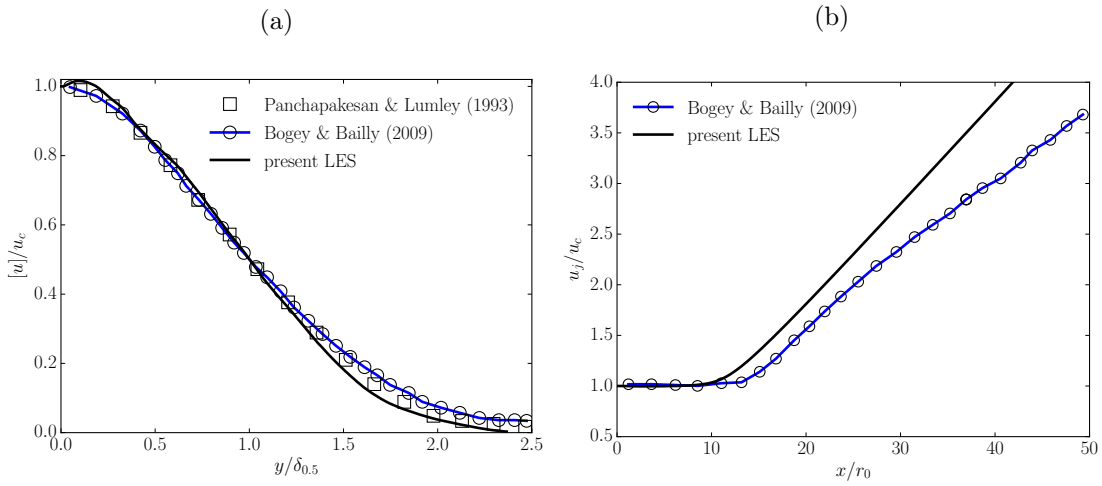

Figure 4.15: Profiles across the self-similar jet in (a) mean axial velocity $[u]/u_c$ and in (b) inverse of centreline mean axial velocity u_j/u_c: ——: present LES at $Re_D = 11{,}000$; –○–: LES of Bogey & Bailly[139]; □: Panchapakesan & Lumley[138]

normalized by the jet centreline velocity, u_c. The mean velocities were obtained by averaging over the range $100r_0 \leq x \leq 140r_0$ in both axial and azimuthal directions. The present results agree well with the self-similarity profiles measured both experimentally and numerically. The radial velocity profile predicts a marginally higher value compared to the LES of Bogey & Bailly[139] due to the different inlet conditions adopted, however, there is reasonable agreement in the prediction of the end of the potential core located at $x/r_0 = 13.0$. Beyond this point, a rapid decay in velocity is observed agreeing with the experiments.

Instantaneous statistics

The transitional flow dynamics are visualized through instantaneous flow structures in this section. The iso-surfaces of Q-criterion, iso-contours of pressure and vorticity are used to identify and visualize the large-scale structures in the instantaneous velocity field. The Q-criterion[140] is the second invariant of the velocity gradient tensor, defined as,

$$Q = \frac{1}{2}[\Omega_{ij}\Omega_{ij} - S_{ij}S_{ij}], \tag{4.4}$$

where the skew-symmetric rate-of-rotation tensor, $\Omega_{ij} = [\partial u_i/\partial x_j - \partial u_j/\partial x_i]/2$, and the symmetric rate-of-strain tensor, $S_{ij} = [\partial u_i/\partial x_j - \partial u_j/\partial x_i]/2$.

Figure 4.16 shows the iso-surfaces of Q-criterion coloured by the instantaneous velocity field.

[140]J. Hunt et al. *Center for Turbulence Research Report*, 193–208, 1988.

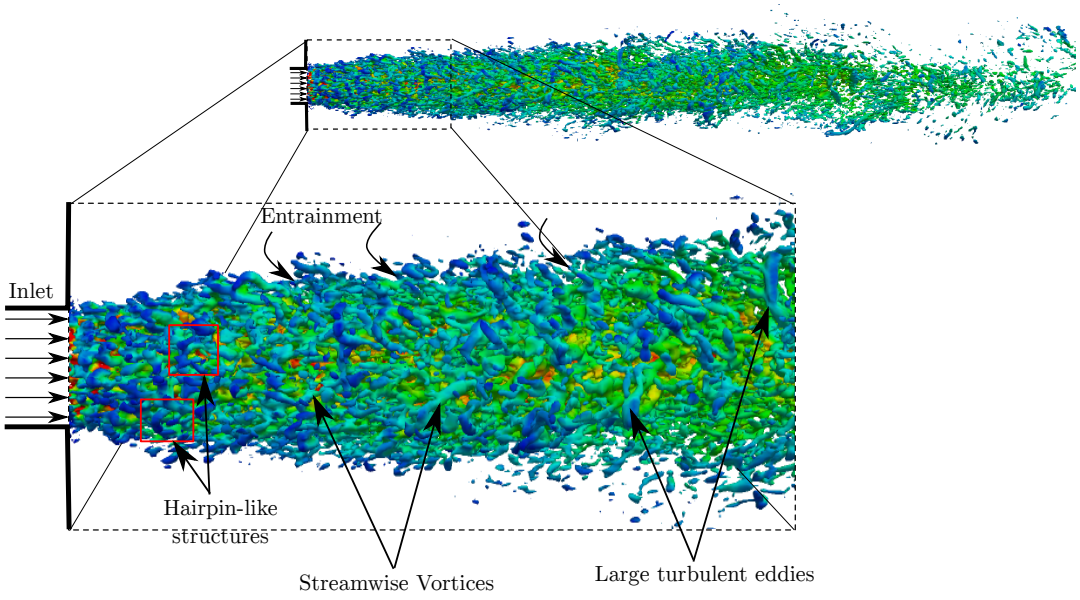

Figure 4.16: Visualization of vortical structures by iso-surfaces of Q at $Q/(U_j^2/D^2) = 0.02$

The jet is seen to emanate from the inlet, become unstable due to the Kelvin-Helmholtz type instabilities forming the coherent large eddy structures before breaking down to exit the domain. Strong events dominate the near-field and the intermediate field of the developing jet compared to the rest of the domain. The hairpin-like structures are observed to form much closer to the inlet, and on travelling further downstream, streamwise vortices are seen. The contours also show strong large-scale structures; however, they are seen much farther away from the inlet. This is believed to be as a result of vortex pairing coalescing to form these large-scale structures. The active regions of entrainment between the vortices are also captured well.

Figure 4.17 shows the vorticity field visualised through contours of vorticity magnitude, $|\omega|$ in the plane cut through the centre line of the jet compared qualitatively with the vorticity field obtained by Bogey & Bailly[139]. Good agreement is observed between the two simulations where the development of the jet is clearly visualised, and the radial spread of the jet further downstream occurs in a similar way to that observed by Bogey & Bailly[139].

Figure 4.18 shows the snapshots of vorticity magnitude, $|\omega|$ on the traverse planes of the developing jet at the same instant in time as figure 4.17. The snapshots show the evolution of the jet in the near-field region. Close to the inlet ($x/r_0 = 0.01$), the vortex ring is remarkably thin and with increase in the downstream distance, the instabilities develop due to the interaction with the quiescent fluid and the vortex ring deforms almost completely by $x/r_0 = 7.0$ with decrease in the vorticity magnitude resulting in the fine-scale vortical structures. As noted in

the literature review, the vortical structures are known to play a major role in heat removal when these jets are targeted at an impingement surface. Therefore, it is necessary that these vortical structures be resolved as accurately as possible and the current computational model effectively meets this requirement.

(a)

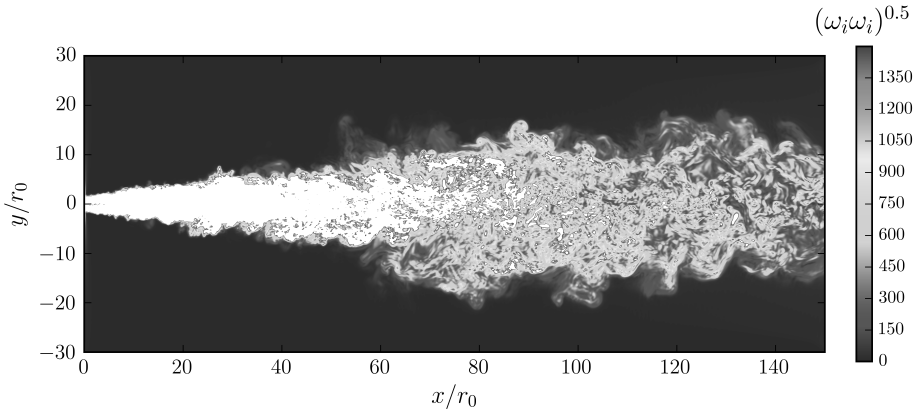

(b)

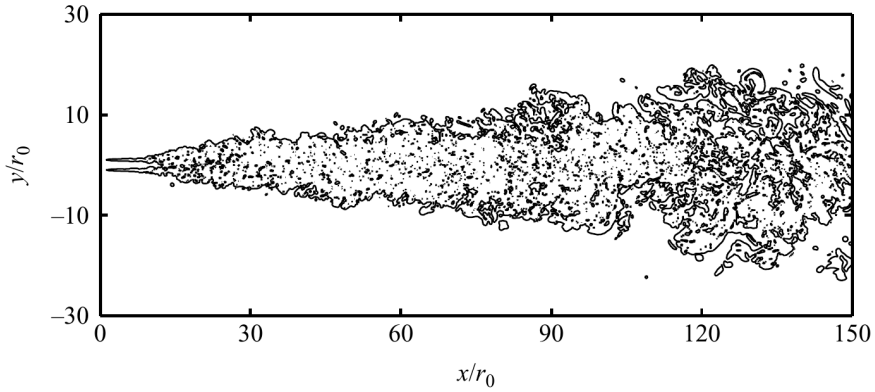

Figure 4.17: Visualization of the free-jet development in the domain with filled contours of vorticity in (a) Present LES at Re_j = 11,000, and in (b) LES of Bogey & Bailly[139]

At the same time instant, the iso-surfaces of pressure normalised by the density and square of the bulk velocity, $p/\rho U_j^2 = -0.002$, is shown in the figure 4.19. Similar features as observed with Q-criterion and vorticity magnitude are seen. The circular shape of the vortex rings are to some extent well defined and are clear compared to the previous vortex eduction methods. The pressure field (figure 4.20) show that high and low-pressure regions are alternating in the near-field of the jet. This phenomenon clearly indicates that as the jet enters the quiescent fluid,

the shear layer becomes unstable and results in the roll up of the fluid creating the vortex rings. The vortex rings have a low-pressure core as they traverse downstream. Thus, the low-pressure contours indicate the presence of the vortex ring and the subsequent high-pressure region shows the space between two vortex rings.

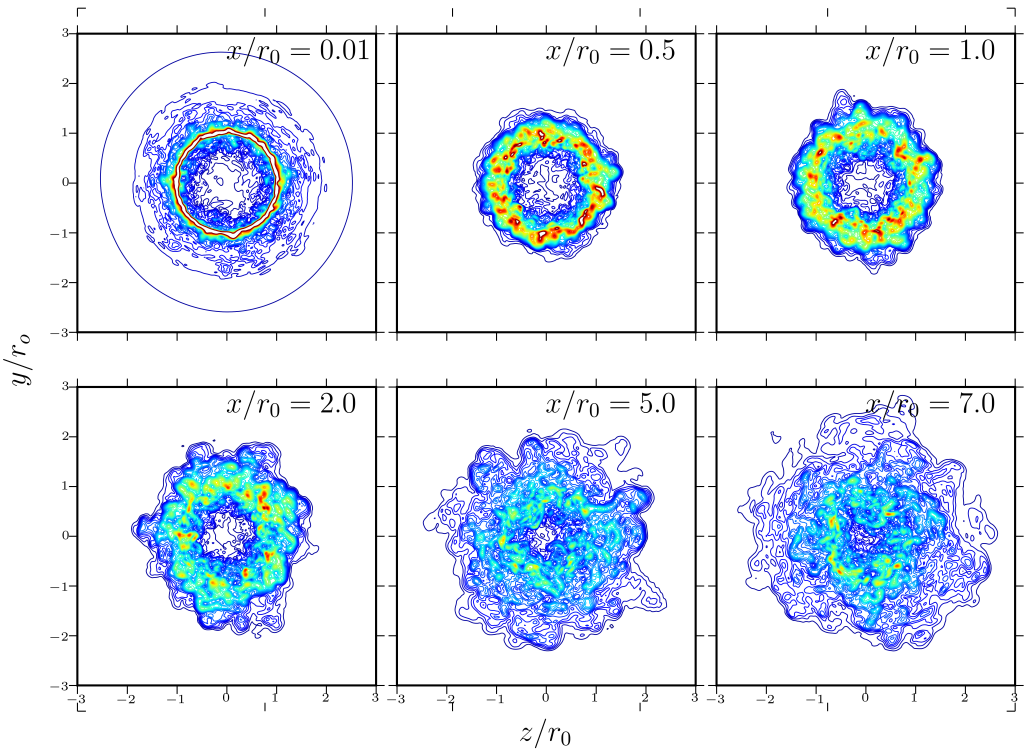

Figure 4.18: Visualization of the free-jet development showing snapshots of vorticity magnitude, $|\omega|$ on transverse planes. Blue indicates low vorticity and red indicates high levels of vorticity.

Pope[141] suggested that 80% of the energy must be resolved everywhere for LES with near-wall resolution. To assess the resolved kinetic energy in the domain, the current LES is analysed based on the quality index proposed by Celik et al.[142] for which the filter length is implicitly related to the grid cell size and with second-order accuracy in time and space and can be independent of experimental or DNS data. The test for the quality index is based on the use of turbulent kinetic energy resolved (k_{res}) versus the total turbulent kinetic energy (k_{tot}). Thus, the quality index or the resolvedness can be defined as,

$$LES\_IQ = \frac{k_{res}}{k_{tot}} \tag{4.5}$$

[141] S.B. Pope. *New J. Phys.*, **6**: 35–35, 2004.
[142] I.B. Celik et al. *J. Fluids Eng.*, **127**: 949–958, 2005.

where the resolved turbulent kinetic energy, k_{res} is given as,

$$k_{res} = \frac{1}{2}(\overline{u'^2} + \overline{v'^2} + \overline{w'^2}) \tag{4.6}$$

and the total turbulent kinetic energy, k_{tot} is given as,

$$k_{tot} = k_{res} + k_{SGS} \tag{4.7}$$

where k_{SGS} is the subgrid scale kinetic energy.

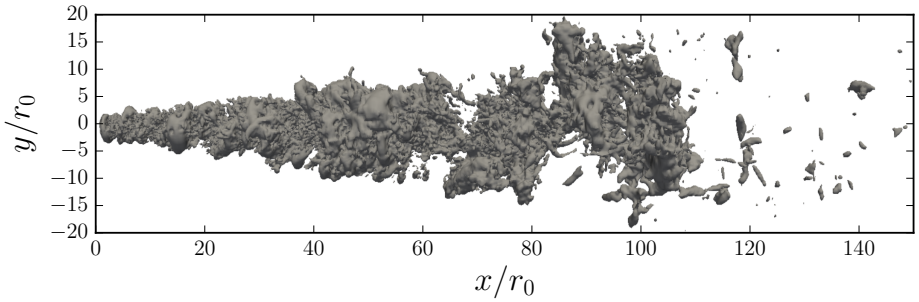

Figure 4.19: Iso-surfaces of pressure at $p/\rho U_j^2 = -0.002$

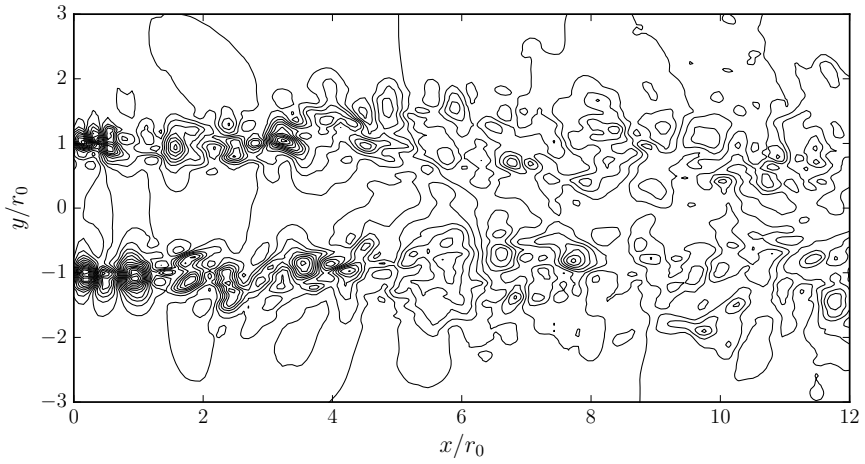

Figure 4.20: Contours of pressure at $p/\rho = -140 - 140$ with step-size 7 in the near-field region of the jet.

The contour plot of the LES quality index or the resolvedness is shown in figure 4.21. It can be seen that in general, the critical zones of the domain are well resolved at an average of about 80%. However, some regions are under-resolved. It is evident from the figure that the shear layer where the development of the instabilities appears are relatively under-resolved compared to the centre line. These are indicated by small black arrows where small bursts of under-resolvedness appear all along the shear layer development.

Pelletier et al.[143] proposed a solution to counter such poor resolvedness in the domain by using an adaptive mesh as shown in figure 4.22. Pelletier et al.[143] used mesh adaptivity to refine the shear layer (where rapid change in solution occurs) of laminar and turbulent impinging jets and eliminate the mesh as a source of error. Although this finite-element based solution is attractive, studies have shown that such mesh adaptations may introduce spurious oscillations in the numerics (see Hadžiabdić & Hanjalić[80]) especially in LES.

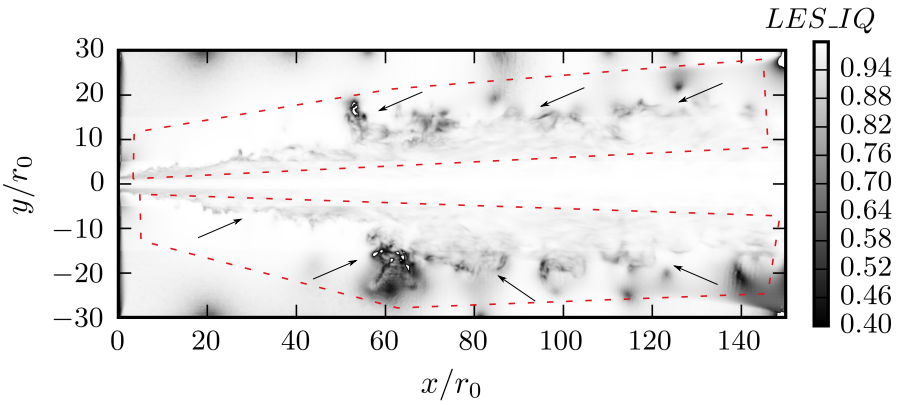

Figure 4.21: Visualization of the resolvedness through quality index, LES_IQ in the domain

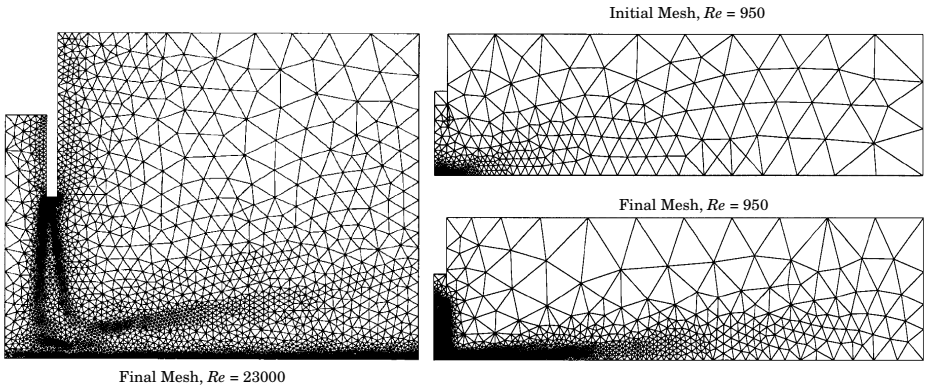

Figure 4.22: Adaptive mesh strategy from Pelletier et al.[143]

This adds further complexity when the impingement surface needs to be set in motion, and the dynamic meshing requirements on a non-hexagonal control volume pose constraints on the current numerics and computational expenses. The grid refinement requirements are unfolded with this simulation of the spatially developing free jet. It may be ideal to use hexahedral cells

[143]D. Pelletier et al. *Int. J. Numer. Methods Fluids*, **44**: 737–763, 2004.
[80]M. Hadžiabdić and K. Hanjalić. *J. Fluid Mech.*, **596**: 221–260, 2008.

and array them in the shear layer with a reduced cell to cell growth ratio rather than choosing a different mesh adaptation strategy.

4.4 Summary

This chapter described in detail the verification and validation of the code applied to three separate sub-systems. The recycled boundary condition was successfully applied to a smooth pipe flow at $Re_D = 24{,}600$ to generate a fully-developed turbulent inflow. This technique is now deemed suitable and is adapted to turbulent inflow for simulations needing such inlet conditions (such as nozzle inlet for impinging jet simulations) without having to run redundant pipe flow simulations externally. The near-wall anisotropy was studied for both the round and planar jet impingement configurations through AIMs. The code is capable of predicting the nature of near-wall turbulence accurately and significant differences between a two-dimensional planar jet and a three-dimensional round jet impingement configuration were seen and discussed. Finally, the modelling of a spatially developing free jet and the spatial accuracy requirements was discussed and the need to capture its instabilities. A quality index or *'resolvedness'* is used to measure the quality of the LES and showed that the shear layer in a jet is the most mesh intensive region and requires a greater resolution to capture precisely these instabilities.

Chapter 5

Jet Impingement on Static Surfaces

The impinging jet configuration with a static impingement surface is thoroughly explored for a Reynolds number, Re_D = 23,000 with a nozzle-to-wall spacing 2.0. We begin by outlining the RANS set-up and its results, drawbacks and then argue the pressing need for LES in simulating turbulent jet impingement heat transfer. We then discuss the results of an LES simulation through mean and instantaneous turbulence statistics (first and second order) of flow and heat transfer. The chapter concludes with a simulation at a lower Re_D (10,000) intended to serve as a basis for investigation in the parameter space when forcing of the impingement surface is introduced in the following chapter.

5.1 Computations with RANS

Since the incompressible Navier-Stokes equations pose a closure problem, several modelling strategies are employed to solve for turbulence. RANS methods are popular in industrial applications due to their relatively low computational cost and are a time/ensemble-averaged method which utilises the Reynolds decomposition to separate averaged and fluctuating terms. This approach introduces apparent stresses, called Reynolds stresses, which must be modelled for closure. While computationally efficient, RANS is better suited to engineering design applications than turbulence research since it discards instantaneous turbulent data. Furthermore, the models have a high empirical content, which requires parameters to be *'tuned'* to a particular flow for best agreement. Consequently, in complex and varied flow-fields, such as an impinging jet, this means a model may perform well in one region and poorly in another.

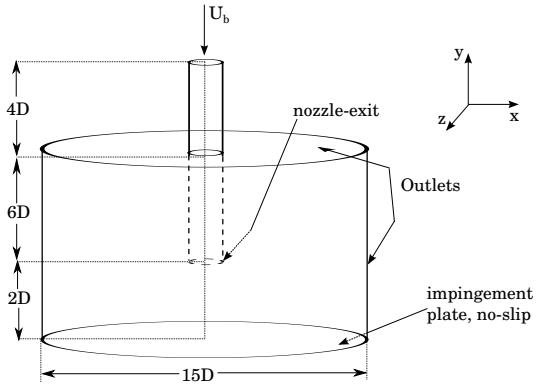

Figure 5.1: Schematic representation of the circular jet impingement configuration with the boundary conditions and the coordinate system used for the RANS simulations.

Reviews (see Zuckerman & Lior[144]) have shown that conventional k-ϵ models perform well in free shear layers with pressure gradients, but poorly in regions of large adverse pressure gradient, such as stagnation regions (see Durbin[145]). Similarly, conventional k-ω models perform well in adverse pressure gradients, and near-wall regions; however, they perform poorly in free-shear layers. In the context of impinging jets, it has been found that k-ϵ methods perform well for the free-jet region, but poorly for the wall-jet, and those k-ω methods are better suited to the wall-jet region, whilst being poorly suited to the free-jet. The k-ω SST model blends k-ω in near-wall regions, with k-ϵ, in free shear-layer regions, and has been found to blend the strengths of the older models, performing better in a wider range of flow conditions; See Launder & Spalding[117], Yakhot & Smith[146] for a detailed review of these eddy viscosity models.

For the system at hand, the most commonly used and commercially available RANS models are assessed for their accuracy and suitability to round-jet thermofluidic studies. The RANS models that were used in this study included the standard k-ϵ, k-ω, k-ω SST, Realizable k-ϵ and the RNG k-ϵ model. Thus, the aim of this section is to perform RANS simulations of impinging jets to fine-tune the LES capabilities by identifying the advantages and shortcomings of using this steady state technique. This also serves as a preliminary validation work for the steady-state configuration.

Accordingly, this RANS study aims to reproduce the flow kinematics, heat transfer and turbulent statistics of a single phase round-jet, impinging normal to a constant heat flux

[144]N. Zuckerman and N. Lior. *J. Heat Transfer*, **127**: 544–552, 2005.
[145]P.A. Durbin. *Int. J. Heat Fluid Flow*, **17**: 89–90, 1996.
[117]B.E. Launder and D.B. Spalding. *Lectures in mathematical models of turbulence.* 1972.
[146]V. Yakhot and L.M. Smith. *J Sci Comput*, **7**: 35–61, 1992.

surface. Parameters have been chosen to facilitate comparison with established numerical and experimental studies. Therefore, a non-dimensional nozzle-to-wall spacing of 2, and a Reynolds number of 23,000 have been specified. Standard properties of air at 293.15K were used.

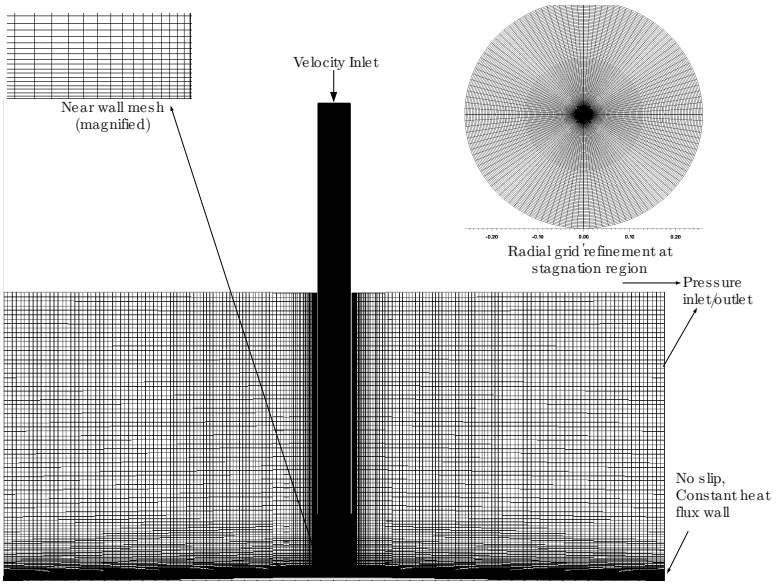

Figure 5.2: Plane view of the mesh used for RANS computations showing the near wall refinement and cell grading.

A schematic overview of the discretized flow domain is shown in figure 5.1, along with a description of the boundary conditions and details of the mesh in figure 5.2. A plane view of the grid (figure 5.2) shows the near-wall refinement and the cell grading within the domain. In the pipe centerline ($0 < r < 0.3D$, $0 < L_y < 9D$) care was taken to cluster the cells from the inlet to the stagnation zone. The circular shape of the domain was discretized with a *'butterfly'* mesh topology that is based on a square outline at the centre and is gradually modified into the circular shape (shown in the inset of figure 5.2). A geometric expansion ratio of the mesh was maintained below 1.2 for the mesh to expand smoothly in the radial direction in the critical areas of interest. The region close to the pipe/nozzle wall region ($0.3 < r < 0.5D$, $0 < L_y < 9D$) where the mesh was finely graded from the nozzle wall towards the axis centre line. It is critical to have a fine mesh in this area to resolve the near-wall statistics which directly influence the impingement wall heat-transfer. Finally, the near-wall region, the cells are configured in uniform annular layers and graded such that maximum $y^+_{wall} \approx 25$ for the finest grid considered. The majority of the cells were arrayed within the region $0 < L_y < 1D$ and $-4D < r < 4D$ so as to capture the shear layer development precisely. All the grids are discretised with hexahedral control volumes. The simulation was configured using Cartesian coordinates, $\mathrm{X} = (x, y, z)$; thus the instantaneous velocity is denoted by $\mathrm{u} = (u, v, w)$ and the mean velocity is denoted

by U = (U, V, W). Thus, in the $x - y$ plane, the radial direction $r = \sqrt{x^2 + z^2}$ is given by x and the azimuthal angle $\theta = arctan(x/z)$. The pressure-velocity coupling was done using the Semi-Implicit Method for Pressure-Linked Equations (SIMPLE) algorithm.

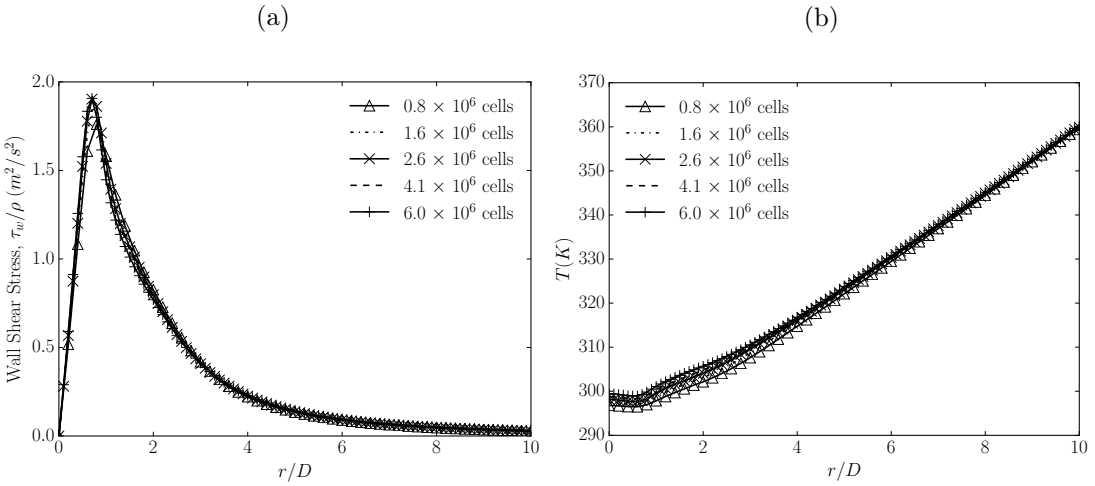

Figure 5.3: Profiles of (a) Wall shear stress, τ_w/ρ, and (b) Wall temperature, T as a function of r/D for the different grid configurations.

Grid sensitivity study: To ensure that the solution does not vary with grid density, a grid independence study was carried out with different mesh densities. Five meshes were used for the study with the following parameters: $Re = 23,000$, k-ω SST model, the non-dimensional nozzle-to-wall spacing is 2, and mesh sizes of 0.8×10^6, 1.6×10^6, 2.6×10^6, 4.1×10^6 and 6.0×10^6. The base mesh was created with 0.8×10^6 cells, and the mesh size was increased by a factor of 1.5 after that. From the plots of the wall shear stress and the surface temperature (figure 5.3), it can be seen that mesh independence is achieved at 2.6×10^6 cells for the RANS computations.

Mean flow statistics: Figures 5.4 and 5.5 show the contours of the averaged flow field obtained through the k-ω SST model. The conventional steady state flow field is reproduced where the jet impinges on the surface creating a high static pressure stagnation region and deflects radially to form the radially developing wall-jet. The maximum velocity appears at r/D = 1.3 after which the flow decelerates. Correspondingly, the turbulent kinetic energy profiles along the axial jet, reach a maximum at $y/D = 0.9$ and upon impingement, the turbulent kinetic energy is seen to increase due to the acceleration and eventually reduces as the wall jet loses momentum.

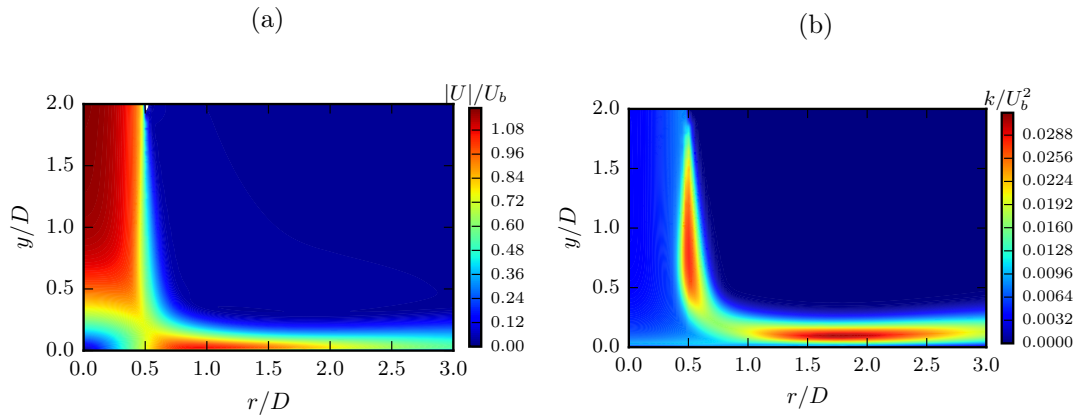

Figure 5.4: Visualization of circular jet impingement at Re_D= 23,000 over a constant $z = 0$ plane with contours of (a) mean velocity magnitude, |U|, normalised by bullk velocity, U_b, and (b) mean turbulent kinetic energy, k, normalised by the square of the bulk velocity, U_b.

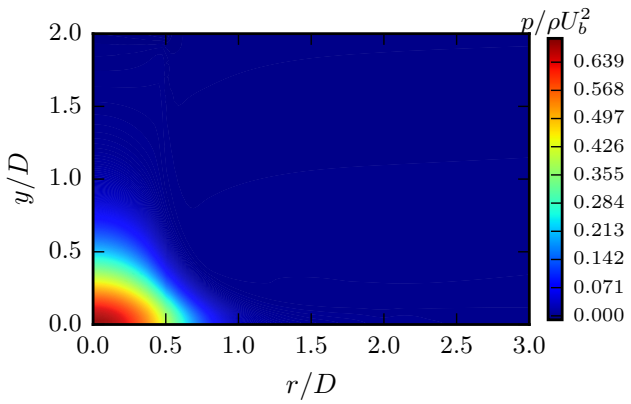

Figure 5.5: Visualization of circular jet impingement at Re_D= 23,000 over a constant $z = 0$ plane with contours of mean pressure, p, normalised by the square of the bullk velocity, U_b, and density ρ.

The velocity distributions obtained from the RANS simulations are compared with the experimental results of Cooper et al.[52] Figure 5.6 provides a comparison of the development of mean velocity at different radial locations of the impingement wall. It can be seen that at $r/D = 0.5$, the free-shear layer at the edge of the jet orifice, the k-ϵ based models perform better than the other models. As we move outwards in a radial direction ($r/D = 1.0$, $r/D = 1.5$) k-ω SST provides much better agreement with experimental data. This finding is consistent with the established trends, outlined in the previous section.

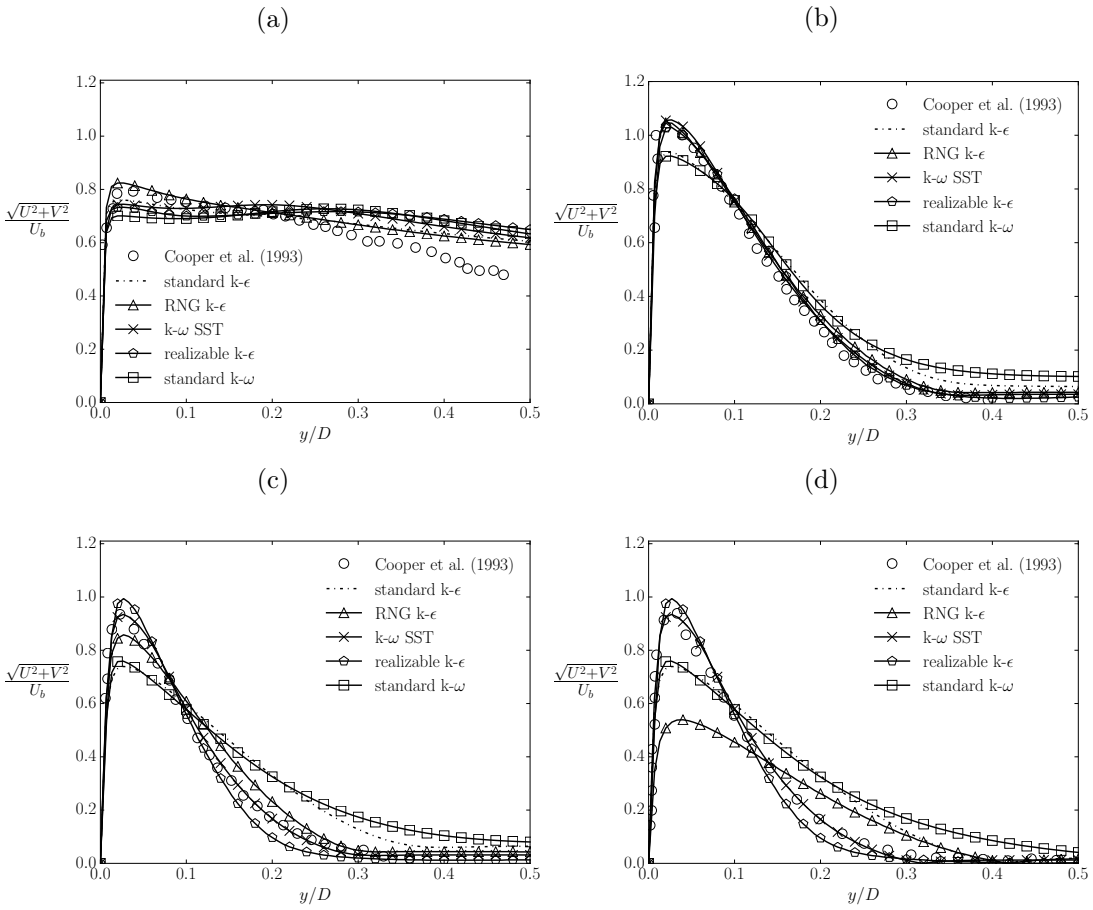

Figure 5.6: Development of mean velocity profile in the near-wall region at (a) $r/D = 0.5$ (b) $r/D = 1.0$ (c) $r/D = 1.5$ (d) $r/D = 2.5$. ○: Cooper at al.[52] at $Re_D = 23{,}000$; Solid lines with symbols: present RANS results for $Re_D = 23{,}000$.

The near wall mean axial velocities are compared in the figure 5.7. The mean velocities at the centre line (at $r/D = 0$) are plotted against the normalised height. Most of the RANS models predict the velocity distributions with reasonable accuracy in the near wall region. This

[52]D. Cooper et al. *Int. J. Heat Mass Transfer*, **36**: 2675–2684, 1993.

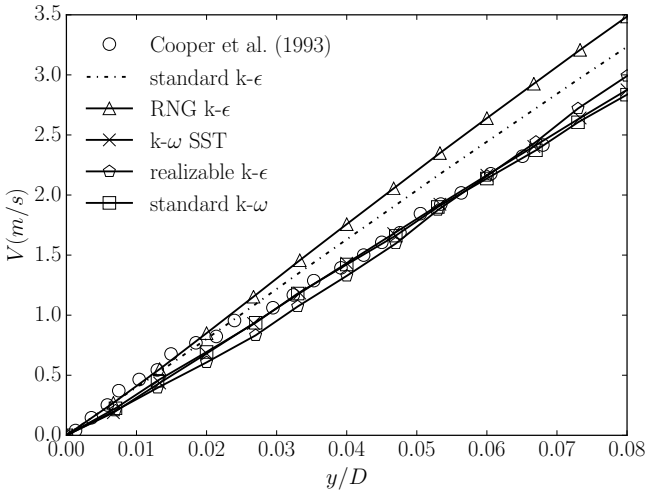

Figure 5.7: Near-wall mean axial velocity. ○: Cooper at al.[52] at Re_D = 23,000; Solid lines with symbols: present RANS results for Re_D = 23,000.

could be attributed to the fact that the mesh was finely graded in the near wall region; however, it is notable that k-ω and k-ω SST perform especially well. Again, this is consistent with previous findings.

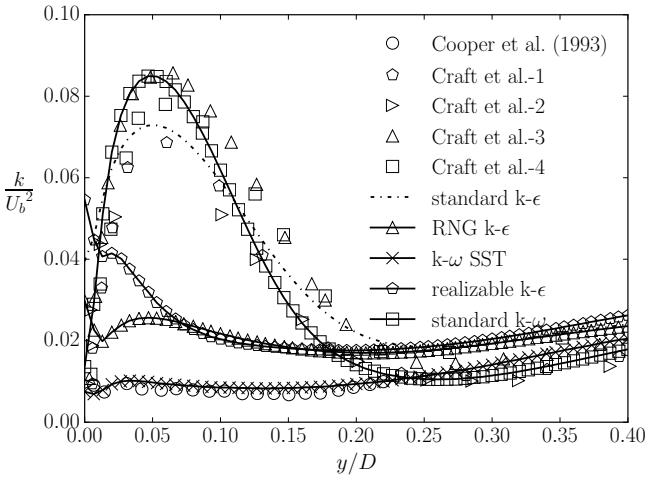

Figure 5.8: Near-wall turbulent kinetic energy k, normalised by the square of the bulk velocity, U_b as a function of y/D at the radial location $r/D = 0.5$. ○: Cooper at al.[52] at Re_D = 23,000; Solid lines with symbols: present RANS results for Re_D = 23,000; Other symbols: RANS results of Craft et al.[53].

The distribution of turbulent kinetic energy is shown in figure 5.8. The plot shows both the RANS predictions compared to that of Cooper et al.[52] As stated by Cooper at al.[52], the

value predicted using k-ϵ models is an order of magnitude higher than the actual measurement. However, the k-ω SST model shows excellent agreement. In figure 5.8, the legend Craft et al.-1 refers to the low Reynolds number k-ϵ model of Launder & Sharma[147] and Craft et al.-2 refers to the basic second-moment closure of Gibson & Launder[148]. As one would expect, our standard k-ϵ model reproduces Model 1, with reasonable agreement. Other models compare well with the formulations used by Craft et al.[53], and it is observed that k-ω SST has the best agreement with the experimental results.

The flow field is assumed to be unaffected by the temperature variations on the impingement wall and advected by the fluid momentum along with molecular diffusion. Hence, the scalar transport equation for heat transfer can be solved with temperature as a passive scalar. The scalar transport equation for a passive scalar is given by,

$$\frac{\partial T}{\partial t} + u_j \frac{\partial T}{\partial x_j} = \alpha \frac{\partial^2 T}{\partial {x_j}^2} \tag{5.1}$$

where α represents the thermal diffusivity. The Nusselt number quantifies the heat transfer from the target wall. The Nusselt number is defined as

$$Nu = \frac{q'' D}{k(T_w - T_\infty)} \tag{5.2}$$

where q'' is the heat flux per unit area and the k is the thermal conductivity.

Since the potential core of the jet is larger than the nozzle to wall spacing, the Nusselt number experiences a local maximum at the stagnation point and then decreases monotonically along the radial direction. The scaled Nusselt number is plotted against the radial direction in figure 5.9 to compare with the experimental work of Cooper et al.[52] and the numerical work of Craft et al.[53] Almost all of the RANS models fail to predict the stagnation point Nusselt number accurately due to the complexity of unsteady flow structures in the stagnation region. The models have close agreement with the experiments at $r/D = 1.5$ which is outside the stagnation region and close to the wall jet region, k-ω SST predicts the closest values to the experiments. This result is consistent with Hoffmann et al.[149], who concluded that RANS models fail in predicting the stagnation point heat transfer but are suited for wall jet heat transfer. As seen in (figure 5.9(b)) the contours of Nusselt number, the values are over predicted compared to the experiments and sharp gradients are observed which do not appear physically.

The RANS computations were carried out to assess the capabilities of the linear eddy viscosity models in predicting both heat and fluid flow statistics. Although the models were

[147] B.E. Launder and B.I. Sharma. *Lett. Heat Mass Transfer*, **1**: 131–137, 1974.
[148] M.M. Gibson and B.E. Launder. *J. Fluid Mech.*, **86**: 491–511, 1978.
[53] T.J. Craft et al. *Int. J. Heat Mass Transfer*, **36**: 2685–2697, 1993.
[149] H.M. Hofmann et al. *Numer. Heat Transfer, Part B*, **51**: 565–583, 2007.

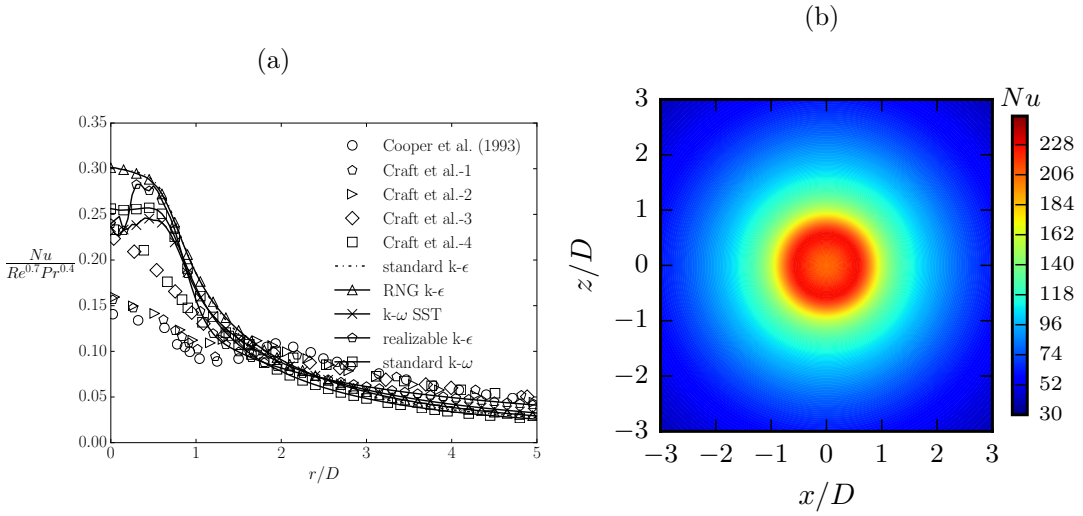

Figure 5.9: Mean and scaled Nusselt number, $Nu/Re^{0.7}Pr^{0.4}$ on the impingement wall as a function of radial distance r/D for the present RANS computations in (a) and visualisation of the impingement surface with contours of mean Nusselt number.

capable of predicting the averaged mean flow statistics with reasonable accuracy, the models predict heat transfer very poorly. The lack of unsteady flow and heat transfer information makes it difficult to provide a plausible explanation to the physics revealed. In summary, it is shown that the behaviour of the various models is consistent with previous studies. In particular, RANS models poorly predict Nusselt numbers in the stagnation region although the k-ω SST model provides the reasonable agreement. However, complex features such as the secondary Nusselt peak is entirely missed by all the RANS models. These findings give an impetus for the application of a more highly resolved approach, LES.

5.2 Computations with LES

5.2.1 Static-wall Circular Jet-impingement (SWJ) at $Re =$ 23,000

Large-eddy simulations are performed for an incompressible turbulent unconfined circular jet-impingement on a stationary wall with uniform heat flux, a jet Reynolds number of $Re_D =$ 23,000 and a nozzle-to-wall distance of $2D$. The variables are chosen in order to replicate

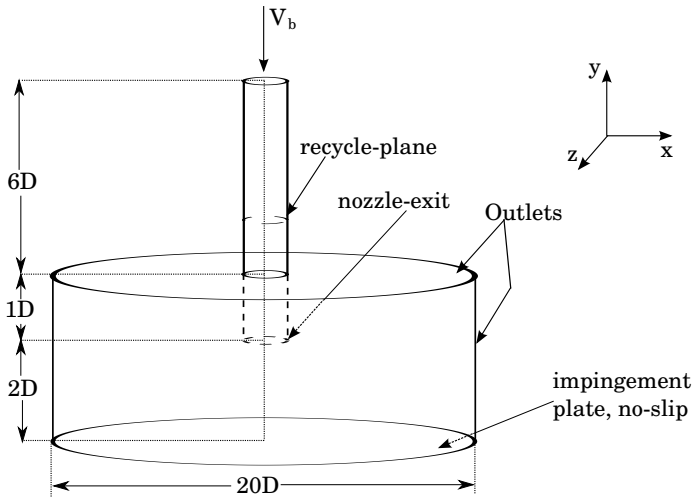

Figure 5.10: Schematic representation of the circular jet impingement configuration with the boundary conditions and the coordinate system used for the simulations.

configurations from previous studies. Both experimental and numerical studies exist for this configuration. The experimental measurements of Cooper et al.[52] are used as a reference. The experiments of Tummers et al.[87], Geers et al.[150], Baughn & Shimizu[24] and, Yan & Saniei[55] are also presented alongside the current LES results for comparison.

A schematic of the flow configuration is presented in figure 5.10. The solution domain is a collocated grid system with Cartesian coordinates, $\mathbf{X} = (x, y, z)$; with 0 as the origin at the center of the domain Ω, where $\Omega = [0, r] \times [0, L_y]$ with $L_y = 9D$ and the radius, $r = 10D$. The instantaneous velocity components are denoted $\mathbf{u} = (u, v, w)$ and the mean velocity components are denoted by $\mathbf{U} = (U, V, W)$. In the (x, y)-plane, the radial direction $r = \sqrt{x^2 + z^2}$ is given by x and the azimuthal angle $\theta = \arctan(x/z)$. The Reynolds number based on the jet-nozzle diameter D, bulk velocity V_b, and the kinematic viscosity ν is given as $Re = V_b\ D/\nu = 23{,}000$. The accuracy of LES tends to a DNS with increasing spatial resolution and reducing filter width. We, therefore, investigate the acceptable levels of mesh resolution for the current configuration.

At the inlet, fully-developed turbulent flow is generated by the recycle plane at an upstream distance of $1D$ from the nozzle exit. At the impingement wall, $y = 0$, a Dirichlet (no-slip) boundary condition is applied hence $\mathbf{U}(x, y = 0, z, t) = 0$. For pressure, a Neumann boundary condition is used which implies $\partial p/\partial y = (x, y = 0, z) = 0$ and a uniform heat flux boundary

[87] M.J. Tummers et al. *Int. J. Heat Mass Transfer*, **54**: 4939–4948, 2011.
[150] L.F.G. Geers et al. *Exp. Fluids*, **36**: 946–958, 2004.
[24] J.W. Baughn and S. Shimizu. *J. Heat Transfer*, **111**: 1096–1098, 1989.
[55] X. Yan and N. Saniei. *Proc. Int. Heat Transfer Conf.*, **5**: 497–502, 1998.

condition is applied at the wall for temperature. On the bounding sides of the domain (i.e., $r/D = \pm 10$, and $y/D = L_y/3$), a mixed boundary condition is applied for velocity where **U** is evaluated from the flux when the pressure is known. With this boundary condition, for an inbound flow, the velocity is obtained using the flux from the first adjacent cell of the boundary, and for outward flow, a zero-gradient is applied. A Dirichlet boundary condition is applied for pressure at the outlets, using the reference pressure of the flow field, $p_0 = p + 0.5|U|^2$, where p_0 is the stagnation pressure, and p is the static pressure at the boundary and is dependent upon **U**. Turbulence statistics are averaged in space and time after ten flow cycles where one flow cycle means that a fluid particle has travelled through the axial and radial dimensions i.e. $9D + 10D$ at the bulk velocity, V_b. The statistical averaging continues for 30 flow cycles. The entire domain was initialized with a converged RANS simulation.

Grid sensitivity study: Three grids are considered for the sensitivity analysis for which the grid parameters are given in Table 5.1. All three grids were discretised with hexahedral control volumes and were generated with the native OpenFOAM mesh utility, *'blockMesh'*. The *'blockMesh'* utility uses a separate dictionary to divide the domain into one or more hexahedral blocks, and the vertices and edges can be modified based on the requirement. The present computational domain is chiefly divided into three blocks, namely the pipe, the impingement domain, and the top boundary. Since the number of cells varies among these blocks, they are listed individually and allow for a realistic comparison with other jet-impingement computational set-ups which tend to use inflow without a fully developed pipe, or the top open boundary replaced with confinement. Grid-I was the coarsest mesh used with a total of 13.5×10^6 cells. The grid had 180 cells in the azimuthal direction. However, this was not sufficient to predict the mean flow characteristics accurately. Grid-II was generated with approximately twice the number of cells of Grid-I, clustering cells in both the radial and azimuthal directions. Although the fluid-flow results improved substantially, the Nusselt number data were under-predicted indicating the need for increased resolution in the azimuthal direction. Grid-III was generated with three times the number of cells in the azimuthal direction as compared to Grid-II with 60×10^6 cells.

The finest mesh has 60×10^6 cells. Hadžiabdić & Hanjalić[80] used 5×10^6 cells and produced the best results with one-quarter of the full domain with symmetry boundary conditions to increase their mesh resolution. It is equivalent to 20 million mesh points if the same mesh was extended for the full three-dimensional domain. It is also noted that they used a hybrid mesh

[80]M. Hadžiabdić and K. Hanjalić. *J. Fluid Mech.*, **596**: 221–260, 2008.

Grids	Pipe ($2D < L_y < 9D$, $0 < r < 0.5D$)				Impingement Domain ($0 < L_y < 2D$, $0 < r < 10D$)				Top Free Boundary ($2D < L_y < 3D$, $0.5D < r < 10D$)			
	N_r	N_y	N_θ	Total	N_r	N_y	N_θ	Total	N_r	N_y	N_θ	Total
Grid-I	112	200	180	4×10^6	309	136	180	7.5×10^6	195	57	180	2×10^6
Grid-II	147	200	260	7.6×10^6	391	136	260	14×10^6	240	25	260	1.5×10^6
Grid-III	190	180	640	22×10^6	354	150	640	34×10^6	260	25	640	4.1×10^6

Table 5.1: Grid parameters for the computational domain.

using both tetrahedral and hexahedral cells and experienced numerical oscillations and used a quadratic upwinding to control the oscillations. Their inflow was from an external pipe flow simulation and read at every time step while the current simulations have the inlet pipe within the domain which requires high grid resolution along the core and near-wall regions of the pipe and extending to the impingement zone. The inlet pipe in the current simulation has 22×10^6 cells. With the inlet pipe excluded, the total cells would be 38×10^6. The quality of the grid is somewhat better than but still comparable with that of Hadžiabdić & Hanjalić[80]. The finest mesh used by Uddin et al.[83] has 13×10^6 cells. The inflow conditions in the case of Uddin et al.[83] is different to the current set-up. Uddin et al.[83] generated velocity fluctuations based on digital filtering of random numbers. Due to the lack of near-wall turbulence structures in the synthetic inlet velocity boundary condition, very fine refinement in the pipe wall and the core region was not necessary for Uddin et al.[83]

A plane view of the grid (Grid-III) is shown in figure 5.11 with crucial zones identified within the domain as (a) to (d). Zone (a) in the domain refers to the pipe centerline ($0 < r < 0.3D, 0 < L_y < 9D$) where care was taken to cluster the cells from the inlet to the stagnation zone. The circular shape of the domain was discretized with a 'butterfly' mesh topology that is based on a square outline at the centre and is gradually modified into the circular shape. A geometric expansion ratio of the mesh was maintained below 1.2 for the mesh to expand smoothly in the radial direction in the critical areas of interest. Zone (b) is the region close to the pipe/nozzle wall region ($0.3 < r < 0.5D, 0 < L_y < 9D$) where the mesh was finely graded from the nozzle wall towards the axis centre line. It is critical to have a fine mesh in this area to resolve the near-wall statistics of the inflow such as axial and the wall-normal components of

[83]N. Uddin et al. *Int. J. Heat Mass Transfer*, **57**: 356–368, 2013.

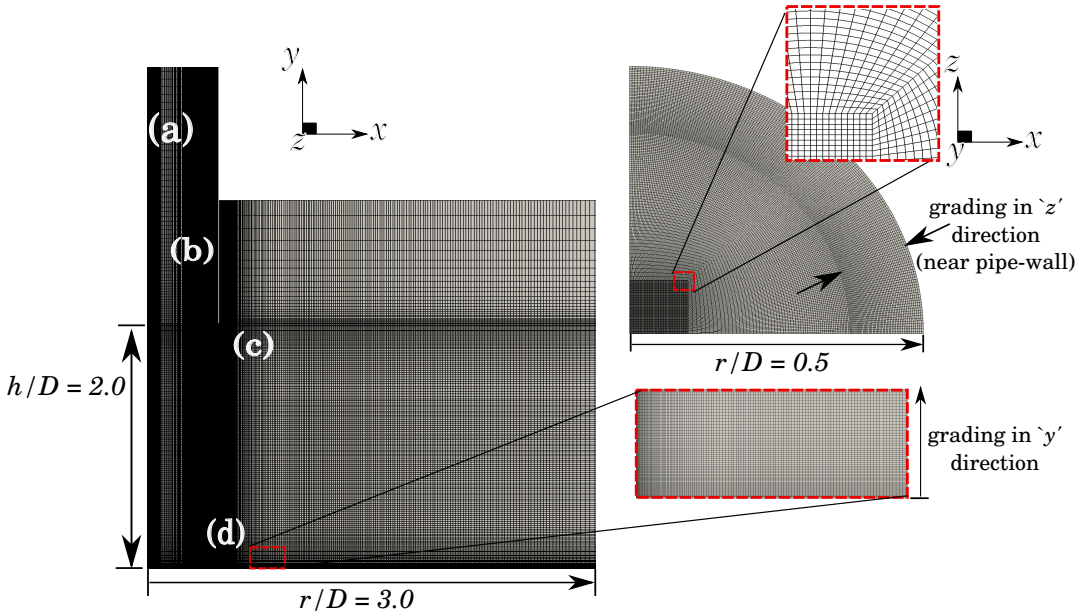

Figure 5.11: Plane and top view of the mesh segments showing critical zones (a)-(d), where zone (a) represents the pipe centreline, (b) the pipe near-wall, (c) the periphery of the nozzle-exit, and (d) the near-wall of the domain respectively.

fluctuations which directly influence the impingement wall heat-transfer. Zone (c) is the region ($1.75D < L_y < 2.2D$) immediately at the nozzle exit, arrayed with cells and graded with a finer mesh so that the instabilities generated due to the shear and sudden expansion of the fluid upon exit are captured effectively. These small-scale phenomena on traversing axially downward, grow and expand radially upon impingement causing significant changes to the wall heat-transfer. Finally, in Zone (d), which is the near-wall region, the cells are configured in uniform annular layers and graded such that maximum $y^+_{wall} \approx 1.0$ which is within the viscous sub-layer. The majority of the cells were arrayed within the region $0 < L_y < 1D$ and $-4D < r < 4D$ so as to resolve the shear layer development. All the grids are discretised with hexahedral control volumes.

The contour plot of the LES quality index or the resolvedness for Grids-II and III are shown in figure 5.12. It can be seen that in general, the critical zones of the domain are well resolved and greater than 90% for Grid-III. However, for Grid-II, some regions are marginally under-resolved. The first region of interest is the region around the nozzle exit (Zone (c)). It can be seen that in the immediate vicinity of the nozzle exit, there is a region of under resolvedness. The quality index in this region drops to well below 75%. This is because there is a sudden expansion in the flow which induces substantial dissipation near the nozzle exit region; Grid-II is

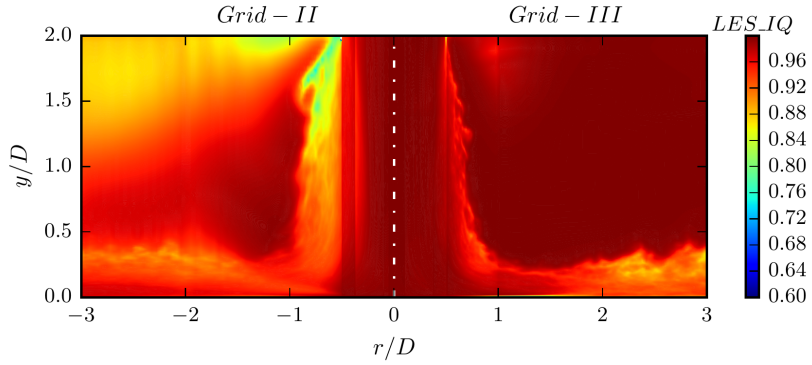

Figure 5.12: Map of resolvedness in the computational domain for Grid-II and Grid-III.

not refined enough at the nozzle exit to represent this phenomenon. Grid-III does not show any such anomalies within the domain, and the grid is sufficiently resolved since a local refinement in the mesh complements this region. The region experiences a sharp gradient in the flow. Because of the development of the radial wall jet and the Kelvin-Helmholtz instabilities formed due to the shear layer, the prediction of the turbulent kinetic energy, though within the acceptable range, requires a mesh close to the Kolmogorov microscales to resolve the finest scales. However, the simulation, in general, has a high-quality index throughout the domain indicating good resolution in the quality of the results.

Instantaneous and mean flow statistics

Figure 5.13(a) shows the base flow of the jet via contours of the instantaneous velocity magnitude normalized by bulk velocity, V_b for Re_D = 23,000. The flow exits the nozzle at the top of the figure and develops as a free-jet creating a shear layer with the quiescent fluid. The flow travels downstream (towards the static wall) forming a free-jet and is seen to impinge on the wall creating a high-pressure stagnation region. Upon impingement, the free-jet deflects and spreads radially as a wall-jet increasing the boundary layer thickness. Deceleration of the velocity field is seen on moving downstream from the stagnation region. Figure 5.13(b) shows the magnitude of instantaneous pressure field in the domain. Low-pressure regions within the shear-layer indicating the eddy roll-up are seen to travel axially downward and deflect radially upon impingement. A local high-pressure region is seen at the stagnation region due to impingement. The interplay with the stationary fluid is visualized through the instantaneous magnitude of vorticity, $(\omega_i\omega_i)^{0.5}$ in figure 5.13(c) where the jet upon exit starts to develop vortices of Kelvin-Helmholtz type due to interactions with the stagnant fluid shown as horizontal planes at varying locations in the free-jet. In the vicinity of the jet exit (y/D = 1.95), the vortex ring is slim and does

not show any severe destablization. However, on travelling axially downward, the vortex ring develops instabilities upon interaction with the quiescent fluid. The 'vortical nests' as referred to by Hadžiabdić & Hanjalić[80] are seen to increase with the increase in axial distance from the jet exit. It is essential that the ring vortex be captured effectively because these vortical structures travelling axially downward, tend to grow by stretching and eventually break down before impinging on the surface at different time instants creating multiple local hot-spots of increased heat transfer. All the contours presented above are for the same instant in time for Grid-III.

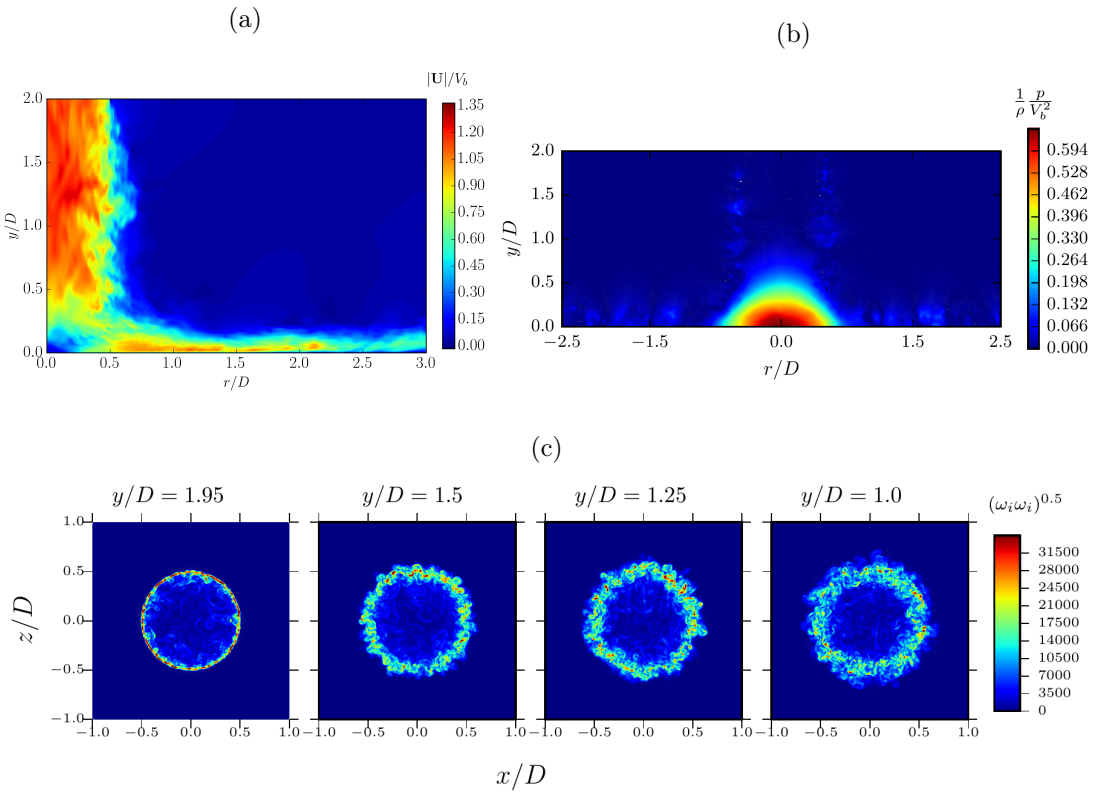

Figure 5.13: Visualization of circular jet impingement at Re_D =23,000 over a constant z plane with contours of (a) instantaneous velocity magnitude, $|\mathbf{U}|$, normalized by bulk velocity, V_b, (b) instantaneous pressure field, and (c) Instantaneous total vorticity magnitude, $(\omega_i\omega_i)^{0.5}$ in four horizontal planes ($y/D = 1.95, 1.5, 1.25$ and 1.0) in the free jet zone.(Note: 'y' is measured from the impingement plane.)

The isosurfaces of the Q-criterion are shown in figure 5.14 in which the Q-criterion is coloured by the distance from the impingement wall. The isosurfaces suggest that the slender small-scale structures are captured efficiently and are oriented along the radial direction. It shows the presence of large-scale structures close to the stagnation region. The small-scale arrangement is

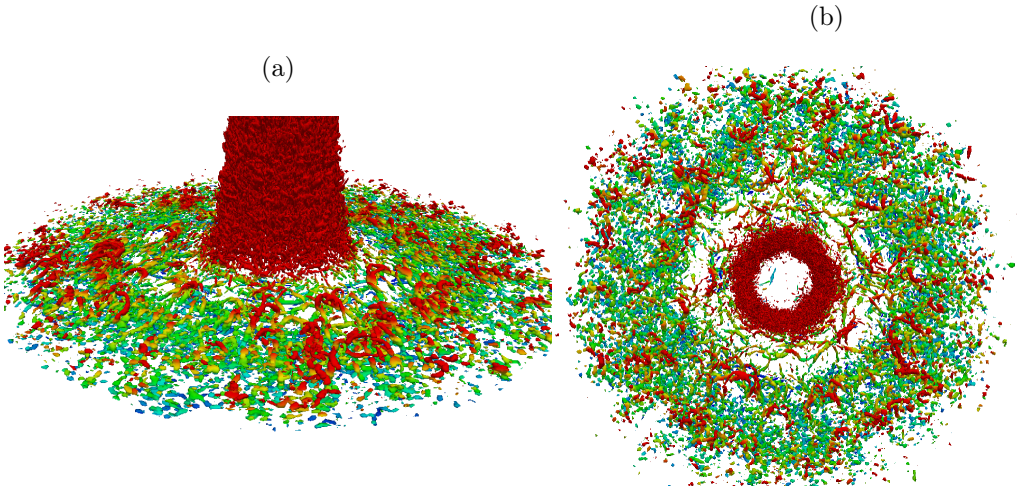

Figure 5.14: Isosurfaces of the Q-criterion ($Q = 30V_b^2/D^2$) for the subdomain $4D \times 2D \times 4D$ with the colours corresponding to the distance y/D from the impingement wall, (a) Perspective view, and in (b) Top view

also seen in the immediate vicinity of the jets which tend to form the braid regions along the shear layer of the jet. The toroidal organisation of the flow is also visible.

The development of the mean velocity magnitude profile normal to the wall for the results of figure 5.13 is shown in figure 5.15. The mean velocity is normalized by the bulk velocity, V_b, and the vertical distance, y, is normalized by the jet nozzle diameter, D. The results presented for the SWJ are averaged in time and the azimuthal direction. The data is compared with the experiments of Cooper et al.[52] and Tummers et al.[87]. The experiments of Cooper et al.[52] were carried out with hot-wire anemometry with an experimental uncertainty of $\pm 2\%$ for the bulk velocity V_b. The results of the present simulation are in good agreement with these experimental works. The spatial development of the wall-jet is seen as the mean flow reaches a maximum between $r/D = 1$ to 1.5 and then begins to decelerate on developing into the wall-jet region losing its momentum on radial spreading. The results of Grid-II at $r/D = 1$ are almost identical to those of Grid-III. However, on moving radially downstream from the stagnation region ($r/D > 1$), the importance of radial resolution is evident through a poor agreement with Grid-I compared with the reference data set. Grid-III gives better agreement with the experiments compared to Grid-I and II particularly in the near-wall ($y/D < 0.1$) region due to the higher spatial resolution of the mesh. For $y/D > 0.8$, the mean velocity remains largely unaffected since the shear layer has a weak influence on the centre of the jet.

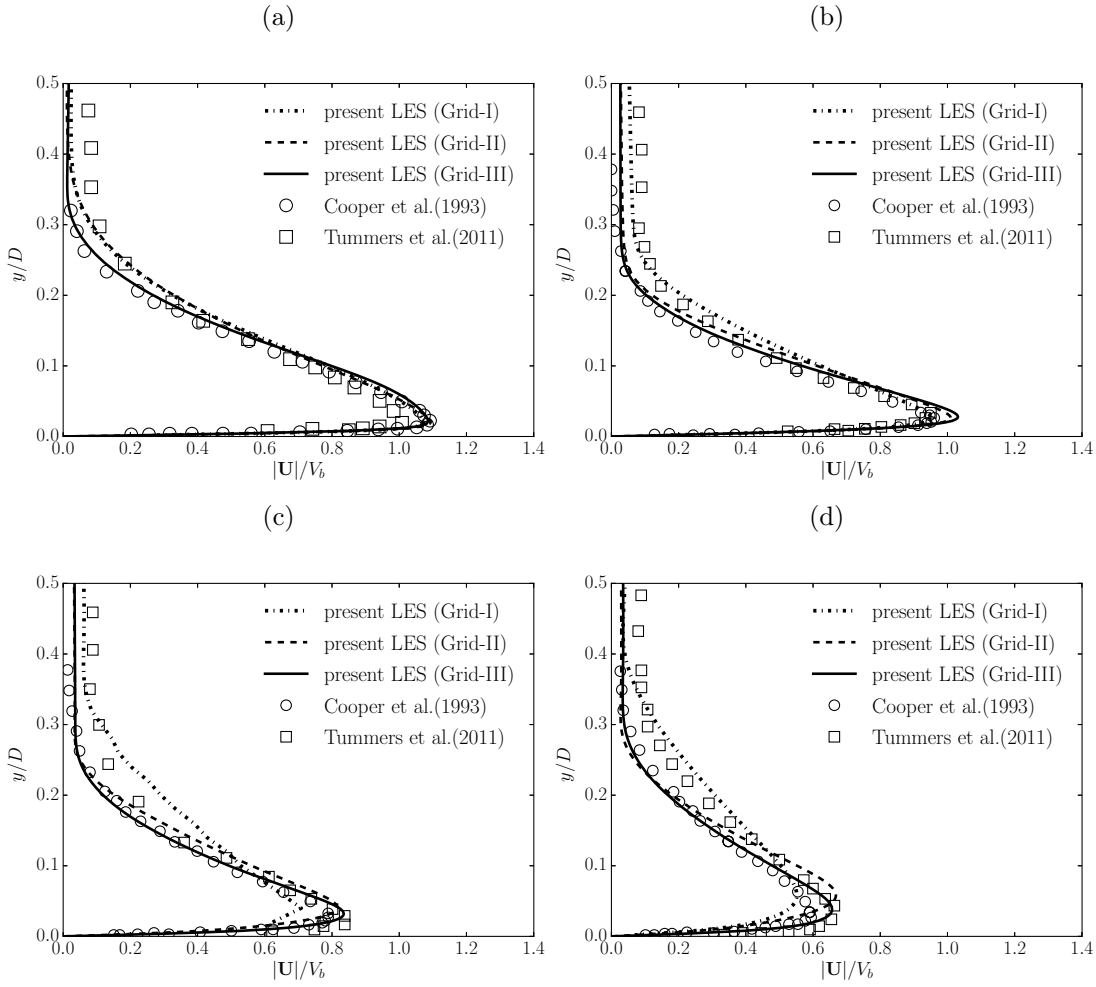

Figure 5.15: Development of mean velocity profile in the near-wall region at (a) $r/D = 1.0$ (b) $r/D = 1.5$ (c) $r/D = 2.0$ (d) $r/D = 2.5$. ——: present LES at $Re_D = 23{,}000$ using Grid-III; - - - - -: present LES at $Re_D = 23{,}000$ using Grid-II;$-\cdot-\cdot-$: present LES at $Re_D = 23{,}000$ using Grid-I; ○: Cooper at al.[52] at $Re_D = 23{,}000$; □: Tummers et al.[87] at $Re_D = 23{,}000$.

Second-order turbulence statistics

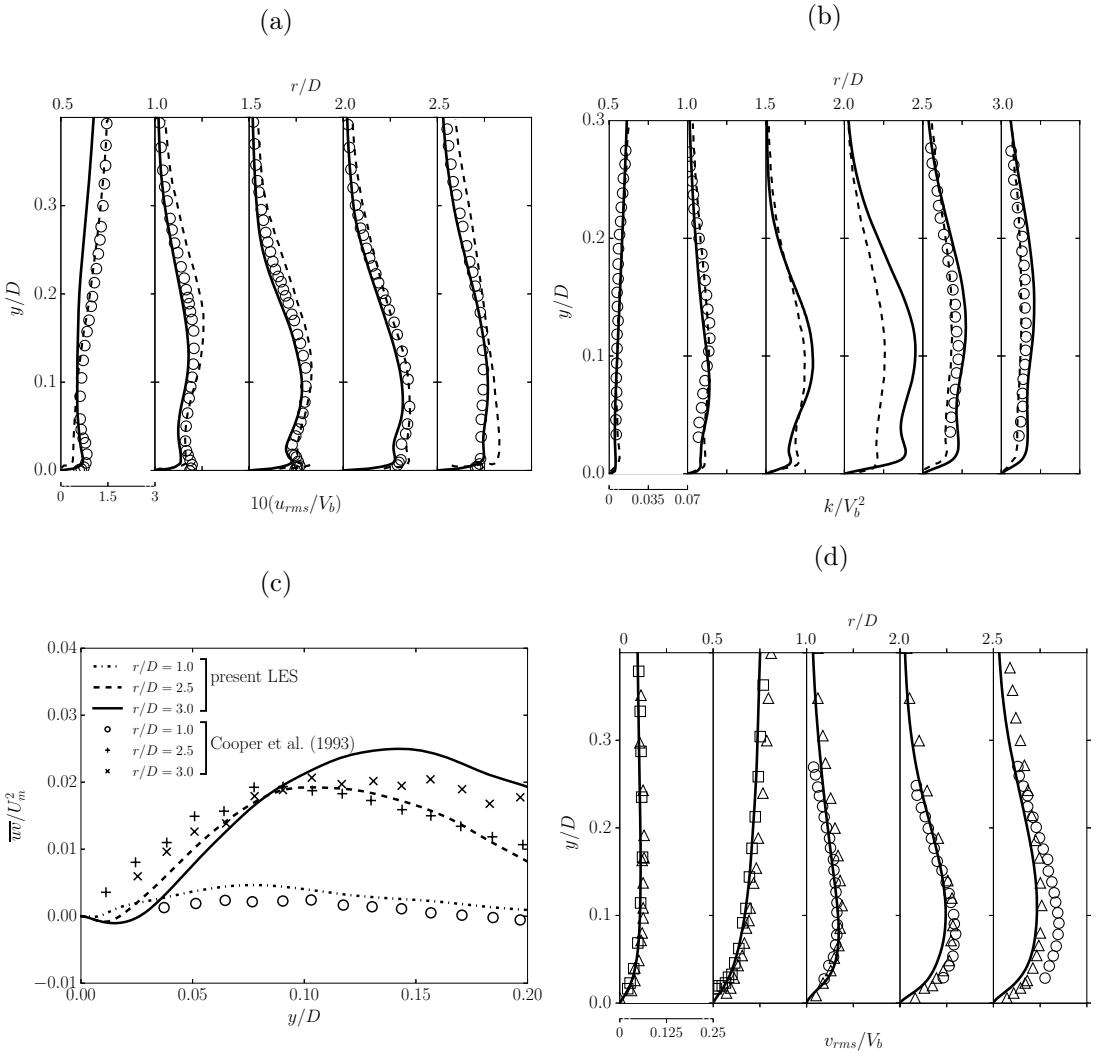

Figure 5.16: (a) Development of root mean square radial velocities in the near-wall region. ——: present LES at Re_D = 23,000 using Grid-III; - - - -: Halqvist[79] at Re_D = 20,000; ○: Cooper et al.[52] at Re_D = 23,000 (b) development of turbulent kinetic energy profiles in the near-wall region. ——: present LES at Re_D = 23,000 using Grid-III; - - - -: Hadžiabdić & Hanjalić[80] at Re_D = 20,000; ○: Cooper et al.[52] at Re_D = 23,000, and (c) turbulent shear stress $\overline{uv}$ at different radial locations. lines: present LES at Re_D = 23,000 using Grid-III; symbols: Cooper et al.[52] at Re_D = 23,000, and (d) wall-normal root mean square velocity profiles. ——: present LES at Re_D = 23,000 using Grid-III; ○: Cooper et al.[52]; △: Tummers et al. [87] at Re_D = 23,000; □: Geers et al.[150] at Re_D = 23,000.

The distribution of the radial r.m.s velocity normalised by the bulk velocity, V_b is shown in

figure 5.16(a). The LES predictions are compared to the experimental work of Cooper et al.[52] along with the LES of Hallqvist[79] ($Re_D = 20,000$) within the shear layer. The present levels of u_{rms} are in good agreement. Peak values of u_{rms} are seen at the radial distance $r/D = 1.5$ to 2.2. This location of the u_{rms} peak is identical to the peak-value location of the turbulent kinetic energy shown in figure 5.16(b). The near-wall fluctuations of the simulation are in agreement with experimental measurements. The values of u_{rms} increase from $r/D = 0.5$ owing to the acceleration of the flow in the wall jet region. In the vicinity of the wall, the viscous dissipation reduces the levels of u_{rms}, and as the radial distance increases, the fluctuations decrease further due to the wall blocking effect.

The evolution of turbulent kinetic energy normalised by the square of the bulk velocity, V_b along the radial direction is shown in figure 5.16(b). The results are compared with the experimental work of Cooper et al.[52] and the numerical work of Hadžiabdić & Hanjalić[80] ($Re_D = 20,000$) within the shear layer. Good agreement is observed with both these experimental and numerical studies. The acceleration region where the turbulent kinetic energy attains a peak value in the wall jet region is from $r/D = 1.5$ through to $r/D = 2.2$. This increase of the turbulent kinetic energy in the wall jet region is due to the high shear and rapid acceleration of the flow due to strong streamline curvature. This peak in the turbulent kinetic energy matches the numerical findings of Uddin et al.[83] and experimental findings of Lytle & Webb[68] who linked this increased turbulent kinetic energy to the formation of the secondary Nu peak. Double peaks are observed in the region $1.5 < r/D < 2.0$, but the peak values are marginally higher compared to those obtained by Hadžiabdić & Hanjalić[80].

Figure 5.16(c) shows the turbulent shear stress profiles of the SWJ normalised by the square of the maximum radial velocity, U_m in the wall-jet. The LES predictions are compared to the measurements of Cooper et al.[52]. The results compare well with the prediction of the level of shear stresses. The negative maximum shear stress values obtained are consistent with the values obtained by Hadžiabdić & Hanjalić[80]. With increasing radial distance, the value of the negative shear stress tends to increase. Hadžiabdić & Hanjalić observed that the maximum wall-jet velocity was not proportional to the minimum shear stress value. This is also seen in the present work, for example, at $r/D = 2.5$ the shear stress value is higher compared to $r/D = 1.0$ but the wall-jet velocity gradient is lower compared to that at $r/D = 1.0$. Due to the turbulent pipe flow boundary condition at the inlet, the wall jet region remains turbulent in all radial positions, and no relaminarization occurs.

[79] T. Hällqvist. *Large eddy simulation of impinging jets with heat transfer*. PhD thesis, 2006.
[68] D. Lytle and B.W. Webb. *Int. J. Heat Mass Transfer*, **37**: 1687–1697, 1994.

The profiles of wall-normal velocity fluctuations of the SWJ normalised by the bulk velocity are shown in Figure 5.16(d). The present LES results are compared with the experiments of Cooper et al.[52], Tummers et al.[87] and Geers et al.[150]. The good correspondence with the experiments is reflected by the accurate predictions of the impingement wall heat-transfer discussed in later in this chapter.

Turbulent kinetic energy budgets

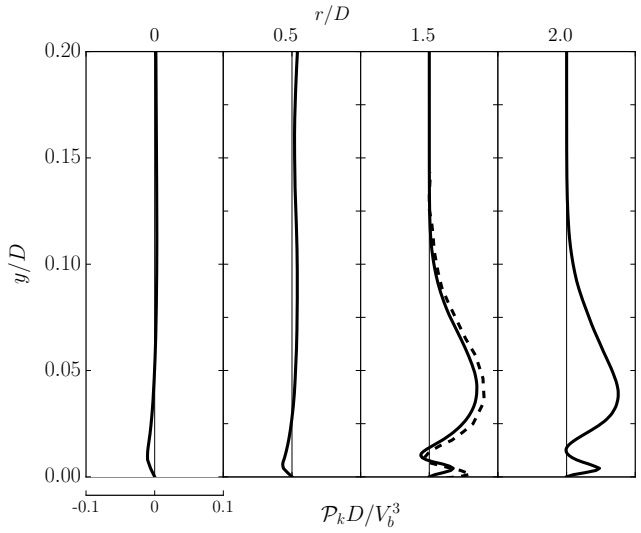

Figure 5.17: Production of turbulence kinetic energy at different radial locations for the SWJ compared with the LES of Hadžiabdić and Hanjalić (dashed lines) at $r/D = 1.5$,

To complement the analysis of the turbulent kinetic energy, the budgets of turbulent kinetic energy have been analysed. The transport equation for the time-averaged kinetic energy can be written as,

$$\underbrace{\langle \bar{u}_j \rangle \frac{\partial k}{\partial x_j}}_{advection\ (\mathcal{C}_k)} = - \underbrace{\left\langle \overline{u_i' u_j'} \right\rangle \frac{\partial \bar{u}_i}{\partial x_j}}_{production\ (\mathcal{P}_k)} - \underbrace{\frac{1}{2}\frac{\partial}{\partial x_j}\langle \bar{u}_i' \bar{u}_i' \bar{u}_j' \rangle}_{turbulent\ diffusion} - \underbrace{\frac{1}{\rho}\left\langle \bar{u}_j \frac{\partial \bar{p}}{\partial x_j} \right\rangle}_{pressure\ diffusion}$$
$$+ \underbrace{2\nu \left\langle \frac{\partial \bar{S}_{ij} \bar{u}_i}{\partial x_j} \right\rangle}_{viscous\ diffusion} - \underbrace{2\nu \langle \bar{S_{ij}} \bar{S_{ij}} \rangle}_{viscous\ dissipation\ (\epsilon_k)} - \underbrace{\left\langle \frac{\partial \tau_{ij} \bar{u}_i}{\partial x_j} \right\rangle}_{SGS\ diffusion} + \underbrace{\langle \tau_{ij} \bar{S_{ij}} \rangle}_{SGS\ dissipation} \tag{5.3}$$

where $\mathcal{C}_k$ denotes the convective transport or advection, $\mathcal{P}_k$ represents the turbulent kinetic energy production and ϵ_k represents the viscous dissipation. Figure 5.17 shows the turbulence

production ($\mathcal{P}_k = -\overline{u_i' u_j'} \partial u_i / \partial x_j$) along the radial direction for the static wall configuration. In the stagnation region, negative production of turbulence kinetic energy was observed by previous experiments (see Nishino et al.[151], Geers et al.[150]) and numerical studies (see Satake & Kunugi[152], Hadžiabdić & Hanjalić[80]) indicating the energy transfer back to the mean field from the turbulent field. This has also been confirmed in the present investigation. For comparison, the LES data of Hadžiabdić and Hanjalić are plotted at $r/D = 1.5$ where the maximum turbulence kinetic energy is observed. Good agreement is observed, and the characteristic twin peaks are reproduced.

Heat-transfer characteristics

The time and azimuthal averaged Nu predicted from the current LES is presented here. Normalisation of Nu by $Re^{2/3}$ was proposed by Martin[44] to remove the influence of Reynolds number. This normalisation has been used in the current work to enable direct comparison of diverse data sets. Works that have previously adopted this normalisation include Uddin et al.[83] and Dairay et al.[27]. The experimental work of Lee & Lee[63] for $Re_D = 20{,}000$ is also compared with the present LES.

Figure 5.18 shows the time averaged radial Nusselt number variation of the static wall case with normalization in (a), and without the normalization in (b) across the radial length of the impingement-wall. The present results agree with the previous experimental works. Grid-I substantially under predicts the value of Nu beyond $r/D > 1.5$ with the secondary Nu peak being clearly absent. Increased azimuthal and radial resolution (Grid-II) resulted in a significant improvement in the prediction of the Nu number profile. However, the secondary peak was significantly under-predicted with only a modest hint of the peak at $r/D = 2.1$. Grid-III has the best agreement predicting both the primary and secondary Nu peaks. The experiments of Lee & Lee[63] used $Re = 20{,}000$ and the effect of Reynolds number is visible in (b) where the magnitude of the Nusselt number decreases with the decrease in Reynolds number. The local minimum is observed at $r/D \approx 1.5$ and a secondary peak at $r/D \approx 2.0$ consistent with the earlier observations in literature for similar configurations. For $r/D > 2.0$, the Nusselt number decreases monotonically.

[151] K. Nishino et al. *Int. J. Heat Fluid Flow*, **17**: 193–201, 1996.
[152] S. Satake and T. Kunugi. *Int. J. Numer. Methods Heat Fluid Flow*, **8**: 768–780, 1998.
[44] H. Martin. *Adv. Heat Transfer*, **13**: 1–60, 1977.
[27] T. Dairay et al. *J. Fluid Mech.*, **764**: 362–394, 2015.
[63] J. Lee and S-J. Lee. *Exp. Heat Transfer*, **12**: 137–156, 1999.

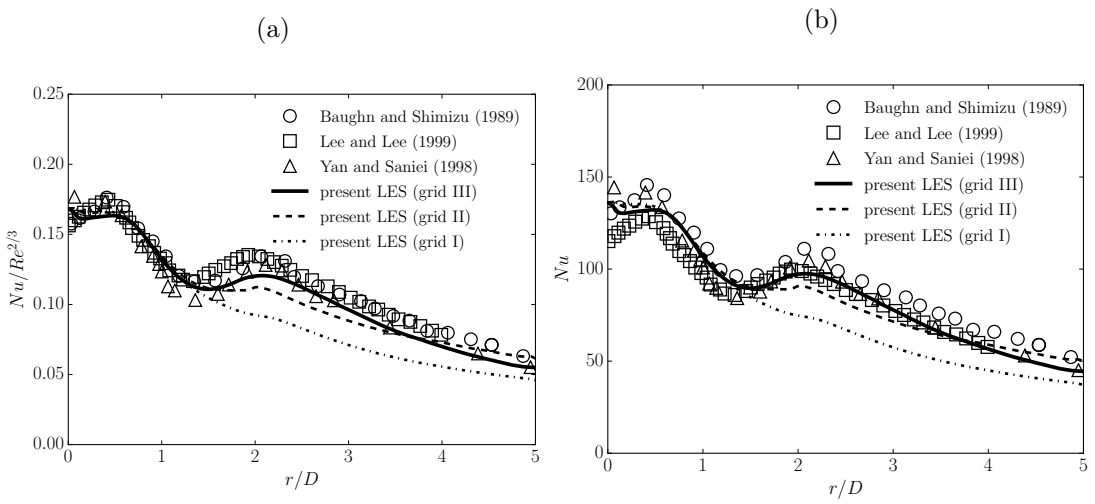

Figure 5.18: Time-averaged and normalized Nusselt number, $Nu/Re^{2/3}$ on the impingement wall as a function of radial distance r/D. ——: present LES at Re_D = 23,000 using Grid-III; - - - - -: present LES at Re_D = 23,000 using Grid-II;– · – · –: present LES at Re_D = 23,000 using Grid-I; ○: Baughn & Shimizu[24] at Re_D = 23,750; □: Lee & Lee[63] at Re_D = 20,000; △: Yan & Saniei.[55] at Re_D = 23,340, (a) With $Re^{2/3}$ normalization (b) Without $Re^{2/3}$ normalization.

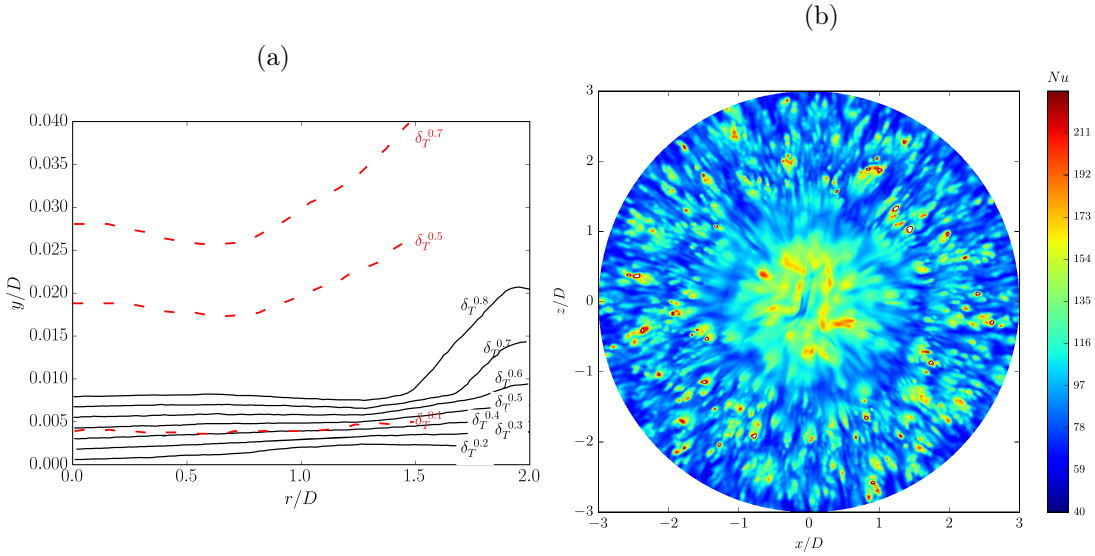

Figure 5.19: (a) Contours of thermal boundary layer thickness factor δ_T^{α} in the near-wall region; ——: present LES at Re_D = 23,000; - - - -: laminar DNS data of Rohlfs et al.[86] at Re_D = 1,804, y/D = 4.5, and (b) visualization of the jet-impingement wall at Re_D = 23,000 with contours of instantaneous Nusselt number.

To visualize the near-wall thermal behaviour, a thermal boundary layer thickness factor denoted δ_T^{α} is used as the thickness at which the fluid temperature near-wall attains a certain fraction of the characteristic local temperature difference as described by Rohlfs et al.[86] The definition of α is given as

$$\alpha = \frac{T_w(r) - T_f(r,y)}{T_w(r) - T_{ref}} \tag{5.4}$$

where T_w is the impingement-wall temperature, T_f is the fluid temperature and T_{ref} is the reference temperature. The levels of δ_T^{α} are shown in figure 5.19(a). The thermal boundary layer thickness is relatively thin when compared to a laminar jet (see Rohlfs et al.[86]) which is evident since the momentum of the fluid in the present case is higher, causing higher advection and thereby restricting the growth of the thermal boundary layer. A local thinning of the boundary layer is observed between $r/D = 1.0$ to 1.5 where the local acceleration of the fluid has also been observed to be a maximum. Beyond $r/D = 1.75$, the boundary layer begins to develop. The instantaneous distribution of the Nusselt number is shown in figure 5.19(b). The maximum normalized Nu is found in the stagnation region and the 'hot', and 'cold' spots are visualized side by side along the radial wall-jet region as proposed by Uddin et al.[83] These could be appearing due to the local unsteady flow separation and reattachment resulting in the increase and decrease of local temperatures.

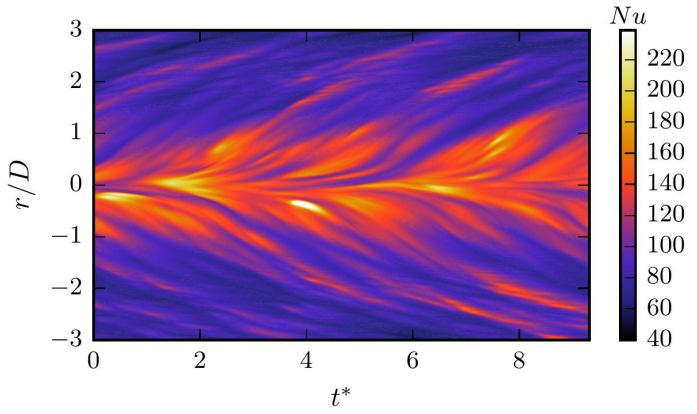

Figure 5.20: Spatio-temporal map at $Re_D = 23{,}000$

The instantaneous space-time contours of Nu are shown in figure 5.20 as function of non-dimensional time $t^* = tU_b/D$. Due to the highly unsteady and turbulent nature of the impinging flow, the impingement heat transfer shows complex streaky patterns. The radial distribution of the Nusselt number from a maximum in the vicinity of the stagnation region and gradually

[86]W. Rohlfs et al. *Int. J. Heat Mass Transfer*, **55**: 7728–7736, 2012.

decreasing downstream is observed. The footprints of the large eddy structures visualised, correspond to a Strouhal number, St ≈0.5. The cold fronts are seen to move at a similar convective velocity as that of the large-scale structures which were also observed by Dairay et al.[27]

The intense events that occur in the near-wall region of the jet cause deviations from the conventional law of the wall. The inner layer is subjected to intense shear especially in the wall-jet region. The plots of dimensionless radial velocity and temperature distributions as a function of

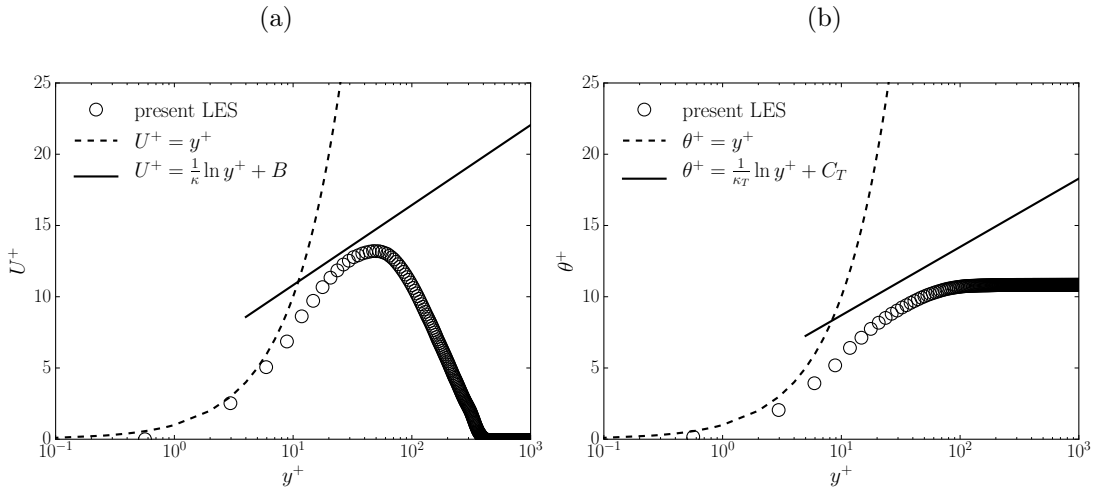

Figure 5.21: (a) Mean radial velocity U^+ as a function of y^+ and, (b) mean temperature θ^+ as a function of y^+ at the radial location $r/D = 2.0$.

wall units ($y^+ = u_\tau y/\nu$) are shown in figures 5.21 (a) and (b). The local temperature difference, θ, is defined as, $\theta = (T_w - T_f)$ where T_w is the wall temperature and T_f is the fluid temperature. Correspondingly, the normalized temperature, θ^+ is given as $\theta^+ = \theta/T_\tau$ where T_τ is the friction temperature given by, $T_\tau = q_w/\rho c_p U_\tau$. The constants used are $\kappa = 0.41, B = 5.2, \kappa_T = 0.48$ and $C_T = 3.9$[153]. The profiles indicate there is slight deviation from the conventional law of the wall (as observed by Uddin et al.[83] , Wygnanski et al.[154]) in the log-law region and with suitable modifications to the constants, can be cast into scaling laws.

Quadrant analysis can be useful to understand the 'hot' and 'cold' events in the near-wall region. Aillaud et al.[155] have constructed the four quadrants (see figure 5.22) based on axial velocity where fluid injection and ejection can occur. Negative axial velocity along with the local fluid temperature indicate hot or cold fluid injections whereas positive axial velocity indicates

[153]P. Bradshaw and G.P. Huang. *Proc. Royal Soc. London*, **451**: 165–188, 1995.
[154]I. Wygnanski et al. *J. Fluid Mech.*, **234**: 669–690, 1992.
[155]P. Aillaud et al. *Phys. Fluids*, **28**: 095110, 2016.

hot or cold fluid ejections. The events can be termed as 'hot' or 'cold' based on the time, and azimuthal averaged local fluid temperature, $\langle T \rangle$ such that when the local fluid temperature, $T > \langle T \rangle$ they correspond to hot events and when $T < \langle T \rangle$ termed as cold events. This analysis also brings insights into the level of mixing in the wall jet region and the dominant event at different radial locations downstream from the stagnation region of the impinging jet.

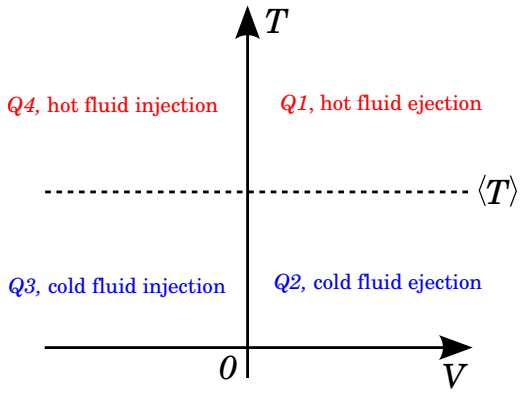

Figure 5.22: Representation of the 4 quadrants in the (V, T) space; Injection and ejection events are identified respectively by $V < 0$ and $V > 0$. Hot and cold events are identified respectively by $T > \langle T \rangle$, where $\langle T \rangle$ is the azimuthal and time averaged local temperature.

Figure 5.23 shows the joint temperature and velocity analysis for the impinging jet at different radial locations. A normalized temperature (following Aillaud et al.[155]) T^* given by,

$$T^* = \frac{T_f - T_{ref}}{T_w - T_{ref}} \tag{5.5}$$

where T_f is the instantaneous local fluid temperature, T_w the corresponding wall temperature and T_{ref} is the reference temperature (inlet temperature of the fluid).

At locations close to the stagnation region, (i.e., $r/D \leq 1.0$) since the flow field is largely dominated by the incoming jet, the dominant event is primarily the cold fluid injection ($Q3$). Upon moving radially away from the stagnation region, the mixing is still evident with strong events of both hot fluid ejection and cold fluid injection until $r/D \leq 2.0$. As the momentum of the jet reduces, and the amount of hot fluid ejection increases with the downstream distance and eventually dominant beyond $r/D = 2.5$.

Overall, the dynamics under jet-impingement, both fluid flow, and heat transfer characteristics are satisfactorily reproduced by comparison with representative experimental and numerical

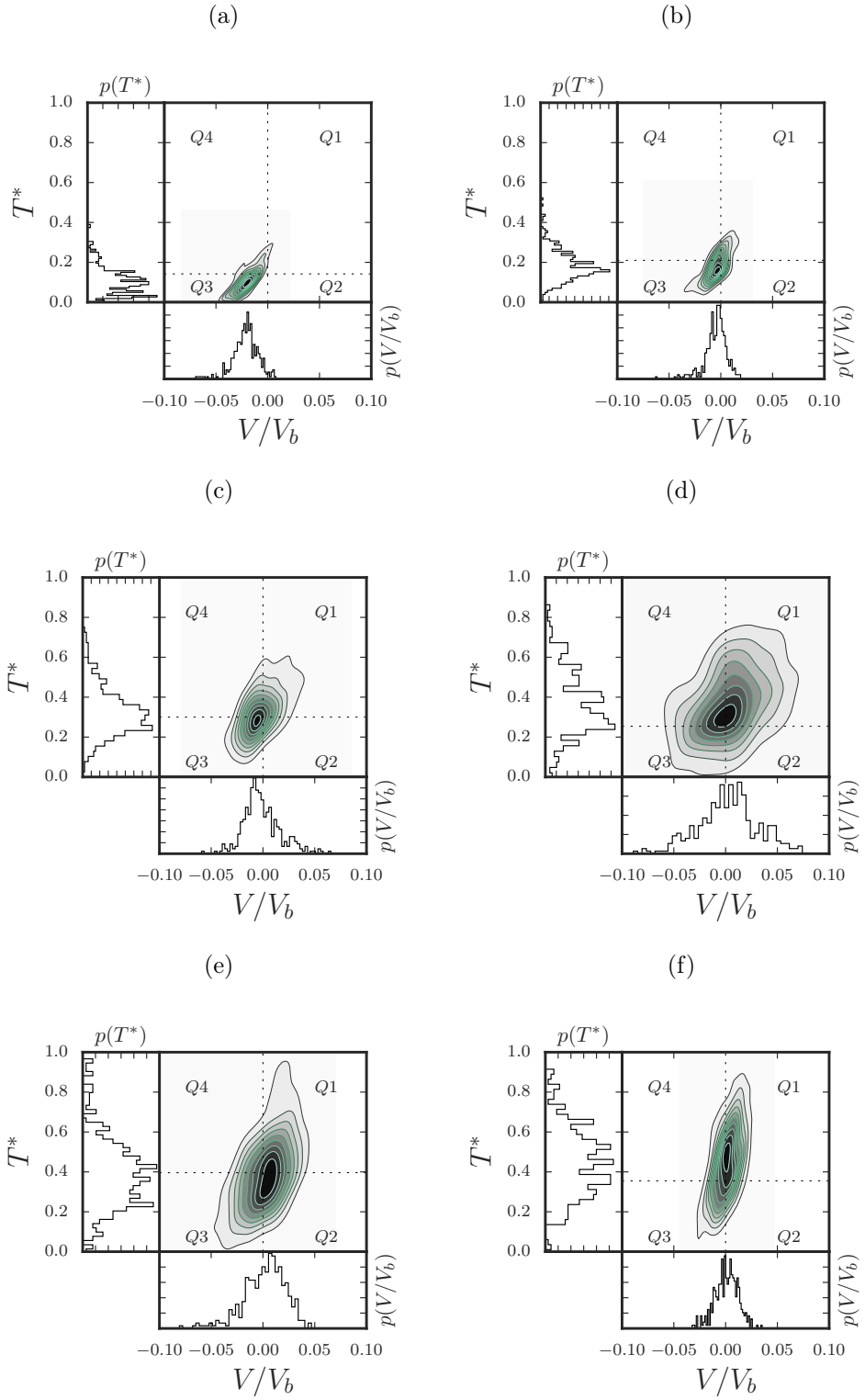

Figure 5.23: Joint probability distribution, $P(V,T)$, at $y/D = 0.01$ for (a) $r/D = 0.5$ (b) $r/D = 1.0$ (c) $r/D = 1.5$ (d) $r/D = 2.0$ (e) $r/D = 2.5$ (f) $r/D = 3.0$; ——: present LES at $Re_D = 23{,}000$; - - - -: limits of the four quadrants; scale: high probability (black) and zero probability (white).

studies. The LES results from the analysed configuration agree favourably and are deemed suitable for capturing the flow features of the impinging-jet.

5.3 Summary

This chapter has demonstrated the successful implementation of the developed code for jet impingement investigations involving both flow and heat transfer. The RANS results show that the mean flow statistics are reproduced with reasonable accuracy whereas the lack of instantaneous data and the poor predictions of surface heat transfer required a highly resolved LES to capture the flow and heat transfer precisely. Both the first order and second order turbulence statistics were reproduced with greater accuracy when compared with previous experimental studies. The near-wall 'hot' and 'cold' events were identified through a quadrant analysis which showed variations in these events on moving further away the stagnation region. It was also shown that the azimuthal resolution was far more important compared to the radial resolution to reproduce the secondary Nusselt number peak.

Chapter 6

Jet Impingement on Vibrating Surfaces

This chapter describes the configurations where the impingement surface vibrates in the direction of the issuing jet axis. We begin with a description of the moving mesh algorithm used and its verification. This is followed by the results of jet impingement configuration for Re_D of 23,000 with a mean nozzle-to-wall distance of $1.75D$ with the wall motion within the region of $0 \leq y/D \leq 0.5$ with the nozzle-to-wall spacing, $y/D = 2$ at the nozzle exit and a vibration frequency of 100 Hz. To understand the consequences of induced impingement surface forcing, the flow and thermal dynamics are thoroughly explored for this configuration. Thereafter we present the effect of frequency and vibration explored in the parameter space. The chapter concludes with the effect of the forcing parameters on the flow and heat transfer in a circular jet impingement configuration.

6.1 Moving Boundary Algorithm

The algorithm used for dynamic mesh displacement and its validations are presented here. The process of impingement surface vibration needs to be transformed from the physical space to the computational space. This physical movement when represented in the discretized computational mesh implies that the domain undergoes changes or deforms during the simulation. It is necessary that the boundary is modified at every time step to meet the prescribed motion

usually specified with a mesh motion equation. We use a vertex based mesh motion method where an equation determines the motion of all the internal vertices in the computational domain[156]. The present code was modified so that equations 3.7, 3.8, 3.58 coupled with the mesh displacement equation (Equation 6.1), are solved concurrently. For the present cases, the mesh points are explicitly specified through the mesh displacement equation. The motion of the impingement wall is defined by,

$$\Delta \mathbf{S} = A \sin(\omega t) \tag{6.1}$$

where $\omega = 2\pi/T$ is the angular frequency, A, the displacement amplitude and T the period of vibration. The predefined mesh motion is prescribed by a moving wall boundary condition implemented as a Dirichlet boundary condition. This boundary condition adjusts the flux due to mesh motion. The total flux, ϕ, through the moving wall is zero by updating the wall-normal velocity component to the corresponding mesh motion. Additionally, the motion velocity is calculated from the volume swept by a face in motion. In the present moving boundary method, the mesh undergoes deformation without undergoing a change in the number and connectivity of the hexahedral control volumes. The control volumes essentially expand and contract to achieve the enforced amplitude of mesh deformation (see Jasak & Rusche[157]). The mesh motion is achieved by direct displacement of the nodes supporting the mesh while preserving the mesh quality. The coordinate system followed is similar to that of the SWJ in Chapter 5. It is important that the mesh at its fully expanded state before compression has a sufficiently high spatial resolution to capture the associated turbulent length scales to bound the local cell Reynolds number. As a result, the mesh at the completely compressed phase leads to tight constraints on the time-step.

Two different moving jet-impingement configurations are validated to test the moving mesh methodology adopted in the present work. First, the experiments of Ichimiya & Yoshida[39] of a planar jet impinging on a vibrating wall are simulated. From the experiments of Ichimiya and Yoshida, a case with a high frequency of 100 Hz and amplitude to nozzle-to-wall distance ratio, ζ = 0.1, covering 10 % of the nozzle-to-wall distance is chosen. Second, the experiments of Wen[40] of a circular jet impinging on a vibrating impingement wall are modelled. With the experiments of Wen, a low frequency of 5.02 Hz and essentially a similar amplitude to nozzle-to-wall distance ratio $\zeta = 0.1$ is chosen.

[156]H. Jasak and Z. Tukovic. , **30**: 1–20, 2006.

[157]H. Jasak. "Dynamic mesh handling in OpenFOAM" in: *47th AIAA Aerospace Sciences Meeting*. 2009. 341

[39]K. Ichimiya and Y. Yoshida. *J. Heat Transfer*, **131**: 11701, 2009.

[40]M-Y. Wen. *Int. J. Heat Mass Transfer*, **48**: 545–560, 2005.

Comparison with the experiments of Ichimiya & Yoshida[39]:

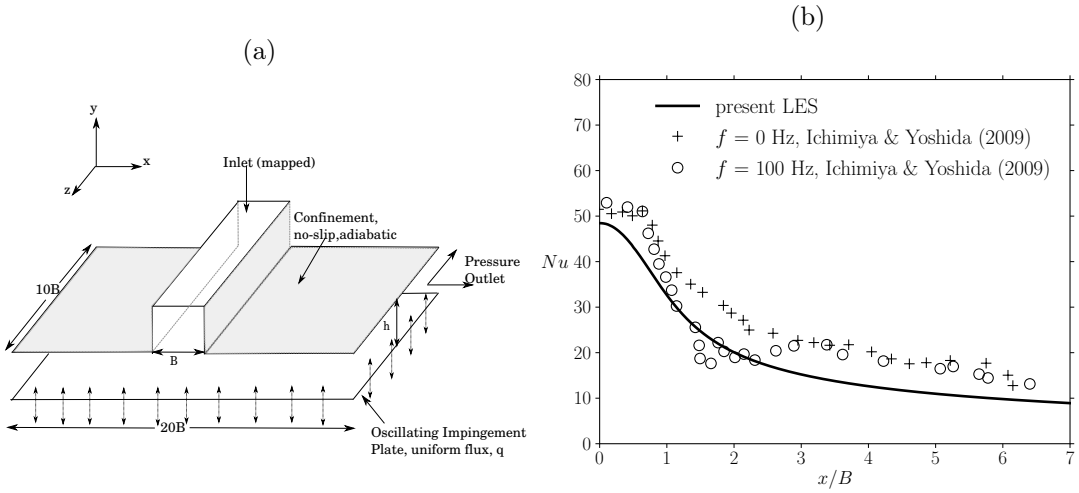

Figure 6.1: (a) Schematic representation of the planar jet impingement configuration with the boundary conditions and the coordinate system used for the simulation, and (b) time-averaged Nusselt number as a function of planar distance x/B. Solid line: present LES at $Re_B = 1{,}000$, $f = 100\,\mathrm{Hz}$; +: Ichimiya & Yoshida[39] at $Re_B = 1{,}000$, $f = 0\,\mathrm{Hz}$; ○: Ichimiya & Yoshida[39] at $Re_B = 1{,}000$, $f = 100\,\mathrm{Hz}$.

A schematic of the computational domain along with the boundary conditions for the planar jet is shown in figure 6.1(a). The domain for the planar jet was discretised with a collocated grid system with the bounds from the origin as $\Omega = [-L_x/2, L_x/2] \times [0, L_y] \times [-L_z/2, L_z/2]$ where $L_x = 20B$, $L_z = 10B$ and $L_y = 8B$, with B as the nozzle width. The non-dimensional distance between nozzle-exit and the impingement wall is $1B$ that is set as the mean position during the vibration. The Reynolds number based on the nozzle width is 1,000 and is defined as $Re_B = V_b 2B/\nu$. The experimental case with vibrating wall frequency of 100 Hz and amplitude of 1.0 mm corresponding to $\zeta = 0.1$ is chosen. The wall was supplied with a uniform heat flux of $q_{unif} = 198\,\mathrm{W\,m^{-2}}$. The domain size and the variables are chosen to match the experimental set-up exactly. The Nusselt number is given as $Nu = hD/k$, where $D = 2B$ with B being the slot width and k the thermal conductivity of the fluid and h is the heat transfer coefficient given by $h = q_{unif}/(T_w - T_0)$, where T_w is the local wall temperature and T_0 is the reference temperature.

The flow at the inlet is generated with the same technique as presented in §5.2.1. The upper boundaries of the domain are confined with an adiabatic wall boundary condition. The exits of the boundary are provided with a mixed boundary condition (similar to the SWJ) which

regulates the flux based on the pressure. On the impingement wall, a moving wall velocity boundary condition is used for the velocity. For the vibration, the frequency and the amplitude are directly specified as input variables to the mesh motion equation. The wall is supplied with a uniform heat flux boundary condition for the temperature. Figure 6.1(b) shows the plot of the time-averaged Nu for a frequency of 100 Hz compared with the experiments of Ichimiya & Yoshida[39]. The static wall case ($f = 0$ Hz) of Ichimiya & Yoshida[39] are also included for comparison. Good agreement is seen between the predictions and the experimental data. The Nusselt number in the stagnation region is marginally under predicted but well within the uncertainty limits of the experiment. With the experiments of Ichimiya and Yoshida, it is interesting to note that the effect of vibration influences the Nu up to a planar distance of $\approx 3B$. However, minor variations are seen in the region $1 < x/B < 3$ between their static and vibrating-wall cases. Additionally, the stagnation region remains unaffected by the induced vibrations for their experiments.

Comparison with the experiments of Wen[40]:

The validation of the circular jet impinging on a vibrating wall against the experiments of Wen[40] is presented here. The impingement wall vibrates at a frequency of 5.02 Hz with an amplitude of 3.6 mm corresponding to $\zeta = 0.1$. Another case with static impingement wall is also simulated and presented alongside for comparison. The Reynolds number of the flow is $Re_D = V_b D/\nu =$ 16,500.

The solution domain is a collocated grid system with Cartesian coordinates, $\mathbf{X} = (x, y, z)$; with 0 is the origin at the center of the domain $\Omega = [0, r] \times [0, L_y]$ where $L_y = 11D$ and the radius, $r = 10D$. This configuration varies from the SWJ in the nozzle-to-wall distance (in this case $5D$), and the Re_D used for computation is 16,500. The distance between the nozzle exit and impingement wall corresponds to the computational domain height in y and is equal to $5D$ when the amplitude of vibration A is zero. The boundary conditions are similar to the SWJ and are the same as in the experimental set-up of Wen[40]. On the moving wall, the boundary conditions are modified to accommodate the mesh movement and heat transfer. The Nusselt number is defined here in terms of the nozzle diameter that is given as $Nu = hD/k$, where k is the thermal conductivity of the fluid and h is the heat transfer coefficient given by $h = q_{unif}/(T_{aw} - T_0)$, where T_{aw} is the adiabatic wall temperature and T_0 is the reference temperature.

The variation of the stagnation-point Nusselt number (Nu_0) with the vibration frequency is shown in figure 6.2. The Nu_0 measurements of Wen[40] show that Nu_0 increased with the

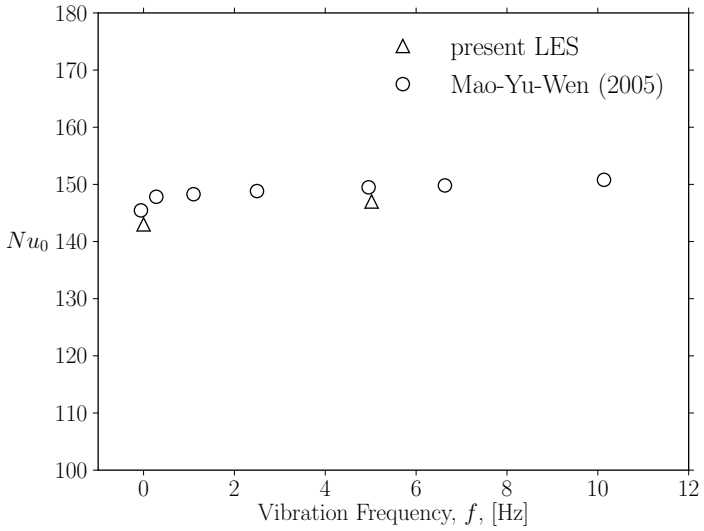

Figure 6.2: Stagnation point Nusselt number, Nu_0 as a function of impingement wall vibration frequency, f. △: present LES at Re_D = 16,500; ○: Wen[40] at Re_D = 16,500.

vibration frequency and an improvement of 3-4% was observed as compared to the static wall case. The present LES results are consistent with the findings of Wen[40]. There is good agreement with the experiments for the low vibration frequencies. Although the configuration examined above is for a vibrating wall circular jet, which is the focus of the present study, the reference work provides inadequate data to use this framework as a baseline for further investigation. Hence, we deem it more useful to introduce vibrations to the impingement wall of the previously investigated SWJ case from § 5.2.1 so that a systematic comparison of static and vibrating-wall cases is attained.

6.2 Vibrating-wall Circular Jet-impingement Configuration (VWJ)

The baseline simulation of a turbulent vibrating-wall circular jet-impingement configuration is now presented. A schematic representation of the configuration along with the boundary conditions is shown in figure 6.3. The following investigations of the baseline vibrating-wall circular jet-impingement configuration are for a Re_D of 23,000 with a mean nozzle-to-wall distance of $1.75D$ with the wall motion within the region of $0 \leq y/D \leq 0.5$ with $y/D = 2$ at the nozzle exit and a vibration frequency of 100 Hz.

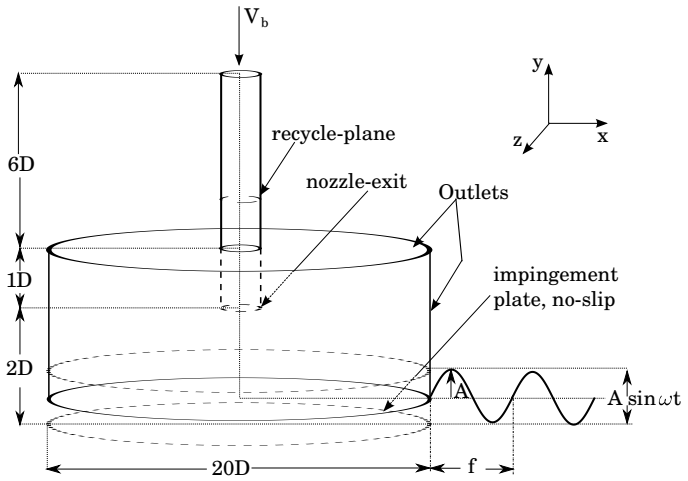

Figure 6.3: Schematic representation of the baseline vibrating-wall circular jet impingement configuration along with the boundary conditions and the coordinate system used for the simulations.

Grid-III, the configuration that produced accurate results in the grid sensitivity study of the static wall jet-impingement is employed herein with relevant changes to the boundary conditions to accommodate mesh motion. The coordinate system followed is similar to that of the SWJ in §5.2.1. The mesh movement was restricted to between $y/D = 0$ and 0.5 with $0.25D$ as the amplitude. All the boundary conditions are similar to that of the SWJ, excluding those of the impingement wall. The wall is set as a moving boundary with a constant heat flux condition for temperature. The amplitude to nozzle-to-wall distance ratio, ζ is 0.14. The simulations are initialized with the LES of the SWJ from § 5.2.1.

6.2.1 Fluid Dynamics

Before analysing the unsteady flow features, it is useful to have an insight into the overall flow field within the domain as a result of the impingement wall vibration. The flow dynamics experience change compared to the conventional flow regimes of an SWJ, due to the periodic mechanical interaction of the wall with the free-jet at varying nozzle-to-wall distances. Figure 6.4 shows the time-mean and phase-averaged results of the SWJ and the VWJ, compared at different axial distances from the nozzle-exit along the radial direction.

In figure 6.4(a), the impingement wall of the VWJ is at its maximum positive displacement, having moved to $y/D = 0.5$ from 0. The normalised time-mean and phase-averaged velocity profiles close to the nozzle exit closely overlap each other, which shows that in regions close to

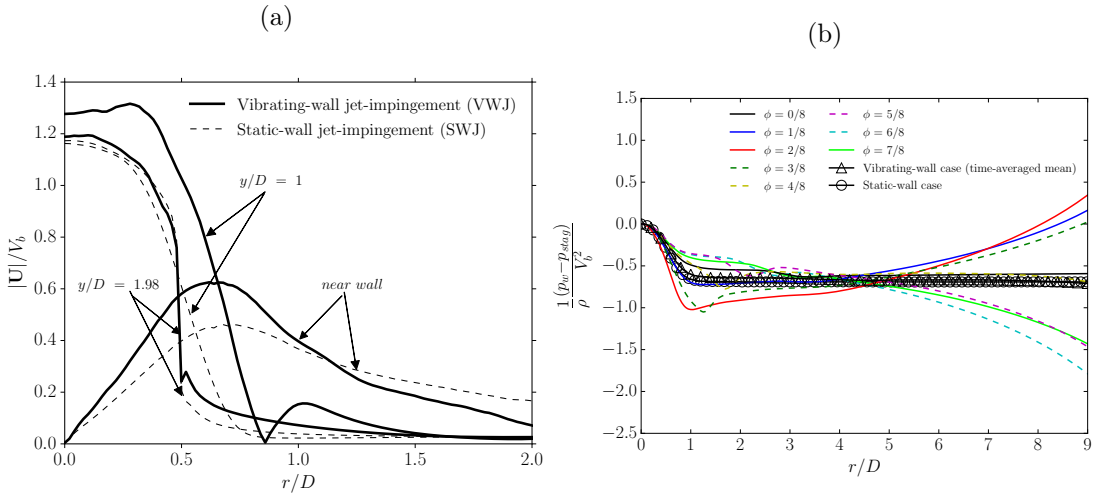

Figure 6.4: (a) Time-mean (SWJ) and phase-averaged (VWJ) velocity magnitude, $|\mathbf{U}|$ normalized by the bulk velocity V_b as a function of radial distance r/D at axial locations, y/D = 1.98, 1 and near-wall. ——: present LES result of the VWJ at Re_D = 23,000; - - - -: present LES result of the SWJ at Re_D = 23,000, and (b) wall pressure as a function of radial location. ——: present LES result of the VWJ during upward movement of the wall; - - - -: during downward movement of the wall; solid line with symbols: Static wall case.

the nozzle-exit (y/D = 1.98), the impact of wall motion for the VWJ is negligible. However, on closer inspection, a short spike at r/D = 0.5 is observed for the VWJ which is at the nozzle boundary edge where the fluid is in contact with the quiescent fluid domain and, as a consequence of the wall motion, the pressure imparted affects the fluid immediately upon exit. On moving further downstream of the nozzle exit, at y/D = 1, the effect of the positive displacement of the wall is observed as a marked increase in the mean velocity. Additionally, there is a translocation in the curve of the VWJ $\approx 0.2D$ indicating that the free-jet at y/D = 1 has expanded in the radial direction. At the near-wall region, the increased velocity is seen until about $1D$ however, the velocity of the VWJ decays faster than its static-wall counterpart.

Figure 6.4(b) shows the pressure profiles on the wall for the static and vibrating wall cases at different phases of wall motion. The typical Gaussian profile is retained for the static wall case. Due to high static pressure in the stagnation region, the favourable pressure gradient drives the flow in the radial direction leading to the formation of the wall-jet. However, for the vibrating case, this characteristic Gaussian profile is altered due to the wall motion. Due to the sinusoidal variation in the movement of the impingement surface, a wider spread in the pressure distribution is seen. During the upward movement of the wall, the gradient is high in the stagnation region meaning the velocity is substantially higher in the stagnation region

compared to the rest of the domain. The increased shear and velocity are seen until about r/D = 4.5, and then the gradient gradually decreases which is seen as a reduction in the velocity of the wall-jet beyond the stagnation zone. During the downward movement of the wall, the gradient is higher beyond the stagnation zone where velocity increase is observed.

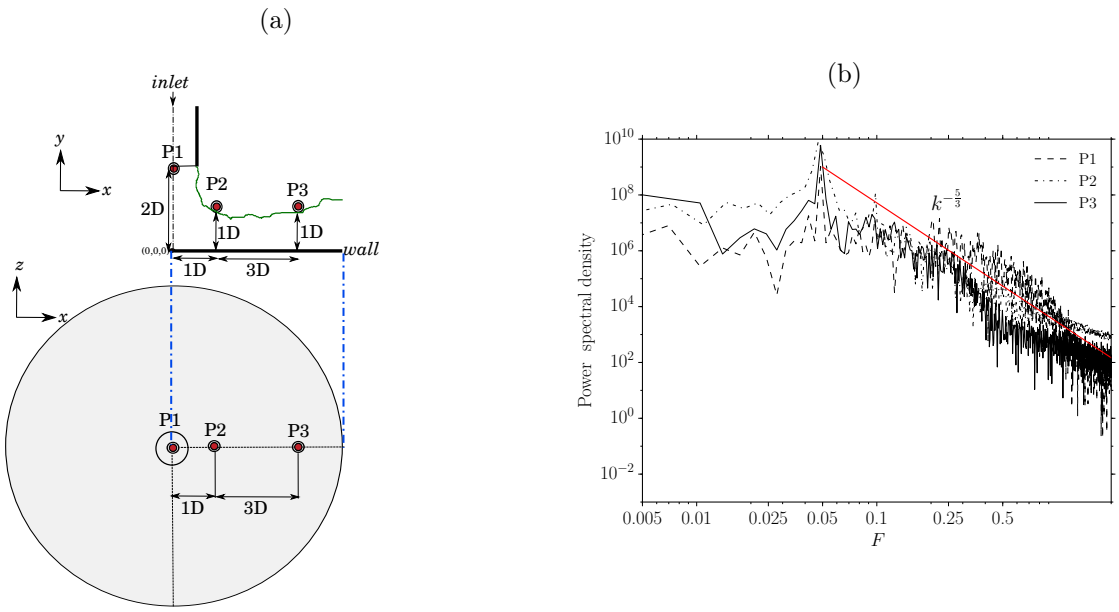

Figure 6.5: (a) Schematic representation of the domain in x-y and x-z planes showing the location of the diagnostic points used for recording velocity signals, and (b) power spectral density as a function of dimensionless parameter F for the recorded instantaneous velocity signals in the domain. - - - -: Point-1; — · — · —: Point-2; ——: Point-3.

Figures 6.4(a) and (b) clearly indicate that the impingement wall vibration has an impact on the mean flow field, and thus requires a more detailed analysis. Phase-averaged/ensemble-averaged information along the required phases of the sinusoidal impingement-wall motion is useful in giving a general insight into the flow field. Therefore, the frequencies of the system need to be analysed since it is necessary to choose the right time scales for observation and ensemble-averaging in a system undergoing periodic change. The frequency characteristics of a system are represented by the Strouhal number defined as $St = fL/U$, where L and U are the lengths and velocity scales respectively; however, the choice of the length scale is not straightforward since it varies due to the vibration. The dimensionless parameter $F = fA/V_b$, which is a modification of the Strouhal number is used following Wen[40] which relates the vibrational frequency, f and the amplitude of vibration, A.

The intrinsic time scales of the observation or ensemble-averaging have to be less than

or equal to the time scales of flow. In the present configuration, the observed frequency of the flow field f_{jet} has to be lower than or equal to the wall vibration frequency, f, to enable the use of the period of wall vibration as the preferred time scale of observation. Diagnostic points were placed at different locations in the domain of the VWJ as shown in figure 6.5(a) to acquire instantaneous velocity signals at every time-step. Point–1 (P1) was located close to the nozzle-exit (at $y/D = 1.98$ and $r/D = 0$) to verify whether the wall vibration influences close to the inlet, Point–2 (P2) was located in the shear layer (at $y/D = 1.0$ and $r/D = 1.0$) and Point–3 (P3) was located further away from the stagnation region (at $y/D = 1.0$ and $r/D = 4.0$) and into the wall-jet.

The power spectral density of the acquired signals are plotted against the dimensionless parameter F in figure 6.5(b) with the $k^{-\frac{5}{3}}$ slope. All the digitised points exhibit a peak at $F = 0.049$ that correspond to a frequency of 100 Hz. Since the applied frequency of wall-vibration ($f = 100$ Hz), is the dominant frequency in the flow field, the vibrational time scale is preferred for the ensemble-averaging. Data acquisition is performed for 8 phases or wall positions in one period of vibration. The phase-averaging is carried out for typically over 15 periods of wall vibration. The phase-averaged results are presented as phases, $\phi = 0/8$ through $7/8$.

Phase-averaged Statistics

The phase-averaged statistics are presented for all the phases ($\phi = 0 \rightarrow 7/8$) of the impingement wall motion. The phase, $\phi = 0/8$ corresponds to the impingement wall position at $y/D = 0.25$, displaces vertically upward attaining the maximum positive displacement at $\phi = 2/8$ ($y/D = 0.5$). The impingement-wall descends through phases, $\phi = 3/8$, $4/8$ and $5/8$ before reaching the phase, $\phi = 6/8$ corresponding to the maximum negative displacement ($y/D = 0$). At $\phi = 6/8$, the VWJ resembles the configuration of the SWJ having a similar nozzle-to-wall spacing of $2D$. Thus, the comparisons with the SWJ are made for this phase alone, and the SWJ results are indicated by dashed lines if presented. The individual phase is indicated at the top of each sub-plot and a marker showing the position of the impingement wall on one vibration period is also shown.

The profiles of phase-averaged mean centre line ($r/D = 0$) axial velocity normalized by the bulk velocity is shown in figure 6.6(a). During the positive displacement of the wall, a negative velocity is seen close to the impingement wall unlike the SWJ due to the moving wall contacting the potential jet core. Although the turbulent jet core is not likely to be completely formed under the present condition where the nozzle-to-wall spacing is less than $2D$, and induced wall

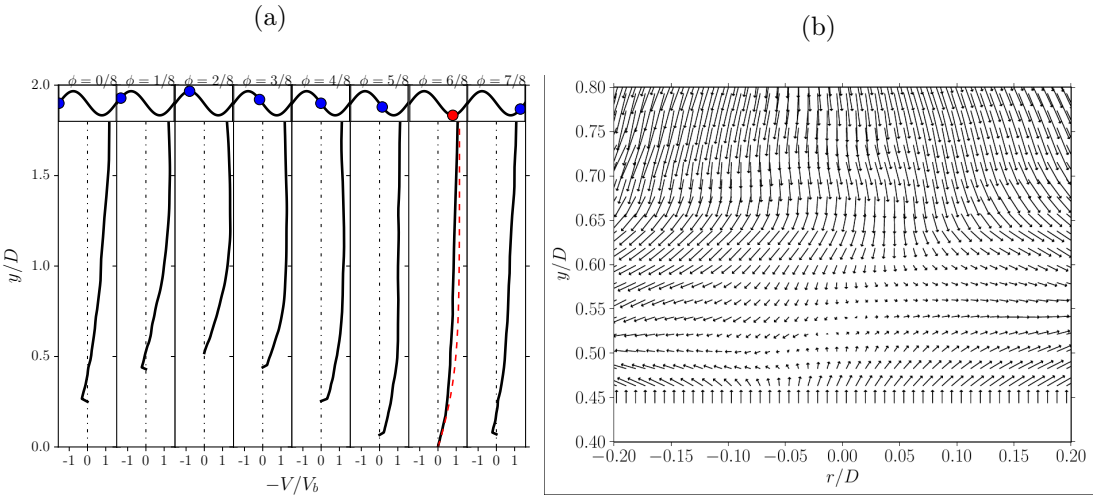

Figure 6.6: (a) Phase-averaged mean axial velocity V normalized by the bulk velocity V_b at $r/D = 0$ for phases $\phi = 0/8$ through $7/8$. ——: present LES result of the VWJ at $Re_D = 23{,}000$; - - - -: present LES result of the SWJ at $Re_D = 23{,}000$; ●: location of the impingement wall in a period of vibration, and (b) visualization of instantaneous near-wall velocity vectors for the present LES of the VWJ at $Re_D = 23{,}000$ and at phase, $\phi = 1/8$, showing reverse flow at $y/D \approx 0.45$-0.55.

motion shortening the potential core length even further, the centerline axial velocity is clearly affected causing a change in the point of inflection. Since the distance required for the jet core to develop is restricted, the vertical component of the momentum from the jet is imparted to the wall. This can be seen in the velocity vectors as shown in figure 6.6(b). The map of velocity vectors in the stagnation region is shown for the VWJ at $\phi = 1/8$ where the vectors are convected away radially and axially from the wall. Reverse flow is seen up to axial distance of $y/D = 0.55D$ for the region between $r/D \pm 0.1$.

As the impingement wall traverses vertically to the maximum positive displacement at phase, $\phi = 2/8$, the change in the point of inflection on the mean axial velocity curve disappears as no further energy from the wall is imparted into the free-jet. When the impingement wall descends ($\phi = 3/8$, $4/8$, $5/8$), the curvature is restored and it assumes the conventional shape. This reappears at phase, $\phi = 7/8$ since the impingement wall begins to displace positively again. This interactive effect is greatest in the jet core where the maximum positive displacement of the wall occurs. On moving radially downstream from the stagnation region ($> r/D \approx 0.5$), this collision effect disappears as seen in figure 6.7.

The fluid accelerates after impingement and spreads radially leading to the formation of

the wall-jet. At $r/D = 1$, the wall-jet has its maximum speed in the near-wall region during the positive displacement of the impingement wall as shown in figure 6.7. However, due to viscous effects, there is a phase lag, and the maximum velocity occurs at $\phi = 3/8$ as opposed to $\phi = 2/8$. The maximum velocity then decreases upon the descent of the wall, owing to mass conservation. It is interesting to note that the velocity magnitude for the SWJ is higher than that of the VWJ. This is because the point of comparison is made at the lowest point of the vibrating impingement-wall stroke. Instead of the mean position, $y/D = 0.25$, the maximum speed of the SWJ lies between the values for the upstream and downstream strokes. The high local velocity created at the beginning of the wall-jet gains no further momentum and starts to decay as the wall descends. The time scales of the vibration are much higher compared to the flow time scales; thus, the generated high velocity of the wall-jet is seen to reduce as the impingement wall approaches its lowest point, at $y/D = 0$.

The above holds until the radial distance of $r/D = 2.0$ (figure 6.7(b)). The phenomenon of velocity increase upon ascent and decrease, or compensation during descent is altered on moving radially downstream into the wall jet region. The maximum velocity in the wall-jet now occurs when $\phi = 5/8$ at $r/D = 2.0$ and when $\phi = 6/8$ at $r/D = 2.5$. The increased local acceleration of the fluid from $r/D < 1$ is realised at different phases of the wall motion at differing radial locations. At $r/D = 2.5$ (figure 6.7(c)), the velocity of the VWJ ($\phi = 6/8$) is higher compared to the SWJ. Because of the variation in the time scales, the effect or the decay of the increased local acceleration is observed after the wall begins to descend, thus creating a higher wall-jet velocity at distances beyond $r/D = 2.0$ (figure 6.7(c)). However, the maximum velocity for both the SWJ and VWJ are at the radial location $r/D = 1$.

The phase-averaged r.m.s of the radial velocity fluctuations at $r/D = 1.5$ and 2.5 are presented in figure 6.8 (a) and (b) respectively. The radial u_{rms} values exhibit the influence of wall motion very strikingly with an increase in the level of r.m.s velocities across the wall-normal direction. This increase is even noticeable on moving radially downstream from the stagnation region. The effect of wall motion influences the velocity fluctuations in the axial direction beyond $0.4D$ from the wall that is not seen in the case of an SWJ. These increased radial fluctuation levels characterise the unsteadiness brought about by the meandering jet as a result of wall motion. The characteristic double peaks seen in the SWJ are no longer observed in the VWJ.

The turbulence production is shown for phases $\phi = 2/8$, $4/8$, $5/8$ and $6/8$ in figure 6.9. The results are compared with the static wall case results at the same radial locations. The acceleration and deceleration of the wall-jet reflected as an increase and decrease in the turbulence production are seen. The maximum turbulence production is almost twice that of the static wall

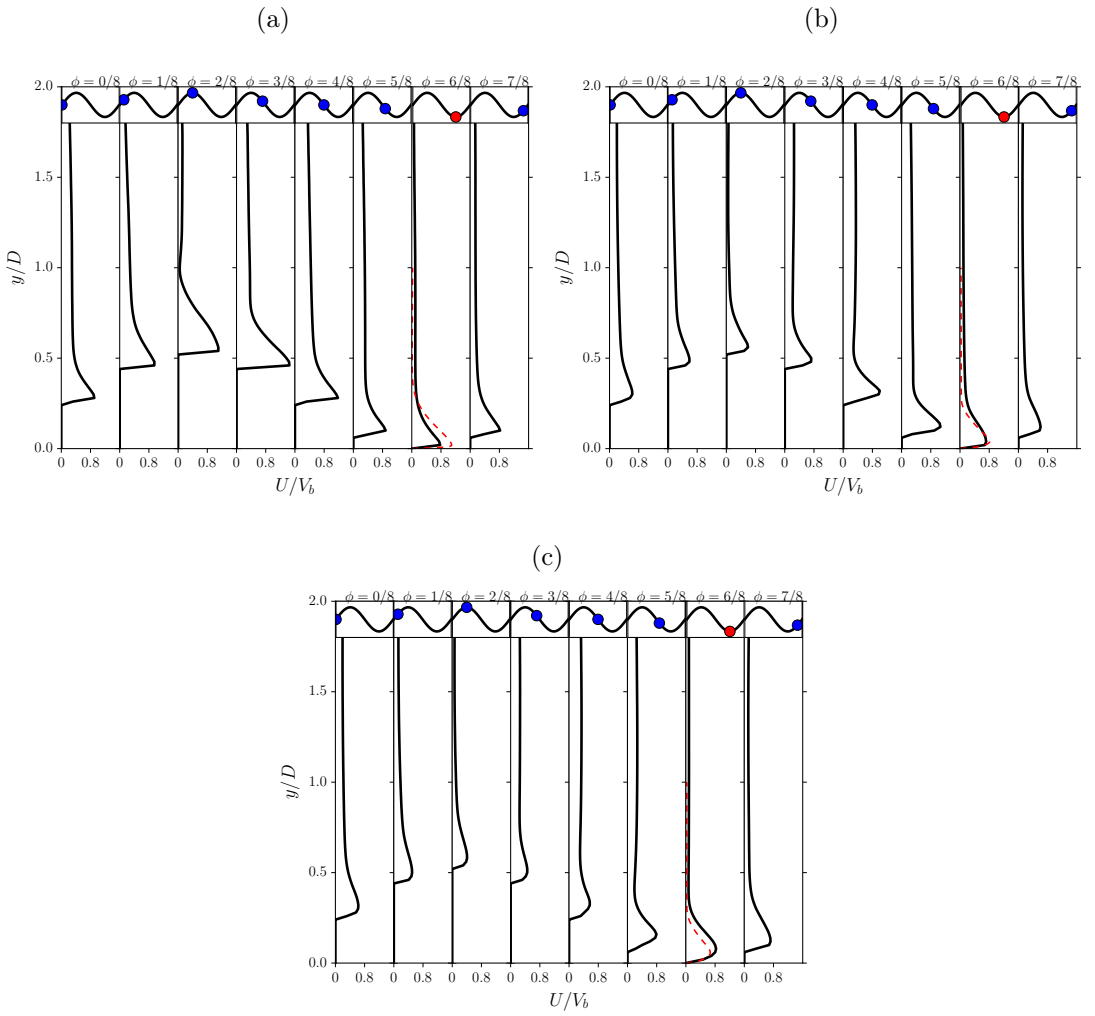

Figure 6.7: Phase-averaged mean radial velocity U normalized by the bulk velocity V_b at (a) $r/D = 1.0$, (b) $r/D = 2.0$, and (c) $r/D = 2.5$ for phases $\phi = 0/8$ through $7/8$. ——: present LES result of the VWJ at $Re_D = 23{,}000$; - - - -: present LES result of the SWJ at $Re_D = 23{,}000$; ●: location of the impingement wall in a period of vibration.

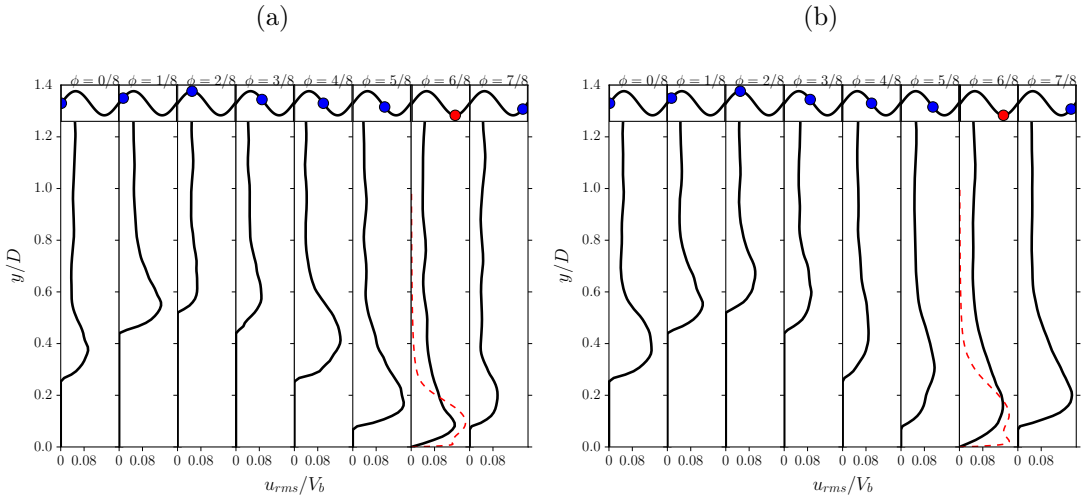

Figure 6.8: Root mean square of radial velocity u_{rms} normalized by the bulk velocity V_b (a) at $r/D = 1.5$ (b) at $r/D = 2.5$ for phases $\phi = 0/8$ through $7/8$. ——: present LES result of the VWJ at $Re_D = 23{,}000$; - - - -: present LES result of the SWJ at $Re_D = 23{,}000$; ●: location of the impingement wall in a period of vibration.

case at $r/D = 1.5$ (at $\phi = 4/8$) while the near wall peak becomes even stronger in the vibrating case. This is due to the high shear caused by the flow, and the moving wall adds energy to the mean flow. It is also interesting to note that this maximum appears at the same radial location for both static and vibrating cases. The viscous diffusion term ($\mathcal{D}_k$) has very low values and did not undergo any significant changes; hence this data is not included.

Vortical Structures and Heat Transfer

The thermal signatures on the impingement wall are presented using Nusselt number profiles. The phase-averaged Nusselt number, Nu_ϕ is given as,

$$Nu_\phi = \int_0^t \frac{1}{\Delta t} Nu(\phi, t) dt \tag{6.2}$$

where ϕ represents the phase of the wall motion for which averaging was performed. The time-averaged Nusselt number, Nu_{avg} is derived to quantify the total effect of the impingement wall vibration on heat transfer and hence averaged over all the phases and is given as,

$$Nu_{avg} = \int_0^\phi \frac{1}{\Delta \phi} \int_0^t Nu(\phi, t) dt d\phi \tag{6.3}$$

The phase-averaged Nusselt number profiles on the impingement wall for the VWJ are shown in figure 6.10(a) at phases, $\phi = 0/8 \rightarrow 7/8$. The figure illustrates the unsteadiness in the

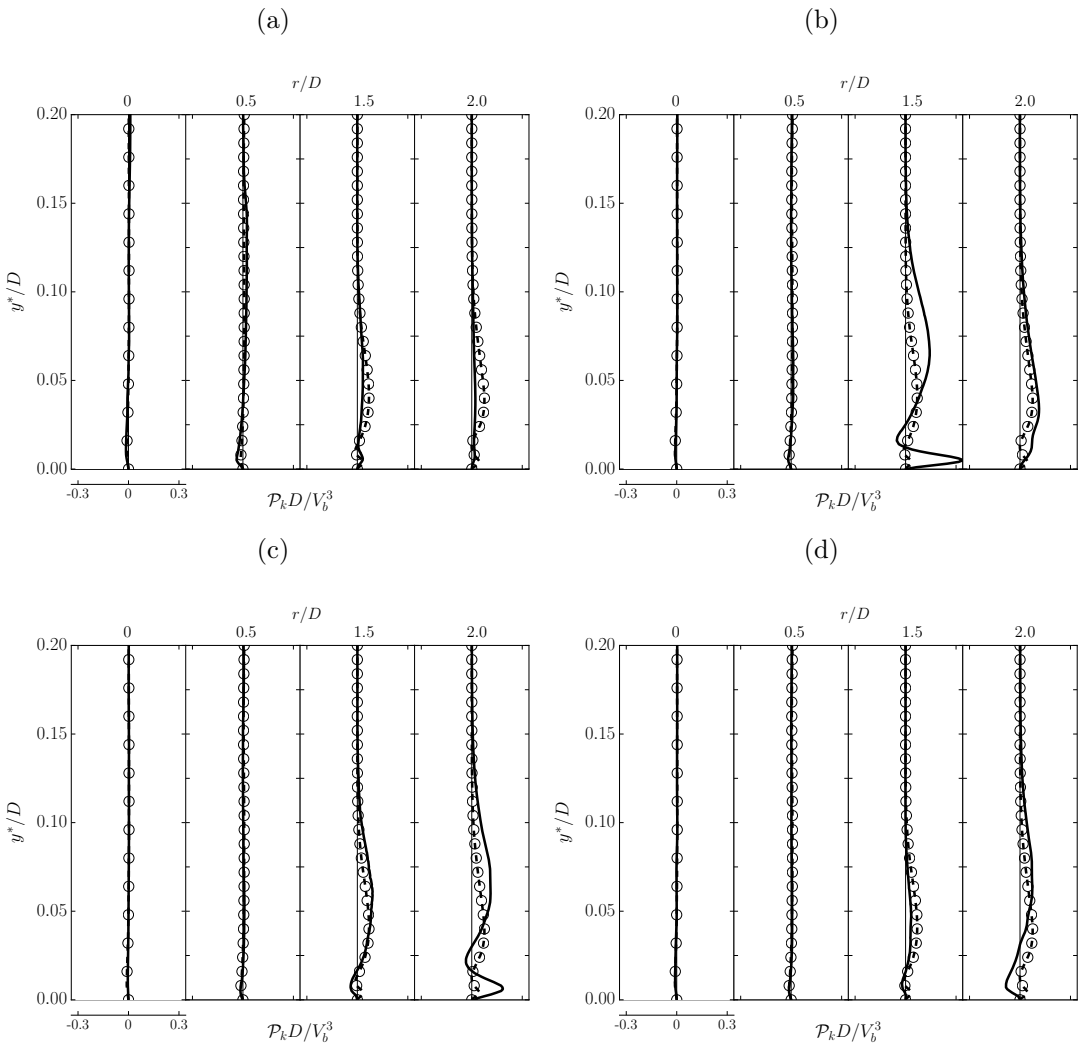

Figure 6.9: Production of Turbulence kinetic energy at different radial locations during phases of wall motion (a) $\phi = 2/8$ (b) $\phi = 4/8$ (c) $\phi = 5/8$ and, (d) $\phi = 6/8$ compared with the present LES of static wall case (dashed line with open symbols).

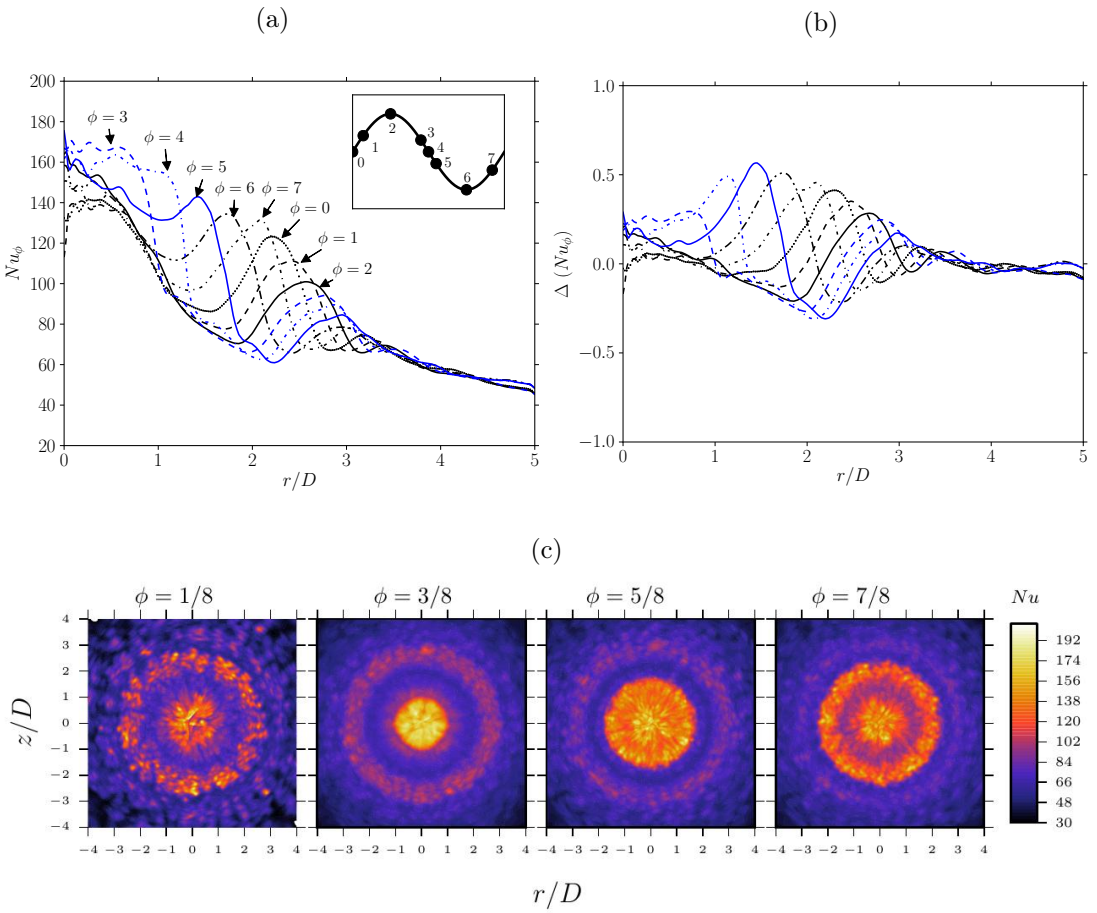

Figure 6.10: (a) Phase-averaged Nusselt number Nu_ϕ on the impingement wall of the VWJ as a function of radial distance r/D for phases, $\phi = 0/8$ through $7/8$. $\cdots$:$\phi = 0/8$; - - - -: $\phi = 1/8$; ——: $\phi = 2/8$; - - - - (blue): $\phi = 3/8$; $-\cdot-\cdot-$ (blue): $\phi = 4/8$; —— (blue): $\phi = 5/8$; $-\cdot\cdot-$: $\phi = 6/8$; $-\cdot-\cdot-$: $\phi = 7/8$; ●(inset): location of the impingement wall in a period of vibration and the corresponding numbers indicating phases, (b) Phase-averaged Nusselt number ratio $\Delta(Nu_\phi)$ as function of radial distance r/D for the VWJ at $Re_D = 23{,}000$ for phases $\phi = 0/8$ through $7/8$. (for legend refer figure 6.10(a)), and (c) visualization of the jet-impingement wall for the VWJ at $Re_D = 23{,}000$ with contours of intantaneous Nusselt number Nu for phases $\phi = 1$, 3, 5 and $7/8$.

flow field through the range of Nu_ϕ vibrations observed at each phase ϕ. However, the spread of the oscillations narrows with increasing radial distance and at $r/D = 3.0$, the fluctuation levels among the phases fall within $\pm 1\%$ indicating that the wall vibration effects become negligible beyond this radial distance. Within the region of interest $r/D < 3.0$, two striking features are observed. First, at the stagnation region, increased rate of heat transfer is observed only after the wall has reached its maximum positive displacement and begun to descend. This region is highly phase time-dependent as there is constant change in the momentum of the fluid impacting the wall. Secondly, periodic shifts in the location of the secondary maximum of Nusselt number are observed. As the wall moves upwards, the secondary Nusselt number peak moves radially outward and the location of the peak is related to the large vortical structures. The location of the dominant vortical structures matches the location of the secondary Nu peaks. Due to the radial fluid acceleration, the vortical structures create strong shear on the impingement wall resulting in a wall renewal effect causing an increase in local heat transfer.

As the impingement wall undergoes positive displacement in the wall-normal direction, it is in contact with the primary vortices generated due to the shear between the free-jet and the quiescent fluid. The flow upon impingement moves downstream interacting unsteadily with the wall resulting in the formation of the secondary vortices. As the wall undergoes a negative displacement, the time scales are such that the formed primary and secondary vortices move radially downstream altering the radial location of the secondary Nu peak. Because of the impingement wall motion and the relative velocity of the wall imparting additional acceleration to the fluid, the strength and location of the secondary vortices are affected which is seen as increase and decrease in the peak value of the secondary Nusselt number peak. As the secondary vortex moves along the radial direction, it removes the heat from the wall and in the process enables the inflow of colder fluid and therefore increasing the thermal boundary layer thickness upstream of the secondary vortex and hence a dip before the outer Nusselt number peak.

Figure 6.10(b) shows the variations in heat transfer relative to the SWJ, visualized by using ΔNu_ϕ, given by the expression $\Delta Nu_\phi = (Nu_\phi - Nu_{swj})/Nu_{swj}$ where Nu_ϕ is the phase-averaged Nu and Nu_{swj} is the time-mean Nu for the static wall jet-impingement configuration from §5.2.1. Enhancement in heat transfer, seen as positive values of ΔNu_ϕ, experience a maximum at $\phi = 5/8$ due to the SWJ experiencing the dip before its corresponding secondary Nu peak at the same location. The enhancement in heat transfer of the VWJ within the region $r/D \leq 2$ reaches up to 45% compared to the SWJ. However, after this radial distance, there is a substantial drop in the heat transfer rate; This is up to 40% in the heat transfer rate at phase, $\phi = 6/8$ of the wall. It is also interesting to note that the peak heat transfer rates which are higher than those of the SWJ occur during the downward displacement of the wall.

Maps of instantaneous Nusselt number are shown in figure 6.10(c) for different phases. Maximum heat transfer within the region $r/D \leq 1$ occurs at $\phi = 3/8$; this is after the maximum displacement ($\phi = 2/8$) because of the momentum lag due to viscous effects (discussed in § 6.2.1). Since the nozzle-to-wall spacing is reduced during the vibrating period, the momentum imparted by the fluid on the wall is also maximum. During the negative displacement, at $\phi = 5/8$, the momentarily accumulated fluid due to the previously traversed phases, coalesce, and increase the radial distance to which the heat removal is enhanced. Although the maximum Nu at this phase is lower in the stagnation region compared to $\phi = 3/8$, the region of increased Nu expands radially to $r/D \leq 1.5$. After the impingement wall has reached its lowest point and begun to displace positively, at $\phi = 7/8$, the intensity of the Nu in the stagnation region weakens further. These mechanisms are reflected in figure 6.10(a) where increased Nu is seen in regions closer to the stagnation region during the positive displacement.

Figure 6.11 shows the effect of wall movement on turbulence in the near wall region. In each figure, the top panel shows the vortical structures represented as contours of vorticity magnitude, $(\sqrt{\omega_i \omega_i})$, of the instantaneous velocity field and centre panel shows the corresponding Nusselt number distribution and the bottom panel shows the phase-averaged radial Nusselt number. Dashed red lines at radial locations $r/D = 1.5$ and 2.8 are used as markers to highlight the dynamics. It is evident from the figures that due to the wall movement, the near-wall vortical structures of high vorticity are accelerated in the radial direction and correspondingly increase the local Nusselt number causing the secondary Nusselt peak to move radially outward. As the vortical structures move outward, the magnitude of vorticity decreases and correspondingly the hot-spots and the Nusselt number intensity also decreases eventually seen as a decline in the magnitude of the secondary Nusselt number peak.

The time-averaged Nusselt number, Nu_{avg} is shown in figure 6.12(a). It is observed that there is a marked improvement in the heat transfer up to $r/D = 1.5$ when compared to the static wall jet-impingement case. The enhancement in heat transfer is nearly 18% in the stagnation region for the vibrating wall case when compared to the static wall configuration. The increase in heat transfer is compensated by the local unsteadiness created in the boundary layer and unsteady separation. However, this may vary from a reduction of impingement wall vibration frequencies and jet Reynolds numbers enabling smoother vortical sweeps and in turn increased heat transfer without undulation. It is also interesting to note that the amplitude of the secondary peak is decreased. Figure 6.12(a) also shows the range of the phase-averaged Nu_ϕ oscillations.

The thermal boundary layer thickness map superimposed on the contours of $\delta_T{}^\alpha$ is shown

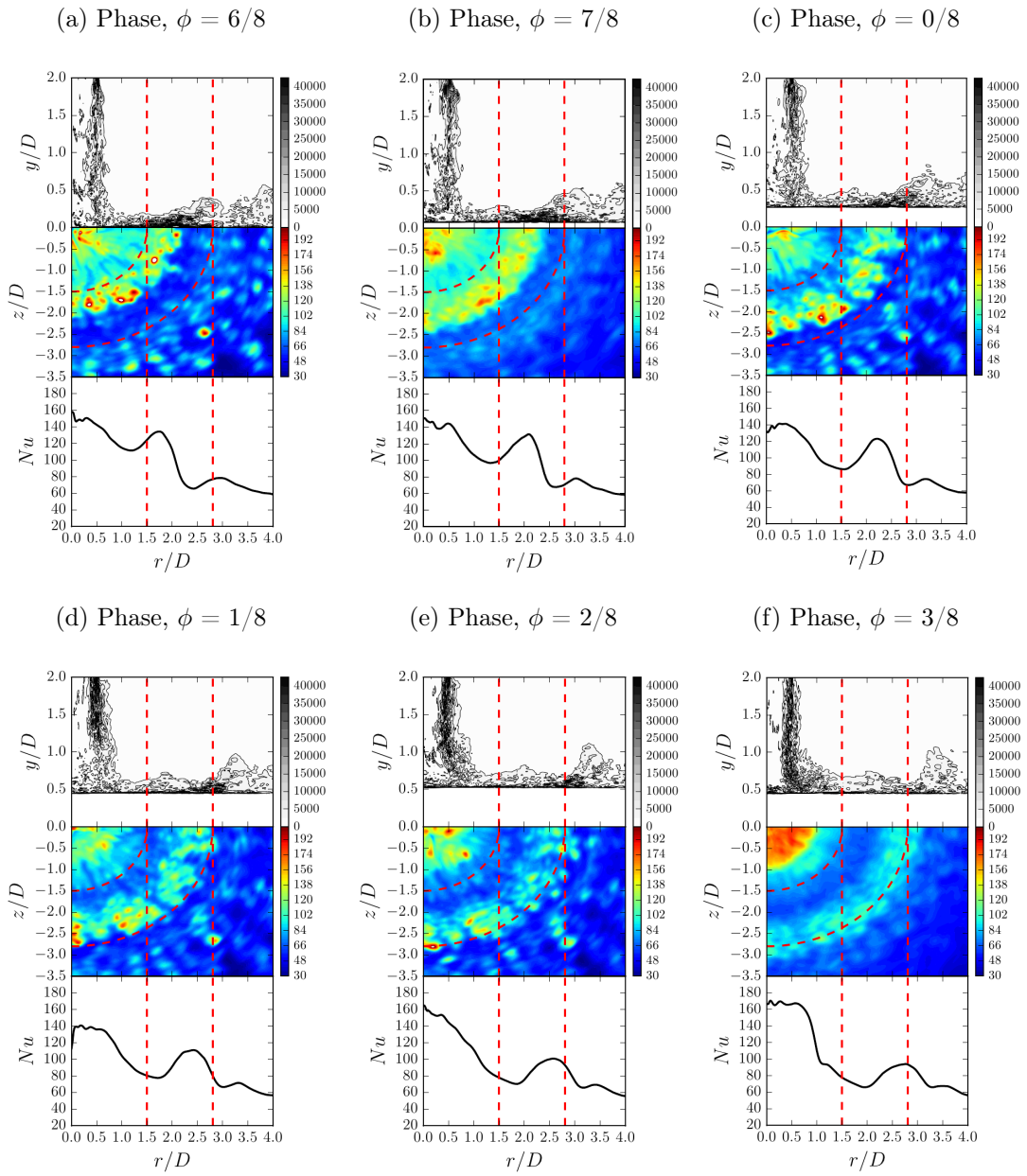

Figure 6.11: Visualization of the VWJ and the effect of wall movement on vortical structures and heat transfer at Re_D = 23,000 over a constant z plane with contours of instantaneous total vorticity magnitude, $(\omega_i\omega_i)^{0.5}$ (top panel), instantaneous Nusselt number distribution (center panel) and phase averaged Nusselt number (bottom panel) at phases, (a) $\phi = 6/8$ (b) $\phi = 0/8$ (c) $\phi = 1/8$ (d) $\phi = 2/8$ (e) $\phi = 4/8$ (f) $\phi = 5/8$. The vorticity contour levels are from 0 to 4.0 $\times$ 10^4 with increments of 5 $\times$ 10^3.

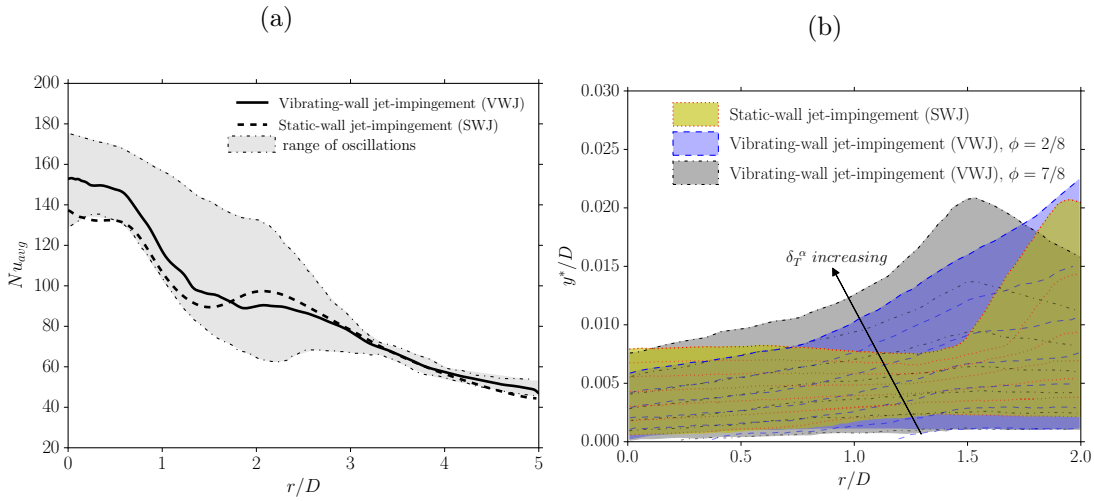

Figure 6.12: (a) Time-averaged Nusselt number Nu_{avg} on the impingement wall as a function of radial distance r/D. ——: present LES result for the VWJ at Re_D = 23,000; - - - -: present LES result for the SWJ at Re_D = 23,000; shaded region: range of oscillations of the phase-averaged Nusselt number Nu_ϕ from the present LES of the VWJ at Re_D = 23,000; and (b) visualization of the thermal boundary layer thickness factor δ_T^α in the near-wall region for Re_D =23,000. $\cdots$: contours of δ_T^α for the SWJ; - - - -: contours of δ_T^α for the VWJ, $\phi = 2/8$; $-\cdot-\cdot-$: contours of δ_T^α for the VWJ, $\phi = 7/8$; The contour levels of δ_T^α are from 0.2 to 0.8 with increments of 0.1 (color shading for the sake of clarity).

in figure 6.12(b). The thermal boundary layer thickness of the VWJ at $\phi = 2/8$ and $7/8$ are compared with the SWJ. The ordinate axis (y^*/D) represents the non-dimensional distance from the wall to enable the comparison of the thermal boundary layer thickness between the SWJ and VWJ configurations with the wall as the reference plane. The contour levels for α used for the map are from 0.2 to 0.8. At $r/D < 0.5$, the thermal boundary layer thickness reaches α = 0.8 at approximately the same distance from the wall (≈ 0.0075) for ϕ=7/8 and the SWJ. At $\phi = 2/8$ (maximum positive displacement of the impingement wall), the thickness of the thermal boundary layer reduces further indicating the higher heat transfer rate in this region. However, the notable difference is in the growth of the boundary layer. The boundary layers for the VWJ ($\phi = 2/8$ and $7/8$) increase in thickness for lower radial distances as compared to the SWJ.

6.3 Effect of Frequency and Amplitude on Fluid Flow and Heat Transfer - Parametric Study

We describe here the influence of varying the forcing parameters (frequency and amplitude of the impingement-wall) to demonstrate the effect they have on fluid flow and heat transfer. The previous section had served to establish a computational model for a turbulent jet impinging upon a vibrating heated wall and then elucidate the dynamics of the system through the inter-relation between momentum and heat transfer. This generated a comprehensive set of results for one set of system parameters and established the foundation for the full parameter space to be explored so that optimum heat transfer and possible control of the localised Nu peaks can be attained for practical applications. For the system parameters used to generate the previous results, the high momentum of the jet means that the wall boundary layer is only moderately affected by the frequency and amplitude of the vibrating wall. Thus, wall vibration may have stronger effects when the momentum of the jet is relatively low. As an attempt to investigate this effect, the present investigations are carried out at the lower Reynolds number, Re_D = 10,000.

The flow structures in the impinging jet have a dominant natural frequency (through mean flow or vortex roll-up) and these tend to impact the impingement heat transfer. Upon induced vibration to the system via an external means (such as the impingement surface vibration) the power spectral density analysis (figure 6.5(b)) show that these large scale structures are excited and correspond to the induced vibration frequency. It is also shown that these large scale structures play a major role in the removal of heat as they impinge and convect radially

Grids	Pipe ($2D < L_y < 9D$, $0 < r < 0.5D$)				Impingement Domain ($0 < L_y < 2D$, $0 < r < 10D$)				Top Free Boundary ($2D < L_y < 3D$, $0.5D < r < 10D$)			
	N_r	N_y	N_θ	Total	N_r	N_y	N_θ	Total	N_r	N_y	N_θ	Total
G-1	147	200	260	7.6×10^6	391	136	260	14×10^6	240	25	260	1.5×10^6
G-2	190	180	640	22×10^6	354	150	400	21×10^6	260	25	640	4.1×10^6

Table 6.1: Grid parameters for the computational domain.

downstream. With this clear information that the large scale structures resonate at the frequency applied in the form of impingement surface vibration, we therefore investigate the effect of varying this frequency and its impact on the flow field and heat transfer. We begin with a brief description of a static jet impingement case at $Re_D = 10{,}000$ to ensure the quality of the mesh, and then proceed to provide a rationale for choosing the magnitude for the forcing parameters. This is followed by the results in the parameter space and the relevant conclusions.

6.3.1 LES of Impinging Jets at $Re_D = 10{,}000$

We first consider the jet-impingement case with the static wall at $Re_D = 10{,}000$. Lower Reynolds number configurations provide an added advantage of reduced mesh size thereby making simulations computationally less intensive. Although the mesh size is not substantially reduced, it still enables a few more simulations in the parameter space thus making it viable for comparison amongst each other. Since the static wall case has been thoroughly investigated in the previous chapter, the purpose of this section is to briefly discuss the key results of the static wall case at $Re_D = 10{,}000$ and then to establish the choice of vibration parameters for the vibrating wall case to understand the Reynolds number effect in such dynamic configurations.

Table 6.1 shows the details of the grids considered. The grids were discretised in a similar way to the grids considered in the static wall case of $Re_D = 23{,}000$. The finest grid was generated with 48×10^6 grid points. Figure 6.13 shows the y^+ values of the two grids considered in Table 6.1. The grid resolution is also compared with the finest grid of Aillaud et al.[155] who performed an LES at $Re_D = 23{,}000$ at a nozzle-to-wall spacing of $y/D = 2.0$. It is seen that the y^+ values are well below 5 in the region of interest and the grid resolution is comparable to that

[155]P. Aillaud et al. *Phys. Fluids*, **28**: 095110, 2016.

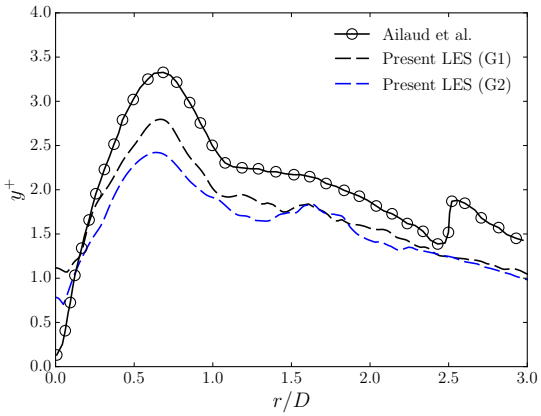

Figure 6.13: y^+ values on the impingement surface as a function of radial distance r/D

of Aillaud et al.[155] Grid G2 was used for the simulations of Re_D = 10,000 for the static wall case as well as the vibrating wall cases presented here. For the static-wall case, the experiments of Lee & Lee[63] are used as a reference. Lee & Lee[63] measured the local heat-transfer rates in the stagnation region with nozzle-to-wall spacings of y/D = 2, 4, 6 and 10 for a Reynolds number ranging from 5,000 to 30,000. The dataset with Re_D = 10,000 and y/D = 2.0 is used for comparisons with the current LES results.

Figure 6.14 shows the base flow of the jet via contours of the mean and fluctuating components for the SWJ at Re_D = 10,000. The mean and instantaneous velocity contours are shown in figure 6.14(a) and (b) where the main regions of the flow are recovered with the LES and exhibit similar features of the SWJ at Re_D = 23,000. In figure 6.14(c) the second order turbulence statistics are shown in the same plane. The change in orientation of the flow upon impingement is reflected as an increase in u_{rms} which reaches a maximum at about r/D = 1.5. The turbulent shear stress profiles of the SWJ are normalised by the square of the bulk velocity, V_b. With increasing radial distance, the value of the negative shear stress tends to increase and is consistent with the established experimental and numerical works.

The instantaneous Nusselt number is visualised through a spatio-temporal map in figure 6.15(a). As witnessed in the high Re_D case of 23,000, the thermal footprints are highly unsteady, and exhibit similar streaks of 'hot' and 'cold' spots along the radial direction. The streaky patterns are such that the maximum occurs close to the stagnation region and moves radially outward with a certain convective velocity. The current LES is again capable of capturing these fine features satisfactorily. Figure 6.15(b) shows the time and azimuthal-averaged radial Nusselt number variation of the static wall case across the radial length of the impingement

[63] J. Lee and S-J. Lee. *Exp. Heat Transfer*, **12**: 137–156, 1999.

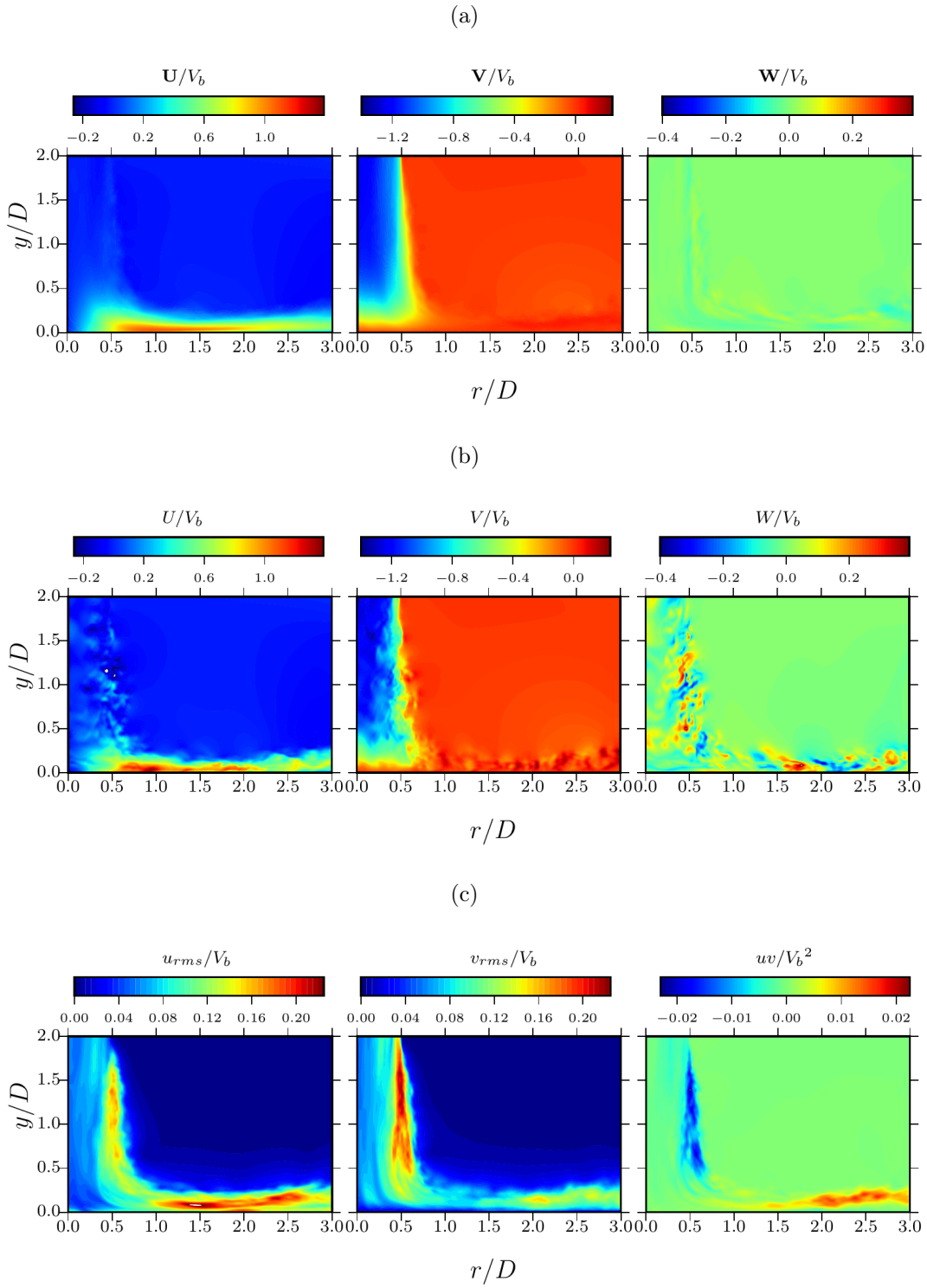

Figure 6.14: Visualisation of circular jet impingement at $Re_D = 10{,}000$ over a constant z plane with contours of mean, instantaneous and fluctuating components.

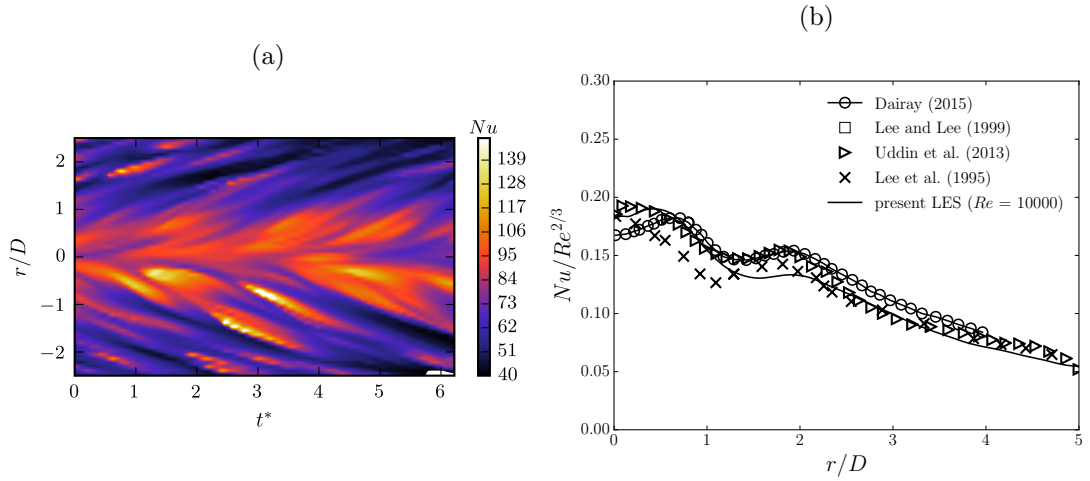

Figure 6.15: (a) Spatio-temporal maps at $Re_D = 10{,}000$ and (b)Time-averaged and normalized Nusselt number, $Nu/Re^{2/3}$ on the impingement wall as a function of radial distance r/D. ——: present LES at $Re_D = 10{,}000$ using Grid-G2; −○−: Dairay et al[27] at $Re_D = 10{,}000$; □: Lee & Lee[63] at $Re_D = 10{,}000$; △: Uddin et al.[83] at $Re_D = 13{,}000$.

wall. The Nusselt number is normalised by $Re^{2/3}$ as discussed in the previous chapter. The stagnation Nusselt number and the secondary Nu peak are predicted with a good agreement, consistent with published experimental and numerical findings.

With the quality of the mesh established through the radial Nusselt number profile, a baseline case in now generated at a low Reynolds number to explore the parameter space.

Choice of Forcing Parameters

The forcing parameters in this configuration are the impingement surface frequency and the amplitude. The nozzle-to-wall spacing imposes the bounds on the choice of amplitudes (i.e., maximum displacement cannot be greater than the nozzle-to-wall spacing). However, the choice of frequency could be in the range of $0 < f < \infty$. Therefore, it is important to choose a set of forcing parameters that interact with the dynamics of the impinging jet. The jet exhibits a fundamental frequency either through vortex roll-up or by the mean flow and this frequency is reported as the dimensionless Strouhal number defined as $St = fD/U$ where *'f'* is the natural frequency of the jet, *'D'* the characteristic length, and *'U'* the characteristic velocity of the system. It may be more reasonable to consider this frequency as a 'basis function' rather than choosing arbitrary frequencies at which to vibrate the impingement surface.

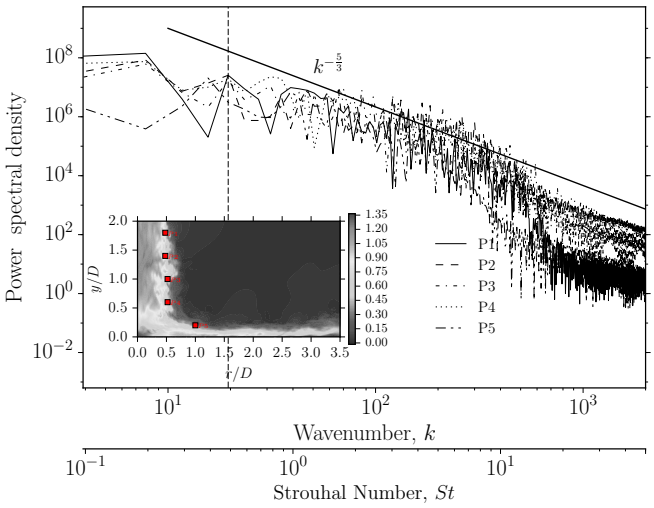

Figure 6.16: Power spectral density as a function of at Strouhal number, St and Wavenumber, k at Re_D = 10,000 for the recorded instantaneous velocity signals in the domain.

Table 6.2 shows the Strouhal number reported for the natural frequency of the jets in previous literature for a similar set-up. The values are predominantly within the range of 0.2–1.4 which is approximately 100 Hz to 720 Hz. The frequency of 100 Hz which is the lowest in the reported values was chosen for the present baseline investigation in order to clearly study the dynamics in the flow field at a low frequency. The Strouhal number corresponding to this frequency of 100 Hz is $St = 0.2$.

The fundamental or dominant frequency of a circular turbulent jet impinging on a static wall is first analysed, now for a jet Reynolds number, Re_D = 10,000 at a nozzle to wall spacing $(y/D) = 2.0$. The frequency of the jet is analysed through instantaneous measurements in the shear layer and the near-wall region and space-time contours of the Nusselt number. Based on this information, the wall vibration frequencies are chosen such that they are sub-harmonic and harmonic to the fundamental frequency of the jet impinging on a static wall. The wall-vibrating cases will have an amplitude of $0.25D$ and $0.125D$ with a mean nozzle-wall spacing of 2.0.

Figure 6.16 shows the power spectrum of the velocity fluctuations extracted at several discrete locations using diagnostic points (P1 to P5) in the shear layer of the jet for a static wall case at Re_D = 10,000. These discrete points are shown in the inset of the figure 6.16. The power spectra show a weak peak frequency corresponding to a Strouhal number, St =0.45 (defined as $St = f_n D/U$ and marked in the figure 6.16 with a dotted line) which corresponds to the natural jet frequency, f_n= 120 Hz. As the flow is fully developed, a single clear dominant frequency is not clearly visible in the spectra. However, this value of Strouhal number (St) is within the

Previous studies	Re_D	y/D	Strouhal Number, St
	Experimental studies		
Crow & Champagne (1971) [23]	10,000 - 130,000	-	0.3
Lui & Sullivan (1996) [158]	12,300	-	1.23/0.61
Han & Goldstein [159]	120,000	1	0.65
Yule [160]	21,000	-	0.6
Gutmark & Ho [161]	7,000 - 82,000	-	0.3 to 0.85
Hwang & Cho [65]	34,000	2-12	1.2
	Numerical studies		
Tsubokura et al. [88]	6,000	10	0.37
Hadžiabdić & Hanjalić [80]	20,000	2	0.64
Dairay et al. [27]	10,000	2	0.4
Chirac & Ortega [162]	750	5	1.1
Hällqvist [79]	20,000	2	1.4/0.7
Chung & Luo [58]	300-1000	4/10	0.2
Uddin et al. [83]	23,000	2	0.328

Table 6.2: Overview of previous experimental and numerical studies with reported natural frequency of jets.

Case	Re_D, [-]	f, [Hz]	A, [-]	Maximum wall speed, $[V_w/V_b]$
Case-I (LFLA)	10,000	60	0.125 D	0.19
Case-II (LFHA)	10,000	60	0.25 D	0.39
Case-III (HFLA)	10,000	120	0.125 D	0.39
Case-IV (HFHA)	10,000	120	0.25 D	0.77

LFLA - Low frequency (60 Hz), low amplitude (0.125 D)
LFHA - Low frequency (60 Hz), high amplitude (0.25 D)
HFLA - High frequency (120 Hz), low amplitude (0.125 D)
HFHA - High frequency (120 Hz), high amplitude (0.25 D)

Table 6.3: Overview of numerical simulations performed along with forcing parameters.

range reported for similar cases.

Hence the wall is excited at the subharmonic frequency of the jet, $(f_n/2) = 60$ Hz and $f_n = 120$ Hz. The cases investigated along with the parameters are shown in Table 6.3.

6.3.2 Flow Dynamics

Figure 6.17 shows the base flow of the jet via contours of instantaneous velocity magnitude normalised by bulk velocity, V_b for $Re_D = 10{,}000$ for the four cases examined at various impingement surface positions ($\phi = 0$, 1, 2, 5 and 6/8). The effect of amplitude and frequency are clearly seen as changes to the flow field. Although the flow field exhibits all the typical regions expected in a canonical jet-impingement flow which are the jet core, the impingement region, and the radial wall-jet region, due to the induced excitation, the flow field appears more chaotic with an increase in amplitude and frequency. The incoming fully developed jet impacts the surface which is also moving in the direction of jet impingement at high speed ($0.77V_b$ for HFHA case) resulting in additional disturbance to the flow field. Low-velocity pockets are seen with an increase in f creating a weak stagnation zone in the axial jet. The corresponding pressure field is also altered.

Earlier in section 6.2.1 it was seen that a negative velocity appeared close to the impingement-wall causing a change in the point of inflection in the centreline axial velocity. This collision effect was seen during the positive displacement of the impingement-wall and reverse flow

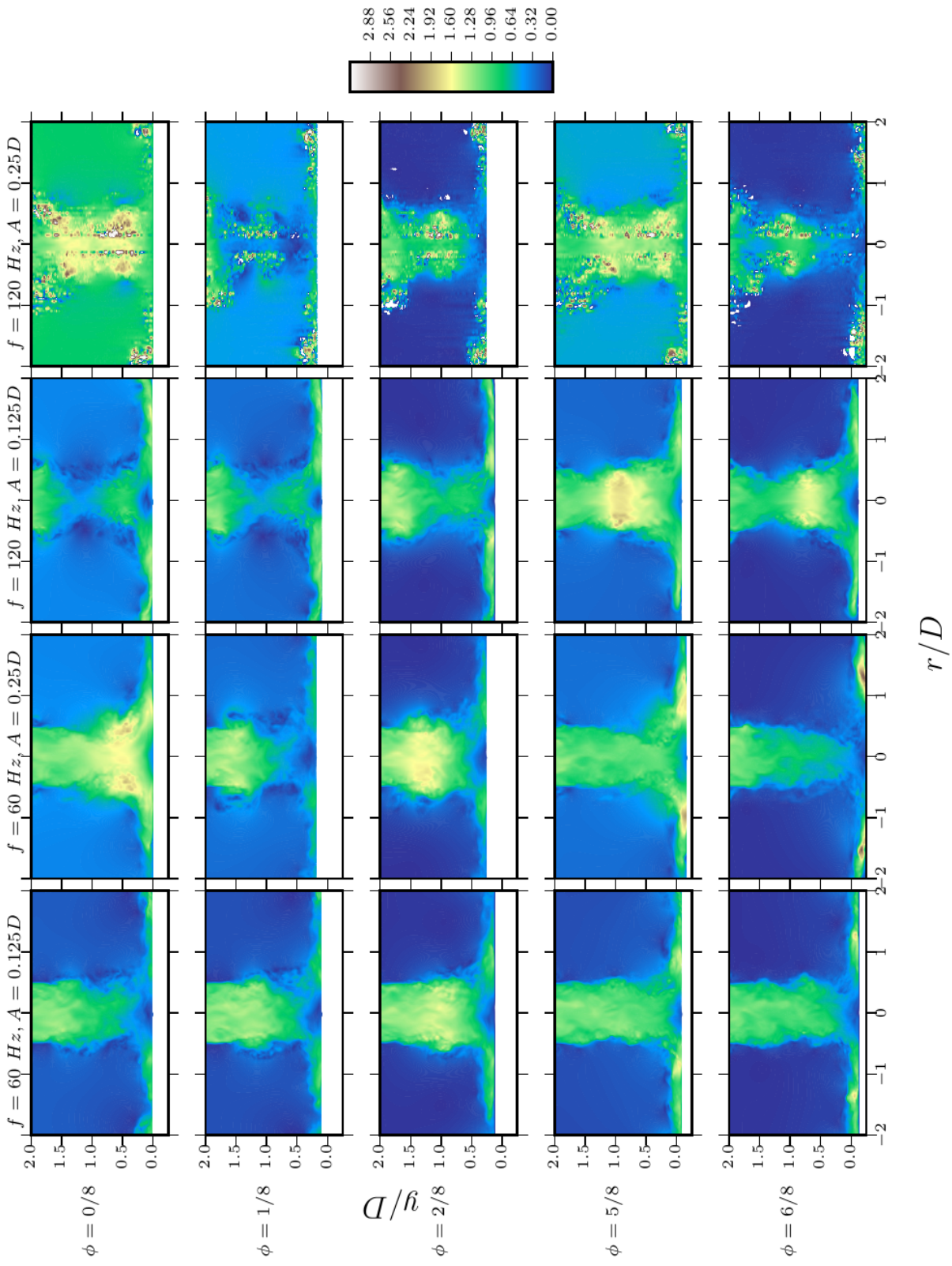

Figure 6.17: Plots of circular jet impingement at $Re_D = 10{,}000$ over a constant z plane as contours of instantaneous velocity magnitude normalized by bulk velocity, V_b for all the four vibrating cases at phases $\phi = 0$, 1, 2, 5 and 6/8.

occurred in the vicinity of the stagnation region. These opposing flows yield a local stagnation flow plane located between the negative axial flow region and the positive axial flow of the jet. This localised stagnation plane has been previously observed for opposing flows in counter jet investigations (see Rolon et al.[163]). Similar stagnation planes are observed for the cases examined and are shown in figure 6.18. The figures show instantaneous velocity vectors on a constant z plane with y^*/D as a function of the radial distance, r/D where y^*/D represents the non-dimensional distance measured from the wall. It is interesting to note that the location of the stagnation plane shifts within a cycle of vibration for a particular case and varies with the change in the magnitude of the forcing parameters. The location of this localised stagnation plane (y/D_{stag}) is analysed in figure 6.19 for all the cases examined.

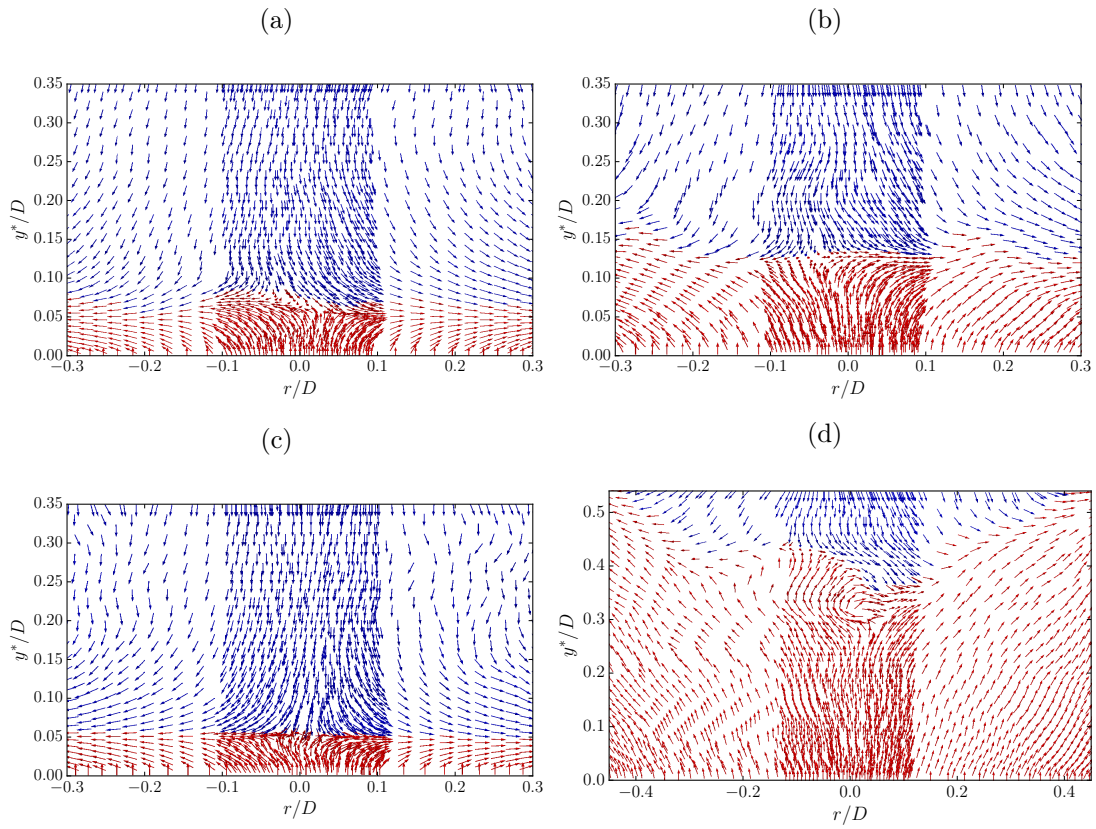

Figure 6.18: Plots of instantaneous near-wall velocity vectors at Re_D = 10,000 with y^*/D as a function of radial distance, r/D for (a) LFLA , (b) LFHA, (c) HFLA, and in (d) HFHA.

The non-dimensional distance up to which the reverse flow is observed, (y/D_{stag}) is plotted as a function of the phase of impingement surface vibration, ϕ for all the four cases. The inset plot shows the location of the impingement-wall and the corresponding phase for clarity. First,

[163]J.C. Rolon et al. *Exp. Fluids*, **11**: 313–324, 1991.

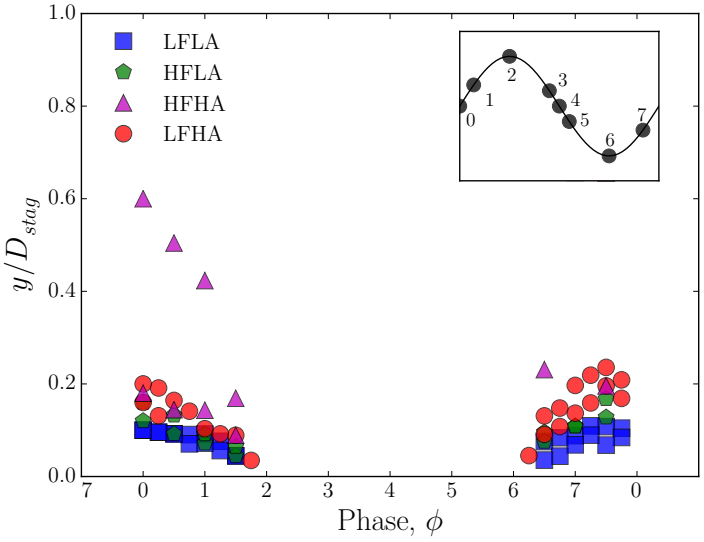

Figure 6.19: Location of the stagnation plane, (y/D_{stag}) as a function of phase, ϕ for the four cases examined at Re_D = 10,000.

the reverse flows occur only when the impingement-wall moves against the direction of the jet (i.e., $\phi = 0/8 \rightarrow 2/8$ and again from $6/8 \rightarrow 2/8$). This effect is observed across the range of parameters examined. Secondly, it can be seen that amplitude has a significant effect in increasing the location up to which the reverse flows occur. For a given frequency, increasing the amplitude alone by a factor of 2, the location of the stagnation plane increases by approximately a factor of 2.

Another notable phenomenon that occurs due to the vibration is the exit of the fluid through the top boundary. The velocity of the fluid leaving the top boundary increases substantially as compared to the static wall case. To illustrate this, figure 6.20 shows the contours of the velocity field and axial velocity profiles for the four cases along the radial direction predicted near the nozzle exit ($y/D = 1.8$). The velocity increases with the increase in magnitude of the forcing parameters. Due to the momentum imparted from the impingement surface, part of the fluid in the shear layer is forced to move towards the top boundary immediately upon the exit from the nozzle. It is also seen that there is a sharp increase in axial velocity towards the top boundary with an increase in the value of forcing parameters. The bulk of the fluid exits closer to the nozzle wall and primarily between $0.5 < r/D < 1.5$. Beyond this region, the velocity is similar for all the cases investigated.

Further downstream, in the free-jet region of the jet, the impingement surface vibration is seen to affect the vortical structures. Figure 6.21 shows the instantaneous vorticity magnitude

$(\omega_i\omega_i)^{0.5}$ in a horizontal plane at $y/D = 1.0$ for all the four cases at the phase $\phi = 0/8$ (mean position). It is interesting to note that despite the increased fluid exit through the top boundary, the 'vortical nests' are seen to appear. However, the effect of amplitude is more pronounced on these vortical structures than the frequency of the impingement surface. When compared to the static wall case, LFLA is the closest with minimal disruption to the vortex ring. Coherent structures are seen to form a ring which is nearly smooth. With the increase in amplitude, the vortex rings appear distorted and highly unstable for the same planar location in the axial jet. For the high-frequency cases, similar patterns repeat although an increase in amplitude substantially modifies the formation of these coherent structures.

(a)

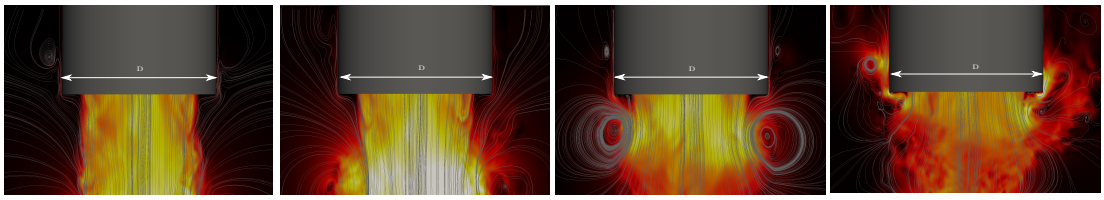

LFLA LFHA HFLA HFHA

(b)

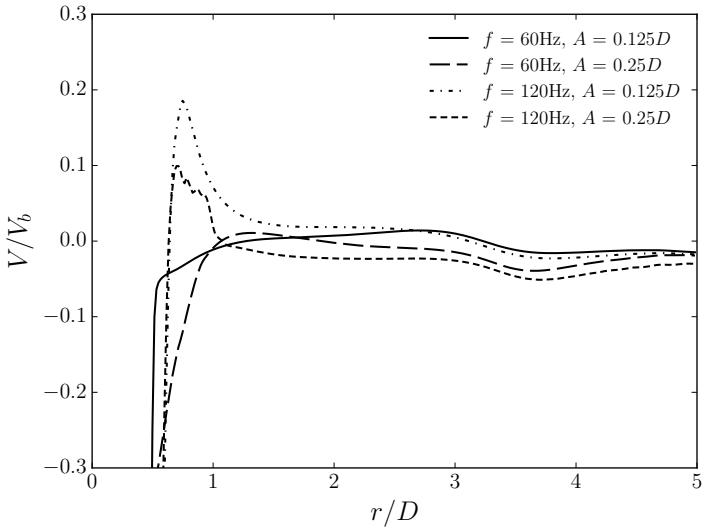

Figure 6.20: Visualisation of the changes near the nozzle through (a) contours of instantaneous velocity, and (b) axial velocity V normalised by the bulk velocity V_b as a function of radial distance.

Upon impingement, it is possible that the vortical structures are preserved for the LFLA case despite the impingement and the induced surface vibration. From figure 6.22 it is seen

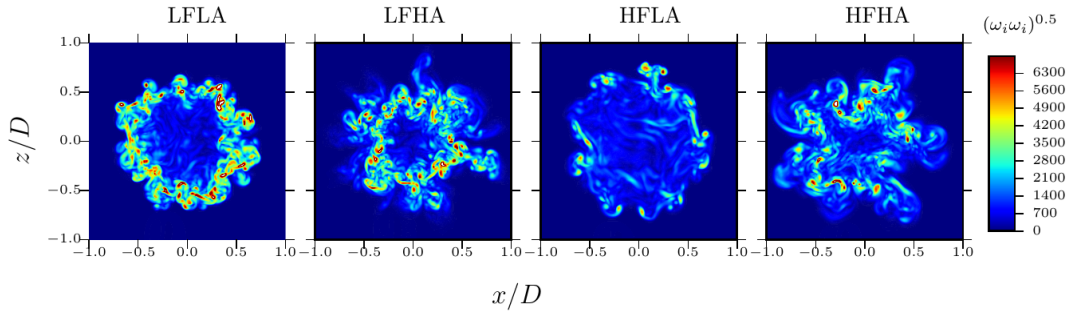

Figure 6.21: Visualisation of circular jet impingement at $Re_D = 10{,}000$ over a constant z plane with contours of instantaneous vorticity magnitude $(\omega_i\omega_i)^{0.5}$ in a horizontal plane at $y/D = 1.0$ in the free jet zone.

that both the primary and secondary structures are clearly captured after these structures have been deflected by impingement. The counter-rotating secondary vortices are seen to create a local wall separation region in turn leading to a local temperature increase. These organised structures are however not clearly detected in the HFHA case. All the cases apart from the HFHA case, show the presence of these structures. It is possible that these secondary vortices are too weak to sustain a clearly organised structure due to significantly high impingement surface speed.

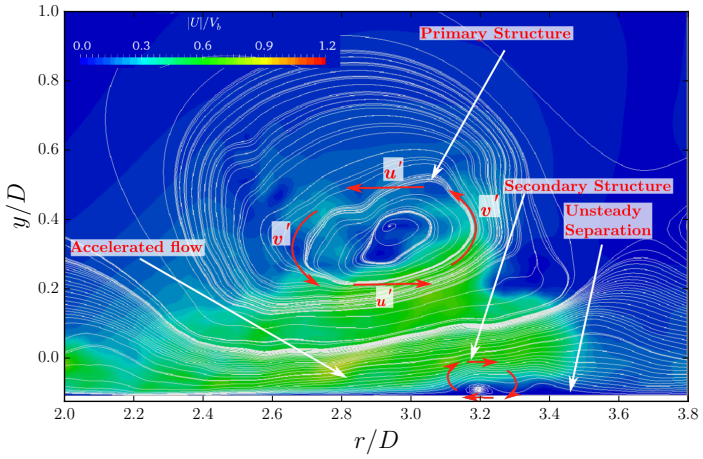

Figure 6.22: Streamlines along with the temperature on the θ plane showing the primary and secondary structures.

Vortex dynamics The large coherent structures are identified and their trajectory is tracked through instantaneous vorticity contours for a complete cycle of vibration as shown in

figure 6.23. A large primary vortical structure, Ω 1 (region of $(\omega_i\omega_i)^{0.5}_{max}$), is seen to emanate from the lip of the nozzle, interact with the quiescent fluid on traversing axially downward and impinge on the surface between phases, $\phi = 4/8$ and $6/8$. Closer to the impingement, Ω 1, convects radially outward and attains maximum vorticity at approximately $r/D = 1.5$. At this point, a counter-rotating secondary vortex is seen below the primary vortical structure located slightly in front of the primary structure, Ω 1. This region of primary and secondary vortex interaction is shown in the inset of the figure 6.23 where the negative vorticity is coloured by red dashed lines indicating counter rotation. As the primary and secondary vortices convect outwards, the size of the secondary vortex increases and eventually leads to a local unsteady separation. A new primary vortical structure, Ω 2, is also seen to be initiated as the impingement surface nears the end of a vibration cycle. This vortex shedding is periodic and continues to repeat for every cycle of impingement surface vibration.

In section 6.2 it was seen that the large scale structures resonate with the applied frequency of the impingement surface. It is perhaps the above mentioned process that results in periodic vortex roll-up that is in-phase with the applied frequency of vibration. Figure 6.24 shows the trajectory of the primary and secondary vortices and their location as a functions of the nozzle-to-wall spacing and the phase, ϕ. The impingement surface behaves like a *'piston'* that enables the periodic vortex roll-up based on the frequency applied to the impingement surface. Similar large scale structures have also been observed in experiments[71,91,164] and numerical investigations[80,86].

The flow structures are further analysed in the impingement region, the contours of velocity magnitude superimposed with iso-lines of λ_2-criterion[165] are shown in figure 6.25 at three different phases of wall vibration, $\phi = 6/8$ (maximum negative amplitude), $\phi = 0/8$ (mean) and $\phi = 2/8$ (maximum positive amplitude). The plane shown is located at a small distance of $0.05D$ above the impingement surface for all the cases shown.

Large patches of high velocity, approximately circular in shape, are seen in the region $r/D < \pm 2$. These high velocity patches are seen to be strongly asymmetrical which perhaps indicates the role of large scale structures impacting the surface at an angle of incidence and being modified due to the impingement surface vibration. This is most clear in the HFHA

[71]S. Roux et al. *Int. J. Heat Mass Transfer*, **54**: 3277–3290, 2011.
[91]C.O. Popiel and O. Trass. *Exp. Therm. Fluid Sci.*, **4**: 253–264, 1991.
[164]P. Grenson et al. *Int. J. Heat Mass Transfer*, **102**: 801–815, 2016.
[80]M. Hadžiabdić and K. Hanjalić. *J. Fluid Mech.*, **596**: 221–260, 2008.
[86]W. Rohlfs et al. *Int. J. Heat Mass Transfer*, **55**: 7728–7736, 2012.
[165]J. Jeong and F. Hussain. *J. Fluid Mech.*, **285**: 69–94, 1995.

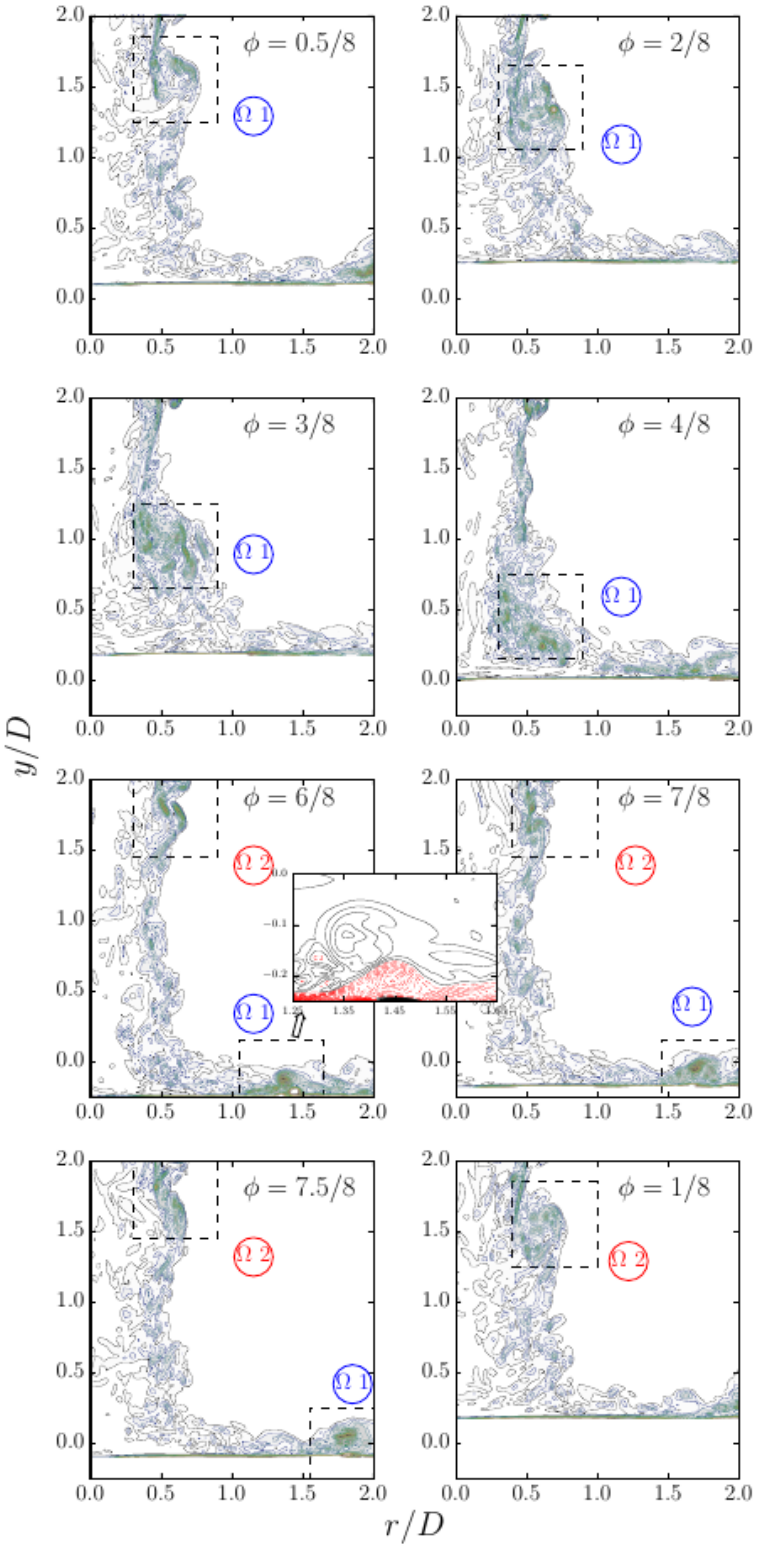

Figure 6.23: Visualisation of the LFHA case at Re_D = 10,000 over a constant z plane with contours of instantaneous total vorticity magnitude, $(\omega_i\omega_i)^{0.5}$ for the phases $\phi = 0/8 \rightarrow 7/8$; Plot on the inset showing secondary vortices in the region coloured by dashed red lines.

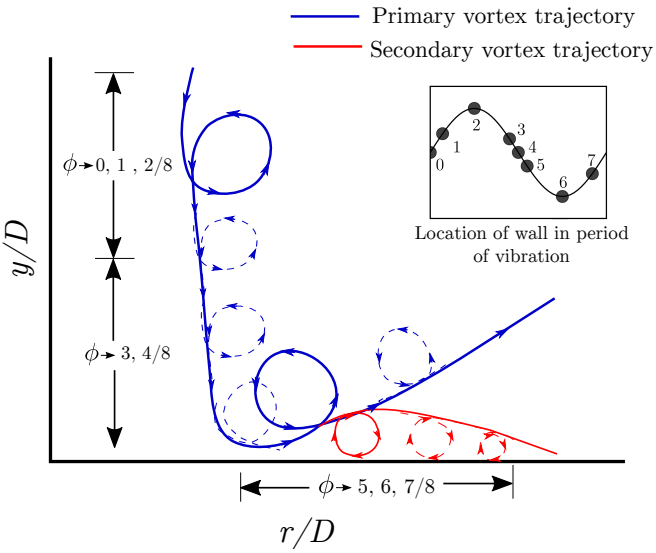

Figure 6.24: Schematic of the trajectory of the vortex structures.

case where these high velocity rings are almost non-existent and the spread in velocity on the impingement surface is clearly visible. The value of the impingement surface vibration amplitude is seen to control this spread in increased velocity. For all the cases examined, at a given frequency, the value of amplitude controls the spread of the increased velocity in the impingement region. Increase in the amplitude results in a greater spread and on the contrary lower amplitudes result in decreased velocity patches around the impingement region. The large scale structures identified through iso-lines of λ_2-criterion are found to be concentrated around the stagnation region and are found to decrease as the impingement surface moves upward. These structures are at the lowest when the impingement surface is at maximum positive displacement, $\phi = 2/8$.

The fluctuating and the turbulent shear stress components are presented as contours in figure 6.26 for two extreme cases (LFLA and HFHA) compared against the static wall case at $Re_D = 10{,}000$. The main regions of the static wall case are well recovered with the LES; however for the vibrating cases, significant changes are observed due to the induced vibration. It is clear that both the radial and axial fluctuation levels significantly increases even for the smallest combination of forcing parameters. The fluctuation levels do not increase above $0.05V_b$ in the jet core and stagnation region for the static wall case; however, for the LFLA case, the fluctuation levels reach a maximum of $0.15V_b$ and approximately $0.4V_b$ for the HFHA case. In canonical jet impingement configurations (static-wall), the maximum levels of fluctuations occur in the shear layer formed upon the jet exit (at about $y/D = 0.8$) and upon impingement at $r/D \approx 1.7$ to 2.0. This is also seen in the current results for the static wall case where the

(a) LFLA ($f = 60$ Hz, $A = 0.125\ D$)

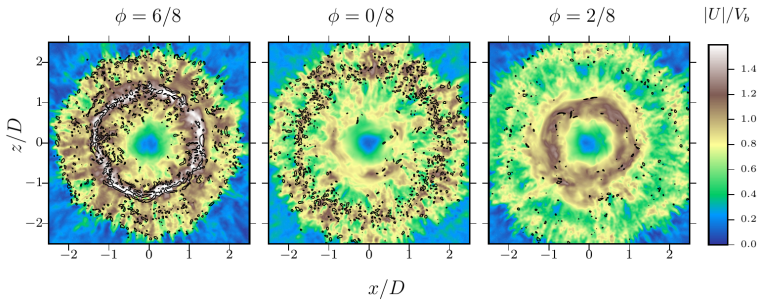

(b) LFHA ($f = 60$ Hz, $A = 0.25\ D$)

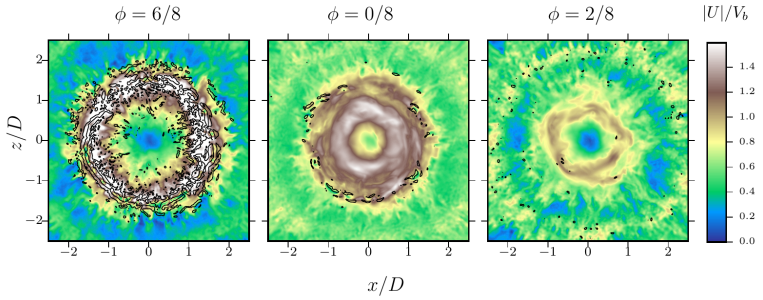

(c) HFLA ($f = 120$ Hz, $A = 0.125\ D$)

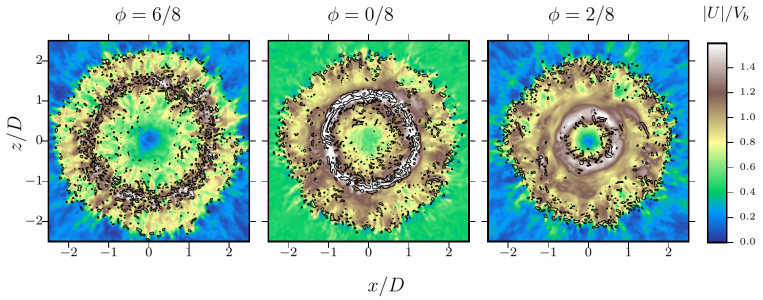

(d) HFHA ($f = 120$ Hz, $A = 0.25\ D$)

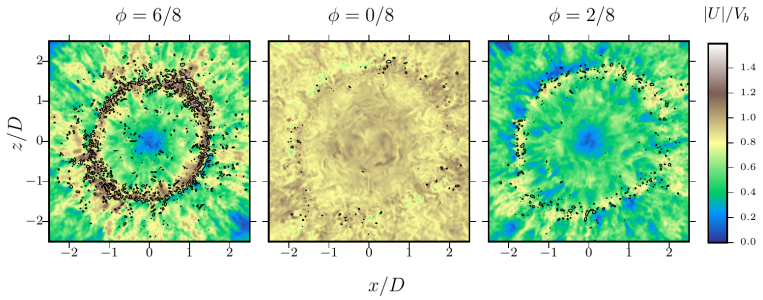

Figure 6.25: Visualisation of circular jet impingement at $Re_D = 10{,}000$ over a constant y plane located at $0.05D$ from the impingement surface with contours of instantaneous velocity magnitude, $|U|$, normalised by the bulk velocity, V_b at phases, $\phi = 0/8$, $2/8$, and $6/8$ superimposed by contours of λ-2.

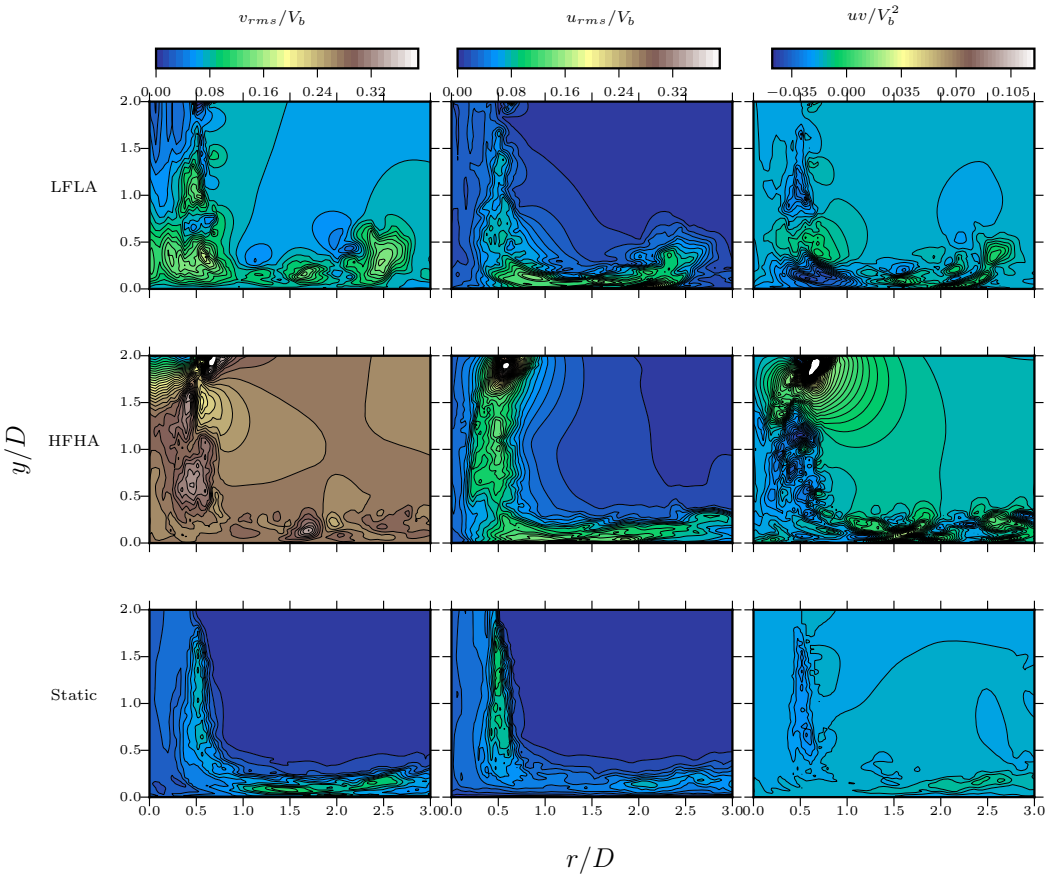

Figure 6.26: Visualisation of the second order turbulence statistics over a constant z plane with contours of (a) axial root mean square velocity, v_{rms}, normalised by the bulk velocity V_b, (b) radial root mean square velocity, u_{rms}, normalised by the bulk velocity V_b, and (c) Reynolds shear stress, uv, normalised by the square of the bulk velocity, V_b.

maximum fluctuation reaches $0.2V_b$. However, with the applied vibration, the fluctuation levels increase to $0.3V_b$ in the shear layer and additionally a high fluctuation region is formed near the exit of the nozzle for the HFHA case as visualised earlier with velocity contours (see figure 6.20). In the wall jet region, the flow is largely dominated by the radial direction, and the fluctuations decrease with increase in the radial distance. It is also noted that the wall jet region remains turbulent in all the radial positions and no relaminarization or transition to turbulence occurs in both the static and vibrating wall cases.

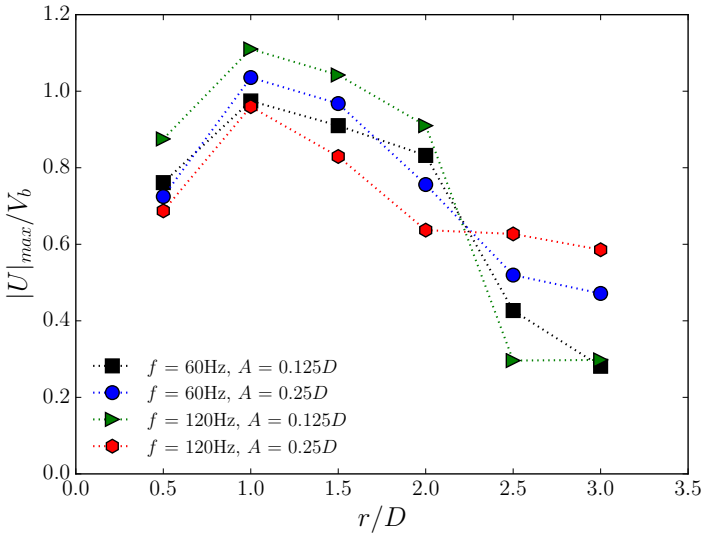

Figure 6.27: Profiles of $|U|max$ normalized by V_b for the vibrating wall cases.

Figure 6.27 shows the time-averaged mean maximum velocity maximum in the wall-jet for the four cases simulated at Re_D = 10,000. All the configurations show an initial acceleration in the wall-jet up to r/D = 1.0 attained due to the change in streamline curvature upon contact with the impingement surface. The gradual decrease of the velocity magnitude begins from r/D = 1.0.

6.3.3 Heat Transfer Statistics

The instantaneous heat transfer data for the vibrating wall cases are presented in this section. Figures 6.28 - 6.31 show the visualization of the jet-impingement surface for all the four vibrating wall cases at Re_D = 10,000 with contours of instantaneous Nusselt number Nu for phases ϕ = 0, 1, 2, 5 and 6/8. The first observation is that throughout the range of cases simulated, the stagnation region $(r/D, z/D \pm 1)$ remains the most affected area on the impingement surface. However, the local Nusselt number in this stagnation region varies within different phases within

a cycle for a configuration as well as with other configurations at the same phase location of the impingement wall.

Within a period of vibration cycle, for all the cases examined, the stagnation heat transfer begins to increase not at the maximum positive displacement but during the down-stroke of the impingement surface. This is due to the viscous effects as discussed in the § 6.2.1. This effect is seen even with the reduction in Re_D and the decrease in frequency and amplitude compared to the baseline case. The 'hot' and 'cold' spots are still seen next to each other beyond $r/D > 1$ for all the frameworks and substantially higher for the HFHA case. As noted earlier, this represents the local unsteady flow separation and reattachment between the impingement surface and the radial wall jet resulting in local increase and decrease of the Nusselt number. With HFHA case, the flow is relatively more unsteady compared to the other cases leading to the spread of these 'hot' and 'cold' spots to a larger radial distance.

From these figures, it is also seen that by tuning the frequency the radial extent of the heat removal can be controlled. For cases, LFLA and LFHA, due to the formation of the clear vortical structures, there exists a circular low Nusselt number band immediately surrounding the high Nusselt number region in the stagnation zone which causes a dip in the Nusselt number profile. These two configurations result in the characteristic Nu profile where a high stagnation region Nu is followed by a dip at $\approx r/D = 1.5$ and immediately followed by the secondary Nu number peak that monotonically reduces with increase in the radial distance. With the HFLA and HFHA cases, this low Nusselt ring diminishes due to the destruction of the vortical structures which are responsible for the heat removal. Although this results in the disappearance of the secondary Nusselt number peak, the unsteadiness induced on breaking up the large scale structures improves the radial spread of the 'hot' and 'cold' spots on the impingement surface.

With the HFHA case, because of the absence of organised large-scale vortical structures, the impingement heat transfer is affected such that the secondary Nusselt peak is not clearly observed. This is expected as the primary vortical structures impinge on the surface resulting in the secondary vortical structures which are then responsible for the secondary Nu peak. Since these structures are clearly distorted because of the induced vibration, the characteristic secondary peak is clearly absent. However, the radial spread of increased Nu increases with increase in frequency and amplitude.

These phenomena can be further analysed through the spatio-temporal maps of instantaneous Nusselt number as a function of the radial distance and non-dimensional time as shown in figure 6.32. The impingement surface positions are indicated as phases at the top of the figure, and the convection velocities are annotated inside the spatiotemporal map. For the LFLA and

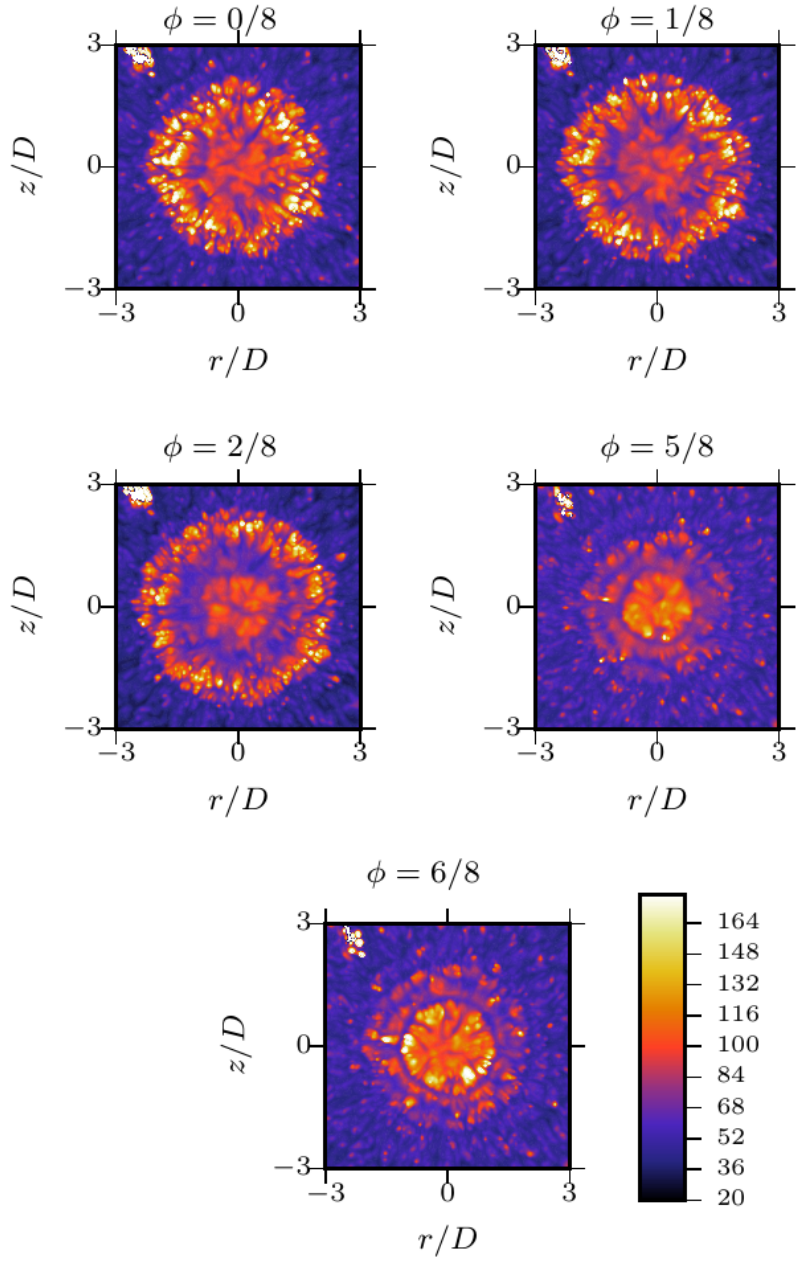

Figure 6.28: Visualization of the jet-impingement wall for at f = 60 Hz, $A = 0.125D$ and Re_D = 10,000 with contours of instantaneous Nusselt number Nu for phases ϕ = 0, 1, 2, 5 and 6/8.

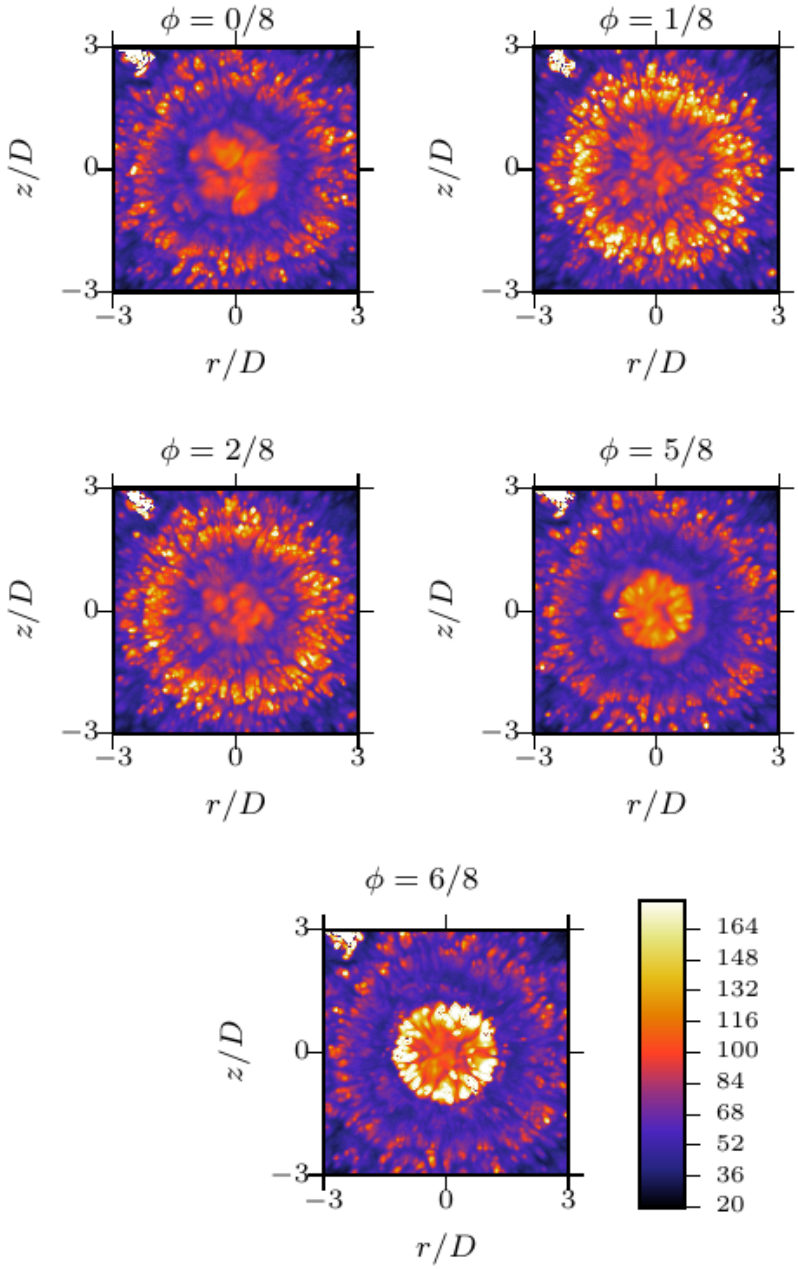

Figure 6.29: Visualization of the jet-impingement wall for at $f = 60$ Hz, $A = 0.25D$ and $Re_D = 10{,}000$ with contours of instantaneous Nusselt number Nu for phases $\phi = 0$, 1, 2, 5 and 6/8.

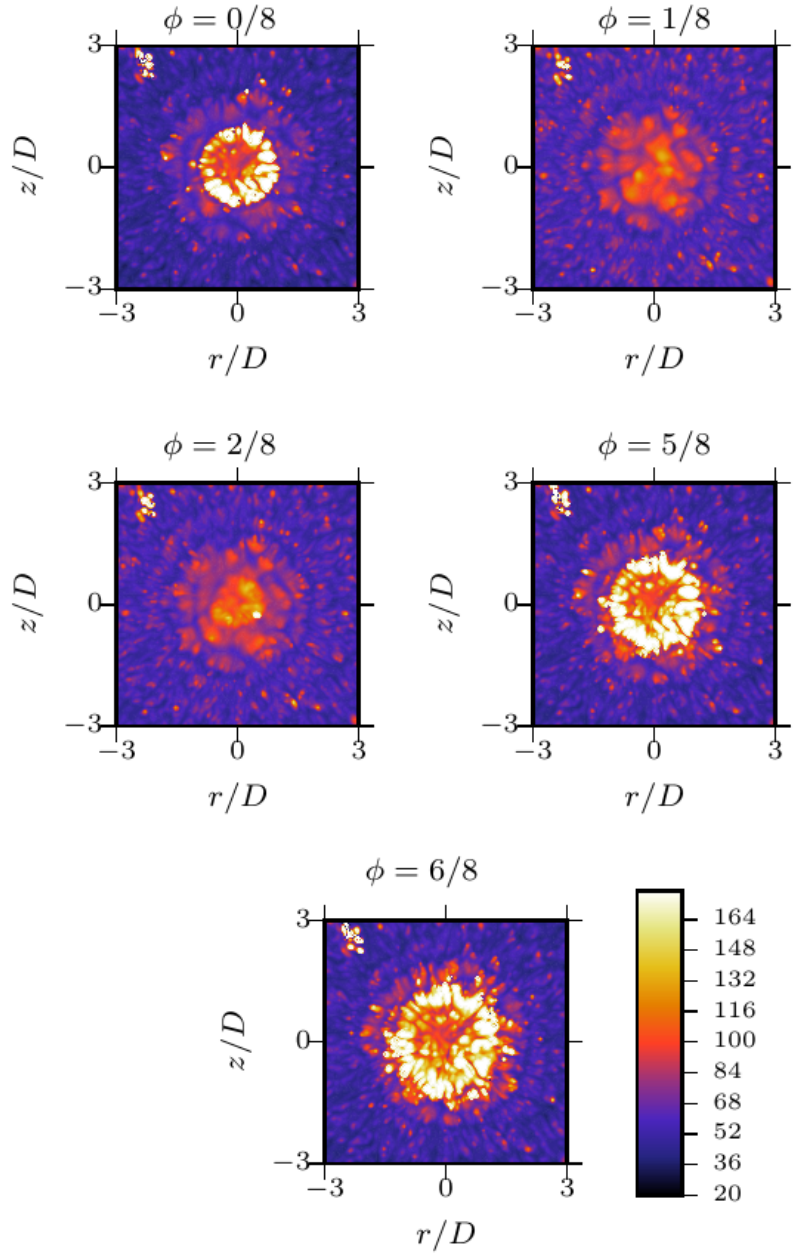

Figure 6.30: Visualization of the jet-impingement wall for at f = 120 Hz, $A = 0.125D$ and Re_D = 10,000 with contours of instantaneous Nusselt number Nu for phases ϕ = 0, 1, 2, 5 and 6/8.

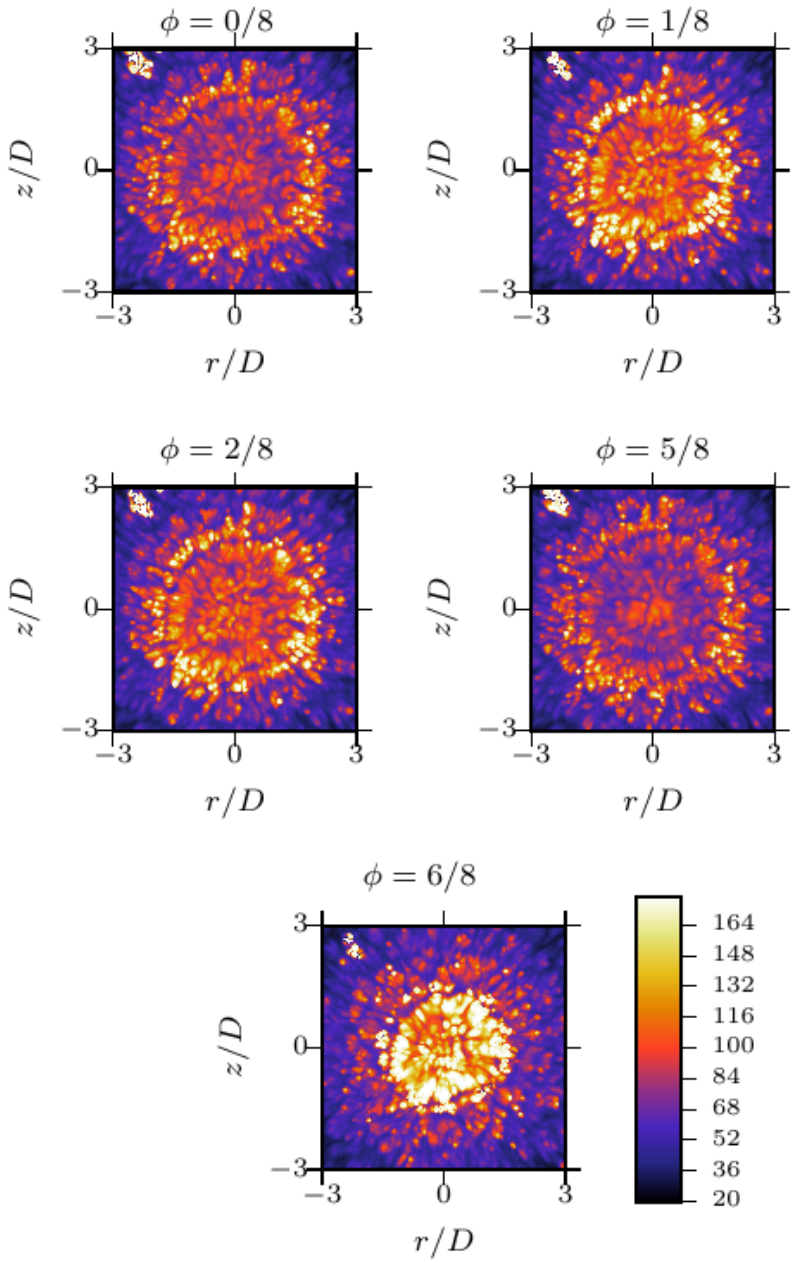

Figure 6.31: Visualization of the jet-impingement wall for at f = 120 Hz, $A = 0.25D$ and Re_D = 10,000 with contours of instantaneous Nusselt number Nu for phases ϕ = 0, 1, 2, 5 and 6/8.

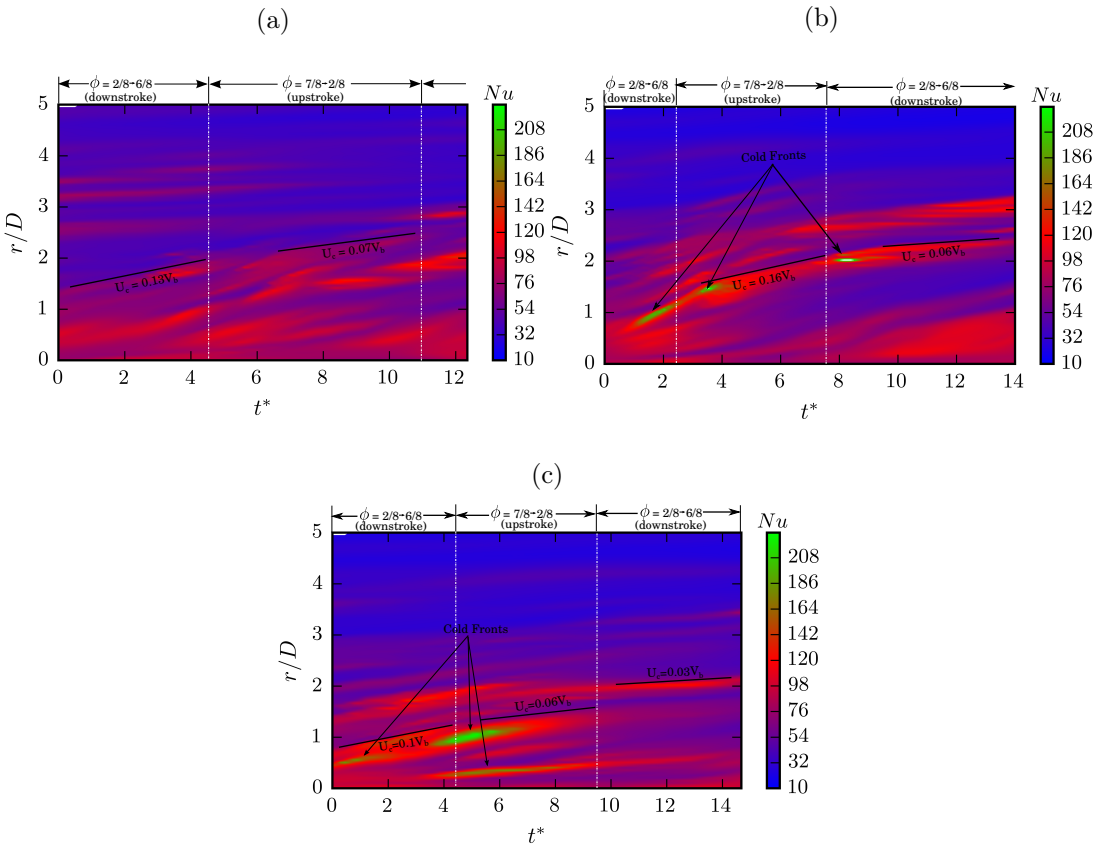

Figure 6.32: Spatio-temporal maps of Nusselt number as a function of radial distance r/D and non-dimensional time, t^* for (a) LFLA, (b) LFHA and (c) HFHA at Re_D = 10,000.

LFHA cases, the convection velocities are seen to be marginally higher than that of the HFHA case. This is expected as the hydrodynamic boundary layer in the wall jet region is more stable in the low-frequency cases compared to the HFHA case. In addition to this, the streak spacing in the LF cases is larger compared to the HF case indicating the role of large-scale primary and secondary vortical structures. The cold fronts are more pronounced compared to the LF cases, and the smaller streak spacing shows that the heat transfer is predominantly high compared to the other cases where thick streaks of low heat transfer are found to coexist.

The radial profiles of the phase-averaged Nusselt number profiles along the radial direction are shown in figure 6.33. It is seen that the induced vibration affects the heat transfer up to a radial distance of $r/D = 3.0$. Beyond this radial distance, the effect of vibration does not play a significant role in enhancing or reducing heat transfer. The maximum heat transfer occurs in the stagnation region ($r/D < 1$) and is seen when the impingement surface reaches the negative maximum. The impingement surface velocity is also seen to affect the stagnation region heat transfer. As shown in the instantaneous Nusselt number visualisations, the Nusselt number trend is almost a plateau extending to a radial distance of up to $r/D = 2.0$ for the HFHA case (see figures 6.33(b) and (c)). The effect of amplitude is seen as a minor increase in Nu in the stagnation region. For a given frequency, an increase in the amplitude increases the stagnation heat transfer when the impingement surface is at its negative maximum. Combined with an increase in frequency, the radial extent of this increased Nu increases.

The time averaged Nusselt number profiles are shown in figure 6.34. Vibration is seen to improve the stagnation heat transfer marginally but only to a radial extent of $r/D = 3.0$. Beyond this region, the induced vibration does not play a role in enhancing or reducing heat transfer. The increase in the plate speeds increases the heat transfer in the stagnation region marginally compared to the static wall case. However, this positive effect is only up to a radial distance of $r/D = 3.0$.

Power requirement It would be instructive to assess the beneficial effects of plate vibration alongside the power requirement to make the plate vibrate. A brief assessment of the engineering system is made because, for example, a system configuration that is very efficient for heat transfer may require inordinate amounts of energy to drive the plate motion. Several methods of power estimation and effectiveness calculations have been proposed and used especially in wall-bounded flows where wall blowing and suction is involved, and the efficiency of the opposition control needs to be estimated (see Chung & Talha[166]). However, in the present

[166]Y.M. Chung and T. Talha. *Phys. Fluids*, **23**: 025102, 2011.

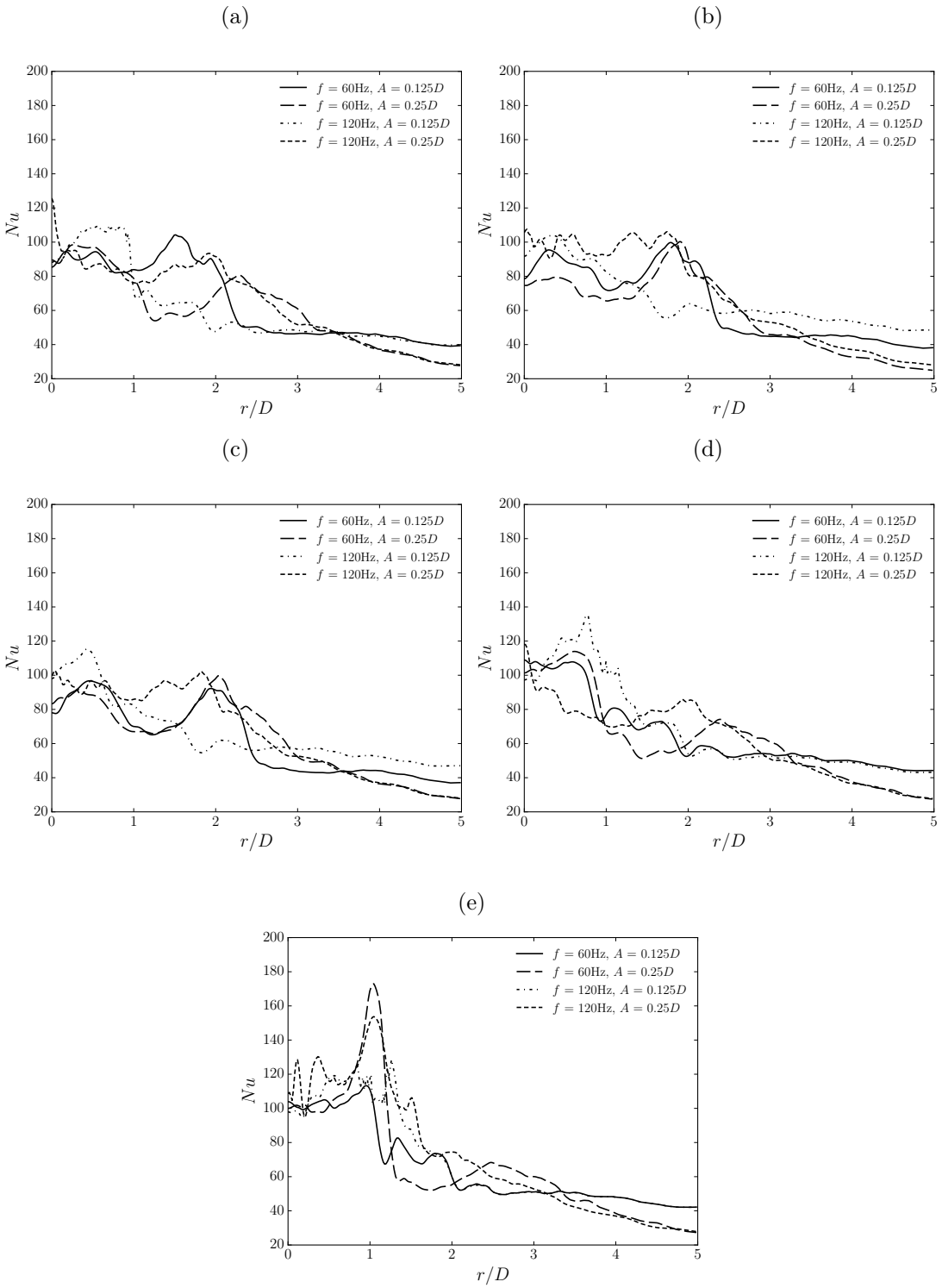

Figure 6.33: Phase-averaged Nusselt number on the impingement wall as a function of radial distance r/D at phases, (a) $\phi = 0/8$, (b) $\phi = 1/8$, (c) $\phi = 2/8$, (d) $\phi = 5/8$, and (e) $\phi = 6/8$.

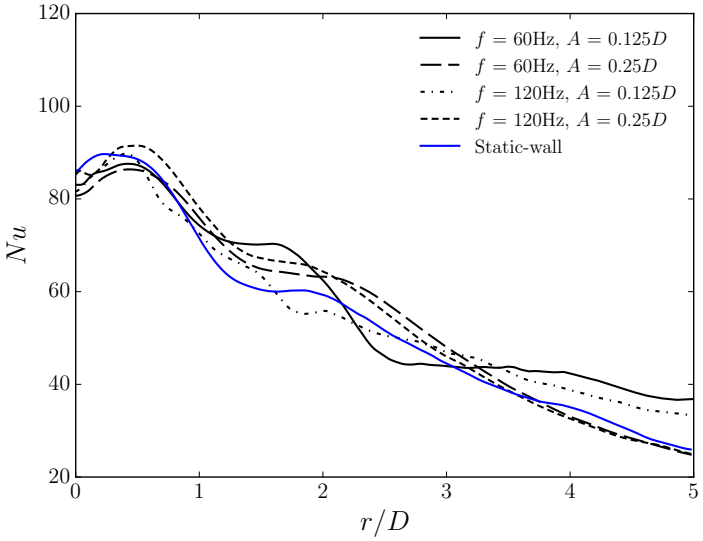

Figure 6.34: Time averaged Nusselt number on the impingement wall as a function of radial distance r/D.

case, this is an ideal quantity since in practical applications the inertia of the impingement surface and other inefficiencies of the plate drive system need to be taken into account and may vary the value of the Power, $\mathbb{P}$. For the current system, the ideal power is given as,

$$\mathbb{P}_{ideal}(t) = \frac{\partial \eta}{\partial t}(t) \int_{r=0}^{r=R} p(r,t)\ 2\pi r dr \tag{6.4}$$

where $\partial\eta/\partial t(t)$ is the vertical speed of the impingement surface (prescribed by choice of forcing parameters) and $p(r,t)$ is the radially averaged gauge pressure on the surface.

Figure 6.35 shows the calculated ideal power values normalised by the bulk density, velocity and the diameter of the impingement surface. It is clear that the power input increases with increase in amplitude and frequency. However, it is interesting to note that the effect of amplitude is higher compared to the effect of frequency on the power input. With an increase in frequency by a factor of 2, for the same amplitude, the power input almost increases by a factor of 5. Thus the role of amplitude can be greater in efficient designing of such dynamic systems.

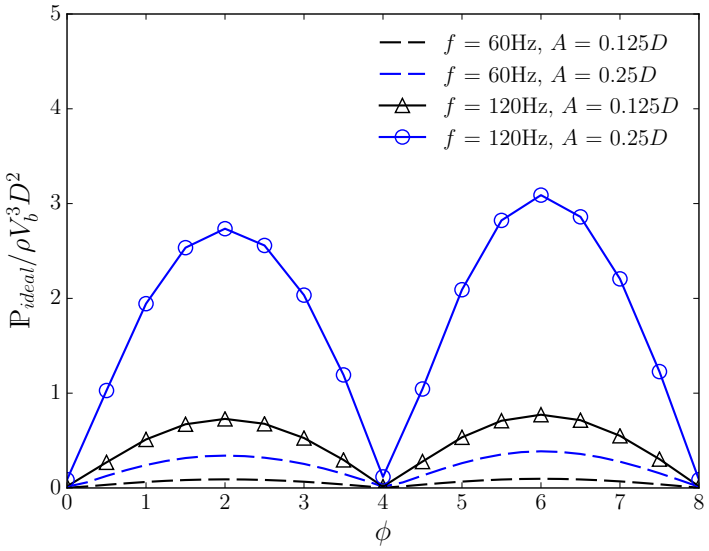

Figure 6.35: Profiles of ideal power, $\mathbb{P}_{ideal}$ normalized by $\rho V_b^3 D^2$ for all the four cases from phases, $\phi = 1 \rightarrow 8$.

6.4 Summary

This chapter has detailed the flow and heat transfer dynamics of a jet impinging onto a vibrating heated surface. A jet impingement configuration for a Re_D of 23,000 with a mean nozzle-to-wall distance of $1.75D$ with the wall motion within the region of $0 \leq y/D \leq 0.5$ with $y/D = 2$ at the nozzle exit and a vibration frequency of 100 Hz was simulated to understand the consequences of induced impingement surface forcing on the flow and thermal dynamics. Radial-flow velocity increase and decrease were found upon positive and negative displacement of the impingement wall respectively. In the stagnation region, counterflow of the fluid was predicted due to the upward motion of the impingement wall causing a change in the axial velocity profiles. An increase in the turbulence kinetic energy production was seen, and the maximum was almost twice that of the static wall case at $r/D = 1.5$. The secondary maximum of the Nusselt number was shown to be a strong function of the eddies present in the flow domain, and it shifted radially based on the location and strength of these eddy structures. Enhancement in heat-transfer was seen as an increase in the time-averaged Nusselt number (Nu_{avg}) up to a radial distance of $r/D = 1.5$ when compared to static-wall jet impingement. The enhancement in the stagnation region is about 18% when compared to the static wall case. For investigations in the parameter space, four configurations were chosen with a diverse set of forcing parameters based on the natural frequency of the jet impinging on a static wall at Re_D of 10,000. Based on this information,

two amplitudes, $0.125D$, $0.25D$ and two frequencies, 60 Hz and 120 Hz for a Re_D of 10,000 were used for the investigations. The large-scale structures were excited irrespective of the Reynolds number and resonated at the applied impingement wall frequency. However, with the increase in magnitude of the forcing parameters, the flow field became increasingly unsteady, making it harder to identify clearly organised large-scale structures in the domain. These structures were a strong function of the amplitude of vibration rather than the frequency of wall vibration. The heat transfer was also seen to be affected by the impingement surface vibration; however, the effect diminished beyond a radial distance of $r/D = 3.0$ across all the configurations investigated.

Chapter 7

Conclusions and Recommendations

7.1 Conclusions

The novel research areas presented in the thesis can be broadly organised into two parts. Firstly, a successful modelling framework has been developed to perform Large-eddy simulations of an incompressible circular jet impinging on static and dynamic target surfaces supplied with a uniform heat flux. Secondly, we have successfully used this computational framework to simulate a jet impinging on a dynamic target surface, producing what we believe to be the first documented Large-eddy simulations predicting both turbulent flow and heat transfer data. The LES was found to be highly sensitive to the grid resolution, especially in the azimuthal direction and along the shear-layer for a faithful representation of the flow and thermal statistics. A clear relationship between the large-scale structures and the resulting heat transfer on the impingement surface exists and was demonstrated through high-resolution LES of both static-wall and dynamic-wall jet impingement configurations. The secondary peak is a result of a counter-rotating secondary vortical structure that forms marginally before the primary vortical structure and was seen in both static-wall and dynamic-wall configurations. Marginal improvements in heat transfer were observed with forcing the impingement surface; however, this improvement was largely confined to the vicinity around the stagnation region.

The following are some of the specific conclusions are drawn from the numerical analysis presented in this thesis:

- The recycled boundary condition was successfully applied to a smooth pipe flow at Re_D

= 24,600 to generate a fully-developed turbulent inflow. This technique was deemed suitable and was adapted to turbulent inflow for simulations needing such inlet conditions (such as nozzle inlet for impinging jet simulations) without having to run redundant pipe flow simulations externally. Hence, this approach is recommended for the analysis of this class of problems.

- The nature of the near-wall turbulence was simulated accurately as significant differences between a two-dimensional planar jet and a three-dimensional round jet impingement configuration were observed. In round jets, near-wall anisotropy exhibits contraction and isotropy at the stagnation zone, and on moving away, the flow undergoes axisymmetric expansion and contraction. In planar jets, the flow does not exhibit any isotropy and remains largely dominated by two-component turbulence. However, similar expansion and contraction of eddies are observed at regions where flow reversal and secondary vortex formation occurs.

- A spatially developing free jet was simulated at Re_j = 11,000 to understand the accuracy requirements and the need to capture the instabilities. A quality index or *'resolvedness'* is used to measure the quality of the LES and showed that the shear layer in a jet is the most mesh intensive and requires a greater resolution to precisely capture these instabilities. It is recommended that the shear layer be resolved to a minimum of 80% or more to capture the second order statistics accurately.

- A turbulent jet impingement configuration with a static impingement surface supplied with a uniform heat flux is simulated with RANS methodology. The results demonstrated the successful implementation of the developed model for jet impingement investigations involving both flow and heat transfer. Though the mean flow statistics were reproduced with reasonable accuracy, the lack of instantaneous data and the poor predictions of surface heat transfer required a highly resolved LES to capture the flow and heat transfer precisely.

- A turbulent jet impingement configuration with a static impingement surface supplied with a uniform heat flux is simulated with LES at Re_D = 23,000. Both the first order and second order turbulence statistics were reproduced with great accuracy when compared with previous experimental studies. It was also shown that the azimuthal resolution was far more important compared to the radial resolution to reproduce the secondary Nusselt number peak. The developed framework was deemed suitable to carry out jet impingement simulations using LES with a fully developed turbulent inflow and an impingement surface supplied with a uniform heat flux.

- The numerical framework was combined with a moving mesh methodology to simulate the flow and heat transfer dynamics of a jet impinging onto a vibrating heated surface. A jet impingement configuration for a Re_D of 23,000 with a mean nozzle-to-wall distance of $1.75D$ with the wall motion within the region of $0 \leq y/D \leq 0.5$ with $y/D = 2$ at the nozzle exit and a vibration frequency of 100 Hz was first established. It was shown that the large-scale structures are excited due to the induced vibration and resonate the applied frequency.

- In the stagnation region, counterflow of the fluid is predicted due to the upward motion of the impingement-wall causing a change in the axial velocity profiles. An increase in the turbulence kinetic energy production is seen and the maximum is almost twice that of the static wall case at $r/D = 1.5$.

- The secondary maximum of the Nusselt number has been shown to be a strong function of the eddies present in the flow domain and it shifts radially based on the location and strength of these eddy structures. Large-eddies with no defined structure are convected away radially from the stagnation region during the positive displacement of the wall and are renewed close to the stagnation point during the negative displacement of the wall.

- The impingement-wall vibration affects the heat transfer only up to a radial distance r/D= 3.0. Beyond this radial distance, the dependence of Nu on radial distance is similar to that of a corresponding static-wall jet impingement configuration. Enhancement in heat-transfer is seen as an increase in the time-averaged Nusselt number (Nu_{avg}) up to a radial distance of $r/D = 1.5$ when compared to static-wall jet impingement. The enhancement in the stagnation region is about 18% when compared to the static-wall case. Apart from the moderate depreciation at $r/D = 2.0$, no further enhancement or depreciation of heat transfer is seen beyond this radial distance.

- The effect of impingement surface forcing parameters were explored in the parameter space for a jet impingement configuration at Re_D of 10,000 with a mean nozzle-to-wall distance of $2.0D$. The results showed that impingement surface vibration affects the large-scale structures in the fluid domain. Low-velocity pockets are seen to increase with the increase in the magnitude of the forcing parameters creating a weak stagnation zone in the axial jet.

- The large eddy structures were found to be a strong function of the amplitude of vibration rather than the frequency of wall vibration.

- The heat transfer was also seen to be affected by the impingement surface vibration; The increase in the plate speeds increases the heat transfer in the stagnation region marginally

compared to the static wall case; however, the effect diminishes beyond a radial distance of $r/D = 3.0$ across all the vibrating impingement-wall configurations investigated.

This thesis has addressed two problems; Firstly, development of a computational framework that is capable of using Large-eddy simulations to simulate turbulent flow and heat transfer under jet impingement on static and dynamic target surfaces. Secondly, the simulation of a jet impingement on a dynamic, heated target surface, and have produced what we believe to be the first documented Large-eddy simulations predicting turbulent flow and heat transfer data. The suitability of the developed framework is demonstrated through excellent agreement with established experiments and numerical data wherever possible. The following section presents some extensions that may be carried out.

7.2 Recommendations for Future Work

Effect of inflow pulsation: The effect of inflow pulsation would be an immediate extension of the current research. Variations coupled with the impingement surface vibration being 'phase locked' and 'out of phase' with the inflow pulsation. The effect of these parametric variations can be explored with tuning the inflow boundary condition to provide a fully developed pulsating turbulent flow within the developed computational framework.

Zumbrennen & Aziz[167] first studied experimental works on pulsating impinging jets and reported enhancement in the heat transfer. Numerical investigations of this work were carried out later by Mladin & Zumbrennen[168] and concluded that high-frequency low-amplitude pulsations provided better results compared to low-frequency and high amplitudes. Numerical work on pulsating laminar jets was done by Poh et al.[169]. The work presented an optimum frequency for a fixed nozzle to wall spacing and Reynolds number. The most widely used turbulence models were tested for their accuracy in predicting pulsating impinging jets by Hofmann et al.[149]. They demonstrated that the k-ω SST turbulence model with the transitional option predicted the heat transfer accurately. However, Behera et al.[170] quantified the effect of jet pulsations using the k-model and concluded that the amplitude of the pulse contributed to the heat transfer rather than the frequency which is contentious to the results of Mladin & Zumbrennen[168].

[167]D.A. Zumbrunnen and M. Aziz. *J. Heat Transfer*, **115**: 91–98, 1993.
[168]E.C. Mladin and D.A. Zumbrunnen. *J. Thermophys. Heat Transfer*, **9**: 181–192, 1995.
[169]H.J. Poh et al. *Int. Commun. Heat Mass Transfer*, **32**: 1317–1324, 2005.
[149]H.M. Hofmann et al. *Numer. Heat Transfer, Part B*, **51**: 565–583, 2007.
[170]R.C. Behera et al. *IEEE Trans. Compon. Packag. Technol.*, **30**: 275–284, 2007.

Several other works including that of Xu at al.[171,172] and the recent work of Buddhika[173] have studied the effect of frequencies and amplitudes for multiple jets with pulsations. However, the issue of pulsating jets augmenting the heat transfer remains irresolute since both significant and marginal effect on heat transfer is reported. Moreover, the right choice of turbulence models is a subject of deeper investigation. High-resolution numerical methods such as the LES have still not been employed to study the effect of oscillating impinging jets.

Jet impingement on compliant surfaces: The current framework is also capable of simulating two-way coupled fluid-structure interaction problems with minor modifications to the framework. Numerical analysis of jets impinging on moving surfaces have been performed by Chen et al.[174], Chattopadhyay et al.[175], and Sharif & Banerjee[176]. This methodology also has been extended to heated nanoporous membranes by Narayanan et al.[177]. However, the jet impingement studies on compliant surfaces have still not been explored. Global flow oscillations are often generated by an excitation mechanism which couples a convectively unstable free shear flow with an upstream feedback effect resulting from either flow impingement or system resonance[178].

Both experimental and numerical studies have not been carried out yet on round jets impinging on compliant surfaces (flat, heated) though they have a variety of applications. Lucey & Carpenter[179] devised a method for predicting the response of a passive compliant wall under strictly inviscid conditions. Ziada[178] performed experimental work on a planar jet impinging on a flexible wedge and generated strong 'lock-in' vibration over a range of inflow velocities to investigate the effect of feedback control. A DNS of turbulent flows over a compliant surface was performed by Endo & Himeno[180] and Xu et al.[181] and more recently an LES of a granular jet on compliant surfaces[182]. These studies also indicate the possible applications of jet impingement

[171]P. Xu et al. *Int. J. Therm. Sci.*, **49**: 1247–1252, 2010.
[172]P. Xu et al. *Int. Commun. Heat Mass Transfer*, **39**: 378–382, 2012.
[173]B.N. Hewakandamby. *Int. J. Heat Mass Transfer*, **52**: 396–406, 2009.
[174]J. Chen et al. *Numer. Heat Transfer, Part A*, **26**: 141–160, 1994.
[175]H. Chattopadhyay et al. *J. Heat Transfer*, **124**: 433–440, 2002.
[176]M.A.R. Sharif and A. Banerjee. *Appl. Therm. Eng.*, **29**: 532–540, 2009.
[177]S. Narayanan et al. *Int. J. Heat Mass Transfer*, **58**: 300–311, 2013.
[178]S. Ziada. *J Fluids Struct*, **16**: 613–626, 2002.
[179]A.D. Lucey and P.W. Carpenter. *J. Fluid Mech.*, **234**: 121–146, 1992.
[180]T. Endo and R. Himeno. "Direct numerical simulation of turbulent flow over a compliant surface" in: *TSFP*. 2001.
[181]S. Xu et al. *J. Fluid Mech.*, **478**: 11–34, 2003.
[182]D. Mukherjee and T.I. Zohdi. *Granular Matter*, **17**: 231–252, 2015.

on a compliant surface and the need for further research in this domain. The combination of pulsatile flow inlet impinging on a compliant surface for efficient heat and mass transfer could be explored on the basis laid down in the current research.

References

[1] ERCOFTAC *ERCOFTAC test cases* http://cfd.mace.manchester.ac.uk/ercoftac/ Accessed Dec 17, 2016

[2] Elias Balaras, Ugo Piomelli, and James M Wallace. Self-similar states in turbulent mixing layers. *Journal of Fluid Mechanics*, **446**: 1–24, 2001.

[3] T. Brunschwiler, H. Rothuizen, M. Fabbri, U. Kloter, B. Michel, R.J. Bezama, and G. Natarajan. Direct liquid jet-impingment cooling with micron-sized nozzle array and distributed return architecture. *The Tenth Intersociety Conference on Thermal and Thermomechanical Phenomena in Electronics Systems.ITHERM'06.*, 196–203, 2006.

[4] D. Fulker, A. Simmons, and T. Barber. Computational Model of the Arterial and Venous Needle During Hemodialysis. *Journal of Biomechanical Engineering*, **139**: 011005, 2017.

[5] T. Aihara, J-K. Kim, K. Suzuki, and K. Kasahara. Boiling heat transfer of a micro-impinging jet of liquid nitrogen in a very slender cryoprobe. *International journal of heat and mass transfer*, **36**: 169–175, 1993.

[6] C.V. Tu and D.H. Wood. Wall pressure and shear stress measurements beneath an impinging jet. *Experimental thermal and fluid science*, **13**: 364–373, 1996.

[7] B.A. Anderson and R.P. Singh. Modeling the thawing of frozen foods using air impingement technology. *International Journal of Refrigeration*, **29**: 294–304, 2006.

[8] A. Sarkar, N. Nitin, M.V. Karwe, and R.P. Singh. Fluid flow and heat transfer in air jet impingement in food processing. *Journal of Food Science*, **69**: 113–122, 2004.

[9] N. Karwa, G-R. Tatiana, P. Stephan, and C. Tropea. Experimental investigation of circular free-surface jet impingement quenching: transient hydrodynamics and heat transfer. *Experimental Thermal and Fluid Science*, **35**: 1435–1443, 2011.

[10] N. Karwa and P. Stephan. Experimental investigation of free-surface jet impingement quenching process. *International Journal of Heat and Mass Transfer*, **64**: 1118–1126, 2013.

[11] R. Viskanta. Heat transfer to impinging isothermal gas and flame jets. *Experimental Thermal and Fluid Science*, **6**: 111–134, 1993.

[12] S. Narumanchi, A. Troshko, D. Bharathan, and V. Hassani. Numerical simulations of nucleate boiling in impinging jets: Applications in power electronics cooling. *International Journal of Heat and Mass Transfer*, **51**: 1–12, 2008.

[13] F. Cirillo and G.M. Isopi. Glass tempering heat transfer coefficient evaluation and air jets parameter optimization. *Applied Thermal Engineering*, **29**: 1173–1179, 2009.

[14] F. Monnoyer and D. Lochegnies. Heat transfer and flow characteristics of the cooling system of an industrial glass tempering unit. *Applied Thermal Engineering*, **28**: 2167–2177, 2008.

[15] B. Končar, P. Norajitra, and K. Oblak. Effect of nozzle sizes on jet impingement heat transfer in He-cooled divertor. *Applied Thermal Engineering*, **30**: 697–705, 2010.

[16] J. Girardeau, J. Pailhes, P. Sebastian, F. Pardo, and J.P. Nadeau. Turbine blade cooling System optimization. *Journal of Turbomachinery*, **135**: 061020, 2013.

[17] J.C. Han. Fundamental gas turbine heat transfer. *Journal of thermal science and engineering applications*, **5**: 021007, 2013.

[18] F.S. Alvi, J.A. Ladd, and W.W. Bower. Experimental and computational investigation of supersonic impinging jets. *AIAA journal*, **40**: 599–609, 2002.

[19] A.J. Reynolds. Observations of a liquid-into-liquid jet. *Journal of Fluid Mechanics*, **14**: 552–556, 1962.

[20] K.J. McNaughton and C.G. Sinclair. Submerged jets in short cylindrical flow vessels. *Journal of Fluid Mechanics*, **25**: 367–375, 1966.

[21] J.W. Gauntner, J. Livingood, and P. Hrycak. Survey of literature on flow characteristics of a single turbulent jet impinging on a flat plate. *NASA Technical Report*, 19, 1970.

[22] W.C. Reynolds, D.E. Parekh, P.J.D. Juvet, and M.J.D. Lee. Bifurcating and blooming jets. *Annual review of fluid mechanics*, **35**: 295–315, 2003.

[23] S.C. Crow and F.H. Champagne. Orderly structure in jet turbulence. *Journal of Fluid Mechanics*, **48**: 547–591, 1971.

[24] J.W. Baughn and S. Shimizu. Heat transfer measurements from a surface with uniform heat flux and an impinging jet. *Journal of Heat Transfer*, **111**: 1096–1098, 1989.

[25] J. Lee and S-J. Lee. The effect of nozzle configuration on stagnation region heat transfer enhancement of axisymmetric jet impingement. *International Journal of Heat and Mass Transfer*, **43**: 3497–3509, 2000.

[26] L.A. Brignoni and S.V. Garimella. Effects of nozzle-inlet chamfering on pressure drop and heat transfer in confined air jet impingement. *International Journal of Heat and Mass Transfer*, **43**: 1133–1139, 2000.

[27] T. Dairay, V. Fortuné, E. Lamballais, and L.-E. Brizzi. Direct numerical simulation of a turbulent jet impinging on a heated wall. *Journal of Fluid Mechanics*, **764**: 362–394, 2015.

[28] D. Violato, A. Ianiro, G. Cardone, and F. Scarano. Three-dimensional vortex dynamics and convective heat transfer in circular and chevron impinging jets. *International Journal of Heat and Fluid Flow*, **37**: 22–36, 2012.

[29] D.H. Lee, J. Song, and M.C. Jo. The Effects of Nozzle Diameter on Impinging Jet Heat Transfer and Fluid Flow. *Journal of Heat Transfer*, **126**: 554–557, 2004.

[30] G. Middelberg and H. Herwig. Convective heat transfer under unsteady impinging jets: the effect of the shape of the unsteadiness. *Heat and mass transfer*, **45**: 1519–1532, 2009.

[31] C. Cornaro, A.S. Fleischer, and R.J. Goldstein. Flow visualization of a round jet impinging on cylindrical surfaces. *Experimental Thermal and Fluid Science*, **20**: 66–78, 1999.

[32] R.J. Goldstein, K.A. Sobolik, and W.S. Seol. Effect of entrainment on the heat transfer to a heated circular air jet impinging on a flat surface. *Journal of Heat Transfer*, **112**: 1990.

[33] B.R. Hollwoth and L.R. Gero. Entrainment effects on impingement heat transfer. II: Local heat transfer measurements. *Journal of heat transfer*, **107**: 910–915, 1985.

[34] M. Behnia, S. Parneix, Y. Shabany, and P.A. Durbin. Numerical study of turbulent heat transfer in confined and unconfined impinging jets. *International Journal of Heat and Fluid Flow*, **20**: 1–9, 1999.

[35] S.V. Ekkad and D. Kontrovitz. Jet impingement heat transfer on dimpled target surfaces. *International journal of heat and Fluid Flow*, **23**: 22–28, 2002.

[36] A.H. Beitelmal, M.A. Saad, and C.D. Patel. Effects of surface roughness on the average heat transfer of an impinging air jet. *International Communications in Heat and Mass Transfer*, **27**: 1–12, 2000.

[37] J.W. Zhou, Y.G. Wang, G. Middelberg, and H. Herwig. Unsteady jet impingement: heat transfer on smooth and non-smooth surfaces. *International Communications in Heat and Mass Transfer*, **36**: 103–110, 2009.

[38] D.H. Lee, Y.S. Chung, and D.S. Kim. Turbulent flow and heat transfer measurements on a curved surface with a fully developed round impinging jet. *International Journal of Heat and Fluid Flow*, **18**: 160–169, 1997.

[39] K. Ichimiya and Y. Yoshida. Oscillation effect of impingement surface on two-dimensional impingement heat transfer. *Journal of Heat Transfer*, **131**: 11701, 2009.

[40] M-Y. Wen. Flow structures and heat transfer of swirling jet impinging on a flat surface with micro-vibrations. *International Journal of Heat and Mass Transfer*, **48**: 545–560, 2005.

[41] K.P. Perry. Heat transfer by convection from a hot gas jet to a plane surface. *Proceedings of the Institution of Mechanical Engineers*, **168**: 775–784, 1954.

[42] R. Gardon and J. Cobonpue. Heat transfer between a flat plate and jets of air impinging on it. *International developments in heat transfer*, 454–460, 1962.

[43] R. Gardon and J.C. Akfirat. The role of turbulence in determining the heat-transfer characteristics of impinging jets. *International Journal of Heat and Mass Transfer*, **8**: 1261–1272, 1965.

[44] H. Martin. Heat and mass transfer between impinging gas jets and solid surfaces. *Advances in Heat Transfer*, **13**: 1–60, 1977.

[45] S. Polat, B. Huang, A.S. Mujumdar, and W.J.M. Douglas. Numerical flow and heat transfer under impinging jets: a review. *Annual Review of Heat Transfer*, **2**: 157–197, 1989.

[46] K. Jambunathan, E. Lai, M.A. Moss, and B.L. Button. A review of heat transfer data for single circular jet impingement. *International Journal of Heat and Fluid Flow*, **13**: 106–115, 1992.

[47] N. Zuckerman and N. Lior. Impingement heat transfer: correlations and numerical modeling. *Journal of Heat Transfer*, **127**: 544–552, 2005.

[48] N. Zuckerman and N. Lior. Jet impingement heat transfer: physics, correlations, and numerical modeling. *Advances in Heat Transfer*, **39**: 565–631, 2006.

[49] B. Han and R.J. Goldstein. Jet-Impingement Heat Transfer in Gas Turbine Systems. *Annals of the New York Academy of Sciences*, **934**: 147–161, 2001.

[50] G.M. Carlomagno and A. Ianiro. Thermo-fluid-dynamics of submerged jets impinging at short nozzle-to-plate distance: a review. *Experimental thermal and fluid science*, **58**: 15–35, 2014.

[51] A. Dewan, R. Dutta, and B. Srinivasan. Recent Trends in Computation of Turbulent Jet Impingement Heat Transfer. *Heat Transfer Engineering*, **33**: 447–460, 2012.

[52] D. Cooper, D.C. Jackson, B.E. Launder, and G.X. Liao. Impinging jet studies for turbulence model assessment—I. Flow-field experiments. *International Journal of Heat and Mass Transfer*, **36**: 2675–2684, 1993.

[53] T.J. Craft, L.J.W. Graham, and B.E. Launder. Impinging jet studies for turbulence model assessment—II. An examination of the performance of four turbulence models. *International Journal of Heat and Mass Transfer*, **36**: 2685–2697, 1993.

[54] T.J. Craft, H. Iacovides, and J.H. Yoon. Progress in the use of non-linear two-equation models in the computation of convective heat-transfer in impinging and separated flows. *Flow, Turbulence and Combustion*, **63**: 59–80, 2000.

[55] X. Yan and N. Saniei. Heat Transfer Measurements from a Flat Plate to a Swirling Impinging Jet. *Proceedings of the 11th Heat Transfer Conference*, **5**: 497–502, 1998.

[56] V. Katti and S.V. Prabhu. Experimental study and theoretical analysis of local heat transfer distribution between smooth flat surface and impinging air jet from a circular straight pipe nozzle. *International Journal of Heat and Mass Transfer*, **51**: 4480–4495, 2008.

[57] M. Bovo and L. Davidson. On the numerical modeling of impinging jets heat transfer—a practical approach. *Numerical Heat Transfer, Part A*, **64**: 290–316, 2013.

[58] Y.M. Chung and K.H. Luo. Unsteady Heat Transfer Analysis of an Impinging Jet. *Journal of Heat Transfer*, **124**: 1039, 2002.

[59] C. Meola, L. de Luca, and G.M. Carlomagno. Influence of shear layer dynamics on impingement heat transfer. *Experimental Thermal and Fluid Science*, **13**: 29–37, 1996.

[60] C.O. Popiel, T.H. Van der Meer, and C.J. Hoogendoorn. Convective heat transfer on a plate in an impinging round hot gas jet of low Reynolds number. *International Journal of Heat and Mass Transfer*, **23**: 1055–1068, 1980.

[61] S. Ashforth-Frost, K. Jambunathan, C.F. Whitney, and S.J. Ball. Heat transfer from a flat plate to a turbulent axisymmetric impinging jet. *Proceedings of the Institution of Mechanical Engineers, Part C: Journal of Mechanical Engineering Science*, **211**: 167–172, 1997.

[62] D. Lee, R. Greif, S.J. Lee, and J.H. Lee. Heat transfer from a flat plate to a fully developed axisymmetric impinging jet. *Journal of Heat Transfer*, **117**: 772–776, 1995.

[63] J. Lee and S-J. Lee. Stagnation region heat transfer of a turbulent axisymmetric jet impingement. *Experimental Heat Transfer*, **12**: 137–156, 1999.

[64] S.D. Hwang, C.H. Lee, and H.H. Cho. Heat transfer and flow structures in axisymmetric impinging jet controlled by vortex pairing. *International Journal of Heat and Fluid Flow*, **22**: 293–300, 2001.

[65] S.D. Hwang and H.H. Cho. Effects of acoustic excitation positions on heat transfer and flow in axisymmetric impinging jet: main jet excitation and shear layer excitation. *International Journal of Heat and Fluid Flow*, **24**: 199–209, 2003.

[66] D.W. Colucci and R. Viskanta. Effect of nozzle geometry on local convective heat transfer to a confined impinging air jet. *Experimental Thermal and Fluid Science*, **13**: 71–80, 1996.

[67] C.J. Hoogendoorn. The effect of turbulence on heat transfer at a stagnation point. *International Journal of Heat and Mass Transfer*, **20**: 1333–1338, 1977.

[68] D. Lytle and B.W. Webb. Air jet impingement heat transfer at low nozzle-plate spacings. *International Journal of Heat and Mass Transfer*, **37**: 1687–1697, 1994.

[69] T.S. O'Donovan and D.B. Murray. Jet impingement heat transfer – Part I: Mean and root-mean-square heat transfer and velocity distributions. *International Journal of Heat and Mass Transfer*, **50**: 3291–3301, 2007.

[70] T.S. O'Donovan and D.B. Murray. Jet impingement heat transfer – Part II: A temporal investigation of heat transfer and local fluid velocities. *International Journal of Heat and Mass Transfer*, **50**: 3302–3314, 2007.

[71] S. Roux, M. Fénot, G. Lalizel, L-E. Brizzi, and E. Dorignac. Experimental investigation of the flow and heat transfer of an impinging jet under acoustic excitation. *International Journal of Heat and Mass Transfer*, **54**: 3277–3290, 2011.

[72] M. Fénot, J-J. Vullierme, and E. Dorignac. A heat transfer measurement of jet impingement with high injection temperature. *Comptes Rendus Mécanique*, **333**: 778–782, 2005.

[73] R.J. Goldstein, A.I. Behbahani, and K.K. Heppelmann. Streamwise distribution of the recovery factor and the local heat transfer coefficient to an impinging circular air jet. *International journal of heat and mass transfer*, **29**: 1227–1235, 1986.

[74] J.W. Baughn, A.E. Hechanova, and X. Yan. An experimental study of entrainment effects on the heat transfer from a flat surface to a heated circular impinging jet. *Journal of Heat Transfer*, **113**: 1023–1025, 1991.

[75] D.R.S. Guerra, J. Su, and A.P.S. Freire. The near wall behavior of an impinging jet. *International journal of heat and mass transfer*, **48**: 2829–2840, 2005.

[76] H.M. Hofmann, D.L. Movileanu, M. Kind, and H. Martin. Influence of a pulsation on heat transfer and flow structure in submerged impinging jets. *International Journal of Heat and Mass Transfer*, **50**: 3638–3648, 2007.

[77] B. Sagot, G. Antonini, A. Christgen, and F. Buron. Jet impingement heat transfer on a flat plate at a constant wall temperature. *International Journal of Thermal Sciences*, **47**: 1610–1619, 2008.

[78] R. Wilke and J. Sesterhenn. "Direct numerical simulation of heat transfer of a round subsonic impinging jet" in: *Active Flow and Combustion Control 2014*. Springer, 2015. 147–159

[79] T. Hällqvist. *Large eddy simulation of impinging jets with heat transfer*. PhD thesis, 2006.

[80] M. Hadžiabdić and K. Hanjalić. Vortical structures and heat transfer in a round impinging jet. *Journal of Fluid Mechanics*, **596**: 221–260, 2008.

[81] R.J. Jefferson-Loveday and P.G. Tucker. Wall-resolved LES and zonal LES of round jet impingement heat transfer on a flat plate. *Numerical Heat Transfer, Part B*, **59**: 190–208, 2011.

[82] S. Kubacki and E. Dick. Hybrid RANS/LES of flow and heat transfer in round impinging jets. *International Journal of Heat and Fluid Flow*, **32**: 631–651, 2011.

[83] N. Uddin, S.O. Neumann, and B. Weigand. LES simulations of an impinging jet: On the origin of the second peak in the Nusselt number distribution. *International Journal of Heat and Mass Transfer*, **57**: 356–368, 2013.

[84] T. Dairay, V. Fortuné, E. Lamballais, and L.E. Brizzi. LES of a turbulent jet impinging on a heated wall using high-order numerical schemes. *International Journal of Heat and Fluid Flow*, **50**: 177–187, 2014.

[85] Y.M. Chung, K.H. Luo, and N.D. Sandham. Numerical study of momentum and heat transfer in unsteady impinging jets. *International Journal of Heat and Fluid Flow*, **23**: 592–600, 2002.

[86] W. Rohlfs, H.D. Haustein, O. Garbrecht, and R. Kneer. Insights into the local heat transfer of a submerged impinging jet: Influence of local flow acceleration and vortex-wall interaction. *International Journal of Heat and Mass Transfer*, **55**: 7728–7736, 2012.

[87] M.J. Tummers, J. Jacobse, and S.G.J. Voorbrood. Turbulent flow in the near field of a round impinging jet. *International Journal of Heat and Mass Transfer*, **54**: 4939–4948, 2011.

[88] M. Tsubokura, T. Kobayashi, N. Taniguchi, and W.P. Jones. A numerical study on the eddy structures of impinging jets excited at the inlet. *International journal of heat and fluid flow*, **24**: 500–511, 2003.

[89] I. B. Özdemir and J.H. Whitelaw. Impingement of an axisymmetric jet on unheated and heated flat plates. *Journal of fluid mechanics*, **240**: 503–532, 1992.

[90] M.D. Fox, M. Kurosaka, L. Hedges, and K. Hirano. The influence of vortical structures on the thermal fields of jets. *Journal of Fluid Mechanics*, **255**: 447–472, 1993.

[91] C.O. Popiel and O. Trass. Visualization of a free and impinging round jet. *Experimental Thermal and Fluid Science*, **4**: 253–264, 1991.

[92] B.J. Davidson. Heat transfer from a vibrating circular cylinder. *International Journal of Heat and Mass Transfer*, **16**: 1703–1727, 1973.

[93] K. Ichimiya and S. Watanabe. Numerical Analysis of a Two-Dimensional Jet Impinging on an Oscillated Heat Transfer Surface. *Journal of Heat Transfer*, **131**: 094505, 2009.

[94] A.K. Agarwal, S.K. Goyal, and D.K. Srivastava. Time resolved numerical modeling of oil jet cooling of a medium duty diesel engine piston. *International Communications in Heat and Mass Transfer*, **38**: 1080–1085, 2011.

[95] G. Nasif, R.M. Barron, and R. Balachandar. Numerical Simulation of Piston Cooling With Oil Jet Impingement. *Journal of Heat Transfer*, **138**: 122201, 2016.

[96] G. Nasif, R. Balachandar, and R.M. Barron. CFD Analysis of Heat Transfer Due to Jet Impingement Onto a Heated Disc Bounded by a Cylindrical Wall. *Heat Transfer Engineering*, **37**: 1507–1520, 2016.

[97] D. Klein and G. Hetsroni. Enhancement of heat transfer coefficients by actuation against an impinging jet. *International Journal of Heat and Mass Transfer*, **55**: 4183–4194, 2012.

[98] S.B. Pope. Turbulent Flows. *Cambridge University Press*, **7**: 35–61, 2000.

[99] A.N. Kolmogorov. The local structure of turbulence in incompressible viscous fluid for very large Reynolds numbers. *Dokl. Akad. Nauk SSSR*, **30**: 301–305, 1941.

[100] H.G. Weller, G. Tabor, H. Jasak, and C. Fureby. A tensorial approach to computational continuum mechanics using object-oriented techniques. *Computers in physics*, **12**: 620–631, 1998.

[101] U. Piomelli. Large-eddy simulation: achievements and challenges. *Progress in Aerospace Sciences*, **35**: 335–362, 1999.

[102] J. Smagorinsky. General circulation experiments with the primitive equations: I. the basic experiment*. *Monthly weather review*, **91**: 99–164, 1963.

[103] M. Germano, U. Piomelli, P. Moin, and W.H. Cabot. A dynamic subgrid-scale eddy viscosity model. *Physics of Fluids A: Fluid Dynamics (1989-1993)*, **3**: 1760–1765, 1991.

[104] D.K. Lilly. A Proposed Modification of the Germano-Subgrid-Scale Closure Method. *Physics of Fluids A:Fluid Dynamics*, **4**: 633–635, 1992.

[105] H. Jasak. *Error analysis and estimation for finite volume method with applications to fluid flow*. PhD thesis, 1996.

[106] R. Courant, K. Friedrichs, and H. Lewy. On the partial difference equations of mathematical physics. *IBM journal*, **11**: 215–234, 1967.

[107] S.V. Patankar and D.B. Spalding. A calculation procedure for heat, mass and momentum transfer in three-dimensional parabolic flows. *International journal of heat and mass transfer*, **15**: 1787–1806, 1972.

[108] R.I. Issa. Solution of the implicitly discretised fluid flow equations by operator-splitting. *Journal of computational physics*, **62**: 40–65, 1986.

[109] R.I. Issa, B. Ahmadi-Befrui, K.R. Beshay, and A.D. Gosman. Solution of the implicitly discretised reacting flow equations by operator-splitting. *Journal of Computational Physics*, **93**: 388–410, 1991.

[110] C.M. Rhie and W.L. Chow. Numerical study of the turbulent flow past an airfoil with trailing edge separation. *AIAA journal*, **21**: 1525–1532, 1983.

[111] M. Klein, A. Sadiki, and J. Janicka. A digital filter based generation of inflow data for spatially developing direct numerical or large eddy simulations. *Journal of computational Physics*, **186**: 652–665, 2003.

[112] G.R. Tabor and M.H. Baba-Ahmadi. Inlet conditions for large eddy simulation: a review. *Computers & Fluids*, **39**: 553–567, 2010.

[113] J.W. Jewkes, Y.M. Chung, and P.W. Carpenter. Modifications to a Turbulent Inflow Generation Method for Boundary-Layer Flows. *AIAA Journal*, **49**: 247–250, 2011.

[114] T.S. Lund, X. Wu, and K.D. Squires. Generation of turbulent inflow data for spatially-developing boundary layer simulations. *Journal of Computational Physics*, **140**: 233–258, 1998.

[115] J. Nordström, N. Nordin, and D. Henningson. The fringe region technique and the Fourier method used in the direct numerical simulation of spatially evolving viscous flows. *SIAM Journal on Scientific Computing*, **20**: 1365–1393, 1999.

[116] D.B. Spalding. A single formula for the "law of the wall". *Journal of Applied Mechanics*, **28**: 455–458, 1961.

[117] B.E. Launder and D.B. Spalding. *Lectures in mathematical models of turbulence*. 1972.

[118] S.H. Seyedein, M. Hasan, and A.S. Mujumdar. Modelling of a single confined turbulent slot jet impingement using various k-ϵ turbulence models. *Applied mathematical modelling*, **18**: 526–537, 1994.

[119] V. Yakhot and S.A. Orszag. Renormalization group analysis of turbulence. I. Basic theory. *Journal of scientific computing*, **1**: 3–51, 1986.

[120] T-H. Shih, W.W. Liou, A. Shabbir, Z. Yang, and J. Zhu. A new k-ϵ eddy viscosity model for high reynolds number turbulent flows. *Computers & Fluids*, **24**: 227–238, 1995.

[121] D.C. Wilcox. *Turbulence modeling for CFD*. vol. 2 1998.

[122] F.R. Menter. Two-equation eddy-viscosity turbulence models for engineering applications. *AIAA journal*, **32**: 1598–1605, 1994.

[123] H.M. Hofmann, R. Kaiser, M. Kind, and H. Martin. Calculations of Steady and Pulsating Impinging Jets—An Assessment of 13 Widely used Turbulence Models. *Numerical Heat Transfer, Part B: Fundamentals*, **51**: 565–583, 2007.

[124] F Pellegrini and J Roman. "Scotch: A software package for static mapping by dual recursive bipartitioning of process and architecture graphs" in: *High-Performance Computing and Networking*. vol. 1067 Springer Berlin Heidelberg, 1996. 493–498

[125] Pawsey *Magnus Technical Specifications* https://www.pawsey.org.au/our-systems/magnus-technical-specifications/ Accessed July 7, 2016

[126] J.M.J. den Toonder and F.T.M Nieuwstadt. Reynolds number effects in a turbulent pipe flow for low to moderate Re. *Physics of Fluids (1994-present)*, **9**: 3398–3409, 1997.

[127] M. Guala, S.E. Hommema, and R.J. Adrian. Large-scale and very-large-scale motions in turbulent pipe flow. *Journal of Fluid Mechanics*, **554**: 521–542, 2006.

[128] J.F. Morrison, B.J. McKeon, W. Jiang, and A.J. Smits. Scaling of the streamwise velocity component in turbulent pipe flow. *Journal of Fluid Mechanics*, **508**: 99–131, 2004.

[129] X. Wu and P. Moin. A direct numerical simulation study on the mean velocity characteristics in turbulent pipe flow. *Journal of Fluid Mechanics*, **608**: 81–112, 2008.

[130] J.G.M. Eggels, F. Unger, M.H. Weiss, J. Westerweel, R.J. Adrian, R. Friedrich, and F.T.M. Nieuwstadt. Fully developed turbulent pipe flow: a comparison between direct numerical simulation and experiment. *Journal of Fluid Mechanics*, **268**: 175–210, 1994.

[131] M.V. Zagarola and A.J. Smits. Mean-flow scaling of turbulent pipe flow. *Journal of Fluid Mechanics*, **373**: 33–79, 1998.

[132] C.J. Lawn. The determination of the rate of dissipation in turbulent pipe flow. *Journal of Fluid Mechanics*, **48**: 477–505, 1971.

[133] J.L. Lumley and G.R. Newman. The return to isotropy of homogeneous turbulence. *Journal of Fluid Mechanics*, **82**: 161, 1977.

[134] K. Nishino, M. Samada, K. Kasuya, and K. Torii. Turbulence statistics in the stagnation region of an axisymmetric impinging jet flow. *International Journal of Heat and Fluid Flow*, **17**: 193–201, 1996.

[135] A.J. Simonsen and P. Krogstad. Turbulent stress invariant analysis: Clarification of existing terminology. *Physics of Fluids*, **17**: 088103, 2005.

[136] P. Krogstad and L.E. Torbergsen. Invariant analysis of turbulent pipe flow. *Flow, turbulence and combustion*, **64**: 161–181, 2000.

[137] H.E. Fiedler. "Control of free turbulent shear flows" in: *Flow Control*. Springer, 1998. 335–429

[138] N.R. Panchapakesan and J.L. Lumley. Turbulence measurements in axisymmetric jets of air and helium. Part 1. Air jet. *Journal of Fluid Mechanics*, **246**: 197–223, 1993.

[139] C. Bogey and C. Bailly. Turbulence and energy budget in a self-preserving round jet: direct evaluation using large eddy simulation. *Journal of Fluid Mechanics*, **627**: 129–160, 2009.

[140] J. Hunt, A. Wray, and P. Moin. Eddies, streams, and convergence zones in turbulent flows. *Center for Turbulence Research Report*, 193–208, 1988.

[141] S.B. Pope. Ten questions concerning the large-eddy simulation of turbulent flows. *New Journal of Physics*, **6**: 35–35, 2004.

[142] I.B. Celik, Z.N. Cehreli, and I. Yavuz. Index of resolution quality for large eddy simulations. *Journal of Fluids Engineering*, **127**: 949–958, 2005.

[143] D. Pelletier, E. Turgeon, and D. Tremblay. Verification and validation of impinging round jet simulations using an adaptive FEM. *International Journal for Numerical Methods in Fluids*, **44**: 737–763, 2004.

[144] N. Zuckerman and N. Lior. Impingement heat transfer: correlations and numerical modeling. *Journal of heat transfer*, **127**: 544–552, 2005.

[145] P.A. Durbin. On the k-3 stagnation point anomaly. *International journal of heat and fluid flow*, **17**: 89–90, 1996.

[146] V. Yakhot and L.M. Smith. The renormalization group, the ϵ-expansion and derivation of turbulence models. *Journal of Scientific Computing*, **7**: 35–61, 1992.

[147] B.E. Launder and B.I. Sharma. Application of the energy-dissipation model of turbulence to the calculation of flow near a spinning disc. *Letters in Heat and Mass transfer*, **1**: 131–137, 1974.

[148] M.M. Gibson and B.E. Launder. Ground effects on pressure fluctuations in the atmospheric boundary layer. *Journal of Fluid Mechanics*, **86**: 491–511, 1978.

[149] H.M. Hofmann, R. Kaiser, M. Kind, and H. Martin. Calculations of steady and pulsating impinging jets — An assessment of 13 widely used turbulence models. *Numerical Heat Transfer, Part B*, **51**: 565–583, 2007.

[150] L.F.G. Geers, M.J Tummers, and K. Hanjalić. Experimental investigation of impinging jet arrays. *Experiments in fluids*, **36**: 946–958, 2004.

[151] K. Nishino, M. Samada, K. Kasuya, and K. Torii. Turbulence statistics in the stagnation region of an axisymmetric impinging jet flow. *International Journal of Heat and Fluid Flow*, **17**: 193–201, 1996.

[152] S. Satake and T. Kunugi. Direct numerical simulation of an impinging jet into parallel disks. *International Journal of Numerical Methods for Heat & Fluid Flow*, **8**: 768–780, 1998.

[153] P. Bradshaw and G.P. Huang. The law of the wall in turbulent flow. **451**: 165–188, 1995.

[154] I. Wygnanski, Y. Katz, and E. Horev. On the applicability of various scaling laws to the turbulent wall jet. *Journal of Fluid Mechanics*, **234**: 669–690, 1992.

[155] P. Aillaud, F. Duchaine, L.Y.M. Gicquel, and S. Didorally. Secondary peak in the Nusselt number distribution of impinging jet flows: A phenomenological analysis. *Physics of Fluids*, **28**: 095110, 2016.

[156] H. Jasak and Z. Tukovic. Automatic mesh motion for the unstructured finite volume method. *Transactions of FAMENA*, **30**: 1–20, 2006.

[157] H. Jasak. "Dynamic mesh handling in OpenFOAM" in: *47th AIAA Aerospace Sciences Meeting*. 2009. 341

[158] T. Liu and J.P. Sullivan. Heat transfer and flow structures in an excited circular impinging jet. *International Journal of Heat and Mass Transfer*, **39**: 3695–3706, 1996.

[159] B. Han and R.J. Goldstein. Instantaneous energy separation in a free jet. Part I. Flow measurement and visualization. *International journal of heat and mass transfer*, **46**: 3975–3981, 2003.

[160] A.J. Yule. Large-scale structure in the mixing layer of a round jet. *Journal of Fluid Mechanics*, **89**: 413–432, 1978.

[161] E. Gutmark and C-M. Ho. Preferred modes and the spreading rates of jets. *Physics of Fluids*, **26**: 2932–2938, 1983.

[162] V.A. Chiriac and A. Ortega. A numerical study of the unsteady flow and heat transfer in a transitional confined slot jet impinging on an isothermal surface. *International Journal of Heat and Mass Transfer*, **45**: 1237–1248, 2002.

[163] J.C. Rolon, D. Veynante, J.P. Martin, and F. Durst. Counter jet stagnation flows. *Experiments in fluids*, **11**: 313–324, 1991.

[164] P. Grenson, O. Léon, P. Reulet, and B. Aupoix. Investigation of an impinging heated jet for a small nozzle-to-plate distance and high Reynolds number: An extensive experimental approach. *International Journal of Heat and Mass Transfer*, **102**: 801–815, 2016.

[165] J. Jeong and F. Hussain. On the identification of a vortex. *Journal of fluid mechanics*, **285**: 69–94, 1995.

[166] Y.M. Chung and T. Talha. Effectiveness of active flow control for turbulent skin friction drag reduction. *Physics of Fluids*, **23**: 025102, 2011.

[167] D.A. Zumbrunnen and M. Aziz. Convective heat transfer enhancement due to intermittency in an impinging jet. *Journal of Heat Transfer*, **115**: 91–98, 1993.

[168] E.C. Mladin and D.A. Zumbrunnen. Dependence of heat transfer to a pulsating stagnation flow on pulse characteristics. *Journal of thermophysics and heat transfer*, **9**: 181–192, 1995.

[169] H.J. Poh, K. Kumar, and A.S. Mujumdar. Heat transfer from a pulsed laminar impinging jet. *International communications in heat and mass transfer*, **32**: 1317–1324, 2005.

[170] R.C. Behera, P. Dutta, and K. Srinivasan. Numerical study of interrupted impinging jets for cooling of electronics. *IEEE Transactions on Components and Packaging Technologies*, **30**: 275–284, 2007.

[171] P. Xu, B. Yu, S. Qiu, H.J. Poh, and A.S. Mujumdar. Turbulent impinging jet heat transfer enhancement due to intermittent pulsation. *International Journal of Thermal Sciences*, **49**: 1247–1252, 2010.

[172] P. Xu, S. Qiu, M. Yu, X. Qiao, and A.S. Mujumdar. A study on the heat and mass transfer properties of multiple pulsating impinging jets. *International communications in heat and mass transfer*, **39**: 378–382, 2012.

[173] B.N. Hewakandamby. A numerical study of heat transfer performance of oscillatory impinging jets. *International Journal of Heat and Mass Transfer*, **52**: 396–406, 2009.

[174] J. Chen, T. Wang, and D.A. Zumbrunnen. Numerical analysis of convective heat transfer from a moving plate cooled by an array of submerged planar jets. *Numerical Heat Transfer, Part A Applications*, **26**: 141–160, 1994.

[175] H. Chattopadhyay, G. Biswas, and N.K. Mitra. Heat transfer from a moving surface due to impinging slot jets. *Journal of heat transfer*, **124**: 433–440, 2002.

[176] M.A.R. Sharif and A. Banerjee. Numerical analysis of heat transfer due to confined slot-jet impingement on a moving plate. *Applied Thermal Engineering*, **29**: 532–540, 2009.

[177] S. Narayanan, A.G. Fedorov, and Y.K. Joshi. Heat and mass transfer during evaporation of thin liquid films confined by nanoporous membranes subjected to air jet impingement. *International Journal of Heat and Mass Transfer*, **58**: 300–311, 2013.

[178] S. Ziada. Active stabilization of a planar jet impinging on a flexible wedge. *Journal of fluids and structures*, **16**: 613–626, 2002.

[179] A.D. Lucey and P.W. Carpenter. A numerical simulation of the interaction of a compliant wall and inviscid flow. *Journal of Fluid Mechanics*, **234**: 121–146, 1992.

[180] T. Endo and R. Himeno. "Direct numerical simulation of turbulent flow over a compliant surface" in: *TSFP*. 2001.

[181] S. Xu, D. Rempfer, and J. Lumley. Turbulence over a compliant surface: numerical simulation and analysis. *Journal of Fluid Mechanics*, **478**: 11–34, 2003.

[182] D. Mukherjee and T.I. Zohdi. Computational modeling of the dynamics and interference effects of an erosive granular jet impacting a porous, compliant surface. *Granular Matter*, **17**: 231–252, 2015.

Every reasonable effort has been made to acknowledge the owners of copyright material. I would be pleased to hear from any copyright owner who has been omitted or incorrectly acknowledged.